Stony Brook University

Synthesis, and/or Structural, Conductivity Investigations of Single and Polycrystalline Fluorides, Ionic Liquids and Conjugated Diynes Using Solid-state Nuclear Magnetic Resonance Spectroscopy and X-ray Diffraction

A Dissertation Presented

by

Stephen A. Boyd

to

The Graduate School

in Partial Fulfillment of the Requirements

for the Degree of

Doctor of Philosophy

in

Chemistry

Stony Brook University

August 2012

Stony Brook University

Stephen A. Boyd

We, the dissertation committee for the above candidate for the **Doctor of Philosophy** degree, hereby recommend acceptance of this dissertation

(Clare P. Grey, D. Phil., Adviser)

Professor, Department of Chemistry, Stony Brook University

(Joseph W. Lauher, Ph. D., Chairperson)

Professor, Department of Chemistry, Stony Brook University

(Michael G. White, Ph. D., Third Member)

Professor, Department of Chemistry, Stony Brook University

(Steven G. Greenbaum, Ph. D., Outside Member)

Professor, Department of Physics and Astronomy, CUNY at Hunter College

This dissertation is accepted by the Graduate School.

Charles Taber
Dean of the Graduate School

Abstract of the Dissertation

Synthesis, and/or Structural, Conductivity Investigations of Single and Polycrystalline Fluorides, Ionic Liquids and Conjugated Diynes Using Solid-state Nuclear Magnetic Resonance Spectroscopy and X-ray Diffraction

by

Stephen A. Boyd

Doctor of Philosophy

in

Chemistry

Stony Brook University

2012

One overarching focus of solid-state chemistry has evolved due to the desire to understand the structures and mechanisms underlying conductivity, whether electronic or ionic, and to seek ways toward enhancement and control of those mechanisms and materials. Modern strategies are also shaped by environmental concerns and these concerns have, in turn, influenced the search for synthetic routes which employ more benign methods. The first sections of this dissertation describe adapted and modified reverse-micellar methods, as applied toward the room-temperature synthesis of several different types of binary and lanthanide-doped, monodisperse, nanoparticle (20-40nm), polycrystalline fluorides. Their structures were investigated using Magic-angle Spinning Nuclear Magnetic Resonance (MAS NMR) and X-ray Crystallography.

The difficulty of applying these aqueous methods toward nanoparticle lead fluoride (PbF_2) was surmounted when a novel crystal, cetyltrimethylammonium hexafluorosilicate monohydrate, was synthesized, its crystal structure solved, and employed as a fluoride delivery mechanism to successfully synthesize both α- and β-phase PbF_2.

MAS NMR spectroscopy is well-suited as an investigative tool for both crystalline and non-crystalline materials. Two sections of the dissertation deal with two types of compounds in which MAS NMR multinuclear pulse techniques (^{19}F, ^{7}Li, ^{1}H, and ^{13}C) play a critical role in the deduction of structure (conjugated diynes) and conductive behavior as a function of temperature (ionic liquids).

The final sections of this dissertation again rely heavily on X-ray crystallography and MAS NMR, as well as Impedance Spectroscopy and EXAFS/XANES via collaborative efforts, to examine fluoride conductivity and temperature-dependent behavior of fluoride materials. The super-Lewis acid, antimony pentafluoride, was used to explore whether morphology affects mobility across grain boundaries when vacancies are artificially induced in both nanoparticles as well as their larger polycrystallite analogs. In a collaborative effort, barium fluoride and calcium fluoride single-crystal heterostructures were grown by the Joachim Maier Group and were used to elucidate the precise mechanisms of observed conductivity enhancement in these heterostructures.

To my parents, Barbara and Bruce,
my adviser, Clare P. Grey, D. Phil.
and
to my Vanessa, Declan, Gavin and Fiona

nur mit Liebe, Stärke und Beharrlichkeit

Table of Contents

Table of Contents.....vii

List of Figures.....xv

List of Tables.....xxvii

Acknowledgments.....xxx

Chapter 1

Introduction

1.1 Introduction to Binary Fluorides and Basic Crystallography.....1

1.2 Reverse Micelle Chemistry.....5

1.3 A Brief Word on Clifford Algebra, Lie Theory and Geometric Algebra.....7

1.4 Solid-state Nuclear Magnetic Resonance (NMR) Spectroscopy.....9

1.4.1 Motivation.....9

1.4.2 Origin and Interactions in NMR.....9

1.4.3 The Radio Frequency Hamiltonian.....13

1.4.4 Intrinsic and Extrinsic NMR Hamiltonians.....15

1.4.5 Chemical Shielding Interactions.....17

1.4.6 Dipole-Dipole Interactions.....21

1.4.7 Indirect (through-bond) Pseudo-dipolar Interaction: Scalar Coupling.....25

1.5 Solid-State NMR Phenomena and Methods.....26

1.5.1 Magic-angle Spinning (MAS).....27

1.5.1.1 Setting the Magic Angle: Practical Aspects.....28

1.5.2 Cross Polarization (CP).....30

1.5.3 Dipolar Recoupling.....32

1.5.4 Variable-amplitude Cross Polarization (VACP).....35

1.5.5 Ramped-amplitude Cross Polarization (RAMP).....37

Chapter 2

Preparation of MF_3 (M = Nd, Sm, Ho, La), MF_2 (M=, La_xCa_{1-x}; x = 0.06;F_{2+x}) Nanoparticles via Reverse Micelle Microemulsion: Synthesis and Characterization

2.1 Introduction....49

2.2 Experimental....52

2.2.1 MF_3 Synthesis....52

2.2.2 PbF_2 Synthesis....53

2.2.3 $La_xCa_{1-x}F_{2+x}$ Preparation....54

2.2.4 Sample Characterization Preparation....54

2.3 Results....55

2.4 Discussion....69

2.4 Conclusion....74

2.5 References....75

1.5.6 Ramped-amplitude Cross Polarization-Polarization Inversion(RAMP-PI).....38

1.5.7 Ramped-amplitude Cross Polariztion - Polarization Inversion RAMP-CP-PI.....39

1.6 Electrochemical Impedance Spectroscopy (EIS)....40

1.6.1 Theoretical Origins of the Impedance Signal observed in EIS....40

1.6.2 Warburg Diffusion Impedance....43

1.6 Aim of the Dissertation....44

1.7 References....45

Chapter 2

Preparation of MF_3 (M = Nd, Sm, Ho, La), MF_2 (M=, La_xCa_{1-x}; x = 0.06;F_{2+x}) Nanoparticles via Reverse Micelle Microemulsion: Synthesis and Characterization

2.1 Introduction....49

2.2 Experimental....52

2.2.1 MF_3 Synthesis....52

2.2.2 PbF_2 Synthesis....53

2.2.3 $La_xCa_{1-x}F_{2+x}$ Preparation....54

2.2.4 Sample Characterization Preparation....54

2.3 Results....55

2.4 Discussion....69

2.4 Conclusion....74

2.5 References....75

Chapter 3

Inadvertent Synthesis of Cetyltrimethylammonium Hexafluorosilicate Dihydrate as a Delivery System for Fluoride Anion in the Successful Room-temperature Synthesis of Nanoparticle α and β-PbF_2

3.1 Introduction....78

3.2 Experimental....81

3.2.1 Failure to substitute Bromine for Fluorine in the CTAB surfactant....81

3.2.2 Sample Characterization Preparation....82

3.2.2.1 Single-crystal X-ray Diffraction....83

3.2.2.2 MAS NMR....83

3.3 Results.....84
3.4 Discussion.....93
3.5 Conclusion.....99
3.6 References.....100

Chapter 4

A Combined, Ramped-Amplitude-Cross Polarization Spectral Editing (RAMP-CP-PI) $\{^{1}H\}^{13}C$ Investigation into Carbon Chemical Shift Assignment of Poly(di-iododiacetylene)

4.1 Introduction.....102
4.1.1 Preparation and Challenges of Polymerized Diacetylenes and Poly(diiododiacetylene) (PIDA).....103
4.1.2 The Cross-Polarization Experiment.....106
4.1.3 Spectral Editing.....112
4.2 Experimental.....114
4.3 Results.....116
4.3.1: Hexamethylbenzene (HMB).....116
4.3.2: PIDA.....119
4.4 Discussion.....126
4.4.1 Chemical Shift Assignment.....126
4.5 Conclusion.....129
4.6 References.....130

Chapter 5

A ^{19}F MAS NMR Investigation into the Mechanisms of Ionic Conductivity of Calcium Fluoride/Barium Fluoride Heterostructures Deposited via Molecular Beam Epitaxy

4.1 Introduction.....133

5.1.1 Space-charge Model Basics Explained.....133

5.1.2 Previous Work.....136

5.1.3 NMR Studies of Transport: the role of T_1 in assessing ionic mobility.....138

5.2 Experimental.....140

5.2.1 Sample Preparation.....140

5.2.2 MAS NMR.....143

5.3 Results.....143

5.4 Discussion.....152

5.4.1 Chemical Shift Assignment.....152

5.4.2 Fluorine motion.....155

5.4.3 Temperature effects.....158

5.5 Conclusions and Future Work.....159

5.6 References.....161

Chapter 6

Investigative studies of Antimony-pentafluoride loaded Micro- and Nanopolycrystalline Barium Fluoride: Structure and Ionic Conductivity

6.1 Introduction....164

6.2 Experimental....165

6.2.1 Sample Preparation....165

6.2.2 MAS NMR....167

6.2.3 X-ray Diffractometry....168

6.2.4 Extended X-ray Absorption Fine Structure (EXAFS) Data....169

6.2.5 Electrochemical Impedance Spectroscopy (EIS)....170

6.3 Results....171

6.4 Discussion....193

6.4.1 MAS NMR....193

6.4.2 XAS/EXAFS....196

6.4.3 Chemical Shift Assignment....198

6.4.4 Powder XRD....198

6.4.5 Spin Diffusion and Fluorine Motion....199

6.4.6 Conductivity....199

6.5 Conclusions....202

6.6 End of Dissertation - Final Statement....203

6.7 References....204

6.8 References (by Chapter)....206

List of Figures

Chapter 1

Figure 1.1: A schematic of the $Fm\bar{3}m$ (fluorite) crystal structure. Note the FCC motif, due to the 1/8 atomic participation at the six vertices and the 1/2-atom participation of each from the faces of the cube to the unit cell.....2

Figure 1.2: A simple schematic of the basic mechanics underlying diffraction in a crystal. Note the planar distances and the angle of incidence (θ) are related by Bragg's Law of Diffraction: $2d\sin\theta = n\lambda$.....4

Figure 1.3: A graphic depiction of the structure of the type of reverse-micellar system used in the syntheses described in this dissertation. This cartoon shows the components used as the delivery vehicles for the ions involved in the synthesis: barium nitrate ($Ba(NO_3)_2$), ammonium fluoride (NH_4F); the long, non-polar tails of cetyltrimethylammonium bromide (CTAB) and racemic 2-octanol. Note the bromide anion is depicted as already having dissociated inside the polar regime.....6

Figure 1.4: a schematic depiction of the allowed spin transitions ($\Delta m = \pm 1$) an the energy associated with that transition (ΔE), in the simplest, spin 1/2 case.....14

Figure 1.5: a schematic depicting precession at a Larmor frequency, ω_0, of a magnetic moment, μ, in a static, homogenous, magnetic field (parallel to the z-direction).....15

Figure 1.6: Diagram representing the three tensorial, ellipsoidal CS components, depicted in increasing order of shielding ($\sigma_{xx} < \sigma_{yy} < \sigma_{zz}$). The Euler angles ($\alpha$, β) are included, which are used to define the orientation of the PAS, relative to the laboratory frame; the value of the γ Euler angle is 0°.....19

Figure 1.7: Diagram representing the two angles (θ, ϕ) which denote the spherical polar components of the internuclear vector r_{IS}. This system is used to describe many systems where polar spherical coordinates are more utile.....23

Figure 1.8: Diagram depicting a principal nuclear spin axis r, precessing at an angle, ζ, with representations of (θ, Ψ) of possible values between r and z/B_0. ω_r = spinning speed of the rotor...29

Figure 1.9 a-c: Schematics representing various interactions. Figure 1.9a: a cartoon of the pulse sequence for the I, S spins for CP-MAS. Figure 1.9b: depiction of the Zeeman splitting (energy difference) between the spins in the laboratory frame. Figure 1.9c: the relative energies as viewed from within the doubly rotating frame, where co-precession in the x-y plane for both spins occurs and, therefore, I→S cross polarization.....32

Figure 1.10: Depiction of the REDOR experiment. The REDOR experiment is performed in two parts. In part A (control), the I spins are perturbed using the echo pulse sequence outlined above, while nothing is imposed on the S spins. In Part B (the double-resonance experiment), which immediately follows (after a proper recycle delay time), the same echo pulse sequence is performed on the I spins while the S spins are subjected to a p-pulse train as outlined above. The timeline for the sequence of pulse events is included at the bottom (starting at time t = 0). τ_R = time for one rotor period; n = number of rotor periods.....34

Figure 1.12: A schematic of the Variable Amplitude Cross Polarization pulse sequence. Note the changes in amplitude on the I spin pulse for the CP-aspect of the pulse, in order to eliminate energetic mismatches by creating a series of Hartmann-Hahn conditions. τ_{CP} = contact time.....36

Figure 1.13: A schematic of the Ramped-amplitude Cross Polarization pulse sequence. Note the smooth (monotonic) increase in amplitude of the cross polarization aspect of the pulse sequence, including the fact that in RAMP-CP, in contrast to VACP, the modulation is on the S spins.....37

Figure 1.14: A schematic of the Cross Polarization Polarization Inversion (CPPI) pulse sequence, adapted from [58]. Note the x, x phase inversion interchanges between the I and S spins during the τ_{PI} portion of the pulse sequence.....38

Figure 1.15: Impedance curve of bulk BaF_2 loaded with 12μl of SbF_5 in comparison to the same mass of nanoparticle BaF_2 with the same loading level. Note the change in conductivity behavior of the bulk (improved) relative to the nanoparticles (poor), but that the mechanism of conductivity for the nanoparticles is purely diffusive.....42

Chapter 2

Figure 2.1: x-ray diffraction pattern of LaF_3 nanoparticle sample with JCPDS Miller Index overlay.....56

Figure 2.2.1: x-ray diffraction pattern of SmF_3 with JCPDS Miller Index overlay.....57

Figure 2.2.2: x-ray diffraction pattern of SmF_3 with JCPDS Miller Index overlay.....58

Figure 2.3: x-ray diffraction pattern of NdF_3 with JCPDS Miller Index overlay.....59

Figure 2.4.1: x-ray diffraction pattern of α, β–PbF_2 with JCPDS Miller Index overlay of only the β-PbF_2 phase (in blue).....60

Figure 2.4.2: x-ray diffraction pattern of α, β–PbF_2 with JCPDS Miller Index overlay.....61

Figure 2.4.3: x-ray diffraction pattern of α, β–PbF_2 with JCPDS Miller Index overlay of both the α and β JCPDS phase reflections overlaid (β-phase in blue; α-phase in pink).....62

Figure 2.5: x-ray diffraction pattern of $La_xCa_{1-x}F_{2+x}$ (x=0.06) with JCPDS Miller Index overlay63

Figure 2.6 x-ray diffraction pattern of SmF_3 nanoparticle sample.....64

Figure 2.7: x-ray diffraction pattern of LaF_3 nanoparticle sample.....64

Figure 2.8: x-ray diffraction pattern of NdF_3 nanoparticle sample.....65

Figure 2.9: x-ray diffraction pattern of HoF_3 nanoparticle sample.....65

Figure 2.10: x-ray diffraction pattern of $La_{0.06}Ca_{0.94}F_{2.06}$ nanoparticle sample.....66

Figure 2.11: TEM image of LaF_3 nanoparticle sample.....68

Chapter 3

Figure 3.1 Depiction of the crystallographic unit cell for $(CTA)_2 \cdot SiF_6 \cdot 2H_2O$.....88

Figure 3.2: Ellipsoid view of the atoms involved in the interactions between the constituents that make up the $(CTA)_2 \cdot SiF_6 \cdot 2H_2O$ crystallographic unit cell. Inset: trimethyl ammonium head.....89

Figure 3.3 Single-pulse excitation, ^{19}F MAS NMR spectrum of the $(CTA)_2 \cdot SiF_6 \cdot 2H_2O$ crystal. Inset: magnified detail of slight shoulder at -123.6ppm. Asterisks which appear indicate spinning side-bands.....91

Figure 3.4: $\{^{19}F\}^{13}C$ VACPx spectrum which indirectly reveal the interactions between the 19F and 13C in the $(CTA)_2 \cdot SiF_6 \cdot 2H_2O$ crystal. Note the ^{13}C signal at 15ppm which designates the methylene carbon (C14) in Table 3.1a and in Figure 3.1. The intense signal at 50ppm is the methyl carbon bound to the N1 Nitrogen, depicted in Figure 3.2 and is tabulated in Table 3.2.....92

Chapter 4

Figure 4.1 a) diiodobutadiyne monomer as the basic building block for **b**; b) poly(diiododiacetylene) PIDA "guest" conjugated polymer: the target molecule; c), d): 1-3- and 1-4-bispyridyl oxalamide co-crystals, A and B, respectively: the "host" crystal which provides a scaffold-like structure, supporting the guest and facilitating topochemical interaction.....104

Figure 4.2: Schematic of a CP-MAS pulse sequence.....107

Figure 4.3a: space-filling, crystallographically accurate rendition of the 1·4bis pyridyl oxalamide co-crystal.....109

Figure 4.3b: detail highlighting approximate distances between nearest protons/carbons; minimum/maximum interatomic C—H distances (see text below) in overlay orange arrows; pyridyl protons are white space-filling spheres. Note the N—I halogen bond (blue and purple space-filling spheres).....109

Figure 4.4: an illustration of a representative Hartmann-Hahn power array experiment. Short ranges of power values (see peaks within oval above) satisfy, but above and below, the combination of power and spinning speed (rotor periods: "n") engenders a loss of signal intensity.....110

Figure 4.5: Schemactic of a VACP pulse sequence.....111

Figure 4.6: Schematic of a RAMP-CP pulse sequence.....111

Figure 4.7a: Graph and times for magnetization buildup curves (T_{IS}) of representative carbon-proton interactions; $I(t) = I_0(1- \exp(t/T_{IS})$. Explicit values for the magnetization buildup times are as follows: T_{IS} (methyl): 350μs; methine: 150μs; methylene: 90μs.....113

Figure 4.7b: Representative curves of carbon $T_{1\rho}$ for selected species.....113

Figure 4.8: Schematic of the new RAMP-CP-PI pulse sequence.....114

Figure 4.9a: RAMP-CP-PI of HMB: the methyl carbon @ 28.5ppm is erect while the benzene carbon (no bound protons) is inverted @ 141ppm. Acquisition conditions: RT; 14kHz spinning speed; 62.5kHz RF power (4μs ⅞ time); 0.1ms (+)CT, 2ms(-)CT. Refer to Table 4.2 (see below) for a complete tabulation of ± contact times and their effects on these respective peaks.....116

Figure 4.9b: (companion Figure to Table 2, see yellow highlighted data): Plot of signal intensity per carbon for the standard used here, HMB, as a function of (-) contact time (200μs - 600μs). NB: (+) contact time remains ***fixed*** at 6ms; Methyl curve dipping below zero indicates peak inversion.....118

Figure 4.10a: Spectrum 1. "Normal" CP-MAS ^{13}C NMR Spectra of the cocrystals (x-axis is in ppm): (A) 1•3 before pressing; (B) 1•3 after pressing to >6 GPa; Blue arrows indicate peaks corresponding to monomer 1 (see Figure 1a) ; red arrows indicate peaks corresponding to the PIDA polymer (see Figure 1b). Reproduced from [3], where this appears as Figure 5, page 4419.....118

Figure 4.10b: RAMP-CP-PI spectrum with a 50μs negative contact time "A" (see Table 4.2).....120

Figure 4.10c: RAMP-CP-PI spectrum with a 269μs negative contact time "B" (see Table 4.2)....121

Figure 4.10d: RAMP-CP-PI spectrum with a 500μs negative contact time "C" (see Table 4.2)....122

Figure 4.10e: RAMP-CP-PI spectrum with a 1ms negative contact time "D" (see Table 4.2)....123

Figure 4.10f: RAMP-CP-PI spectrum with a 1.25ms negative contact time "E" (see Table 4.2)...123

Figure 4.10g: RAMP-CP-PI spectrum with a 2ms negative contact time "F" (see Table 4.2).....124

Chapter 5

Figure 5.1: Graph (reprinted from [4]) depicting conductivity parallel to the interface as a function of temperature and layer thickness. Colors indicate semi-infinite space-charge zones (red) and finite space-charge zones (green) as compared against the bulk (black). The materials investigated in [4] were grown via MBE to a total thickness of ~500nm.....136

Figure 5.2: TEM of heterostructures (reproduced from [6]) with a period (interlayer thickness) of 18nm. Arrows indicate local distortions due to different lattice constants or different crystallographic orientations within individual layers.....137

Figure 5.3: (reprinted from [7]): The Debye Length ($n\lambda$) as illustrated for cationic vacancies V'_M and cationic interstitials, M^+_I, for charge (c) and length into the bulk (eg lim $x \rightarrow \infty$).....137

Experimental Figure 5.2.1: Graphical depiction of the MAS NMR rotor, packed with sanded, cut discs with Al_2O_3 almost completely removed, in order to maximize the insertable number of discs.....141

Figure 5.4: MAS NMR spectrum of BaF_2/CaF_2 heterostructures taken at room temperature (RT). The * and # symbols depict spinning side bands of BaF_2, CaF_2, respectively. The spectrum was acquired with a one-pulse sequence with a 45s pulse delay between scans.....145

Figure 5.5: ^{19}F SPE MAS NMR spectrum of BaF_2/CaF_2 heterostructures taken at 100°C. Symbols †,◊ depict spinning side bands of the new peaks at -4.4, -121.7ppm, respectively.....145

Figure 5.6: ^{19}F single-pulse excitation (SPE) MAS NMR spectrum of BaF_2/CaF_2 heterostructures taken at 200°C.....141

Figure 5.7: Single pulse spectrum taken at RT, following prolonged (35h) heating at 240ºC. The sharp peaks have vanished, presumably due to extended heating. Repeated experiments confirmed that this process is irreversible. The peak at -165ppm was never clearly resolved and is very likely an overlapping sideband.....148

Figure 5.8: A stacked plot (a "pulse-delay" array) of the spectra at the four different pulse-delay times of 1, 5, 10 and 20s collected at RT. The integrated areas of the different resonances are tabulated in Table 5.3, above.....150

Figure 5.9: A plot of the data that appear in Table 2; curve fitting to the following formula: $M(t) = M_0 (1 - e^{-t/T1})$ permits an estimate of actual T_1 times (see inset). All times were measured at 200ºC.....151

Chapter 6

Figure 6.1 a-c: a) pure BaF_2 nanoparticles b) SbF_5-loaded (monolayer) BaF_2 nanoparticles, pre-heating, Ar environment c) post-heating for 2h to 240°C, Ar environment. Wavelength used to collect a) and c) is 0.91Å. Wavelength used to collect b) is 0.89Å. Samples run at the National Synchrotron Light Source (NSLS), Brookhaven National Laboratories. Magenta dotted line at 67° 2θ (420 reflection) is inserted as a visual guide to denote slight changes in reflections, post heating. Post-processing was performed with Jade Powder XRD softare, Rigaku Corporation.....176

Figure 6.1d: A re-depiction of Figure 1b is represented here, with JCPDS overlay of SbF_3 (green) and $Mg(SbF_6)_2$ (orange), isomorphic to $Ba(SbF_6)_2$, which does not exist in the JCPDS database...177

Figure 6.2: ^{121}Sb csecho MAS NMR spectrum collected on a 500MHz spectrometer. Sample was spinning at 18kHz. 36,000 scans were acquired, using an 800ms pulse delay between scans.....178

Figure 6.3: ^{19}F MAS NMR Stackplot demonstrating the temperature dependence of various species in sample A. The fluorine environments represented by the peaks at -14, -28ppm remain unchanged, whereas the SbF_3, SbF_6^- fluorines represented by the peaks at -103, -119ppm are highly influenced by temperature. 14kHz spinning speed, 360MHz. The vertical lines at -28, -119ppm serve as visual guides. Asterisks denote spinning sidebands.....179

Figure 6.4: a ^{19}F MAS NMR SPE stackplot representing spectra of different loadings (samples A, B, F) at 50°C. Magenta, tailed arrow meant to highlight the absence of the characteristic peak -28ppm peak for sample B. Asterisks denote spinning sidebands.....180

Figure 6.5: a ^{19}F MAS NMR SPE stackplot representing spectra of different loadings (samples C, D, E) at 50°C. Note the absence of the peak at -28ppm Spectra were acquired at a field of 360MHz, 1024 scans each.....181

Figure 6.6: ^{19}F MAS NMR SPE Stackplot of a series of single-pulse experiments used to determine T_1 times (see Table 1 for accompanying T_1 times) as a function of temperature. Note the appearance of j-coupling observed with the antimony fluoride species (the manifolds beginning at -88ppm and then in the -109ppm range) at 20°C (293K) during this high-spinning speed (30kHz) series of experiments.....183

Figure 6.7: 2DME Experiment on sample A, acquired at room temperature. Spectrum recorded on a 600MHz Bruker spectrometer, at a 30kHz sample spinning speed, carrier frequency of 564.71MHz. Interaction is evident from the off-diagonal intensities present for each, relative to the other. Purple dotted line inserted as reference for main diagonal. Off-diagonal relationships are indicated by (n,n´) pairs to the on-diagonal signals.....184

Figure 6.8a: XAS μ(E) (in eV; x-axis) versus mu (μ) of sample A (red line), sample F, (dark blue line) pure SbF_3 standard (green line) and pure $NaSbF_6$ standard (royal blue line).....185

Figure 6.8b: non-normalized Fourier Transform moduli in R space of sample A (red line) , sample F (dark blue line), pure SbF_3 standard (green line) and pure $NaSbF_6$ standard (royal blue line).....186

Figure 6.9a: Electrochemical Impedance Spectroscopy (EIS) curve of pristine bulk and nanoparticle BaF_2..... 187

Figure 6.9b: EIS curve of bulk BaF_2 loaded with 6µl of SbF_5 in comparison to the same mass of nanoparticle BaF_2 with the same loading level.....188

Figure 6.9c: EIS curve of bulk BaF_2 loaded with 10µl of SbF_5 in comparison to the same mass of nanoparticle BaF_2 with the same loading level.....189

Figure 6.9d: EIS curve of bulk BaF_2 loaded with 12µl of SbF_5 in comparison to the same mass of nanoparticle BaF_2 with the same loading level. Note the change in conductivity behavior of the bulk (improved) relative to the nanoparticles (poor).....190

Figure 6.9e: EIS stackplot of impedance curves of bulk BaF_2 increasing loadings of SbF_5: ◆ = 6µl, ■ = 8µl, ▲ = 10µl, × = 12µl, × = 16µl.....191

Figure 6.9f: EIS Stackplot of different loadings of nanoparticle BaF_2, in comparison to no-load bulk and nanoparticle BaF_2 (magenta circle, dark blue diamond).....192

Discussion Figure 6.4.1a, b: Reprinted from [12, 13, respectively]. Appearance of F^- interstitial in nanocrystalline CaF_2 in 1a (inset) and in 1b (asterisk). NB: No explanation is given in [13] for the discrepancy in chemical shift assignment (see 1b: 0ppm for CaF_2 should be -109ppm, despite peer-review references to ^{19}F MAS NMR data for CaF_2 in the author's dissertation.....194

List of Tables

Chapter 3

Table 3.1a A list of the elements, crystallographic positions, and U_{eq} for the atoms contained within the $(CTA)_2 \cdot SiF_6 \cdot 2H_2O$ single crystal unit cell.....86

Table 3.1b (Table 3.1a, cot'd) A list of the elements, crystallographic positions, and U_{eq} for the atoms contained within the $(CTA)_2 \cdot SiF_6 \cdot 2H_2O$ single crystal unit cell.....87

Table 3.2: A list of the constituent atoms and their crystallographic positions which make up the trimethyl ammonium head.....90

Table 3.3: Important F—H distances between the cetyltrimethylammonium backbone and the fluorines of the SiF_6^{2-} anion; see Figure 3.2 for labels and relative positions.....96

Chapter 4

Table 4.1: Representative C—H intermolecular distances between oxalamide A protons on the pyridyl ring, methylene groups and diiodobutadiyne monomer carbons. See Figure 3b for a space-filling rendering of the molecules, corresponding labels used in this table and their approximate spatial orientations. For reference, H6a,b, though not visible in Figure 3b, are the methylene protons attached to the pyridinyl ring.....105

Table 4.2: Dependence of peak resolution/suppression on positive and negative contact times. The (ΔC(s/n)) term denotes signal-to-noise ratio. NB: asterisk indicates negative (-) peak.....117

Table 4.3: Tabulation of general morphology per PIDA carbon peak, correlated to negative contact time: ø = flat; (-) = inverted peak; (+) = erect peak. Experiment letters correspond to Figures 9a-f. Peak values are in ppm.....118

Chapter 5

Table 5.1: Tabulation of peak and corresponding integrated area, versus temperature. A one-pulse sequence was used and the pd is 45s. The values are normalized to a scan number of 4896 scans. Only isotropic peaks were integrated; spinning sidebands were not included in the tabulation of these intensities.....149

Table 5.3: integrated area increase per peak, per time interval. These areas correspond to the peaks in the stack plot of Figure 5.8, below.....150

Table 5.4: Table of $T2^{-1}$(kHz) for each peak as a function of temperature.....151

Table 5.5: A tally displaying the ratio of mobile species, relative to the bulk.....151

Table 5.6: Tabulation of peak and corresponding τ_c, τ_c^{-1} values at STP. Colors are just a visual aid to discriminate between the two groups of peaks associated with their respective bulk materials. σ, σT calculated with equations 4-6, using an $H_R = 1$.....156

Chapter 6

Table 6.1: a tabulation of T_1 times for each peak found in the spectrum for sample A, as a function of temperature. The data were collected on a Bruker 600Mhz (14.1T) Avance Spectrometer at a spinning speed of 30kHz. Figure 6.6 (see next page) are the spectra collected from which the data which appear in this table were extracted.....182

Acknowledgments

I am very much at a loss for words as to how grateful and inspired I am by my adviser, Prof. Clare Grey. It is a very odd thing to have been so profoundly moved by another person. Even stranger is the feeling that I am left with, after this simultaneously most traumatic, yet cerebrally and emotionally fulfilling exercise I surely will ever experience. Now that I am a parent, I can say with certitude that it is emotionally identical. What makes the PhD program easily the single most precious experience, however, is that the training I have received has also kindled an unimitigated and accelerating need for more knowledge about how matter works at its most fundamental levels.

Having had less interaction with the Members of my Committee, Professors Michael White, Joseph Lauher and Steven Greenbaum, I nevertheless retain invaluable pedagogic moments that I have had with every single one of them, including crucial information which permitted me to write two Chapters of this Dissertation.

I am truly honored to have worked with so many sharp minds, not only in the Grey Research Group, but beyond. Dr. Luming Peng first initiated me to Nuclear Magnetic Resonance, Dr. Peter Chupas and Dr. Santanu Chaudhuri both guided me upon my arrival and beyond. I am grateful to Dr. Julien Brèger and Dr. Nicolas Dupre, Dr. Jordi Cabana-Jiménez and Bariş Key for their patient explanations of pair distribution function, GSAS, Rietveld refinements and additional esoterics of x-ray crystallography. Some of the most valuable tricks regarding electromagnetics, tuning and pulse sequences was from Prof. Brian Philips. Dr. Sylvio Indris was crucial in his tutelage, which manifested in a chapter of this dissertation. Without him, I would not have understood the subtleties of adiabatic passage. Dr. Rangeet Bhattacharyya was fabulous in explaining the quantum fundamentals of angular momentum and I remember what he taught

me every time I pick up A.R. Edmonds' seminal book, which is happily, quite often. I am very grateful to Dr. Lesley and Dr. Christopher Wilhelm for the exhaustive hours of pulse programming and probe surgery. I honestly do not know how many times I took apart the proton amplifier to get our experiments working.

I look very fondly to both Prof. Phil Grandinetti and Dr. Nicole Trease for showing me the truly functional beauty of nuclear magnetic resonance. Indeed, my conversations with them and the talks they have given are why I chose to focus on the Electric Field Gradient for both my Third Meeting, as well as a future project. I have kept my promise to Dr. Trease, so I will soon be reading her dissertation with great joy, but have yet to turn a single page.

One of the most cherished friends and colleagues I thankfully have found are Dr. Paul Sideris, Dr. Patryk Gumann and Dr. John Palumbo. Collectively, I have learned as much from these three individuals as one could learn in a lifetime of scientific and mathematical training. I sincerely hope I can collaborate with them on future physics, chemistry and mathematics efforts, as well as an occasional Hefe Weizen.

Chapter 1

Introduction

Prologue

Fluorides and ionic transport within their structures were found to be best studied by the use of Magic-angle Spinning Nuclear Magnetic Resonance, X-ray diffraction and Electrochemical Impedance Spectroscopy.

1.1 Introduction to Binary Fluorides and Basic Crystallography

Fluorides in general and binary fluorides in particular represent effective structures to study, due toe their simple makeup. Binary fluorides fall into the class M_xF_y. When the x:y ratio is 1:2, the system is so common that an alternative, acceptable term referring to this class of compounds is the term *fluorite*, due to the ubiquity of this type of crystal found in nature and its early historical discovery. When the x:y ratio is 1:3, the historical term *tysonite* is historically (but sometimes incorrectly) used. Prior to discovery of different phases of the tysonite crystal, which nevertheless share the same molecular formula (yttrium trifluoride: YF_3), it was assumed that only a single crystallographic structure existed[1,2]. The subtle differences between these two phases are covered in more detail in the relevant chapters of this dissertation.

The basic counting molecular counting unit for crystals representing the simplest repeating unit is called the *crystallographic unit cell* and variants of this term will often appear in this dissertation. The geometric positions where the atoms sit in the unit cell vary, and are the reason why so many different crystals can be classified in so few categories. These positions are called lattice points and are where each atom occupies and is to vibrate.

Tens of thousands of different crystal systems can be categorized into only 14 Groups, eponymously called Bravais Lattices, due to Auguste Bravais' discovery in 1850. A total of 230 subroups were subsequently discovered, based on their symmetry, which are called Space Groups.

The *packing structure* for atoms refers to how atoms (conceptualized as spheres) can be thought of as three-dimensionally arranged or stacked. In the fluorite crystallographic unit cell, this stacking is called cubic-close packed. Two of three Bravais Lattices will be talked about for MF_2 systems here, called Face-centered Cubic (FCC). As the name implies, the system is cubic: the length, width and height of the unit cell are equal and the angles that make up the vertices of the cube are all 90° (see Figure 1.1, below).

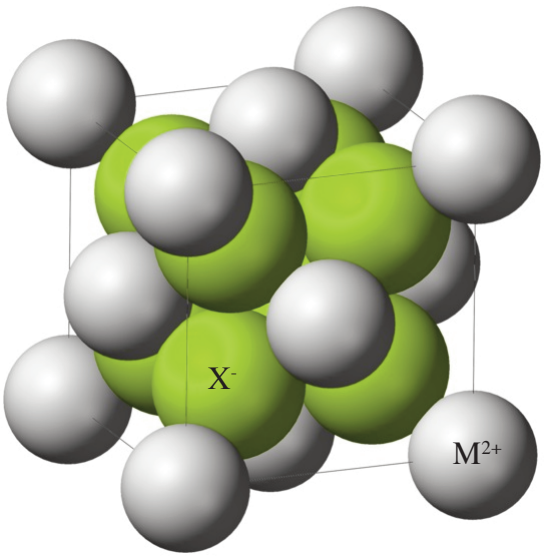

Figure 1.1: A schematic of the $Fm\bar{3}m$ (fluorite) crystal structure. Note the FCC motif, due to the 1/8 atomic participation at the six vertices and the 1/2-atom participation of each from the faces of the cube to the unit cell. Cations are represented by M^{2+} and anions by X^-.

Because of the high symmetry of the arrangement of atoms within the fluorite unit cell, these systems appear very structurally simple. Of the two, the FCC system will largely be discussed in this dissertation and the space group for the crystal system $Fm\bar{3}m$, depicted in Figure 1.1, below.

1.1.1 X-ray Diffraction

Almost every chapter of this dissertation describes at least the incidental use of powder-crystal, single-crystal or other X-ray crystallographic techniques to confirm the structure, determine the purity, the mean crystallite size, changes in reflection due to the deliberate introduction of dopants or the use of more advanced X-ray techniques to deduce oxidation state of a cation within a material. As such, a cursory explanation of X-ray crystallography is provided for the reader, which follows. X-ray crystallography involves the use of extremely narrow-range (e.g. monochromatic) wavelengths of electromagnetic radiation (EMR) in the X-ray band of the electromagnetic spectrum, usually 0.8-50Å or ~$1x10^{14\text{-}16}$Hz. Two means of producing monochromatic X-rays predominate: metal target or synchrotron radiation. In the metal-target method, electrons are liberated from a cathode material and guided via high (~50kV) voltage to a metal target. The target is often Cu, due to the wavelength it produces (1.545Å), although other metal targets such as Cr or Co are also used. Electron collisions with the target eject $1s^n$ electrons from the metal atom (historically called Kα, referring to the first shell of the Bohr model). These inner-shell electrons are replaced by higher shell electrons and the energy shed as the electron migrates to the lower-energy inner shell is the x-ray radiation used.

A second method is via synchrotron radiation. In this method, *bunches* of electrons (usually between 20-50) are managed as a group, accelerated to approximately 0.9c around a large ring. The bunch of electrons is then subjected to a magnetic array at specific points during the circumference, which forces their deceleration. As the electrons decelerate, they shed their accrued energy as monochromatic EMR (hence the etymology of the German word for X-ray, *Bremstrahlung*, or braking radiation). The shear magnitudes involved in synchrotron radiation production are sought after, because these methods result in extremely bright, short-wavelength (<1Å) X-ray radiation, which is desirable for crystalline systems whose atoms have high absorbance coefficients and, therefore, do not produce strong diffraction patterns.

As with any crystal described by the 230 Space Groups, the periodic arrangement of the

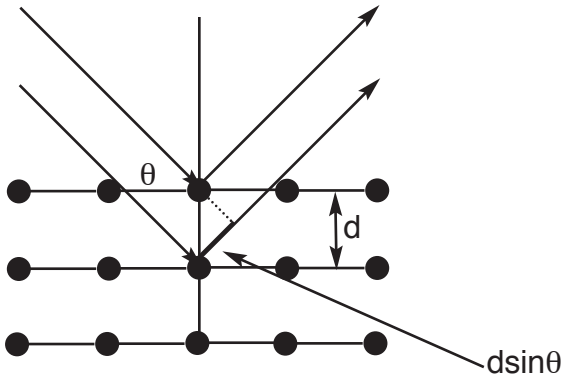

Figure 1.2: Schematic of the basic mechanics underlying diffraction in a crystal. Note the planar distances and the angle of incidence (θ) are related by Bragg's Law of Diffraction: $2d\sin\theta = n\lambda$.

atoms which make up these 3D lattices can be conceptualized as 2D planes, given an arbitrary "view" in some direction. These planes are given crystallographic designations, based on the absolute geometry of the atoms in each unit cell, consistent with a Space Group.

Because of the mechanics involved in X-ray diffraction, these crystallographic designations and the accompanying atomic planes, called Miller Indices (h,k,ℓ), are in reciprocal space. Miller directions [h,k,ℓ] are orthogonal to the planes in reciprocal space. Reciprocal space is used because EMR can be mathematically represented as a plane wave using Euler's axiom ($e^{i\theta} = \cos\theta + i\sin\theta$). If the plane wave has the same periodicity as the crystallographic plane, this manifests as a constructive peak because the two plane waves constructively interfere to a value of unity. Very often this is represented as amplitude in arbitrary units (a.u.), since this value is dependent upon the intensity of the incoming light. A Fourier Transform is required for this information to have geometric meaning, because this reciprocal space needs to be transformed back into so-called real space, for reflections to provide information regarding the atomic positions of the atoms within the crystal.

Diffraction occurs because the EMR interacts with the electron densities surrounding each atom. With both spherical-atomic and unit-cell symmetry in mind, the periodicity of the atoms engenders constructive interference of the EMR in integer multiples (n) of the wavelength of that light (the $n\lambda$ term of Bragg's Law, above, Figure 2), resulting in patterns corresponding to

those crystallographic planes.

Figure 2 is a schematic depicting a simple, arbitrary crystal and the integer trigonometry involved in the calculation, as dictated by the relationship expressed in Bragg's law: $2d\sin\theta = n\lambda$. As will appear in the X-ray Diffraction (XRD) patterns which appear in the chapters of this dissertation, the abscissa of the graphs is in units of 2θ, a logical choice, given the angle of incidence = angle of reflection.

1.2 Reverse Micelle Chemistry

The first approach used to synthesize fluorides in this work involved the use of reverse micelles as microreactor platforms demonstrate several advantages over other synthetic methods. Firstly, the ternary ratios of surfactant, co-surfactant and water mediate surface tension and, therefore, reverse micelle size[3,4]. Secondly, a number of different anionic, cationic and non-polar surfactants and co-surfactant systems (some even with functionalization) to add additional moieties to the resultant precipitated nanocrystal[5,9]. Third, quasi linear control over particle size is achieved merely by the time the cosystems are allowed to react[6,7]. Finally, reverse micelles have been investigated since the early 1980s and the aqueous behavior of fundamental constituents such as cetyltrimethylammonium bromide (CTAB) have been well-studied[9]. Some disadvantages to reverse micelle syntheses are the difficulty involved in the scaling up the volume of synthesized product, as well as the low yield, relative to the amounts of reagents used.

Both a regular micelle and reverse micelle are represented in Figure 1.3 a and b. Micelles refer to hydrophobic (often hydrocarbon) tails of surfactants surrounded by aqueous environments. The reverse micelle is opposite of that used to describe the micellar solvation sphere of surfactant molecules surrounding a non-polar object in an aqueous medium. In this case, both types of micellar structures, CTAB is used. In the reverse micelle, the polar objects are contained within a polar sphere, supported by a boundary mediated by the hydrophilic head and hydrophobic tail of the surfactant (here, CTAB) and co-surfactant/solvent (here, racemic 2-octanol).

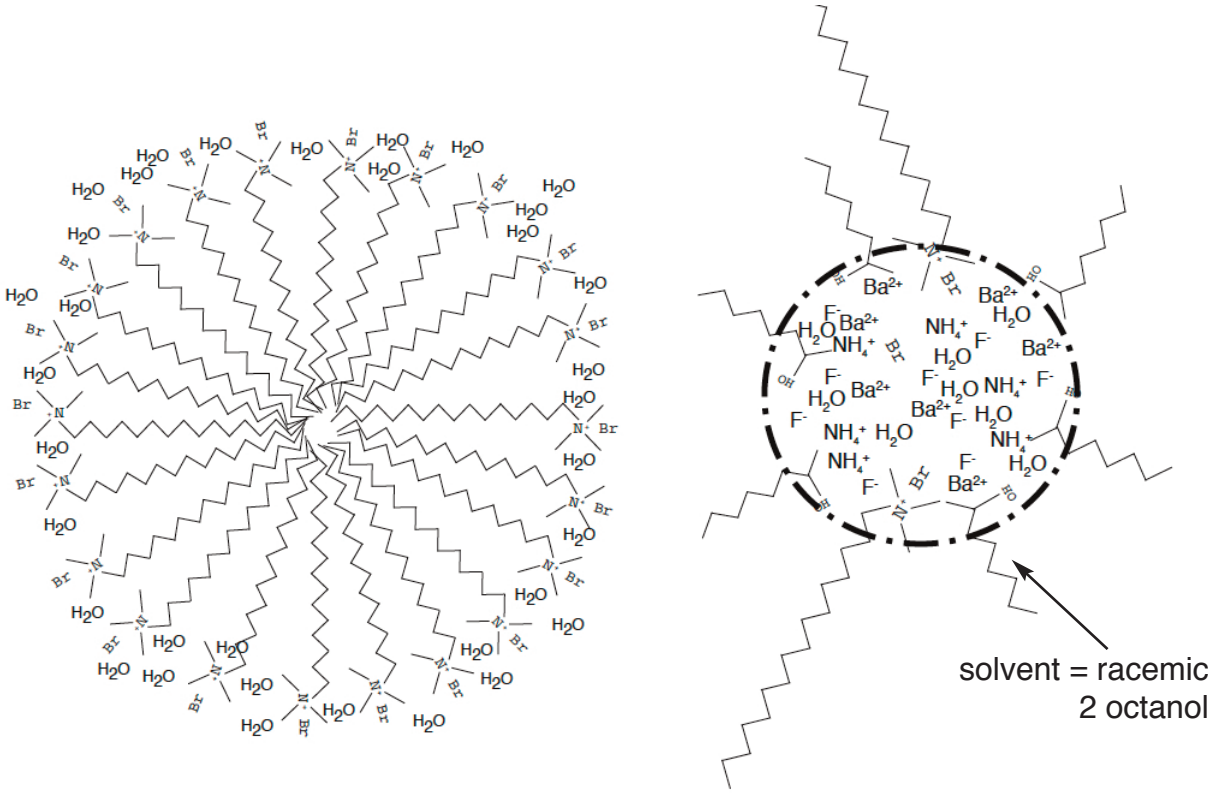

Figure 1.3a, b: **a**) Graphic depiction of a micelle, using the same CTAB molecule as the surfactant, although in this case, the hydrophobic alkyl tails face inward. **b**) A graphic depiction of the structure of the type of reverse-micellar system used in the syntheses described in this dissertation. This cartoon shows the components used as the delivery vehicles for the ions involved in the synthesis: barium nitrate ($Ba(NO_3)_2$), ammonium fluoride (NH_4F); the long, non-polar tails of cetyltrimethylammonium bromide (CTAB) and racemic 2-octanol. Note the bromide anion from CTAB is depicted as already having dissociated inside the polar regime.

A delicate suspension is created (described in detail in following chapters) and is obvious when formed, because the initial mixture is opaque and white, whereas the reverse micelle suspension is transparent. The low vapor pressure of solvents (here, 2-octanol) mandates additional precautions. Simple variables such as ambient laboratory temperature and faulty fume-hood fans contribute to the failure of the reverse micellar suspension to form. In the experiments conducted here, even 10-degree deviations from room temperature either prevented suspension entirely or doubled the time needed for reverse micellar suspension formation.

1.3 A Brief Word on Clifford Algebra, Lie Theory and Geometric Algebra

The unusual nature of Nuclear Magnetic Resonance stems from the fact that nuclear spins behave as quantum mechanical (QM) objects and exhibit the properties of objects studied in Quantum Field Theory (QFT), such as superpositions of states, no adherence to the First Law of Thermodynamics, Markovian behavior, n-dimensional Hilbert Spaces, etc. NMR, with its classic pedagogic representation of spin-vector behavior in flat, three-dimensional space, $\mathbb{R}^3$, is a near perfect example of the spanning nature of QM systems in general, where simple Cartesian axes in $\mathbb{R}^3$ are adequate for explaining basic physical and mathematical operations. The Clifford Algebra lends itself perfectly to NMR, because the Clifford is, by definition, the algebra of orthonormal, positive-definite basis sets in n-dimensional, flat space. In fact, all NMR theory is taught using the tools of the Clifford[18,19,20]. Nuclear spins, like other QM classes of spins, represent a closed, definite, simple Group. The linear, component composition of representations of spin vectors and the naturally closed nature of grouping of mathematical operations and QM objects have again been historically and accurately represented by Lie Groups, consistent with Lie Theory, often thought of as a matrix-based extension of the Clifford. One difficulty with this approach, however, is that not all Lie matrices lend themselves completely to Lie Algebra[21].

As recently as the 1970s, however, a much more advanced method of representing both orthonormal and non-orthogonal dual spaces called Geometric Algebra (GA) was proffered most notably and completely by Hestenes, et al[22,23,24,25,26,27]. The two fundamental differences which make GA superior are i) comprehensive inclusion of different mathematical objects of different dimensions are included within a single Geometric Product, based largely on the geometric object of the bivector (where some bivector, $a \wedge b$, is the wedge product) and ii) the powerful object of the Rotor ($\mathcal{R}$), which is structurally similar to the so-called sandwich operator, a mathematical direction which is heavily used in photonics, NMR and several other fields.

As described in i), above, the advantage of using the basic geometric object of the bivector as a primary tool permits complete work within real, flat space $\mathbb{R}^n$. As is well known, the imaginary plane is simply a rotation applied to a real function (a + *i*b, for example), but the *i* term remains and segregates the imaginary terms from the real terms. Multiplication of *i* by a bivector, however (c + *i*d∧e), merely results in an in-plane rotation of the bivector by $\pi/2$, thereby retaining information contained within these terms. Doran et al. demonstrate their inclusion in $\mathbb{R}^n$ uncovers much valuable information which impacts the physics as a whole[28,29,30,31]. As implied in ii), the Rotor is a powerful mathematical object that decomposes all rotations into a series of hyperplane half reflections within a basis set. This streamlines mathematical operations as a whole, and a single Rotor can be applied to all the manifestations of the bivector contained used in GA, which results in revealing geometric and physical implications for any system to which GA is applied.

A more modern and comprehensive treatment of Spin and Unitary Groups employing GA has been effectively treated by Gull, Lasenby and Doran, falling under the Special Orthogonal and Unitary Group designations SO(n) and U(n)[28-31]. In these later works, particular attention was paid to the utility of GA as streamlined tool to not only encompass spin angular momentum but in fact reveal more information about the nuclear spin system and all but obviate density matrices, given that GA affords a more complete treatment of spin coherence in coupled systems. In fact, U(n) is easily proven to relate to SO(n) simply by dint of the transform from **Im** to **Re**.

In this dissertation, classical pedagogic methods are used to give a brief overview of the phenomenology and some basic tools of NMR and MAS NMR. No GA was used to reformulate these classic methods. It should be noted, however, that a rich and apparently superior reformulation of these classic methodologies is encompassed by GA. The limited reading that this author has done appears to substantially confirm this and that more reading and adoption of GA methods as applied to mathematical physics may be recommendable for future students of NMR.

1.4 Solid-state Nuclear Magnetic Resonance (NMR) Spectroscopy

1.4.1 Motivation

Nuclear Magnetic Resonance and Solid-state NMR in particular are well-suited to examine both crystalline and noncrystalline systems, because the phenomenon of nuclear magnetic resonance relies on the interactions between an applied magnetic field and nuclear spin, which inherently interacts with the electron densities surrounding the nuclei under investigation, resulting in a very sensitive means of probing local atomic and molecular environments. First discovered in 1931, the extreme sensitivity, elemental specificity and atomic-level, quantitative nature of NMR make it an invaluable tool for investigating the physical, chemical and electronic properties, as well as molecular structure of matter[10]. The following paragraphs explain the basics of some nuclear magnetic resonance phenomena, some fundamentals regarding the accommodations that need to be made for solid-state NMR spectroscopy and some specific applications and modifications of the broad canon of NMR pulse sequences and their employment in this dissertation.

1.4.2 Origin and interactions in NMR

The phenomenon of nuclear magnetic resonance arises from the non-zero *spin angular momentum* (often simply referred to as *spin*) that a nucleus may possess. While the baryons (protons and neutrons) which make up the nucleus each possesses non-zero spin (a value of 1/2), it is the number and arrangement of these subatomic particles which afford the nucleus this intrinsic property as a whole. NMR is then synonymously referred to as the method by which bulk magnetization, arising from a sample of spin-active nuclei, often referred to as an *ensemble of spins*, is detected.

The intrinsic angular momentum of a nucleus is proportional to the spin angular momentum or spin via the following equation:

$$\vec{A} = \hbar\hat{I} \qquad 1.4.1$$

where $\hbar$ is Planck's constant, divided by 2π. The magnitude of the of the nuclear spin quantum number, $\vec{A}$, can be defined as:

$$A = \hbar[I(I+1)]^{1/2} \qquad 1.4.2$$

where $\hat{I}$ is the spin of the nucleus.

Consistent with quantum mechanics is the application of one or a series of *operators* or mathematical directives (called *Hamiltonians*) so as to satisfy the linear Schrödinger Equation. Managing QM phenomena in NMR is no different. In NMR, many different Hamiltonians are used which allow one to elucidate the nature of the interactions, as depicted in eq. 1.4.11 below (and which will be discussed in more detail in Section 1.3, whence this equation was reproduced)

$$\hat{H}_{NMR} = \hat{H}_Z + \hat{H}_{rf} + \hat{H}_{cs} + \hat{H}_{D-D} + \hat{H}_J + \hat{H}_Q \qquad 1.4.11$$

Another heavily used mathematical tool in NMR originally found in classical mechanics is the tensor, an object which describes the intercoordinate relationship that exists between two or more coordinate systems (the number of coordinate systems involved designated by the *rank* of the tensor). The individual components of the total NMR Hamiltonian (1.4.11 above) represent the respective interactions of the nuclear spins with their coupling partners. The coupling partner of a spin, I, can be anything found in the system, from an applied magnetic field, to a local magnetic field, another spin, ***I***, or a different spin, ***S***, all of which are vectors and in this particular example here, all of these objects are also valid rank-1 tensors. Again in this particular case here, the product of two vectors (or rank-1 tensors) V⊗W, is a rank-2 tensor, Z_{ij}, The general expression of these types of Hamiltonians is:

$$\hat{H}_\eta = C_\eta \mathbf{I} \cdot \mathbf{Z}_\eta \cdot \mathbf{S}_\eta \qquad 1.4.3$$

Where C_η represents a constant for some interaction, η, Z represents the spatial relationship of two objects and S_η represents the coupling partner (spin, field, etc.) of said interaction with some spin I. This equation can be safely combined by creating a new rank-2 tensor, T_η, which is the tensor product of the spin and the interaction terms ($I \cdot S_\eta$):

$$\hat{H}_\eta = C_\eta Z_\eta \cdot T_\eta \qquad 1.4.4$$

The reformulation of this general Hamiltonian is structurally significant, because it validly represents the Hamiltonian as composed of a spatial component and a spin component.

As with many phenomena in quantum mechanics, the energies associated with the states of the atom, nucleus or what have you, are *degenerate* or of the same energy. The application of such an operator lifts the degeneracy of the energetically equivalent states into separate eigenstates of differing energies. The first operator which can be thought of as being applied in NMR is that of an external magnetic field, which engenders the so-called Zeeman splitting of spin states into 2I+1 separate levels, where I is, again, the spin of the nucleus. This first Hamiltonian can be represented as a coupling of the field to the system:

$$\hat{H} = -\vec{\mu}\vec{B_0} \qquad 1.4.3$$

Upon insertion into a static, homogeneous, magnetic field, the nuclear spins are forced to align either parallel or antiparallel to the direction of the field, yet precess around the oriented direction of the magnetic field (conventionally represented as the +z direction) at a rate which is nucleus-specific. The angular momentum and, therefore, the spin are proportional to the magnetic moment of the nucleus by the relation:

$$\vec{\mu} = \gamma\hbar\hat{I} \qquad 1.4.4$$

where γ is the gyromagnetic ratio, a ratio of a nucleus' angular momentum to its magnetic moment. It is appropriate to introduce γ here, because it is due to the application of the magnetic

field that γ becomes relevant, due to the phenomenon of precession. With the introduction of the relationship between γ and μ, the previous Hamiltonian, 1.3.3., can then be rewritten as:

$$\hat{H} = -\gamma\hbar I_z \vec{B}_0 \qquad 1.4.5$$

Eigenvalues for I_z (the discrete values that come as a result of applying the Hamiltonian along the conventional z-direction) are the total number of spin values which range from -I, -I+1...I are either odd-numbered multiples of 1/2 or whole-number integers, depending on the spin of the nucleus (whether it is a boson, with integer spin or a fermion with n/2-integer spin; n = ±1,3,5...). Selection rules require a unitary change in spin number, $\Delta m_s = \pm 1$ (see Figure 4, below). This requirement for a whole-integer step-up or step-down, simplifies eq. 1.4.5 to:

$$\hbar\omega = -\hbar\gamma\vec{B}_0 \qquad 1.4.6$$

or

$$\omega = -\gamma\vec{B}_0 \qquad 1.4.7$$

as eq. 1.4.6 represents the resonant frequency for a given nucleus in a given magnetic field (see Figure 1.5, below, for a graphic depiction of Larmor Precession). The Larmor frequency, ω_0, in Hz, is the S.I. standard, yet *ppm*, a non-S.I. unit that nevertheless remains the convention often used. This is due to the discovery of the precessional phenomenon in 1895 by J. Larmor[11]. Subsequent calculation of diamagnetic susceptibility of ferromagnetic resonance by Landau and Lifschitz in 1936, soon after Rabi's discovery of nuclear magnetic resonance in 1931, it was found that all were of equal scale (10^{-6}) and indeed, similar in phenomenological origin[12,13,14].

As the correct resonant frequency, ω_{rf} (in MHz, or more commonly, r.f.), is applied, spin transitions (see above) are prompted to take place, because the spins, precessing at the Larmor frequency, ω_0, absorb the frequency. The signals necessary to compile a spectrum begin at the point when the resultant energy, emitted by the spins and received as induced radio frequency in the probe coil, as the magnetization vector rotates in the x—y plane, eventually relaxing back to precessional parallel with the magnetic field.

1.4.3 The Radio Frequency Hamiltonian

In NMR, a collection or *ensemble* of nuclear spins is excited by a pulsed radio-frequency (RF) field with a frequency, ω_{RF}, the so-called carrier frequency, which is usually equal to or near the Larmor frequency. Any difference between the Larmor frequency and the carrier frequency is called the frequency offset. The Hamiltonian is described by the following:

$$\hat{H}_{rf} = -\gamma_I \hbar \hat{I} \cdot \vec{B}_1 \qquad 1.4.9$$

The RF field is always applied perpendicular to the static field, $\vec{B}_0$. If the field is chosen along the x-direction, it can be described by the following column vector:

$$\begin{pmatrix} 2B_1 cos[\omega_{rf} t + \phi] \\ 0 \\ 0 \end{pmatrix} \qquad 1.4.10$$

where B_1 and ϕ represent the magnitude and the phase of the RF pulse, respectively. One can then combine eq.s 1.4.9 and 1.4.10 to form the following:

$$\hat{H}_{rf} = -2\gamma_I \hbar B_1 cos\left[\omega_{rf} t + \phi\right] I_x \qquad 1.4.11$$

Very often in NMR, it is more convenient (as well as mathematically simpler) to transform a Hamiltonian system from one that is time-*de*pendent to one that is time-*in*dependent. This is done by conceptualizing the system as if one were in the rotating frame and this is done so by mathematically transforming the Hamiltonian into the rotating frame, combining term into the column vector:

$$\begin{pmatrix} B_1 cos\phi \\ B_1 sin\phi \\ 0 \end{pmatrix} \qquad 1.4.12$$

Now, eqs. 1.4.11 and 12 can be combined to reformulate the Hamiltonian in the rotating frame, as depicted below:

$$\hat{H}_{rf} = -\gamma_I \hbar B_1 \left(I_x cos\phi + I_y sin\phi\right) = -\hbar\omega_I \left(I_x cos\phi + I_y sin\phi\right) \qquad 1.4.13$$

where $\omega_I = \gamma_I B_I$

This rotor-frame transformation introduces a fictitious magnetic field, $\vec{B}_f = -\omega_{rf}/\gamma$ in the

rotating frame with a direction opposite to the direction of the external magnetic field, $\vec{B}_0$. The external magnetic field along the z-direction in the rotating frame has now become:

$$\vec{B}_z = \vec{B}_0 - \vec{B}_f = \frac{1}{\gamma_I}(\omega_0 - \omega_{rf}) \qquad 1.4.14$$

The rf frequency, ω_{rf}, is usually set very near or equal to ω_0. The (ω_{rf} - ω_0) term is called the resonance or frequency offset. When $\omega_0 = \omega_{rf}$, the rf radiation is said to be *on-resonance*. In general, $\omega_{rf} >> (\omega_{rf} - \omega_0)$, which means that the effective field in the rotating frame, $\vec{B}_{eff} \approx B_1$. In most (but not all) cases, this is requisite for effective saturation of the spins with rf radiation. As such, one can consider the bulk magnetic moment or magnetization (the net sum of all the nuclear spin vectors), rotating along in the direction of the $\vec{B}_1$ field, actually in the rotating frame when an rf pulse is applied. The duration of the applied rf field, called a pulse, τ_p, determines the tip angle of the magnetization:

$$\theta_p = \gamma_I B_I \tau_p \qquad 1.4.15$$

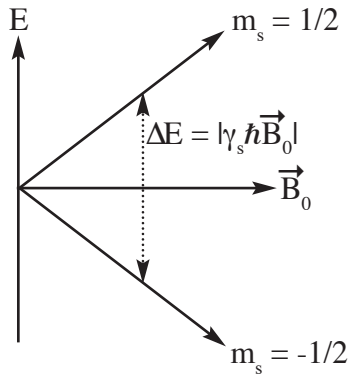

Figure 1.4: a schematic depiction of the allowed spin transitions ($\Delta m = \pm 1$) an the energy associated with that transition (ΔE), in the simplest, spin 1/2 case.

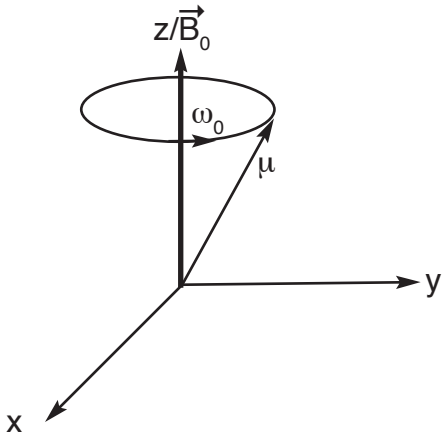

Figure 1.5: a schematic depicting precession at a Larmor frequency, ω_0, of a magnetic moment, μ, in a static, homogenous, magnetic field (parallel to the z-direction).

1.4.4 Intrinsic and Extrinsic NMR Hamiltonians

In liquids, the kinetics of tumbling of molecules averages *inter*molecular interactions to zero, leaving the smaller, *intra*molecular interactions intact. In solids, the atomic positions are fixed, so interactions as a result of this state play a more dominant role, as the energetics of their interactions are greater in scale than intramolecular ones. The solid-state Hamiltonian includes all interactions and is represented as follows:

$$\hat{H}_{NMR} = \hat{H}_Z + \hat{H}_{rf} + \hat{H}_{cs} + \hat{H}_{D-D} + \hat{H}_J + \hat{H}_Q \qquad 1.4.11$$

The first two Hamiltonians in the above summation equation, the ZEEMAN ($\hat{H}_z$), and RF, ($\hat{H}_{RF}$) are external and depend on experimental conditions. As outlined above, they detail the interaction between the applied magnetic field ($\vec{B}_0$) and the time-dependent radio-frequency field (also called the local field induced by the coil surrounding the sample or $\vec{B}_1$). The Hamiltonians that follow correspond to interactions stemming from the nuclear properties of the system under

consideration. For example, the chemical shielding (CS) Hamiltonian depends on the relative orientation of the atoms in the system, relative to the magnetic field. The dipole-dipole interaction (D-D) is a through-space interaction between spins. The D-D interaction is one that is often relied upon in this dissertation, as it can yield valuable information about the interactions as well as internuclear distances between nuclei. The through-bond, indirect spin-spin coupling (J) is a weaker interaction, as it represents the relationship that neighboring spins have, as shared by covalent bonding. This weaker interaction, typically on the order of Hz, is usually overwhelmed by stronger interactions such as dipolar or quadrupolar coupling. This j-coupling phenomenon is nevertheless observed in both the ^{121}Sb as well as some of the ^{19}F MAS NMR experiments described in one chapter of this dissertation. The phenomenon is made manifest by the magnetic interaction between each nucleus and the electron spin density surrounding it, together with the exchange coupling of the electron spins with each other. The through-bond interaction between the I and S spins is sometimes manifested in the splitting of the peak(s) in the spectrum of the I spin into 2S+1 peaks.

The Quadrupole Hamiltonian ($\hat{H}_Q$) is very often (though not always) the highest magnitude interaction of all the Hamiltonians. In the experiments detailed in this dissertation, only the quadrupoles ^{121}Sb and ^{7}Li are examined (and ^{121}Sb only from a cursory perspective). Although ^{7}Li is extensively investigated in one of the chapters of this dissertation using the REDOR MAS NMR pulse sequence, the robust, broad field of quadrupolar interactions will not be treated in this introductory chapter, because the first- and second-order quadrupolar interactions are not exploited in the investigations for the information they contain. The magnitude of the quadrupolar coupling constant of the spin-3/2 ^{7}Li isotope, despite the low-symmetry environment in which it sits in the system investigated in this dissertation, is so small (only approximately 140kHz) that first- and second-order effects do not come into play.

The next sections briefly explain the interactions and phenomenologic origins of these interactions which figure more prevalently in solid-state NMR.

1.4.5 Chemical Shielding Interactions

Any nucleus is surrounded by electrons. Given that they are also charged particles with their own spin, one could imagine that they will play a role in the observable effects to be had on a nuclear spin. When placed in an external magnetic field, a secondary field is generated by the electron current, due to their response to the field and precession, which opposes the applied magnetic field(s). Therefore, the magnetic field experienced by the nucleus is less than the applied, external magnetic field, $\vec{B}_0$, due to the nuclear spins coupling with this *induced* magnetic field. The magnitude of this *shielding effect* and relative (though not absolute) orientation of this effect can be quantified. This *chemical shielding interaction* between the nuclear spin and the local field introduced by the surrounding electron density, can provide valuable information about the relative orientation the systems, relative to the external field.

If the charge distribution about a nucleus is spherically symmetric, the induced field at the nucleus, $\vec{B}_{ind}$, is opposite in direction to the applied magnetic field and can very simply be described by:

$$\vec{B}_{ind} = -\sigma \vec{B}_0 \qquad 1.4.12$$

where σ is a scalar, measured experimentally, is in Hz/ν_0 (in ppm) and is independent of applied field. A spherically symmetric electron density provides somewhat limited information about the local environment in which the nucleus resides. More often than not, the electronic distribution in solid-state systems interacting with a nucleus of interest is much less symmetric and, therefore, can be more expository regarding the local atomic environment surrounding that nucleus. Deviations from spherical symmetry require more advanced mathematical tools to understand

relative orientations between the local frame and the laboratory frame, for example. Working between different sets of (often Cartesian) axes requires the use of a *tensor*, a mathematical object that permits the deduction of the relative anisotropies between different sets of axes.The *rank* of a tensor is determined by the number of sets of axes involved. In the case here, for the *chemical shift anisotropy* or CSA tensor, a rank-2 tensor is used, to define the relative orientational dependence of the electron density, with respect to the laboratory frame. The Hamiltonian for this interaction is given by:

$$\hat{H}_{cs} = -\gamma\hbar\hat{I}\cdot(-\sigma_{ij})\cdot\vec{B}_0 = \gamma\hbar\hat{I}\cdot\sigma_{ij}\cdot\vec{B}_0 = \gamma\hbar\hat{I}\cdot\vec{B}_{ind} \qquad 1.4.13$$

where σ_{ij} is the rank-2 Cartesian tensor discussed above and the other terms which appear have the same meaning as previously defined. The rank is indicated by the number of (here, subscripted) indices present and the magnitude of these two indices represents the number of dimensions in which one is working (here, i, j = 1, 2, 3).

The two tensor indices in almost all of NMR study are often omitted, because NMR spectroscopy works largely within covariant tensor systems (the opposite being contravariant). This simply means that in the transform between coordinate axis systems (e.g. one basis set to another), the components of each vector must *co-vary* to retain the same geometric meaning. Mathematically, they are *bijective homomorphisms* or two (bijective) sets of one-to-one (linear: 'homo' or same) mappings of *dual spaces* (the space of functions on vectors). Since tensors in NMR deal exclusively with rotations and reflections (for example, from the molecular frame to the lab frame), it is natural to work with covariant tensors. The CS (or any NMR-related) rank-2 tensor is constructed from the nine components which make up the 3×3 (eg. 3-dimensional) matrix which specify the orientation of the tensor, with respect to the laboratory frame (see eq. 1.4.15, below). Tensors can be decomposed into symmetric and antisymmetric parts. Here, six

$$\sigma_{ij} = \begin{pmatrix} \sigma_{xx} & \sigma_{xy} & \sigma_{xz} \\ \sigma_{yx} & \sigma_{yy} & \sigma_{xz} \\ \sigma_{zx} & \sigma_{zy} & \sigma_{zz} \end{pmatrix} \xrightarrow{CS\ \text{to}\ PAS} \begin{pmatrix} \sigma_{xx} & 0 & 0 \\ 0 & \sigma_{yy} & 0 \\ 0 & 0 & \sigma_{zz} \end{pmatrix} \qquad 1.4.14$$

independent components make up the symmetric part and three make up the antisymmetric part. This aspect is important, because it defines the so-called Principal Axis System (PAS). and the transform is depicted in eq. 1.4.14, above. The ellipsoidal shape is determined by the eigenvalues of the tensor (the scalar values extracted following diagonalization of the matrix).

The spectra generated in NMR are largely determined by the symmetric components, so the primary focus remains largely within the six symmetric components[15,16]. The symmetric tensors can then be interpreted as 3-space ellipsoids (see Figure 6, below). Three of the elements are used to define the size and shape of the ellipsoid and the other three define the orientation of the ellipsoid in the laboratory frame, using the main diagonal components σ_{ii} (i = j), the sum of which is called the *trace* (TR) of the matrix (see eq. 1.4.14, right matrix, above), where the z-axis is conventionally parallel to the applied magnetic field, $\vec{B}_0$ (see Figure 5, above). In some cases in NMR, matrices are traceless ($TR = \zeta_{11} + \zeta_{22} + \zeta_{33} = 0$). In the case of j-coupling and CSA, however, this is not the case.

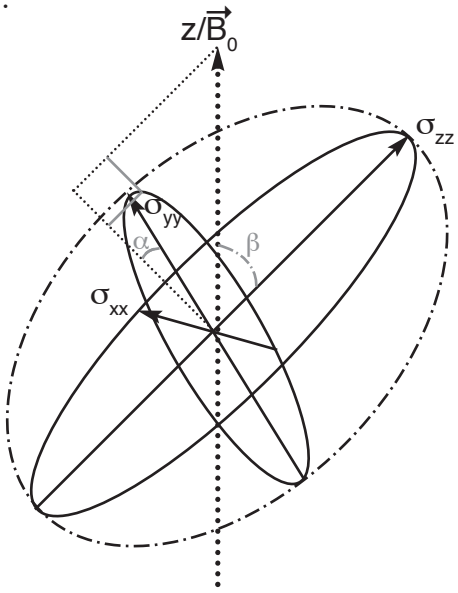

Figure 1.6: Diagram representing the three tensorial, ellipsoidal CS components, depicted in increasing order of shielding ($\sigma_{xx} < \sigma_{yy} < \sigma_{zz}$). The Euler angles (α, β) are included, which are used to define the orientation of the PAS, relative to the laboratory frame; the value of the γ Euler angle is 0°.

$$\sigma_{zz} = (sin^2\beta cos^2\alpha)\sigma_{11} + (sin^2\beta sin^2\alpha)\sigma_{22} + (cos^2\beta)\sigma_{33} \quad 1.4.15$$

In a strong magnetic field ($\vec{B}_0 >>> \vec{B}_1$), the only quantity which can be measured regarding the shielding tensor components is the σ_{zz} component in the laboratory frame. It can be expressed in terms of a linear combination of the trace (see eq. 1.4.10, above). The values for the angles which appear in eq. 1.4.10 are the so-called Euler angles (α, β, γ), which can be seen depicted in Figure 6.

During an NMR experiment, the signal is recorded in ppm and the difference from being on Larmor resonance is called chemical shift. The deviation from chemical shift, due to chemical shielding effects is related by the following:

$$\delta_{sample} = 10^6 \left(\nu_{sample} - \nu_{ref}\right) / \nu_{ref} \cong \sigma_{ref} - \sigma_{sample} \quad 1.4.16$$

This facilitates the reformulation of the components of the CS tensor into δ_{ij}, from σ_{ij}, such that the influence of the CS effects can be accommodated. The relative "strengths" of the components are conventionally defined as $\delta_{11} \geq \delta_{22} \geq \delta_{33} \geq$, from least shielded ($\delta_{11}$) to most shielded ($\delta_{33}$). A mean or isotropic chemical shift can also be calculated, where $\delta_{iso} = (\delta_{11} + \delta_{22} + \delta_{33})/3$. CSA is often very useful to distinguish between chemically similar species, but in the solid state, the magnitude of the CSA in many cases is simply too broad from which to garner any chemical meaning. Techniques such as magic-angle spinning NMR (MAS NMR) have been developed to attenuate these effects without eliminating them, so as to preserve the unique chemical signature of species in a sample. MAS NMR will be discussed later in this Introductory Chapter.

The power of the CSA and the tensor eigenvalue distribution from σ_{11} ... σ_{33} is that it can be thought of as a unique signature for one local environment within a particular sample. In the liquid state, CSA is averaged to zero, given the fact that simple Brownian motion in a liquid sample engenders a spherical distribution of molecular tumbling, thereby averaging CSA to zero. Given the complex, fixed nature of solid solutions (to cite only one example), several different local environments can simultaneously exist, yet it is feasible to discern each local environment with a unique CSA fingerprint, the requirement being that magic angle spinning (MAS) techniques be employed. In the solid state, spectra are usually made broader and less well-defined, due to anisotropic interactions. High-resolution spectra can be obtained using magic-angle spinning (MAS) techniques, whereby these anisotropic interactions are focused down to their primary in-frame components[17]. Examination of CSA can reveal much about a system, including local atomic ordering schemes as well as ionic mobility. In this dissertation, much time will be spent on discussing ionic mobility of different homonuclear species within the same system, as a function of local environment, temperature or intrinsic thermodynamic properties as they impact the dynamics of a particular system. In the following sections, more detailed treatment of interatomic interactions will be covered.

1.4.6 Dipole-Dipole Interactions

Nearby spins are constantly influenced by nearby spins, as spins in general can be thought of as magnets, imparting their own local magnetic fields. This interaction between two dipoles (again relying on the classic bar magnet analogy) depends on both the distance as well as the magnitude and direction of the internuclear vector with respect to the direction of the applied magnetic field. For a two-spin system (designated I, S), the Hamiltonian can be represented as:

$$\hat{H}_{D-D} = \hat{I} \cdot D_{D-D} \cdot \hat{S} = \hbar \cdot D_{D-D} \left[\hat{I} \cdot \hat{S} - 3 \left(\hat{I} \cdot \vec{r}_{IS} \right) \left(\hat{S} \cdot \vec{r}_{IS} \right) / r_{IS}^2 \right] \qquad 1.4.17$$

where $D_{D\text{-}D}$ is the dipolar coupling tensor:

$$D_{D-D} = R_{D-D}\begin{bmatrix} 1-3x^2 & -3xy & -3xz \\ -3xy & 1-3y^2 & -3yz \\ -3xz & -3yz & 1-3z^2 \end{bmatrix} \quad 1.4.18$$

which is symmetric about the TR and traceless. In eq. 1.4.16, the $\vec{r}_{IS}$ terms is the dipolar vector between spin I and spin S. In eq. 1.4.17, $R_{D\text{-}D}$ is the dipolar coupling constant:

$$R_{D-D} = \frac{\mu_0}{4\pi}\frac{\gamma_I\gamma_S\hbar}{r_{IS}^3} \quad 1.4.19$$

Note the appearance of r_{IS} in both eq. 1.4.16 and 1.4.18, the internuclear distance between the two spins and that it is inversely proportional to the cube of the distance between the two spins. Recall that μ_0, the constant of magnetic permeability in free space, in the dipolar coupling constant term (4π x 10^{-7} kg · m · s^{-2} · A^{-2}; kg · m · s^{-2} = N).

The Dipole-Dipole Hamiltonian is often expressed in spherical polar coordinates and often referred to as the dipolar alphabet (see eq. 1.4.19, below), because of the impressive number of individual interactions which occurs as a result of dipolar proximity:

$$\hat{H}_{D-D} = \hbar R_{D-D}(A+B+C+D+E+F) \quad 1.4.20$$

where:

$$\begin{aligned} A &= \left(3cos^2\theta - 1\right) I_z S_z \\ B &= -\frac{1}{4}\left(3cos^2\theta - 1\right)\left[I_+S_- + I_-S_+\right] \\ C &= \frac{3}{2}sin\theta cos\theta e^{-i\phi}\left[I_+S_z + I_zS_+\right] \\ D &= \frac{3}{2}sin\theta cos\theta e^{i\phi}\left[I_-S_z + I_zS_-\right] \\ E &= \frac{3}{4}sin^2\theta e^{-2i\phi}\left[I_+S_+\right] \\ F &= \frac{3}{4}sin^2\theta e^{2i\phi}\left[I_-S_-\right] \end{aligned} \quad 1.4.21$$

where I_z, S_z, I_+, I_-, S_+, S_- are all nuclear spin operators, with the $A_\pm$ (A = I, S) are the raising/lowering (aka "ladder") operators, respectively. The ladder operators are defined as $A_\pm = A_x \pm iA_y$.

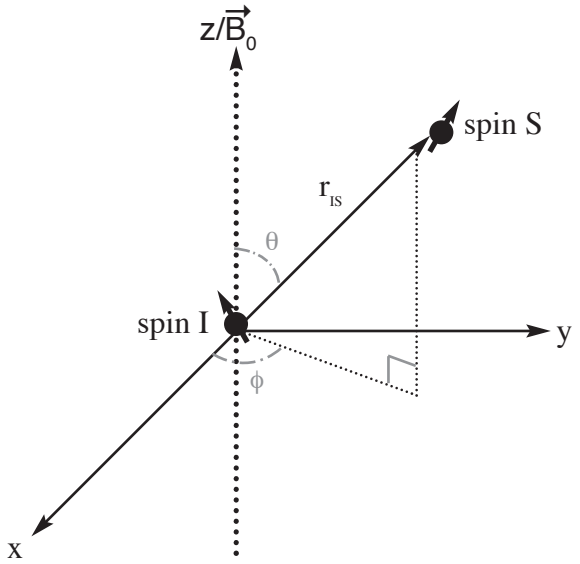

Figure 1.7: Diagram representing the two angles (θ, ϕ) which denote the spherical polar components of the internuclear vector r_{IS}. This system is used to describe many systems where polar spherical coordinates are more utile.

The first term (A) is the secular dipolar coupling term. This contributes to perturbations in the Zeeman Hamiltonian, which results in a broadening of the NMR spectrum. As may be evident to the reader, Term B interchanges ladder operators for the spins ($I_+S_- + I_-S_+$) and this flip-flop exchange Term connects spins which only differ in polarization. As described in the Chapter of this Dissertation where this term plays a major role (in the two-dimensional magnetization exchange, 2DME, pulse sequence, in that the I and S spins exchange energy via mutual reorientation of their spins. This system is conservative and so contributes to nuclear magnetic relaxation, provided $\Delta\omega$ ($\omega_I - \omega_S$), the difference between the two resonance frequencies is less than the magnitude of the dipolar coupling strength, $R_{D\text{-}D}$. The single-quantum terms, (C and D) and the double-quantum terms, E and F, also cause mixing of the Zeeman states and can make significant contributions to relaxation.

As mentioned before, the convenience and utility of working within the rotating frame is significant and in this case, the same applies. Only Terms A and B in eq. 1.4.20 remain the same, regardless of the frame of reference (hence the use of the term *secular* in their description). The other terms in the rotating frame become time dependent with frequencies ω, 2ω and so in the high-field approximation, the time-dependent terms (C - F) can be safely neglected, since they are no longer in resonance with the secular terms. The resultant Hamiltonian can then be reformulated as follows:

$$\hat{H}_{D-D} = -hR_{D-D}\left(3cos^2\theta - 1\right)\left[I_zS_z - \frac{1}{4}\left(I_+S_- + I_-S_+\right)\right] = \qquad 1.4.22$$

$$-\frac{1}{2}hR_{D-D}\left(3cos^2\theta - 1\right)\left[3I_zS_z - \hat{I}\cdot\hat{S}\right]$$

In heteronuclear spin systems (which are also examined in this Dissertation), further simplification can be found due to weak heteronuclear coupling by dropping all terms that involve transverse spin operators (those associated with the ladder operators, I_+, I_-):

$$\hat{H}_{D-D} = -hR_{D-D}\left(3cos^2\theta - 1\right)I_zS_z \qquad 1.4.23$$

Dipole-dipole interactions are angle-dependent. In solids, where polycrystallites are overwhelmingly the type of solid material that one has to work with, the dipolar vectors in this type of medium are spherically distributed (due to the randomness of the crystallites). This engenders a distribution of resonance frequencies. As mentioned above, dipolar broadening and CSA as a result of some of the coupling terms in the Hamiltonian (eq. 1.4.20) sometimes obscure observation of chemical shifts of chemically distinct (yet related) spins. This angular dependence of several Hamiltonians can be attenuated, but only when MAS techniques are employed. Dipole-dipole interactions are extremely useful in the investigation of systems. The power to prohibit, permit or deliberately reintroduce dipole-dipole interactions has led to the development of many exceptional pulse sequences which can be employed to reveal many pieces of chemical and structural information. These will be discussed in more detail in Section 1.6.1 of the

Introductory chapter of this Dissertation.

1.4.7 Indirect (through-bond) Pseudo-dipolar Interaction: Scalar Coupling

The nuclear-spin interaction which prevails in liquids lies among the molecules themselves, from the perspective that nuclear spins can commute information via the electron-mediated bonds which hold the atoms together. This indirect or pseudo-dipolar coupling (commonly called j-coupling) can be readily observed among interactions of spins in liquids within molecules, but is also evident as a result of hydrogen bonding[32,33,34,35]. The j-coupling Hamiltonian is written as follows:

$$\hat{H}_j = \hat{I} J_{ij} \hat{S} \qquad 1.4.24$$

where the J_{ij} term, another rank-2 tensor, represents the orientationally dependent j-coupling effect (relative to the magnetic field). The J tensor is axially symmetric its unique component coincident with the internuclear dipolar vector ($\vec{r}_{is}$). The trace of the J tensor, like the CSA tensor σ_{ij}, is not zero (traceless), unlike the D-D tensor. Geometrically, this can be interpreted as the interactions represented by the j-coupling components are not fixed.

The isotropic value of the J tensor ($J_{ISO} = T_R/3$) can be contrasted with the anisotropic value ($\Delta J = J_{|} - J_{\perp}$), given the axial symmetry of the object. As mentioned previously, since ΔJ is geometrically coincident with $R_{D\text{-}D}$, the contributions of each to the overall NMR lineshape cannot be segregated. As such, the two are usually combined as the effective dipolar coupling constant, R_{eff}:

$$R_{eff} = R_{D\text{-}D} - \Delta J/3. \qquad 1.4.25$$

The through-bond interaction between the I and S spins results in the splitting of the peak(s) in the spectrum of the I spin into 2S+1 peaks. This relation is basically evident in the ^{121}Sb spectrum (Figure 6, Chapter 6) of this dissertation, although the spectrum in Figure 6 noted here is

made more challenging, due to the quadrupolar interactions of the ^{121}Sb spin, as well as a competing signal. Unlike the dipolar interaction, the j-coupling interaction is not averaged to zero due, for example, to molecular tumbling. This is why j-coupling is observable in both the solid and liquid state.

1.5 Solid-State NMR Phenomena and Methods

As mentioned above, the molecular kinetics of the liquid state average out anisotropic interactions, leaving only narrow isotropic resonances from which to deduce connective and molecular information. The goal of solid-state NMR is similar: obtain isotropic information from the system. Additionally, in solid-state NMR, one also carefully manages the anisotropic interactions, as they, too, contain valuable information regarding local molecular geometries and the connectivity among and between nearby nuclei. Recalling again from previous sections of this

$$\hat{H}_{NMR} = \hat{H}_Z + \hat{H}_{rf} + \hat{H}_{cs} + \hat{H}_{D-D} + \hat{H}_J + \hat{H}_Q \qquad 1.4.12$$

Introductory Chapter, each term in the encompassing NMR Hamiltonian ($\hat{H}_{NMR}$) see eq. 1.4.12 above) can be validly represented as the tensor product of a spatial component and a spin component. Recall, however, that the first two terms ($\hat{H}_Z$, $\hat{H}_{RF}$) are extrinsic; the last four terms are intrinsic to the system and conform to eq. 1.4.1, 2: the spatial part of each of the latter four Hamiltonians contains the anisotropic information regarding the nucleus' surrounding local environment(s). To optimize the amount of information that can be gained from such a system, however, special accommodations need to be made, given the challenges of studying a particulate-based solid, such as a polycrystalline powder, polymer or what have you. Control of these anisotropic interactions allows their attenuation (to reveal isotropic information of a system). Reintroduction of these influences further yields valuable spatial information of the local structure of a system.

1.5.1 Magic-angle Spinning (MAS)

Researchers discovered that rotating a sample at specific angles corresponding to mathematical terms in the Legendre Polynomial series, permitted a reduction of first-order anisotropies associated with a system, regardless of the system being studied[36,37]. As seen in eqs. 1.4.21 - 23, several parts of the respective Hamiltonians depicted in those equations include a $(3\cos^2\theta - 1)$ angular dependence, with respect to the static, magnetic field, $\vec{B}_0$. Remarkably, this corresponds to the body diagonal of a unit cube $(1/\sqrt{3})$.

The origin of the angular dependence is explained with the brief overview of Legendre Polynomials, the class of functions discovered in 1782, which are the solutions to the second-order differential Legendre equation. As the name implies, second-order solutions exhibit two linearly independent terms $P_{(m)}^{(\ell)}$, $Q_{(m)}^{(\ell)}$, and conform to fixed, symmetric (or antisymmetric) functions when the $P^{(\ell)}$, $Q^{(\ell)}$ super/subscripts are integers. It should be noted that the subscripted Legendre term, m, is omitted, because it is not fixed. When viewed as fixed positions (using Wigner 3j coefficients) with angular dependence (θ, ϕ), these are famously manifested as the closely related polynomial series, LaPlace's Polynomials. LaPlace's Polynomials are referred to as Spherical Harmonics($Y_{(m)}^{(\ell)}$,) when describing molecular orbitals.

The symmetric Legendre terms ($P^{(2)}$, $P^{(4)}$) correspond to first- and second-order interactions in NMR and it is this first $P^{(2)}$ term $(3\cos^2\theta - 1)$ wherein the dependence lies. Solving for the roots of the Legendre polynomial reveals the zeroes for each term in the Legendre Polynomial and the solution for this first $P^{(2)}$ term = $\tan^{-1}(1/\sqrt{3}) = 54.74°$. Solving for the $P^{(4)}$ term reveals two equivalent angles (30.56°, 70.12°) for which second-order quadrupolar terms can be minimized, although the rich field of NMR involving these second-order perturbations is not covered in this Dissertation[33].

1.5.1.1 Setting the Magic Angle: Practical Aspects

All MAS NMR probes have a stator: the small piece of plastic within the probe which houses the coil and into which the sample is inserted. The stator is mounted onto a set of gimbals, which allows the stator to rotate, such that the angle of the coil axis (and, therefore, the sample rotor) can be set to the magic angle. In many cases, this is a trivial process, because several commonly found compounds can be used, such as sodium nitrate, potassium bromide or deuterium-containing solids[59,60]. This is usually done by simply maximizing the number of rotational echoes seen on an unprocessed Free-induction Decay (FID) spectrum.

Very often, the natural abundance of ^{79}Br (~50%) usually makes tuning the magic angle by using the FID on small (≤3.2mm) rotors difficult, as the signal-to-noise ratio is poor. As such, the use of the convenient *repeat scan and process* function available in Chemagnetics/Varian Spectrometer software (coupled with a 200ms pulse delay) allows effective tuning by using the shape, symmetry and amplitude of the satellite and central transitions of the processed ^{79}Br MAS NMR lineshape. This was found to be superior to using the rotor-echo FID method to confirm no change in magic angle setting had occurred due to temperature-dependent contraction of the probe materials at lower (<-50°C) temperatures. Early in these investigations, many attempts at using KBr as both a temperature and magic-angle indicator at low temperatures by packing it in the bottom of the rotor, followed by a homemade Torlon minispacer, and ionic liquid were not successful, despite literature to the contrary[65].

Consider a principal axis $\vec{\mathbf{r}}$ of a nucleus in a sample rotating about an axis at an angle θ, with respect to B_0 (see Figure 8, below). The Hamiltonian for a particular interaction under these conditions can be parsed into time-independent and time-dependent hamiltonians, respectively:

$$\hat{H}_\eta = \langle \hat{h}_\eta \rangle + \hat{h}_\eta(t)$$

where $\langle \hat{h}_\eta \rangle$ is the time-independent, mean expectation value ($\langle ... \rangle$) representing the isotropic components of the interaction and $\hat{h}_\eta(t)$ is the time-dependent term which contains the anisotropic components of the interaction and demonstrate the $(3\cos^2\theta - 1)$ dependence. When the nucleus is rotating, θ will vary over a conical path during the motion. As implied in Figure 8, below,

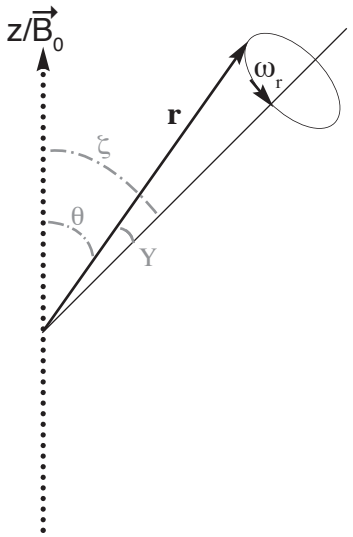

Figure 1.8: Diagram depicting a principal nuclear spin axis r, precessing at an angle, ζ, with representations of (θ, Ψ) of possible values between r and z/B_0. ω_r = spinning speed of the rotor.

a mean can then be calculated, as represented below:

$$\langle 3cos^2\theta - 1 \rangle = \frac{1}{2}\left(3cos^2\zeta - 1\right)\left(3cos^2\Upsilon - 1\right) \qquad 1.4.26$$

As stated in earlier sections of this Introductory chapter, the spherical distribution of the nuclear axis, **r**, means the angle subtended by **r** and $z(\vec{B}_0)$ can range from $-\pi/2 \leq \mathbf{r} \leq \pi/2$, so when $\zeta = \theta$, $\Upsilon = 0^o$ (see eq. 1.4.26 above), anisotropies are attenuated and isotropic resonances become evident. The caveat that remains is that the $(3\cos^2\theta - 1)$ dependent coupling strengths (measured in Hz) must be less intense than the spinning speed (ω_r; so, $\omega_\eta < \omega_r$), in order for this condition to be attained. When anisotropy exists in the system and the ($\omega_\eta < \omega_r$) condition is met, the static NMR

lineshape is parsed into the image of the NMR lineshape re-represented as spinning sidebands (the distance between each sideband = ω_r) in the MAS NMR spectrum, whose sideband peaks reflect the initial function (kernel) generated by the original NMR signals. This combination of peaks neatly represents both the isotropic and anisotropic parts of the total spectrum. When ($\omega_\eta << \omega_r$), the anisotropic interactions are completely suppressed and only the isotropic effects are visualized. One can then view Figure 1.8 and eq. 1.4.26 more intuitively, such that the "strength" of a time-independent interaction can be superseded by a time-dependent strength, such that the time-independent and dependent frames of reference begin to become one.

1.5.2 Cross Polarization

Cross Polarization (CP) MAS pulse sequences are routinely used in MAS NMR to enhance the sensitivity of less numerous spins (usually designated *S spins*) via the transfer of magnetization from the more numerous spins (designated the *I spins*), provided certain conditions are met[38,39,40,41]. Two major benefits are realized from these types of experiments. Firstly, the intensity of the dilute spins can be increased by as much as γ_I/γ_S. Secondly, the spin-lattice relaxation times (time taken for the nuclear spins to relax back to their initial, precessive states around z/$\vec{B}_0$, following excitation by a pulse; abbreviated T_1) of the I spins govern the relaxation times for the experiment, as the T_1 times for the I spins are usually much shorter than the S spins. An appropriate number of scans comprises a typical experiment and the time between scans (sometimes called recycle delay) is governed by those T_1 times. In some cases, direct excitation of spins can take hundreds or even thousands of seconds to relax back, so CP MAS experiments can prove to be a substantial advantage in acquiring a clean spectrum with a high signal/nose ratio in a short period of time.

In the rotating frame, a $\pi/2$ pulse along the y-direction (conventionally) on spin I is used to prepare the transverse magnetization along the x-direction (see Figure 9a). Then, an rf pulse along the x-direction is applied to both the I and S spins, so as to lock (so-called *spinlocking*) the magnetization for both along the y-direction (conventional right-hand rules for electromagnetic radiation apply). This rf pulse is called the *contact time* or the time permitted for the spins to remain in the x—y plane to cross polarize. It is during this period that the amplitudes and time needed for the I and S spins to efficiently transfer polarization are optimized, such that:

$$\nu_{1I} = \gamma_I B_{1I} = \gamma_S B_{1S} = \nu_{1S} \qquad 1.4.26$$

the so-called Hartmann-Hahn condition[40].

Polarization transfer occurs via the "flip-flop" terms (I_+S_- or I_-S_+) in found in parts E, F of eq. 1.4.21 of the dipolar Hamiltonian. These terms are responsible for the single-quantum transitions for the dipolar components for the I, S spins, respectively ($\pm|1/2> \leftrightarrow \mp|1/2>$) and are responsible for spin-diffusion experiments, like the 2-Dimensional Magnetization Experiment (2DME) highlighted in Chapter 6 of this dissertation, Figure 8. Polarization transfer, as mentioned in section 1.4.3, above, is conservative and so energetic optimization of the spin-transfer parameters is requisite for efficient cross polarization. In homonuclear systems (like those performed and depicted in Chapter 6, Figure 8), the resonance disparity is small. For heteronuclear systems, satisfying the Hartmann-Hahn condition (eq. 1.4.26, above), is more challenging and care must be taken to determine the energies needed to satisfy the match.

Spinlocking presents yet another substantive example of the advantages underlying geometric conceptualization among reference frames. In the x—y plane, following satisfaction of the Hartmann-Hahn matching condition, the two spins co-precess in the so-called *doubly rotating frame* (see Figure 9c, below). Viewing the system from the laboratory frame, however, the two Larmor frequencies for the two spins are obviously different and polarization transfer is not

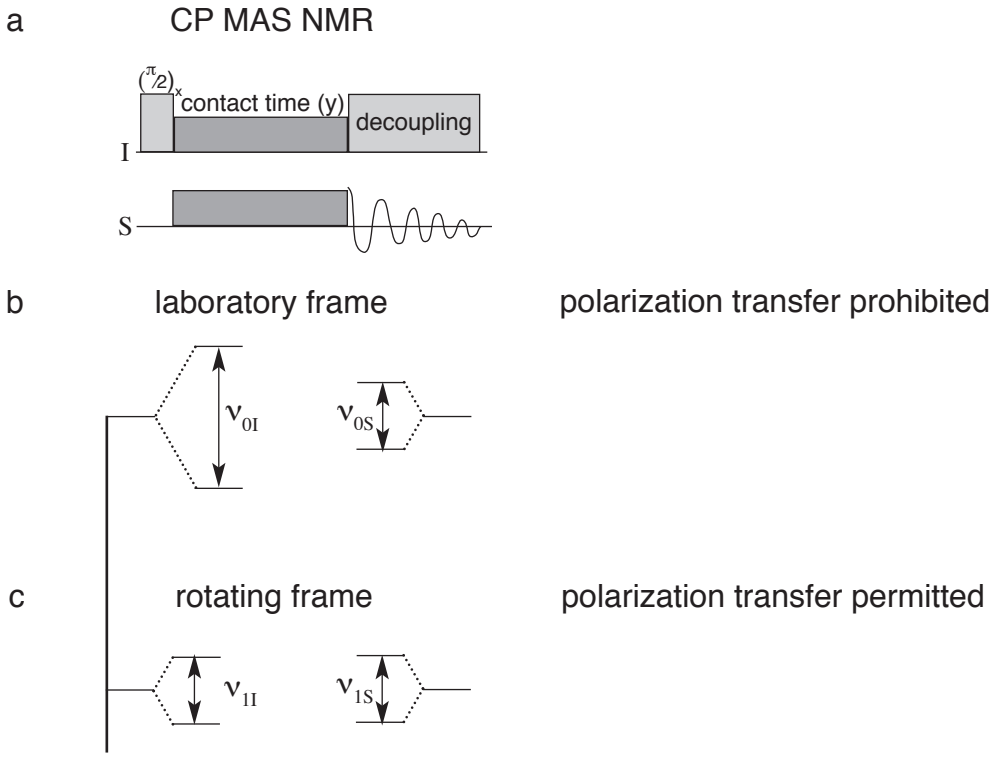

Figure 1.9 a-c: Schematics representing various interactions. Figure 1.9a: a cartoon of the pulse sequence for the I, S spins for CP-MAS. Figure 1.9b: depiction of the Zeeman splitting (energy difference) between the spins in the laboratory frame. Figure 1.9c: the relative energies as viewed from within the doubly rotating frame, where co-precession in the x-y plane for both spins occurs and, therefore, I→S cross polarization.

permitted (see Figure 1.9b, above). Within the doubly-rotating frame, however, the rf fields become time-independent and the Zeeman splitting within B_1 become equal (see Figure 1.9c, above, where $\nu_{1I} = \nu_{1S}$). The dipole-dipole interaction is time-dependent and the optimization equations are as follows[41,42]:

$$\omega_{1I} = \omega_{1S} + n\omega_r \quad n = \pm 1,2. \qquad 1.4.27$$

1.5.3 Dipolar Recoupling

As indicated in previous sections, dipole-dipole interactions contain very valuable struc

tural information regarding spatial arrangements of nuclei, relative to the spin of interest, this inverse-cubic relationship (see section 1.4.5, above, with eqs .1.4.17, 18 and $R_{D\text{-}D}$, the denominator of the dipole coupling constant = r^{-3}). MAS techniques were developed to eliminate or at least attenuate the anisotropic information which often obscures the isotropic information of a particular molecular system. Careful reintroduction of dipolar interactions is useful for spectral editing of the NMR lineshape. Because of the various linear combinations by which dipolar coupling can be reintroduced, either by synchronization with rotor period or by timed-pulse introduction in conjunction with rotor synchronization, a far-reaching panoply of different pulse sequences has been developed over the decades. The pulse sequences fall into two classes: heteronuclear and homonuclear. Examples of heteronuclear pulse sequences are REDOR, TRAPDOR, TEDOR, and REAPDOR and several variants such as VACP (Variable Amplitude Cross Polarization) had been developed thereafter[43,44,45,46,52]. Homonuclear examples include BABA, C7, DRAMA, RFDR and Rotational Resonance). Rotational Resonance and RFDR involve both the A (I_zS_z)and B ($I_+S_- + I_-S_+$)terms in eq. 1.4.21 in their zero-quantum dipolar recoupling pathways[47,48,49,50,51]. The DRAMA, C7 and BABA pulse sequences involve the double-quantum terms (I_+S_+ and I_-S_-) found in the dipolar Hamiltonian components E and F in eq.1.4.21. Heterocoupling techniques (such as those used in the ^{7}Li ^{19}F REDOR experiments in Chapter 4 of this Dissertation) only exploit the I_zS_z term, due to the gross energy mismatch between two dissimilar spins. These pulse sequences involve the application of a π pulse in the middle of the pulse "train", thereby inverting the sign of the Hamiltonian ($I_zS_z \rightarrow -I_zS_z$). Thus, the dephasing magnetization is not completely refocused at the end of the rotor period.

The REDOR (Rotational Echo DOuble Resonance) pulse sequence is commonly used and one used extensively in chapter 4 of this Dissertation, depicted in Figure 10, below. Although the TRAPDOR sequence (conceptually and structurally similar to REDOR) was also extensively used during investigations, the data were considered not substantive enough to be

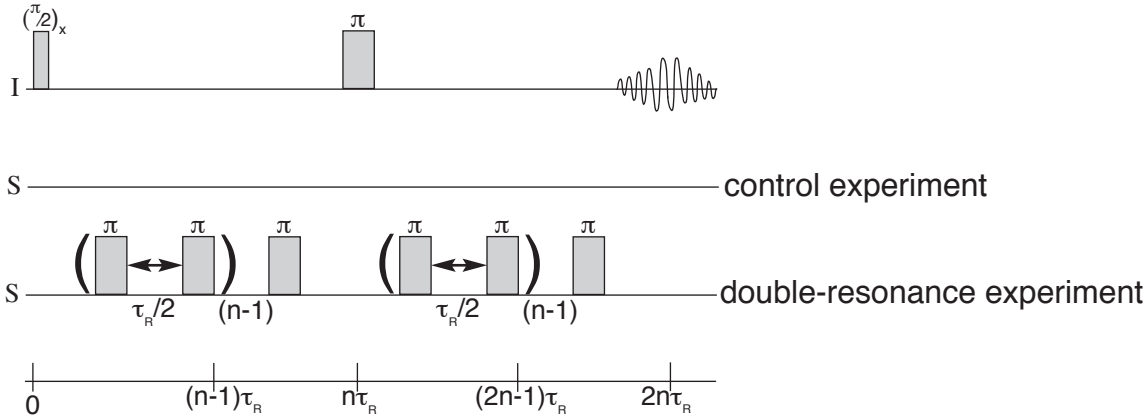

Figure 1.10: Depiction of the REDOR experiment. The REDOR experiment is performed in two parts. In part A (control), the I spins are perturbed using the echo pulse sequence outlined above, while nothing is imposed on the S spins. In Part B (the double-resonance experiment), which immediately follows (after a proper recycle delay time), the same echo pulse sequence is performed on the I spins while the S spins are subjected to a p-pulse train as outlined above. The timeline for the sequence of pulse events is included at the bottom (starting at time t = 0). τ_R = time for one rotor period; n = number of rotor periods.

included in this body of work. As is evident in Figure 10, a train of π pulses is applied to the S spins half way through ($\tau_R/2$) the rotor period. Because of the r^{-3} dependence on dipolar coupling, application of these π pulses at the $\tau_R/2$ point quantitatively prevents refocusing magnetization of proximal I spins as $f(r^{-3})$. The effect of the π pulse train is to accumulate signal intensity according to dipolar coupling strength, thus permitting a tabulation of the REDOR fraction $((1-S_f)/S_0)$, where S_f and S_0 are the double-resonance and control experiments, respectively. As the signals incrementally dephase, the magnitude of the dipolar coupling constant and, accordingly, internuclear distance are extractable.

This deducible change in signal intensity can be quantified in several ways. The most common method is the plotting of these subtractive experiments ([control] - [double resonance]) in order to create so-called REDOR curves or via normalized intensity as depicted in the above paragraph. Once the data are collated, computer modeling of the system is then employed

using the collected data, quadrupolar coupling constants, γ_I, γ_S, etc. in order to simulate the resultant curves.

1.5.4 Variable-amplitude Cross Polarization (VACP)

As explained in section 1.5.2, above, CPMAS NMR presents rich opportunities to enhance the signal intensity of dilute S spins as a result of a transfer of magnetization via the single-quantum transitions ($\pm|1/2> \leftrightarrow \mp|1/2>$) from more abundant I spins within a system, owing to the "flip-flop" terms (I_+S_- or I_-S_+) in found in parts E, F of eq. 1.4.21 of the dipolar Hamiltonian. Further, this increase in intensity is accompanied by a decrease in recycle delay times between scans during an experiment since the I spins govern this parameter, thereby permitting improved signal-to-noise ratios in shorter periods of time.

The effect of dipolar coupling strength can be described readily for the upper and lower limits. In the lower limit (weak dipolar coupling), it is relatively trivial to satisfy the Hartmann-Hahn matching conditions between two spins, such that the relative precession frequencies about their respective RF fields (the doubly rotating frame) exhibit approximate in-frame synchrony. In the upper limit of dipolar coupling ($w_{D\text{-}D} \approx w_R$), it becomes challenging to satisfy the Hartman-Hahn matching conditions, because the ($\Delta\omega_I = \omega_{1I} - \omega_{1S} \approx w_R$), so more mundane limitations become relevant. Practically speaking, as $\lim\Delta\omega_I \rightarrow 0$, slight but inevitable changes in spinning speeds, inconsistencies RF pulse amplifier performance or probe tuning drift from variable-temperature experiments, ambient humidity, etc. will all contribute to the difficulty of maintaing the demands of maintaining such a tight Hartmann-Hahn frequency window.

Some challenges of dipolar coupling were addressed by Peerson and Metz in the early 1990s in two related ways[56,57]. In the first of the two papers, Variable Amplitude Cross Polarization (VACP) treats the I spin spinlocking pulse as a one of constant phase but as a chain of

changing (usually increasing) amplitudes. In effect, several different Hartmann-Hahn match conditions are being created within τ_{CP}, the CP time frame, thereby eliminating any mis

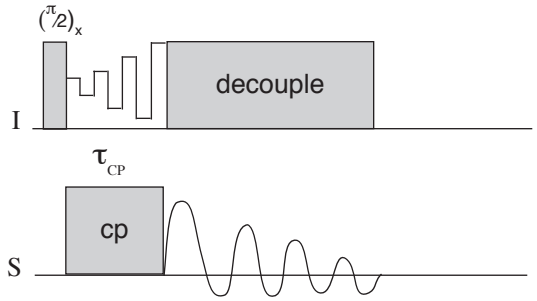

Figure 1.12: A schematic of the Variable Amplitude Cross Polarization pulse sequence. Note the changes in amplitude on the I spin pulse for the CP-aspect of the pulse, in order to eliminate energetic mismatches by creating a series of Hartmann-Hahn conditions. τ_{CP} = contact time.

matches that exist as a result of the challenges listed above. Yet another challenge arises as a result of faster speeds which must be attended to, however. Since dipolar coupling strength is measured in the same metric as most other phenomena in NMR (Hz), one can envision oscillatory behavior arise as a result of harmonic interplay between the various species in the sample being suppressed and the spinning speed. VACP attends to this harmonics issue, because of the multiplicity of Hartmann-Hahn matching conditions which occurs during the contact time, τ_{CP}.

The caveat of this exercise is that the number and amplitude of step sizes must then be carefully chosen, such that they are suited to the types of species within a sample, as well as the spinning speed of the experiment. The number of amplitudes and the size of each step (in Hz) govern the field strength range, such that $\Delta_{1H} = (n\text{-}1)w_{STEP}$[57]. With this improvement, flat, consistent Hartmann-Hahn matching curves are achieved, are are largely impervious to the variance in dipolar coupling strengths between I and S spins within a sample.

1.5.5 Ramped-amplitude Cross Polarization (RAMP)

Closely related to VACP, Ramped-amplitude Cross Polarization was developed by the-same group at Yale, soon following the publication of [57] in 1993[58]. The RAMP-CP pulse sequence includes a CP segment with monotonically increasing amplitude, rather than the stepwise, phase-consistent CP segment outlined in Figure 12, above. Further, RAMP is applied to the S spins, rather than the I spins, in contrast to the VACP sequence. The reasons for this, as the authors point out, are that the strong field strength over the I spins can be maintained and, per

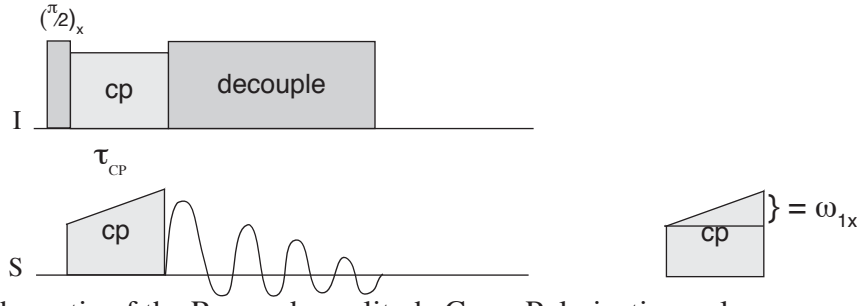

Figure 1.13: A schematic of the Ramped-amplitude Cross Polarization pulse sequence. Note the smooth (monotonic) increase in amplitude of the cross polarization aspect of the pulse sequence, including the fact that in RAMP-CP, in contrast to VACP, the modulation is on the S spins. The ω_{1x} depicted on the right of the cartoon represents the range of in-frame rf power for spin x (I or S; here, S).

haps more importantly, the spinlocking for the S spins is retained at the end of the contact time-where the most distant dipolar interactions will be influenced[57]. As indicated in Figure 13, above, the amplitude of the ramp equals the field strength of the S spins. Although technically, steps are still involved, the step size (ω_{STEP}) is constant, unlike the amplitude control in the VACP pulse sequence. Addtionally, the Spinsight spectrometer software permits up to 255 steps, given the high speed at which spectrometer equipment can function. This permits near zero lag time between changes in amplitude, meaning that it is effectively piecewise smooth. As pulse shape has an obvious effect on magnetization transfer efficiency, these papers ushered in a wide variety of usage

regarding shaped pulses in MAS NMR for both dipolar and quadrupolar manipulation including hyperbolic shapes, multiple-quantum MAS improvements through decaying exponential shapes and rotationally induced pulse shapes[58,59,60,61].

1.5.6 Ramped-amplitude Cross Polarization-Polarization Inversion (CP-PI)

A signal intensity for an S spin can be further segregated by selectively changing the phase of the NMR pulse being applied, based on the phase of the pulse, hwere there are four possibilities in the x—y plane: x, $\bar{x}$, y ,$\bar{y}$. Wu, Burns and Zilm proved this in 1994 when they demonstrated that Cross Polarization followed by Polarization Inversion (CPPI) would permit spectral editing of the total NMR spectrum with different species within a sample predicted[62]. As further explained in Chapter 3 of this Dissertation, each species (for example methyl, methylene, methine carbons) exhibits a time constant of magnetization (T_{IS}) which is specific to each moiety. This is due to the different magnitudes that the number of I spins has on the transfer of magnetization has on a particular S spin. Control of contact time (τ_{CP}) between the spins, therefore, plays a role in whether or not the constant is achieved. As Wu, et al., demonstrated, signals associated with specific moieties may be suppressed or *nulled* so as to edit out (and therefore confirm, for example) the chemical shift assignment of a particular signal[62].

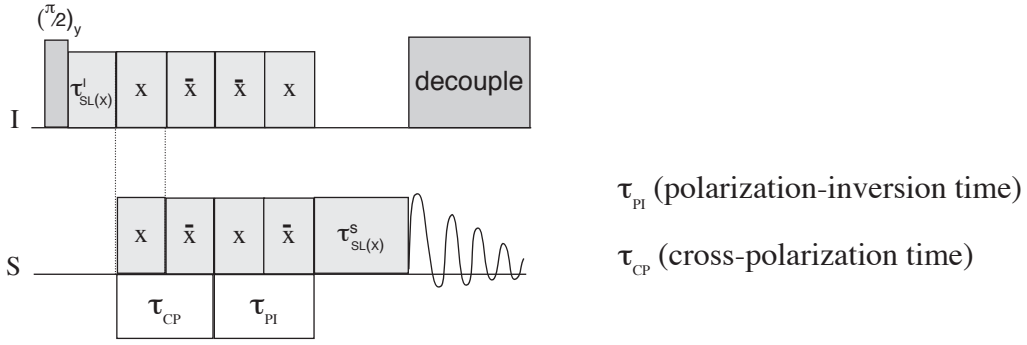

Figure 1.14: A schematic of the Cross Polarization Polarization Inversion (CPPI) pulse sequence, adapted from [62]. Note the x, $\bar{x}$ phase inversion interchanges between the I and S spins during the τ_{PI} portion of the pulse sequence, which ensure equal suppression.

1.5.7 Ramped-amplitude Cross Polariztion - Polarization Inversion RAMP-CP-PI

In [62], the authors chose a model compound with representative S spins (S = ^{13}C: CH_3, CH_2, CH, C). This highlighted the control which could be effected, depending on the T_{IS}, $T_{1\rho}$, of the moiety due, of course to dipolar coupling between directly bound and spatially proximal spins. However, the compound chosen, monoethylfumarate, has a low molecular weight and, therefore, few carbons from which to discriminate[62]. Further, their chemical shifts are relatively distant from one another, making for a clearly visible spectrum. In compounds such as that investigated in Chapter 3 of this Dissertation, 1·4bis pyridyl oxalamide - diiodobutadiyne, specta tend to be much more complex. The high number of similar carbons, in addition to the shear number, combined with chemical shift overlap due to magnetically similarity and proximity to the iodine, which induced spin-orbit coupling all contributed to the production of a difficult spectrum to interpret.

A modification of the RAMP-PI pulse sequence was written in an effort to physically edit the spectra generated from the experiment, which was named RAMP-CP-PI. The term *polarization inversion* (correctly) conveys an inversion of the phase of the applied rf pulse. However, if an additional, inverted τ_{CP} along -x for the S spins is also applied, in addition to a negative contact time for the I spins, it is possible to also *physically invert* the signal intensity generated by each spin, resulting in an inverted peak, below the baseline. Using a so-called negative contact time (-ct: $-\tau_{CP}$) along -x, it is logical to predict that T_{IS} constants for the various S spins (in this case, ^{13}C) will shorter for the various moieties. Due to inherent inefficiencies during the inversion process, some magnetization will be lost, due to incomplete irradiation and this is reflected in the overall shorter T_{IS} for each species. Nevertheless, an inverted spinlocking for the I spins, combined with a survey of $-\tau_{cp}$ proved useful in being able to selectively flip the signal intensity for each of the species in the sample.

1.6 Electrochemical Impedance Spectroscopy

Also known as AC Impedance, Electrochemical Impedance Spectroscopy (EIS) is one means of measuring conductivity through the bulk and also across an interface. Measurements which involve sinusoidal input, followed by measurement of output fall under the heading of Transfer Functions, because the general equation can be considered a linear mapping of one basis set onto another. EIS involves the application of a periodic, small-amplitude alternating current (AC) signal and measuring the linear response to the imposition of that signal[54]. When a range of AC frequencies are applied, a curve of impedance (components of resistance in the real and imaginary planes) is plotted, as impedance gives an indication of the response of the system to the applied current.

EIS is heavily employed in measurements of ionic conductivity. The challenge is that for materials such as those described in Chapter 7 of this Dissertation, a perceived local inhomogeneity likely exists with respect to charge concentrations and static fields within the sample itself. This can be due to erose grain boundaries, irregular load sorption or even slight differences in crystallite grain size. Although differences in grain size are minimized, due to the synthesis methods outlined in the first Chapter of this dissertation, the combination of these conditions limited the utility of EIS to qualitative differences in conductivity. The limited utility proved useful, if merely fundamental in determining the method of conductivity.

1.6.1 Theoretical Origins of the Impedance Signal observed in EIS

Consider an application of a time-dependent potential V(t) to a resistance, R. Solving for current, one obtains $i(t) = V(t)/R$, where i(t) is the time-dependent current, using conventional notation found in physics where i = current and $j = \sqrt{-1}$. If a capacitor is added to this series circuit, where capacitance is defined as $V(t) = Q(t)/C$, and Q is the charge (in Coulombs)

stored in the capacitor, the following equation results:

$$V(t) = i(t)R + \frac{Q(t)}{C} = i(t)R + \frac{1}{C}\int_0^t i(t)dt \qquad 1.5.28$$

Applying the LaPlace Transform to convert time domain into frequency domain:

$$\mathcal{L}[f(t)] = \bar{f}(\nu) = F(\nu) = \int_0^\infty f(t)e^{-\nu t}dt \qquad 1.5.29$$

yields:

$$i(\nu) = \frac{V(\nu)}{\left(R + \frac{1}{sC}\right)} \qquad 1.5.30$$

In the above transform, the conversion from time to frequency is represented by the greek letter nu (ν), as this conventionally indicates that the frequency (here, s) has both real and imaginary parts, such that s = ν + jω, where ω =2πf. Applying the above results for an alternating current (AC), and recalling that the LaPlace Transform for a sine function is:

$$\mathcal{L}[sin(\omega t)] = \frac{\omega}{\nu^2 + \omega^2} \qquad 1.5.31$$

gives the following:

$$i(\nu) = \frac{V_0\omega}{\nu^2 + \omega^2}\frac{1}{R + \frac{1}{\nu C}} = \frac{V_0\omega}{R}\frac{1}{\nu^2 + \omega^2}\frac{1}{\frac{\nu+1}{RC}} \qquad 1.5.32$$

Recalling that the LaPlace transforms for sine and cosine are inverses of one another, eq. 1.5.32 can be simplified into:

$$i(t) = \frac{V_0}{R\left(1 + \frac{1}{(\omega RC)^2}\right)}\left[sin(\omega t) + \frac{1}{\omega RC}cos(\omega t)\right] \qquad 1.5.33$$

By introducing tan φ = 1/ωRC, the eq. 1.5.33 is then rearranged to be:

$$i(t) = \frac{V_0}{\sqrt{R^2 + \frac{1}{(\omega C)^2}}}sin(\omega t + \phi) = \frac{V_0}{|Z|}sin(\omega t + \phi) \qquad 1.5.34$$

where φ is the phase angle between the current and the potential: $\varphi = \tan^{-1}(\omega t + \varphi)$. So, the current and the potential have the same frequency, but are merely shifted by a phase φ; the units of Z are in ohms and its scalar is the sum of two vectors R, 1/ωC. As indicated above, impedance has both real and imaginary terms. As such eq. 1.5.34 it can be more streamlined:

$$Z(j\omega) \equiv \hat{Z} = Z' + jZ'' = \underbrace{R}_{\text{Re}} + \underbrace{\frac{1}{j\omega C}}_{\text{Im}} = R - j\frac{1}{\omega C} \qquad 1.5.35$$

to reflect both the real (Z´) and imaginary (jZ´´) components of the resistance. Taking the absolute value of Z (|Z|), one can then solve for the length. However, a simple extension of the Euler equation can be applied here, such that:

$$Z(j\omega) = |Z|e^{j\phi} = |Z|\,[cos(\phi) + jsin(\phi)] \qquad 1.5.36$$

where, as mentioned above, $\tan^{-1}(-1/wRC) = \varphi$ or the phase angle between the real and imaginary Z components.

An Argand plot of Z´ v. Z´´ (erroneously called a Nyquist plot), is very useful from the perspective that, although it cannot identify specific frequencies at which events directly occur, it can qualitatively describe the type of conduction occurring[53]. Figure 11, below, reproduced from Figure 9d in Chapter 6 of this dissertation is an example of the qualitative use of an Argand plot.

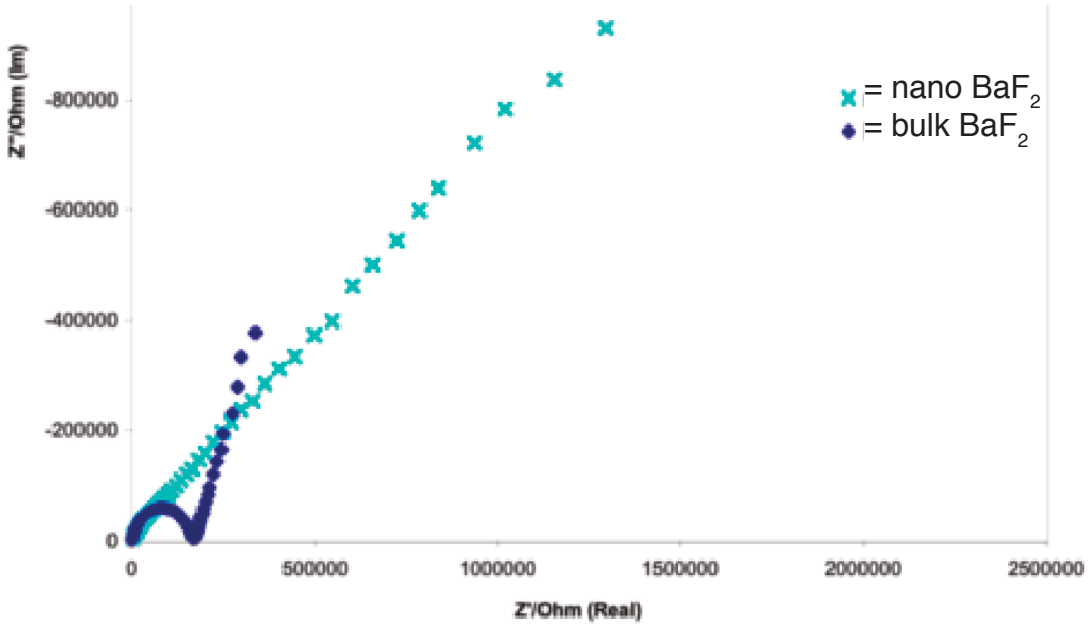

Figure 1.15: Impedance curve of bulk BaF_2 loaded with 12µl of SbF_5 in comparison to the same mass of nanoparticle BaF_2 with the same loading level. The dark blue curve (bulk BaF_2) demonstrates classic conduction, hallmarked by the frequency-dependent, semicircular curvature in the lower frequency range, preceded by the frequency-independent, linear part of the curve where ionic conductivity is largely diffusive. The light blue curve (nanoparticle BaF_2) shows exclusively diffusive conductivity, with no classic behavior.

Although not used in this dissertation, a second, common method of plotting EIS data is by use of a Bode plot. In a Bode plot, log[|Z|] and φ v. log[ν], which has the advantage of identifying the specific frequencies for a change in impedance to occur. Changes in impedance can either be positive or negative and the inverse of impedance is called admittance, measured as $Z^{-1}(\nu)$. When both impedance and admittance are found to occur in a plot, the pair are referred to as immittance. As depicted above, the primary conductivity mechanisms for bulk v. nanoparticle loaded barium fluoride were fundamentally different; bulk conductivity exhibited both conductive and diffusive mechanisms and nanoparticle samples were explicitly diffusive.

1.6.2 Warburg Diffusion Impedance

The complete EIS circuit consists of contributions from the electrolyte, the electrode-solution interface and the electrochemical reactions taking place on the electrode. Diffusion in EIS can be thought of not as a point-particle charge, but as a distribution over a finite region. Further, the charges can either be uncharged or mobile, where mobile species may contribute significantly to system impedance. Often (as in the cases investigated here), a near-even contribution between the real and imaginary components of the impedance occurs. Thus, the phase shift is π/4 and the event is independent of frequency. Frequency independence in purely diffusive systems also reflect the domains of both extensive and intensive properties of a system[55]. This is because at high frequencies, diffusion will occur only in proximity to the electrode and are therefore intensive. Lower frequencies will approach the resonant frequency of the circuit and

$$Z_w(\omega) = Z_w(0)\frac{\left[\tanh\left\{i\left(l/l_d\right)^2\right\}^{0.5}\right]}{\left\{i\left(l/l_d\right)^2\right\}^{0.5}} \qquad 1.5.37$$

extensive properties of the material will then emerge. Eq. 1.5.37 below reflects these properties,where l is the separation between the electrodes; $Z_w(0)$ is resistance, proportional to l and, therefore extensive. At high frequencies, tanh→*1*, and $Z_w(0) \rightarrow l_d$.

1.7 Aim of the Dissertation

The Studies described in his Dissertation could generally be described as having a three-fold goal: synthesis, variation and reporting results of the effect of this on properties such as conduction.

The theme of these efforts is to explore various aspects of ionic conductivity and whether changes to size, vacancy number and temperature have any effect on increasing ionic conductivity within the systems under study. Firstly, to advance basic synthesis, efforts were made to explore and report the details of monodisperse nanoparticle synthesis of different types of pristine binary (MF_2; M = Ba, Ca; LnF_3; Ln = La, Sm, Ho, Gd, Nd) fluorides, as well as low-level doping of two different Group II binary fluorides: CaF_2 and BaF_2. Difficulties ensued when these modified synthesis methods (the reverse-micelle method described in Section 1.2 of this Introductory Chapter) were applied toward the synthesis of PbF_2. As such, efforts were made to find a surfactant which would eliminate the apparent solubility challenges of dissolved bromide and fluoride ion. This resulted in the inadvertent synthesis and single-crystal characterization of a novel, fluoride-based crystal, which was successfully used in the synthesis of PbF_2.

Secondly, variation took on several aspects. In one chapter, the super-Lewis acid, antimony pentafluoride, was used to artificially induce vacancies in both nanoparticle and bulk BaF_2 to see what the enhancements and ionic behavior resulted. In another chapter, extensive changes in ionic conductivity were examined as a function of temperature in an unusual system of CaF_2/BaF_2 layering, synthesized by Molecular Beam Epitaxy. Both of these chapters had at their root the principles of space-charge theory and how applicable this theory is toward different types of systems where ionic conductivity is nevertheless a common theme.

Finally, a modified pulse sequence was developed to address challenges which accompany complex spectra of scarce spins in carbon samples. The results were reported on an actual system, following testing, where spectra could be edited and inverted as a function of changes in contact time, following a selective change in spin phase during the experiments.

1.8 References

1) Zalkin, A., Templeton, D. H. J. Am. Chem. Soc., 1953, 75 (10), pp 2453–2458

2) Rotereau, K., Gesland, J. Y., Daniel, P., Bulou, A. *Mat. Res. Bull.*, 28, (1993), 813-819

3) Pileni, M.P. *J. Exper. Nanosci.*, 1,1, (2006)

4) Boutonnet, M., Kizling, J., Stenius, P. *Coll. Surf.*, 5 (1982)

5) C. Petit, C., Lixon, P., Pileni, M.P. *J. Phys. Chem.* 94, 1598 (1990)

6) Hua, R. Zang, C., Shao, C., Xie, D., Shi, C. *Nanotechnology* 14 (2003)

7) Desai, A., Varade, D. Mata, J. Aswal, V., Bahadur, P. *Coll. Surf. A* 259 (2005)

8) Muller, N., Pellerin, J.H., W. Chen., W.W. *J. Phys. Chem.*, 76, 21, (1972)

9) Pinna, N., Wild, U., Urban, J., Schlögl, R. *Adv. Mat.* 15, (2003)

10) Breit, G.; Rabi, I. I. *Phys. Rev.*, 38, 11, (1931)

11) Larmor, J. *Phil. Trans.* 1894-95-97

12) Becker, R. *Elektronnaia Teoriia*. Moscow-Leningrad, 1936. (Translated from German.)

13) Landau, L. D., Lifschitz, E.M., Teoriia polia, 5th ed. Moscow, (Teoreticheskaia Fizika, vol. 2.) (1967)

14) Grosso, G., Pastori-Parravicini, G. Solid State Physics. Academic Press, San Diego, CA (2003)

15) Anet, F.A.L; O'Leary, D.J. *Concepts in Magn. Reson.* 3, 193 (1991)

16) Haberlein, U. High Resolution NMR in Solids: Selective Averaging; Academic Press: New York (1976)

17) Andres, E. R. *Int. Rev. Phys. Chem.* 1 (1985)

18) Zaloznykh, V.M., Fedorov, L.A. *J. Struct. Chem.* 29, 5 (1989)

19) Blümich, B., Spiess, H.W. *J. Mag. Reson.*, 61 (1985), 356-362.

20) T.F. Havel, T.F., Cory, D.G., Somaroo, S.S. C.-H. Tseng, S.S. *Geometric Algebra Methods in Quantum Information Processing by NMR Spectroscopy* in Geometrical Algebras with Applications in Science and Engineering (eds E. Bayro-Corrochanno & G. Sobczyk), Birkhauser (2001)

21) Doran, C.J.L., Lasenby, A. Geometric Algebra for Physicists. Cambridge University Press 2005.

22) Hestenes, D. *J. Math. Anal. Appl.*, 24:313 (1968)

23) Hestenes, D. *Am. J. Phys., 30*: 1013 (1971)

24) Gurtler, R. Hestenes, D. *J. Math. Phys.*, 16, 3, (1975)

25) Hestenes, D. *Am. J. Phys.*, 47, 5 (1979)

26) Hestenes, D. *A Unified Language for Mathematics and Physics*. Clifford Algebras and their Applications in Mathematical Physics. J.S.R. Chisholm and A.K. Common (editors). 1st ed. D. Riedel Publishers, Dordrecht (1986)

27) Hestenes, D. *On Decoupling Probability from Kinematics in Quantum Mechanics*. Maximum Entropy and Bayesian Methods, Kluwer Academic Publishers, Dordrecht (1990).

28) Doran, C.J.L., Hestenes, D., Sommen, F., van Acker, N. *J. Math. Phys.* 34(8) (1993)

29) Doran, C.J.L., Lasenby, A.N., Gull, S.F. *Grassmann Mechanics, Multivector Derivatives and Geometric Algebra*. Spinors, Twistors and Clifford Algebras. Oziewics. Z. Borowiec, A. Jancewicz, B. (editors), Kluwer Academic Publishers, Dordrecht (1993).

30) Gull, S.F., Lasenby, A.N., Doran, C.J.L. *Found. Phys.*, 23, 9 (1993).

31) Gull, S.F., Lasenby, A.N., Doran, C.J.L. *Found. Phys.*, 23, 9 (1993).

32) Blake, P., Lee, B., Summers, M., Adams, M., Park, J.-B., Zhou, Z., Bax, A. *J. Biomol. NMR.* 2, 5 (1992)

33) Blake, P. R., Park, J. B., Adams, M. W. W., Summers, M. F. *J. Am. Chem. Soc.* 114, 12 (1992)

34) Ewen, H. I.; Purcell, E. M. *Nature* 168, 356 (1951).

35) Carr, H. Y.; Purcell, E. M. *Phys. Rev.* 94, (1954)

36) Andrew, E.R; Bradbury, A; Eades, R.G. *Nature* 182 (1958)

37) Lowe, I. J. *Phys. Rev. Lett.* 2 (1959)

38) Samoson, A., Lippmaa, E., Pines, A. *Mol. Phys.* 65,4 (1988)

39) Mehring, M. Principles of High-resolution NMR in Solids; 2nd Ed.; Springer-Verlag, New York (1983)

40 Hartmann, S.R; Hahn, E.L. *Phys. Rev.* 128 (1962)

41) Pine, A., Gibby, M.G., Waugh, J.S. *J. Chem. Phys.* 59 (1973)

42) Stejskal, E.O., Schaefer, J. Waugh, J.S. *J. Magn. Reson.* 28 (1977)

43) Gullion, T., Schaefer, J. *J. Magn. Reson.* 81, (1989)

44) Grey, C.P., Vega, A.J. *J. Am. Chem. Soc.* 117 (1995)

45) Hing, A.Wl, Vega, S., Schaefer, J. *J. Magn. Reson.* 96 (1992)

46) Gullion, T. *Chem. Phys. Lett.* 246 (1995)

47) Raleigh, D.P., Levitt, M.H., Griffin, R.G., *Chem. Phys. Lett.* 146 (1988)

48) Bennett, A.E., Ok, J. H., Griffin, R. G., Vega, S. *J. Chem. Phys.* 96 (1992)

49) Tycko, R., Dabbagh, G. *Chem. Phys. Lett.* 173 (1990)

50) Feike, M., Demco, D.E., Graf, R., Gottwald, J., Hafner, S., Spiess, H.W. *J. Magn. Reson. A.* 122 (1996)

51) Lee, Y. K., Kurur, N. D., Helmle, M., Johannessen, O. G., Nielsen, N. C., Levitt, M. H. *Chem. Phys. Lett.* 242 (1995)

52) Wu, X., Burns, S. T., Zilm, K. W. *J. Magn. Reson. A* 111 (1994)

53) Macdonald, J.R. *Ann. Biomed. Eng.*, 20, (1992)

54) Vladikova, D. *Proceedings of the International Workshop "Advanced Techniques for Energy Sources Investigation and Testing"* 4 – 9 Sept. 2004, Sofia, Bulgaria

55) Bard, A.J., Faulkner, L.R. Electrochemical Methods: Fundamentals and Applications. Wiley; 2nd ed. (2002)

56) Peerson, O. B., Wu, X., Kustanovich, I., Smith, S.O. *J. Magn. Reson. A* 104 (1993)

57) Metz, G., Wu, X., Smith, S.O. *J. Magn. Reson. A* 110 (1994)

58) Siegel, R. Nakashima, T.T., Wasylishen R.E. *Chem. Phys. Lett*. 388 (2004) 441–445

59) Shangwu Ding, S., McDowell, C.A. *J. Magn. Reson*. 135, 1 (1998)

60) Rovnyak, D., Kennedy, P.E. J. Mag. Reson. 196 (2009)

61) K. H. Lim, K.H., C. P. Grey, C.P. *Sol. State NMR* 13, (1998).

62) Wu, X., Burns, S.T., Zilm, K.W. *J. Magn. Reson. A* 111 (1994)

63) Frye, J.S., E. Maciel, G.E. *J. Mag. Reson*. 48 (1982)

64) Bryce, D. L.; Bernard, G. M.; Gee, M.; Lumsden, M. D.; Eichele, K.; Wasylishen, R. E. *Can. J. Anal. Sci. Spectrosc*. 46, (2001)

65) Tycko, R., et al. *J. Mag. Res*. 196 (2009)

Chapter 2

Preparation of MF_3 (M = Nd, Sm, La), MF_2 (M=, La_xCa_{1-x}; x = 0.06;F_{2+x}) Nanoparticles via Reverse Micelle Microemulsion: Synthesis and Characterization

Abstract

Benign methods and synthetic conditions for the preparation of pure and/or doped monodisperse, LnF_3 nanoparticles (Ln = select lanthanides: La, Sm, Ho, Gd) are desirable from research and industrial perspectives. To date, very little research on synthesis of pristine or doped BaF_2/ CaF_2/ ($M_{1-x}N_xF_{2+x}$) or LnF_3 has been performed. A modified, reverse-micelle method has been developed and successfully applied to synthesize LnF_3 and La-doped BaF_2. Xray crystallography and TEM was used to characterize pure BaF_2 and LaF_3 nanoparticles, having a mean particle size of 20.0 and 8.5nm, respectively. In the synthesis of pure BaF_2, CaF_2 and ($M_{1-x}N_xF_{2+x}$), particle size can be approximately controlled by interrupting the reaction/nucleation process. In contrast to MF_2 synthesis however, no time-dependent control over particle size appears available for synthesis of the LnF_3 nanoparticles.

2.1 Introduction

Controlled doping of select cations into a nanoparticle would present new opportunities to researchers in several fields including optics, and solid-oxide fuel cells. In preparation for an attempt to dope in lanthanum cations in controlled amounts into BaF_2 nanoparticles, careful synthesis and characterization of LaF_3 nanoparticles was performed. In addition to the interest spurred by the solid-state laser compound $LiYF_4$ in the 1990s, trifluorides of the α, β YF_3 type also sparked considerable research over the past decades because of their high anionic conductivities.[1,2]. Due to the high fraction of surface area relative to the bulk, it has long been thought that nanoparticles may afford increased anionic mobility of the material, despite the activation energies associated with the grain boundary. Bulk lanthanum fluoride has been known to exhibit high fluoride conductivity and here it was surmised that higher anionic conductivities could be achieved by preparing a nanometric LaF_3 sample[3].

Trifluorides in the form MF_3 (M = La - Eu) usually form the tysonite structure adopting the P^6_3/mcm space group, although some confusion with the $P\underline{3}c1$ space group appeared early on due to twinning, and the orthorhombic phase can also be induced or predominate, provided conditions and elements are correct (Gd - Lu = *Pnma*)[4,17,19]. Consistent with the results presented in this chapter, the hexagonal form dominates at room temperature although the data presented in this chapter do appear to indicate that this synthetic method can produce the orthorhombic (*Pnma*) phase [5, 6,18].

Recently, Hua et al., detailed the preparation of barium fluoride nanoparticles, as well as a slightly (3 mol%) Ce-doped BaF_2 from a microemulsion[7]. Additionally, Bender, et al. prepared Nd-doped BaF_2 (in dopant concentrations as high as 51 mol.%) nanoparticles, although the technique was different from Boutonnet. In Boutonnet's method, three components are used to form the microemulsions: water, cetyltrimethylammonium bromide (CTAB) and racemic 2-octanol. Bender's method also makes use of the reverse micelle, but triflates in addition to nitrates were used, and a cyclohexane support for the non-ionic surfactant IGEPAL© CO-520 (polyoxyethylene nonylphenol) was utilized. This differs substantially, since the polar head of CTAB, the primary surfactant used in these syntheses as well as those of Boutonnet, Hua, directly participates in the polar interior of the micelle [8, 10].

Emulsions are suspensions of fluid droplets that differ in either density, charge and/or surface tension from the surrounding, suspending medium, such that a static condition is acheived. The hallmark of a typical emulsion is that the droplets or micelles are nonpolar and the suspending medium is less nonpolar. A ***reverse*** micelle is, as the name implies, the opposite of what is typically considered a micelle. As outlined in Chapter One of this Dissertation, reverse micelles contain polar constituents within spherical (or sometimes rodlike) droplets surrounded by a nonpolar medium, with the charge-compensating components of the micelle surface being the polar substituents of the surfactant and/or co-surfactant. In a reverse microemulsion, the droplets are on the micron scale (diameter) and the individual droplets are extremely small (on the order of microns).

This chapter describes the synthesis and characterization of $MF_{2,3}$ (M = Pb; La, Nd, Ho, Sm) nanoparticles using different, particular ratios of the three micelle components: water, CTAB, cosurfactant (2-Oct) and the appropriate reagent salts dissolved in water. Here, a modified method was used (indicated below), yielding substantial amounts of monophasic metal fluorides. The intent of this investigation is to explore the viability of this synthetic method as a means of creating a broad range of monodisperse nanoparticles of the type MF_2, MF_3, as well as its potential for controlling the amount of dopant added. Additionally, β-PbF_2 and a La-doped CaF_2 ($La_xCa_{1-x}F_{2+x}$; x = 0.06) sample were synthesized and characterized.

Binary fluorides of this type (such as LaF_3 and β-PbF_2) have historically exhibited very high conductivities . The mechanisms of fluoride anion conductivity for this class of fluorides in the bulk have been well-described in the literature[20-22]. MAS NMR, in conjunction with other methodologies, lends itself well to analysis of these fluorides and local motion, so the establishment of the microemulsion synthesis described in this chapter as a consistent, reproducible means could provide the scientific community with an environmentally friendly, scalable, recoverable system to produce pure, doped, morphologically varied, yet monodisperse samples for accelerated study[23-25,30].

2.2 Experimental

2.2.1 MF_3 Synthesis

A 3.3:1 molar ratio of the corresponding precursor salts were prepared using water purified in a Barnstead milipure system (~18MΩ resistance). The two salt solutions, NH_4F and $M(NO_3)_3$ (M = La, Nd, Sm, Ho, Gd) at 0.798 M and 0.242M, respectively, were prepared by dissolving the respective salts in purified water obtained from a Barnsted millipure system. The high solubility of the salts made dissolution under ultrasonic conditions facile.

Using a percent-mass ratio of 70.85:17.7:11.44 between the 2-Octanol:CTAB:H_2O-salt solutions, two separate beakers of 2-Oct and CTAB according to the aforementioned ratios were measured, covered with parafilm and mixed at room temperature for approximately two hours. Once the two mixtures were homogeneous, the beakers were labelled A and B and the respective salt solutions were added dropwise using two burettes and in equal volumes. The two beakers were then covered with paraffin film and allowed to stir for another two hours at room temperature.

Once the contents of the two beakers, A and B, became either clear or translucent, the two beakers were then mixed together. Upon mixing, the contents became turbid. Approximately six minutes elapsed before the mixture was transferred to glass centrifuge tubes. Typically, we used a six-minute period, due to the loose correlation between mixing time and particle size as indicated by Hua, but we also varied this time to explore the effects on the resulting products[7].

The resultant slurry, approximately 195ml, was then centrifuged for approximately six hours at 1.6kHz using covered centrifuge tubes. Again, covering was essential, as the 2-oct evaporated leaving fractal-like CTAB crystalline masses covering the centrifuge tubes, trunnion and basket tubes.

After centrifugation, a clear supernatant dominated at over 98% of the total volume of the graduated centrifuge tubes. A small amount of opaque mass remained at the bottom. A Büchner funnel vacuum filtration setup was created using an unlaminated PTFE microfilter (Sterlitech Corp. 22027 70th Av. S. Kent, WA 98032) placed in the base of the funnel.

The supernatant was decanted and the opaque mass was carefully removed and washed thoroughly with an equimolar acetone/ethanol solution. The caked powder which remained after washing/filtration was then ground in a mortar and pestle, washed three more times and then allowed to air dry overnight under vacuum filtration.

2.2.2 PbF_2 Synthesis

A dilute ($3.6x10^{-2}M$) solution of $Pb(NO_3)_2$ was prepared and a 52.5:32.5:15 ratio of 2oct:CTAF*:H_2O was also prepared for the lead nitrate precursor. CTAF* is defined as a carefully ground crystalline sample with the following stoichiometric formula: CTA:SiF_6:H_20, which was synthesized previously. The preparation of this CTAF* salt was prepared to reduce the concentration of the bromide anion, which was (apparently correctly) suspected to be interfering with the synthesis of the target fluoride salts. The synthesis and characterization of this salt will be elaborated upon in more detail in Chapter 3.

A corresponding 2.5:1 molar ratio [(NH_4F:$Pb(NO_3)_2$] of aqueous NH_4F was also prepared. In this case, however, CTAB, rather than CTAF*, was used to complete creating the suspension for the the ammonium fluoride component (in the previously reported ratio). Although using CTAF* would have been ideal to use in the preparation of the NH_4F precursor suspension as well, the CTAF* synthesis is challenging and prolonged, so care was taken to use the CTAF* sparingly.

As with the MF_3 precursors, the contents of the two beakers were allowed to stir at room temperature until completely transparent. The two were then combined and the same methods used to generate, wash, dry and collect the precipitate were used.

2.2.3 $La_xCa_{1-x}F_{2+x}$ Preparation

A 0.4M solution of $Ca(NO_3)_2$ was prepared in the aforementioned manner. A 0.024M solution of $La(NO_3)_3$ was also prepared in the same manner and combined into a single Nalgene bottle for future use. A corresponding 2.5:1 [NH_4F: Z; Z=16.67:1 $Ca(NO_3)_2$:$La(NO_3)_3$] in a 17.71:70.85:11.44 mole ratio of 2oct:CTAB:H_2O were prepared as before.

General Note on These Reverse-micelle Synthesis Procedures

The same procedures outlined above were followed regarding the mixing, washing and drying of these samples. As part of the synthesis, covering the beakers with paraffin film was found to be essential, as the 2-Oct tended to quickly evaporate and the remaining CTAB crystallize into fractal-like formations which extended past the griffin beaker and/or centrifuge tubes. The reverse micelle was evident after approximately two hours' mixing time, as the initially opaque/white mixture became completely transparent in the case of the $La(NO_3)_3$ mixture and translucent in the case of the NH_4F.

2.2.4 Sample Characterization Preparation

Upon drying, the samples were ground in a mortar and pestle, weighed and then a small amount was either captured in a capillary tube or carefully placed in a small-xray-profile sample holder and prepared for x-ray diffraction (XRD). Either a Scintag Xray diffractometer (1.5405Å) was used to collect the data or a Rigaku Miniflex XRD [(either 1.5405Å (Cu) or 2.2896Å (Cr), as indicated] was used

to collect the powder diffraction data. Typically, the data are collected over a six-hour period with a step size of 0.02. Also, pyrex capillary tubes were filled in air, flame-sealed and run at Brookhaven National Laboratory's National Synchrotron Light Source (NSLS) beamline X7-B (0.898Å).

The small particle size and high absorption thought to be due to the lanthanides were thought to generate the poor signal-to-noise ratio. Therefore, the XRD data were smoothed in post-processing using Match! (v. 1.10) software (Crystal Impact, GbR; Rathausgasse 30 D-53111 Bonn, Germany) (see Figures 2.6-2.10).

The methodology used is the Savitzky-Golay smoothing algorithm, which takes three adjacent points around each point into account: The smoothed intensity at each point is a weighted sum of the point itself and the six adjacent points (three in each direction)[16]. Weighting factors used are outlined in "Numerical Recipes in C", Second ed., p. 651.

The TEM images were created using a Philips CM12, operating at 120KV. Small samples of the crysalline powders were dispersed in ethanol and sonicated for 20 minutes. A 20uL drop of the solution was placed on formvar-coated lacey-carbon TEM-grid, and air dried.

2.3 Results

Figures 2.1-2.5 depict stoichiometric LnF_3 and MF_2 XRD (Ln, M = as indicated in the Figures as well as tallied in Table 2.1). As mentioned in the Experimental Section, Figures 2.6-2.10 depict the same XRD patterns as in Figures 2.1-2.5, but with background subtracted and the smoothing methodology employed by the Match! software program. These Figures are included to enhance the clarity of the lineshapes for the reader.

Using the available, non-overlapping peaks, a mean particle size of 5nm was calculated for LaF_3. The mean particle size for NdF_3 was 30.6nm; $La_{0.06}Ca_{0.94}F_{2.06}$: 13.5nm; YF_3: 24.1nm;

SmF_3: 27.6nm; PbF_2: 17nm. As can be observed, for example, in Figure 1, below, significant peak overlap due to small particle size made use of the Debye-Scherrer method to determine particle size difficult. For example, peaks at 80 and 120, 2θ have shoulders associated with other peaks, again consistent with LaF_3.

If two phases are present in each sample, they are indicated in the figure (where applicable); it appears that both fluoride phases can formed during this synthetic process. Since XRD is, by definition, an average, one would prefer to exploit this fact and quantify the relative amounts of each phase present, were it not for the poor signal-to-noise ratio. Commercially available, bulk (>5μm) samples are monophasic.

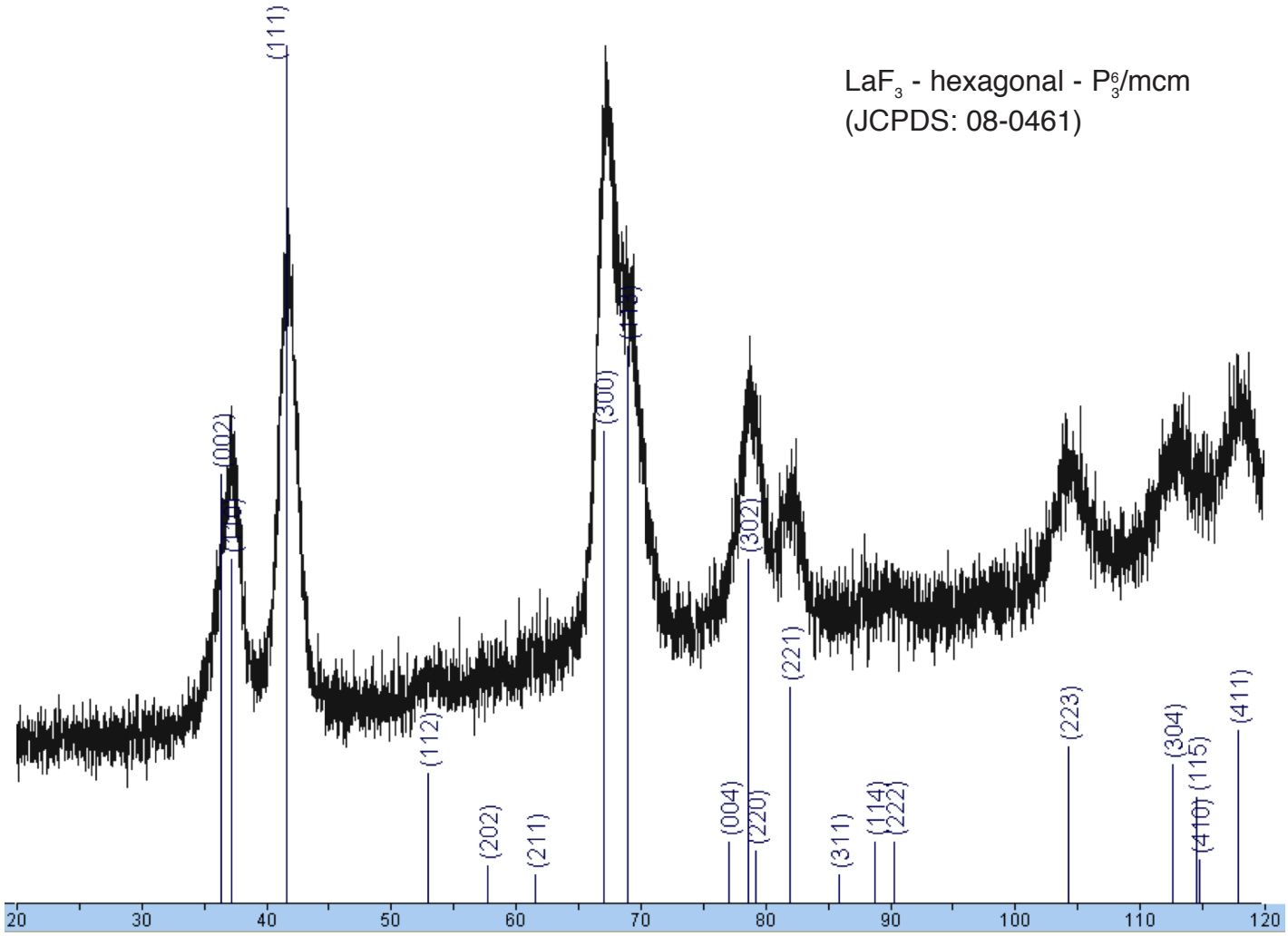

Figure 2.1: x-ray diffraction pattern of LaF_3 nanoparticle sample with JCPDS Miller Index overlay

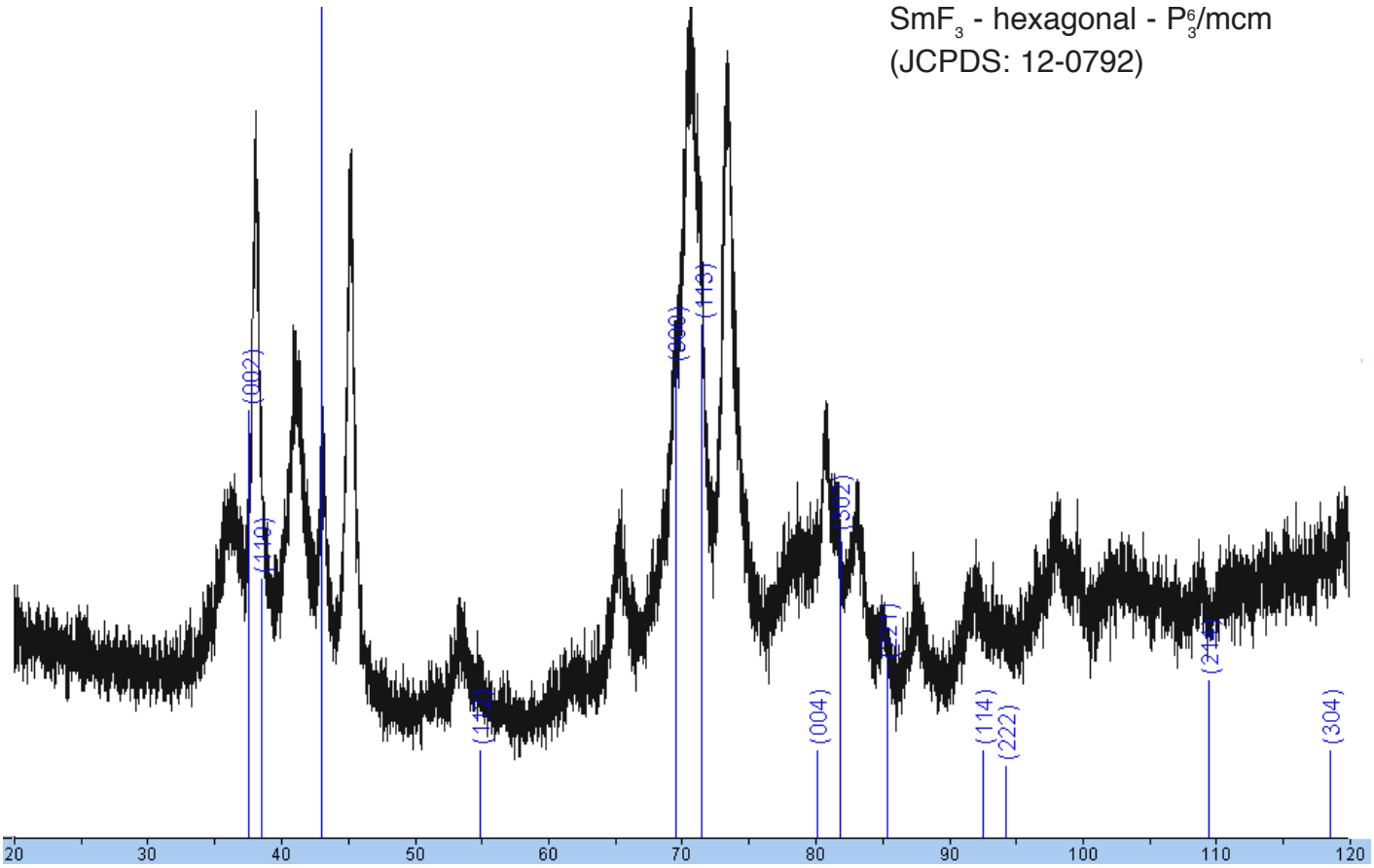

Figure 2.2.1: x-ray diffraction pattern of SmF_3 with JCPDS Miller Index overlay

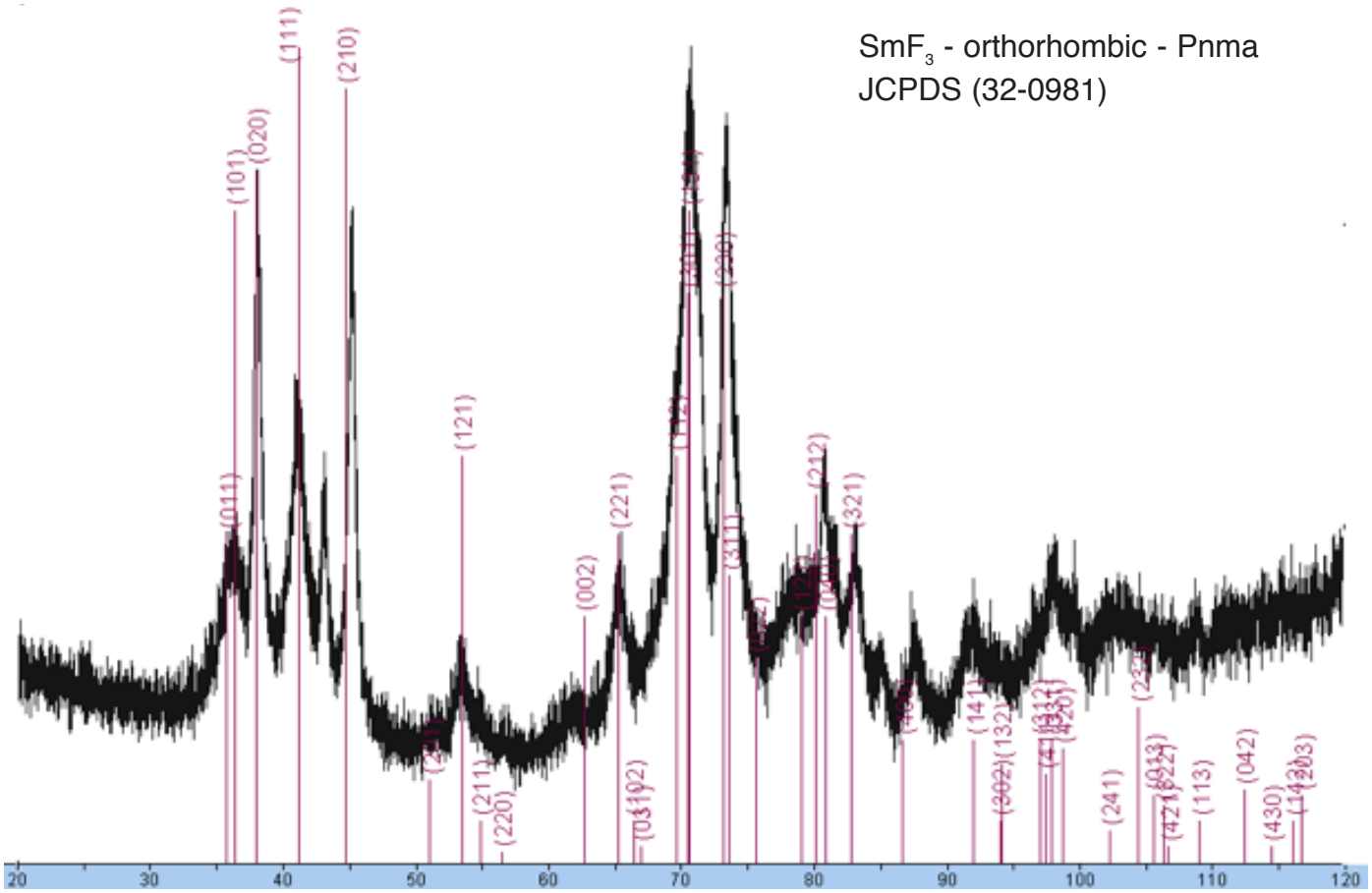

Figure 2.2.2: x-ray diffraction pattern of SmF_3 with JCPDS Miller Index overlay

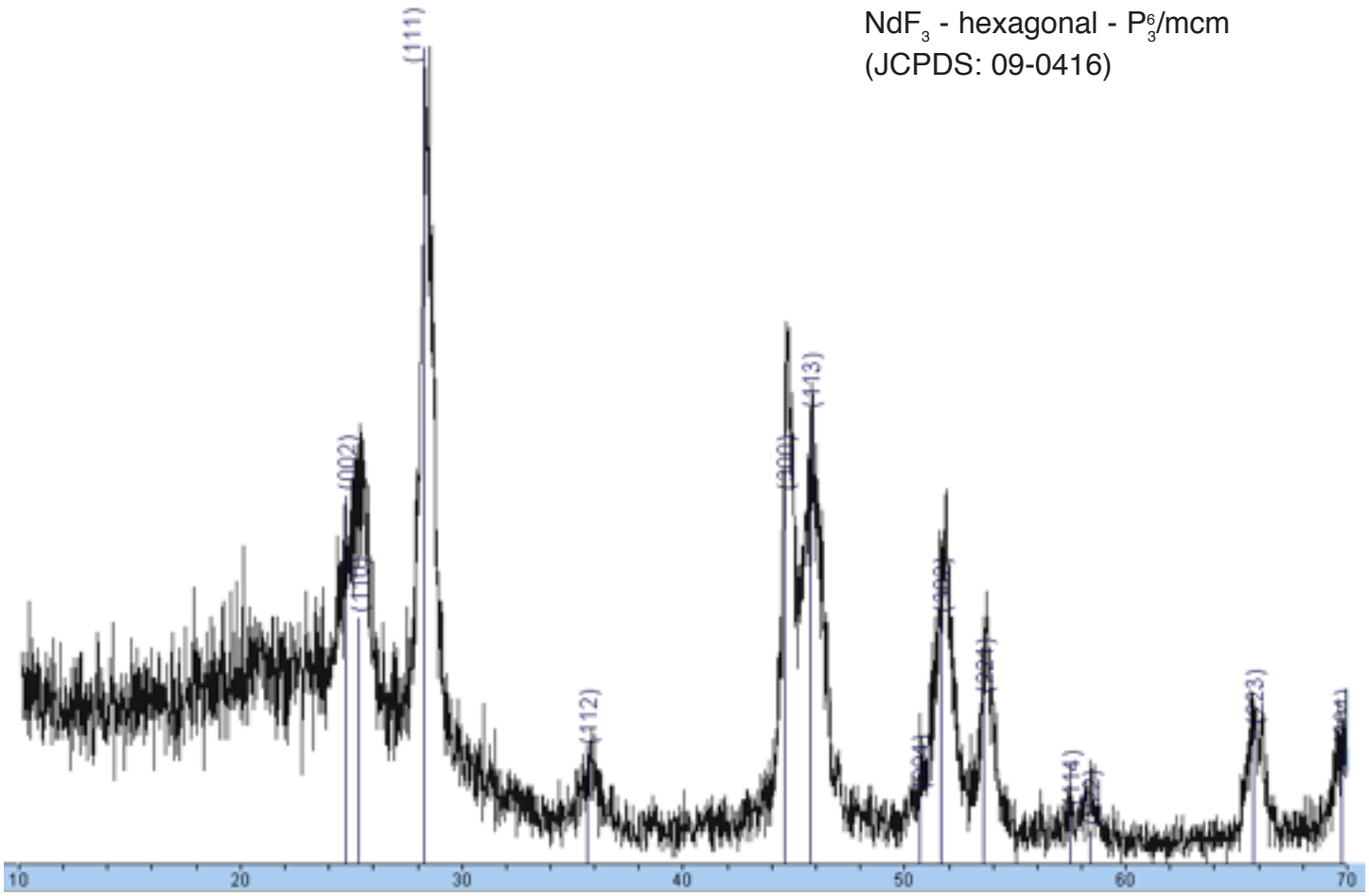

Figure 2.3: x-ray diffraction pattern of NdF_3 with JCPDS Miller Index overlay

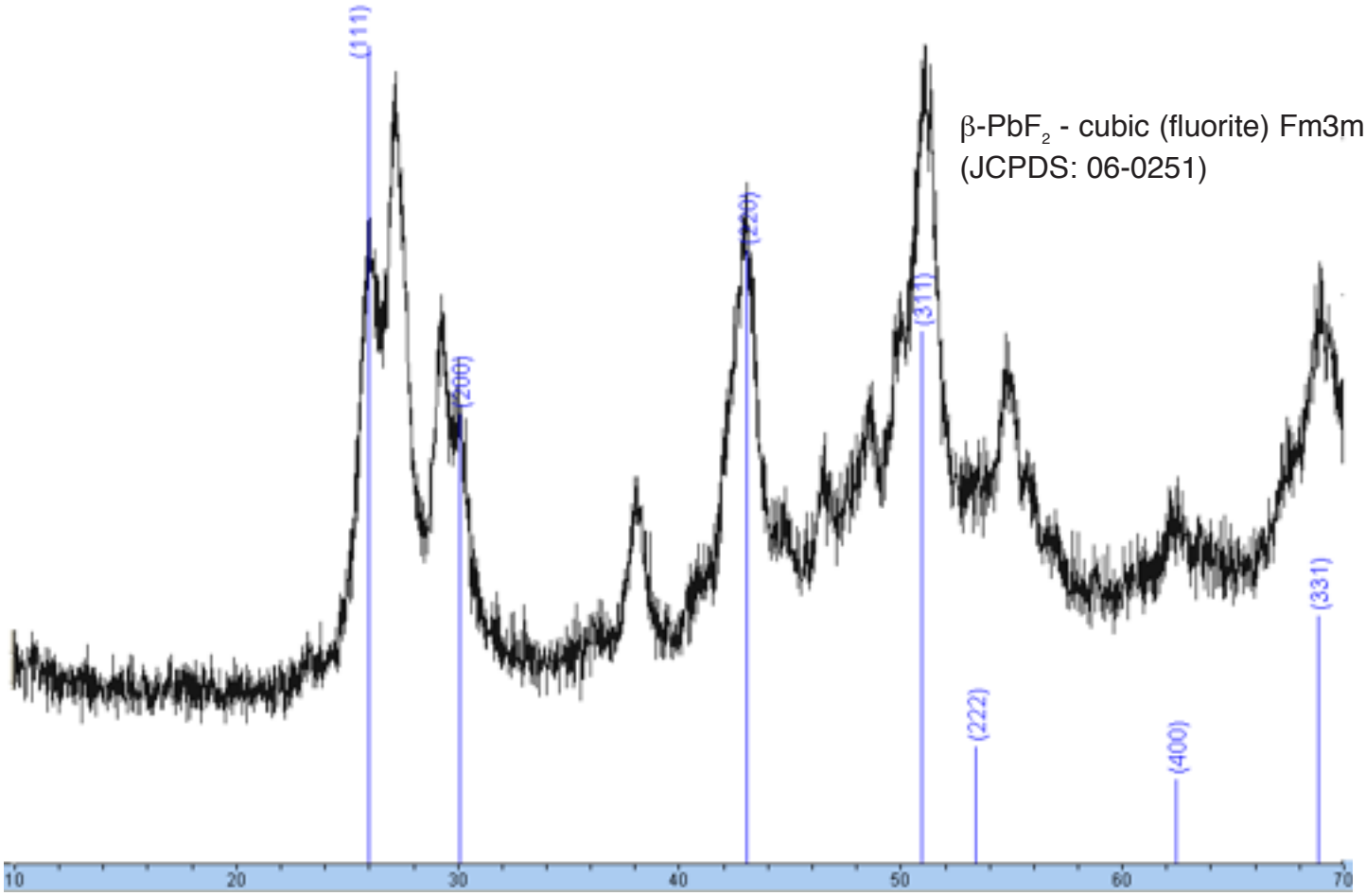

Figure 2.4.1: x-ray diffraction pattern of α, β–PbF_2 with JCPDS Miller Index overlay of only the b-PbF2 phase (in blue)

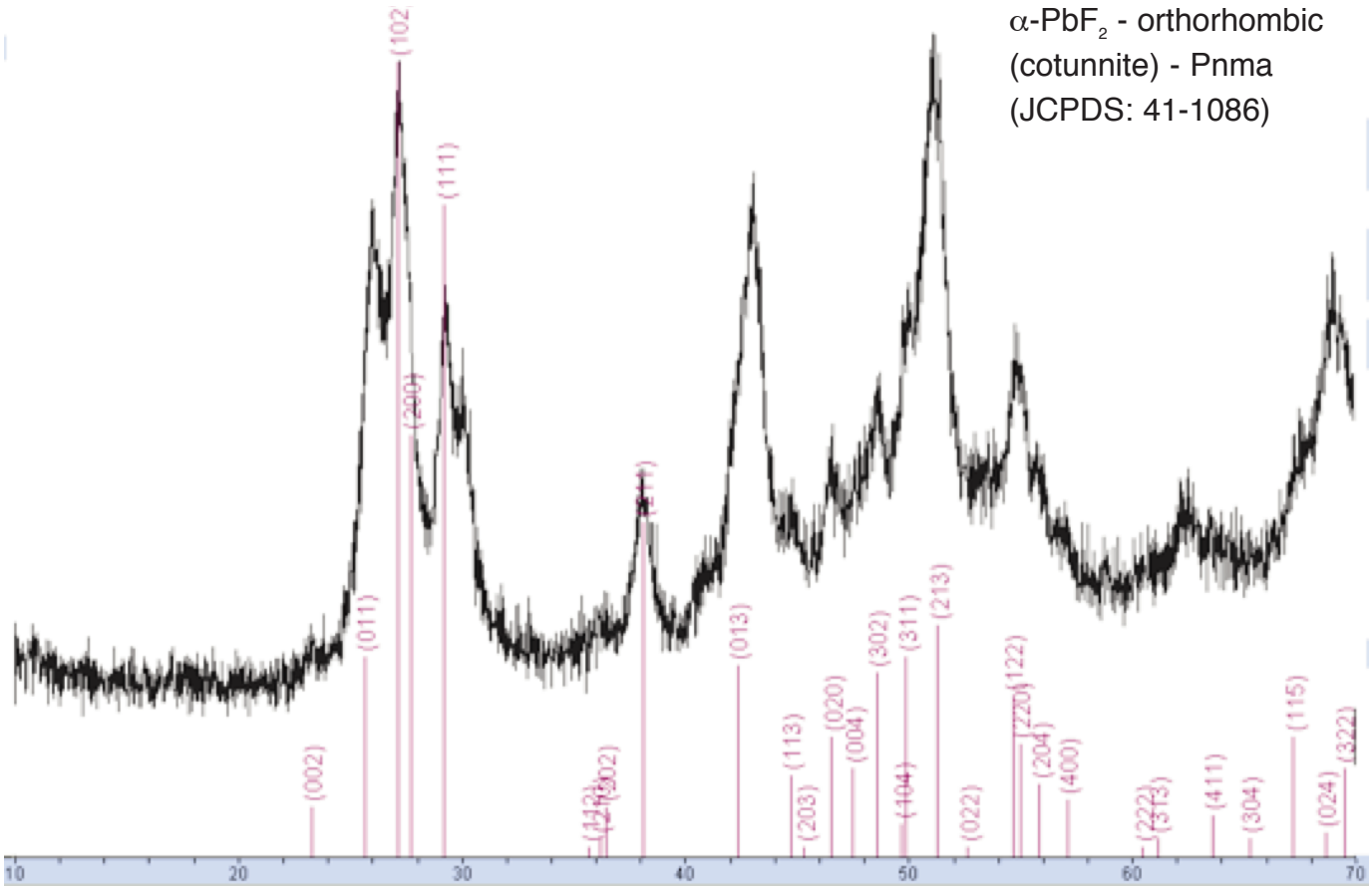

Figure 2.4.2: x-ray diffraction pattern of α, β–PbF_2 with JCPDS Miller Index overlay.

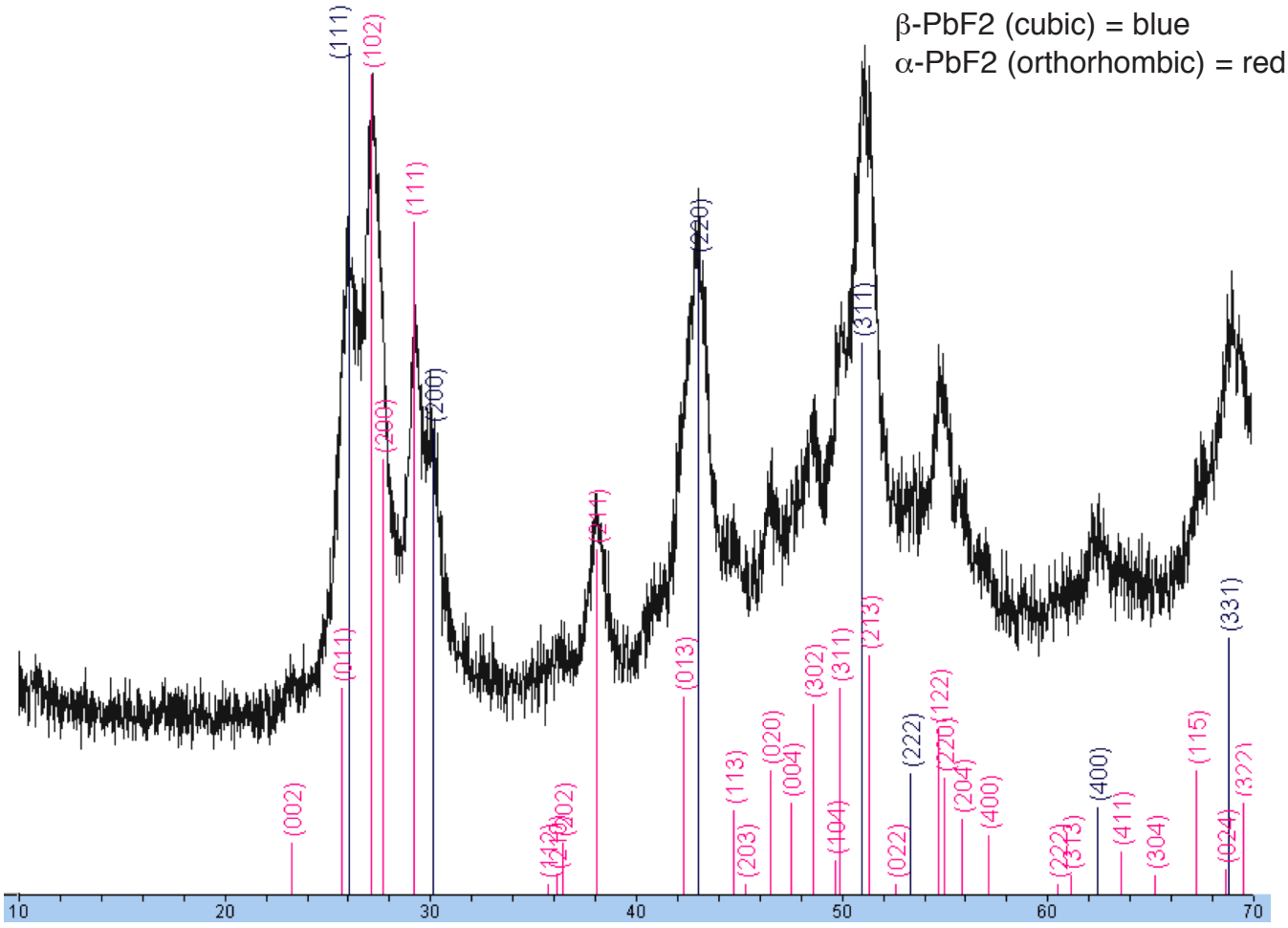

Figure 2.4.3: x-ray diffraction pattern of α, β–PbF_2 with JCPDS Miller Index overlay of both the α and β JCPDS phase reflections overlaid (β-phase in blue; α-phase in pink)

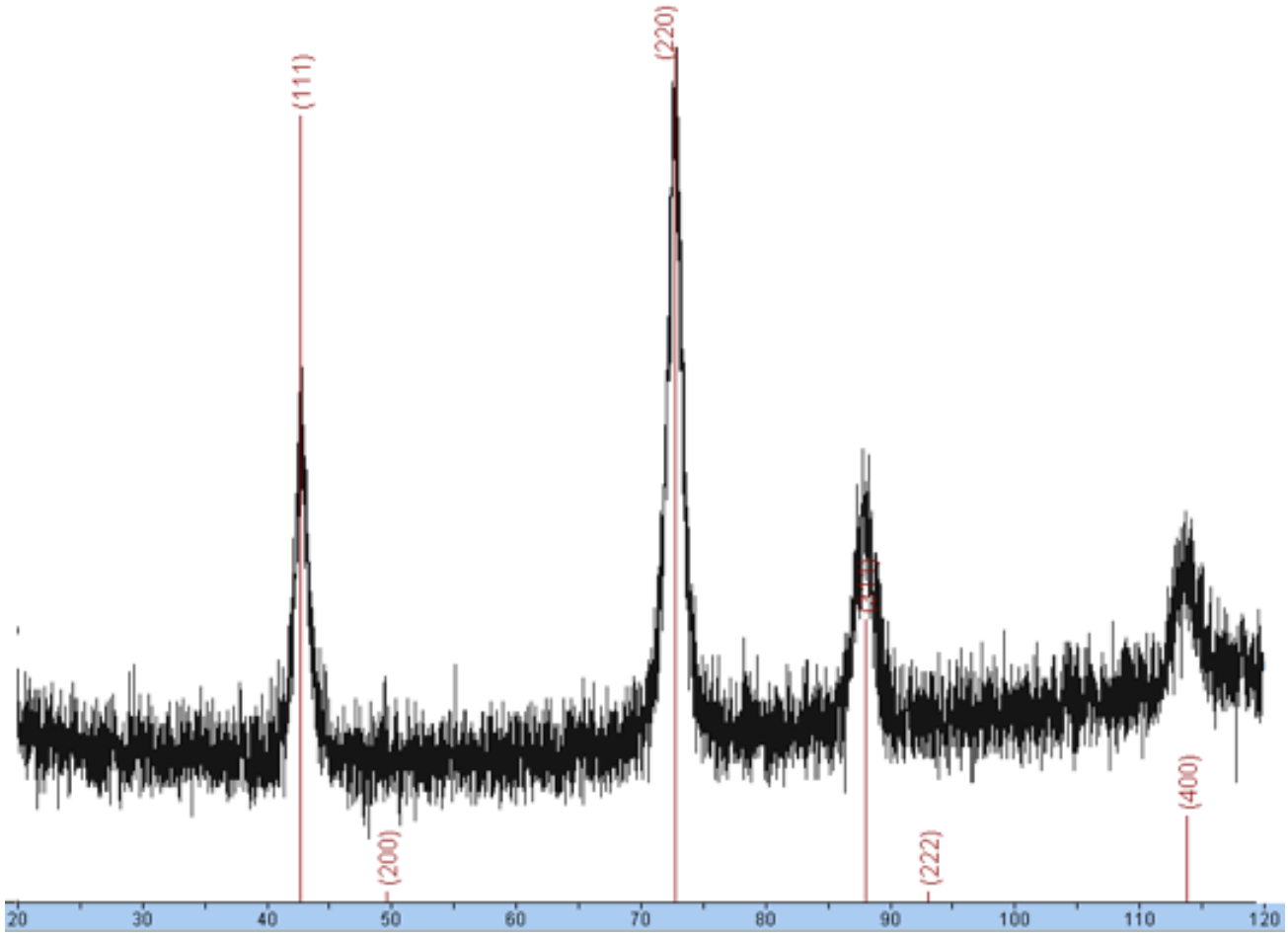

Figure 2.5: x-ray diffraction pattern of $La_xCa_{1-x}F_{2+x}$ (x=0.06) with JCPDS Miller Index overlay

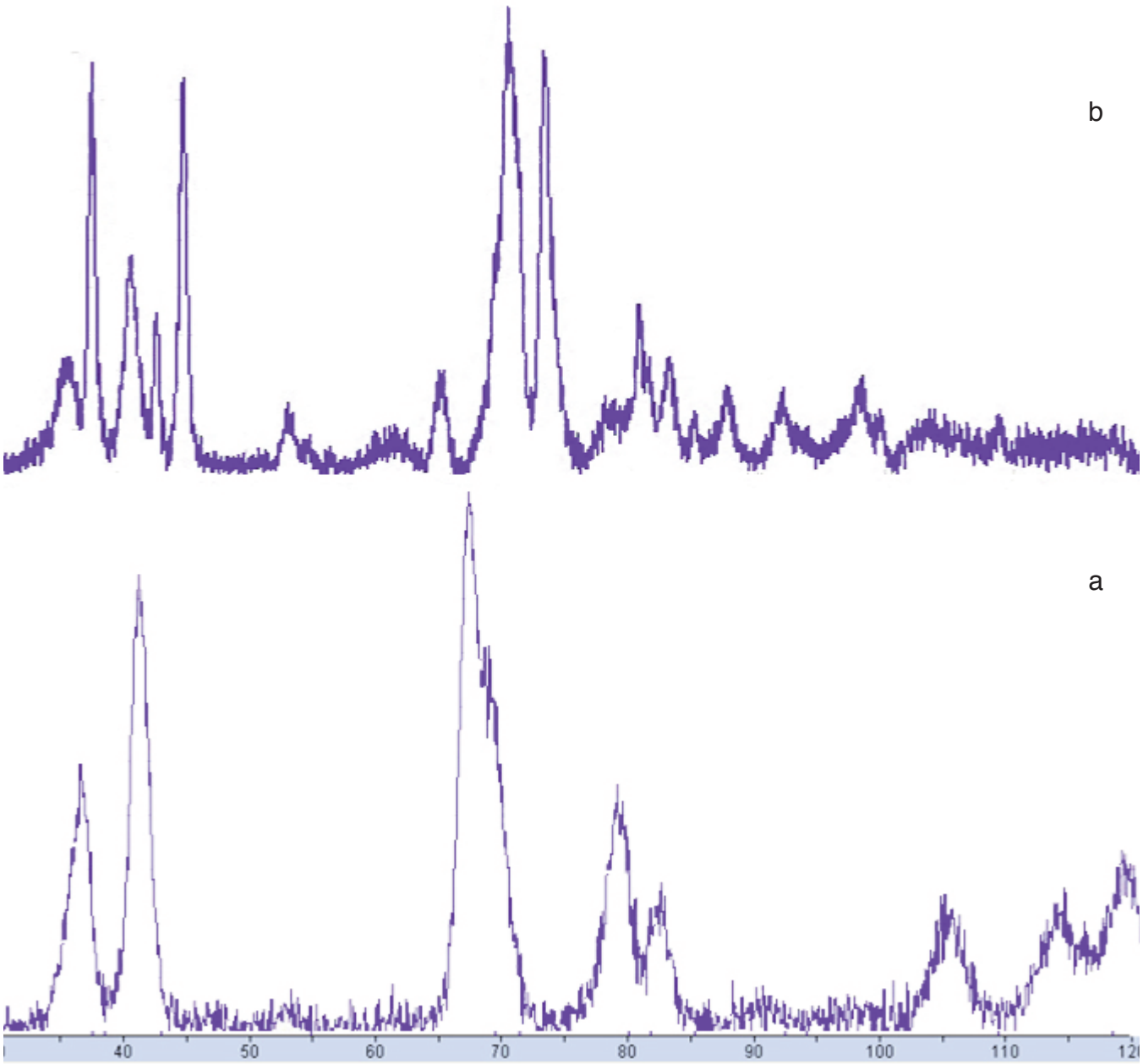

Figure 2.6 a, b: x-ray diffraction pattern of LaF_3 nanoparticle sample (a) and SmF_3 (b) with background removed using Match! software.

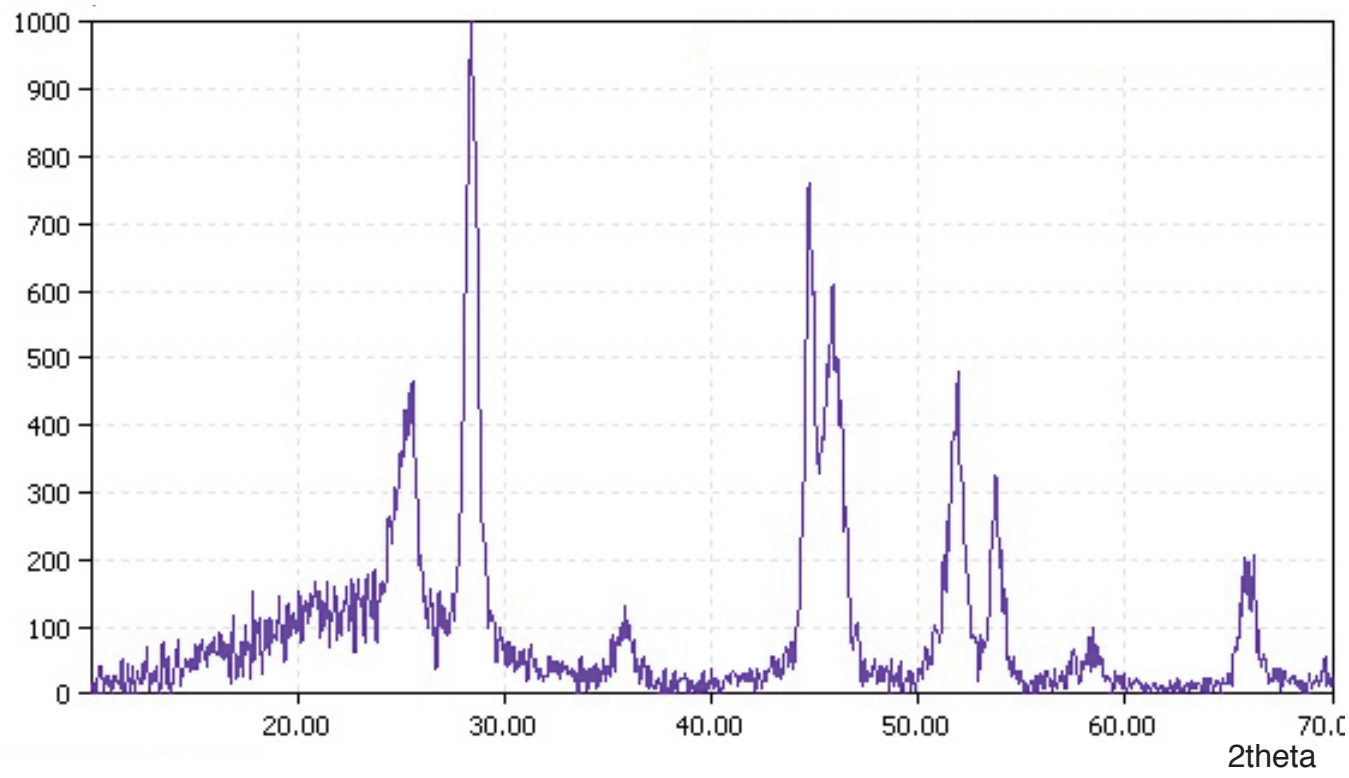

Figure 2.8: x-ray diffraction pattern of NdF_3 nanoparticle sample.

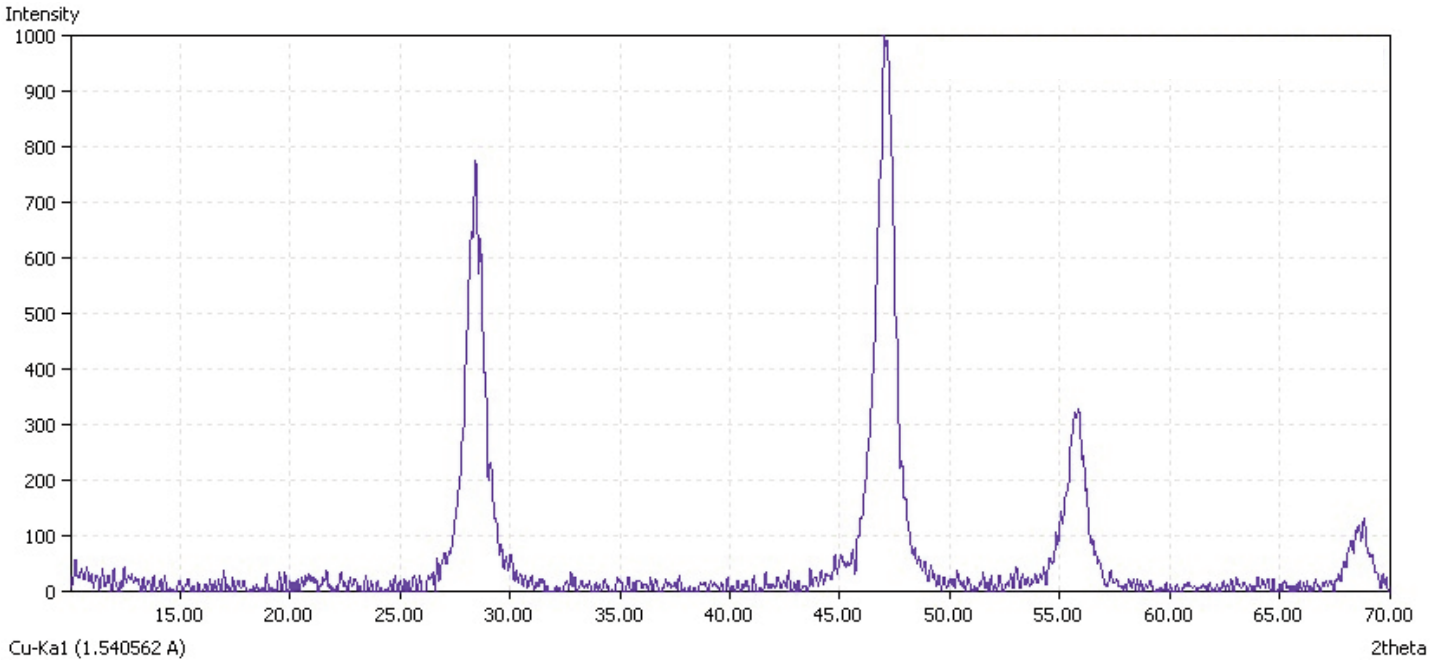

Figure 2.10: x-ray diffraction pattern of $La_{0.06}Ca_{0.94}F_{2.06}$ nanoparticle sample

The explicit intent of these experiments was to produce the smallest particle size in a reproducible fashion. Several additional experiments were conducted to confirm the relationship indicated by Hua, et al., that there was a roughly direct relationship between mixing time and particle size[7]. Because the goal of these experiments was to create the smallest particles (with some reasonable yield), no in-depth time:particle-size relationship was constructed. What was observed, however, was that no relationship between particle size and time was found during the LnF_3 syntheses. For the lanthanide samples, as much as a 40-minute time frame was used to allow the two precursor beakers (A and B) to mix together and no apparent change in particle size was observed.

Syntheses were performed according to time: as described in the Experimental section, the two beakers with the two parent reverse-micelle suspensions of nitrate and fluoride salts, respectively, were mixed together and a stopwatch was started. The reaction is stopped by decanting the mixture into centrifuge tubes and starting centrifugation. It was found that a rough correlation between mixing time and particle size was found.

Material	Expected Phase	Observed Phase	Particle Size (nm)	Reaction time (min.)
LaF_3	H	H	8.5	40(n/a)
NdF_3	H	H	30.6	40(n/a)
SmF_3	H	H+O	27.6	45(n/a)
PbF_2	O	C+O	17	6
BaF_2	C	C	20	6
$La_{0.06}Ca_{0.94}F_{2.06}$	C	C	13.5	6

Legend:

H = hexagonal
C = cubic
O = orthorhombic

Table 2.1: Tally of the MF_2, LnF_3 fluoride salts synthesized; M = Pb, Ba, Ca; Ln = La, Nd, Sm. The results were expected to be monophasic, particularly with the PbF_2, due to differences in energies of formation; this was not found to be the case. This is indicated in the Figures above which have more than one consistent JCPDS pattern. A six-minute reaction time was used for the MF_2 syntheses as a particle-size/time dependence was found only for the MF_2 particles. No time dependence on particle size was found with the LnF_3 particles (indicated by the use of *n/a* in the table above).

As is evident in Figures 2a,b and 4a,b, orthorhombic phases for SmF_3 and PbF_2 clearly appear to co-exist with the hexagonal phases. Some basic observations are tallied in Table 2.1, above. As mentioned in the caption below Table 2.1, one interesting observation made during these synthesis experiments is that there was a roughly linear time dependence on the particle size of the MF_2 particles. Although very desirable in the Figures, the poor signal-to-noise ratio and extremely broad, overlapping peaks due to small particle size unfortunately made Rietveld refinement impossible.

Brunauer-Emmett-and-Teller (BET) measurements were also made, although not reported here. The assumption made for BET surface-area measurements is that the particles are generally cuboidal in shape and have zero porosity, given the nature of these types of binary fluorides. As such, one asserts a simple relationship between the mean number of nitrogen molecules (N_2 was the analysis gas used) that could span the six surfaces of one cuboidal particle in a monolayer. Weibel, et al. have noted the difficulty in concretely determining particle size and suggest that several modalities be employed to narrow the error inherent to such precise measurements[9]. BET measurements for particle size on LaF_3 ($d = 6/S_0\rho$; $\rho_{LaF3} = 5.9 g/cm^3$), for example, yielded a mean particle size of approximately 8.5nm (consistent with the Debye-Scherrer technique), but repeated BET experiments on the different systems yielded inconsistent results.

Transmission electron microscopy was performed on the LaF_3 sample (see figure 2.11, below), yielding a somewhat uniform morphology w/ an apparent particle size of approximately 8 nm (see scale, inset). Four representative particles were used to approximate size are denoted by arrows.

One interesting note which apparently had no effect on the formation or size of pure, nanoparticle LaF_3 was the brief period of a translucent, greenish-yellow tint to the $La(NO_3)_3$ mixture. Color changes (though not as intense) were noted for the other lanthanides. The mixture eventually became clear and transparent after about 40 minutes; synthesis experiments were performed on both this greenish-yellow stage (about 15 minutes) as well as the transparent stage and no effect on particle size or purity was found with either route.

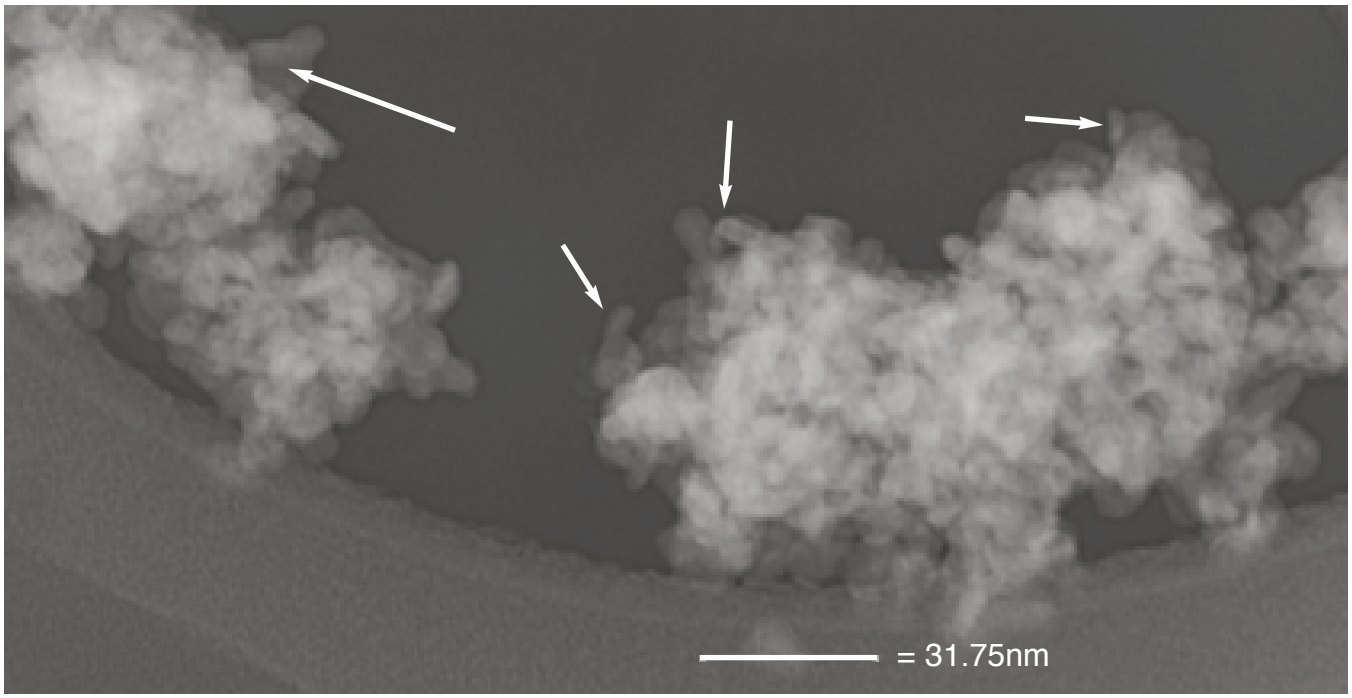

Figure 2.11: TEM image of LaF_3 nanoparticle sample. The four arrows indicate the representative crystallites which were measured to determine approximate particle size.

Numerous attempts at synthesis of β-PbF_2 using CTAB failed, despite many changes having been made to the CTAB/2-Oct/H_2O ratios. It was thought that either the bromide anion in the CTAB may hinder the formation of the fluoride salt or the polarizable Pb^{2+} cation may also interact unfavorably in some manner with either the somewhat polar 2-octanol co-solvent, CTAB, water or some combination of the three. Many unsuccessful attempts were made to synthesize the *fluoride* analog of CTAB, CTAF, so as to try and eliminate the possible influence in-situ bromide may have had within the reverse micelle. A new surfactant, cetyltrimethyl ammonium hexafluorosilicate dihydrate, ($(CTA)_2•SiF_6•2H_2O$; abbreviated CTAF*) was synthesized. The synthesis and characterization of this novel surfactant is described in the following Chapter of this Dissertation. As indicated in Figures 2.4.1-3, the synthesis of the α, β phases of PbF_2 were successful and it is due to this novel $(CTA)_2•SiF_6•2H_2O$ crystal.

Also, concentrations of $Pb(NO_3)_2$ were incrementally reduced in series of experiments until a successful precipitate was formed. Because the ultimately successful concentration was so dilute and the amount of CTAF* was somewhat limited (although the CTAF* synthesis eventually became facile to carry out, once the route was discovered), smaller yields (about 60% of theoretical) were achieved. The time needed for the $Pb(NO_3)_2$ suspension was significant. Almost two hours was needed for the components to suspend and complete transparency was never achieved; the mixture went from white/opaque to merely translucent.

The interesting observation made during the PbF_2 synthesis experiments was the fact that both the orthorhombic and cubic (α and β, resepctively) phases were produced (see Figure 2.4.1-3, indicated by the color-coded JCPDS patterns). The α-orthorhombic form was so named because it was the first one discovered[11,13]. The β-cubic phase was discovered later, following heating of the a phase which afforded the higher symmetry phase. Co-precipitation of both phases here was found to be unique, given the additional energy which was historically necessary to convert the α to the higher symmetry β phase[12,13].

2.4 Discussion

In contradiction to Hua, et al., no apparent relation between reaction time and particle size emerged during synthesis experiments performed for LaF_3 or for any of the lanthanide MF_3 samples[7]. For example, Hua, Boutonnet, et al., indicated either directly or indirectly that particle size is roughly proportional to the mixing time, once the two beakers have been mixed together[7,10]. This was confirmed when pure BaF_2 was synthesized and characterized and was again consistent with the $La_{0.06}Ca_{0.94}F_{2.06}$, α, β-PbF_2 samples.

It seems apparent that, consistent with the findings of both Rodenas and Desai, particle size may be more a function of percent-volume ratio among the three reverse micelle components, rather than,

as Hua had found, that nucleation time appears to be the governing parameter for MF_2[16,17]. As briefly mentioned in the **Experimental** and **Results** sections of this chapter, this hypothesis was explored, both in the times used to produce and track mean particle size for the MF_2 samples.

Future studies are planned which will analyze the phase diagram created by Rodenas, et al. which may lead to additional clues about the roles the three parent materials play (CTAB, 2-oct, H_2O)[15]. The fact that a single ternary ratio was used for all of the lanthanides, combined with the fact that nucleation time was irrelevant, may lead one to conclude that pool radius (droplet size), only in the case of the lanthanides, could be the major and sole contributing factor to particle size.

Pileni has investigated the extent to which water droplet size contributes to the size of the nanoparticulate[14]. Although their investigions are strictly limited to the AOT method and metals/semiconductors, they do indicate a clear, single-variable trend, with a size dependence based on their relative concentrations as the following $D(nm) = 0.3[H_2O]/[AOT]$. Rodenas, et al. found that water content played a major role in pool radius, yet aggregation was controlled by the CTAB surfactant and, perhaps more importantly, the interaction between the surfactant and co-surfactant (here, the relatively polar racemic 2-Oct)[15].

The droplets themselves were found to be on the order of tens of microns, according to Rodenas (ranging, depending on the CTAB-2Oct-H_2O ratio), which may be consistent with the hypothesis that particle size is exclusively governed by pool radius, yet the findings of other authors clearly point to other factors which must be included in the overall analysis. For example, a thorough investigation by Tani, et al., determined that both powder and single-crystal LaF_3 dissolve non-stoichiometrically at the surface/solution interface, leaving a net-positive surface charge[27].

This is demonstrated, such that $[F^-]/[La^{3+}] > 3$, $[F^-]/[La^{3+}]_{powder} >> [F^-]/[La^{3+}]_{sing.\ xtal}$ and the dissolution rate changes with changes in pH. Fortunately, Tani, et al., used $NaNO_3$ as the source of the (nitrate) anion, which was found to charge-compensate for the positively charged surface vacancies in close to a 1:1 manner. This lends itself well to a possible scenario in the MF_3 syntheses presented here: the relative ratios of CTAB:2Oct:H_2O and the parent salts ($M^{III}(NO_3)_3$ and NH_4F) determine the micelle size (therefore, the surface charge/tension) and pH; an equilibrium is achieved within the micelles which is concomitantly pH- and surface-charge-dependent, such that particle growth stops when the chemical potential is matched by the dissolution potential. This, in turn, may be how particle growth can be controlled.

Micelle surface charge and complementary surface tension are directly influenced by choice of co-surfactant, which influence not only nucleation but on particle morphology as well[16,17]. Clearly however, the relationship between surfactant, water and co-surfactant is more complicated and, ultimately, at least partially salt-dependent, owing to the pH of the salts used and the role that plays on the interaction of the polar heads at the micellar surface.

The case of α, β-PbF_2 is clearly the outlier. The apparent fact that both phases (and particularly the cubic phase) were formed at room temperature and with such small size appears significant, yet not understood. The α-phase, the metastable phase with the lower (orthorhombic) symmetry, is the one that has historically been found and synthesized at STP conditions[30]. Only one example of room-temperature formation of bulk (>5μm), β-phase PbF_2 was found in the literature, and performed in carefully controlled circumstances by Sauka, et al.[31]. The synthetic and interconversion methods described in in the literature are both dependent on the energetics: fast precipitation produced the α-phase and

extremely slow precipitation with Sauka. In the case of Kennedy, interconversion between the two phases depended upon on the rate at which heat was applied. In reverse micelle synthesis, it may be the case that k_s is not constant. Rather, the intramicellar dynamics at the beginning of synthetic process may favor the α-phase, but that k_s may level off and that as dk_s/dt levels off, the β-phase may be favored, as Sauka had discovered[31].

The cationic size of Pb^{2+} is obviously smaller than the lanthanide cations. In this case, three variables appeared to contribute to the difficulties. What is most curious is the relatively high solubility of lead nitrate (52g/100ml @ 20°C) as reported in the CRC, far lower than barium nitrate (10.4g/100ml @ 25°C), which was also made with little difficulty (but not reported in this Chapter). Given these two facts, the only two variables left are pH and competing energies of formation between $PbBr_2$ and PbF_2. Dissolved lead nitrate is somewhat acidic: 3-4 at relatively low concentrations - lower than both calcium and barium nitrate (pH = 5) or lanthanum nitrate (pH = 7.4) at similar concentrations.

While it may still be feasible, given a careful construction of a ternary phase diagram, to find a suitable CTAB/2-Oct/H_2O ratio to precipitate β-PbF_2, it was not found during these experiments. Consistent with Rodenas, the water ratio, perhaps to handle the internal micelle stabilization for the polarizable Pb^{2+} cation in the polar, saline medium appears to be a factor[15].

This is by no means certain, however, since a thorough investigation of ratios was not consistently cataloged as the focus of the experiments centered largely on the dilution of the lead salt solution. A more convincing investigation would involve the techniques employed by Rodenas, et al[15]. whereby a four-dimensional analysis of micelle size as a function of CTAF*/2-Oct/H_2O ratio, compared against successful production of precipitate, could be carried out.

Since an excess of fluoride anion (a weak conjugate base) appears to be introduced into the micelle, the pH and resultant effects on the surface tension of the micelle must also be called into question. The lower concentration of bromide anion (a weaker conjugate base) and the extremely low concentration of nitrate anion (the weakest conjugate base present) and their interactions with the polar surfactant/co-surfactant will all have dynamic effects on the pH and may influence precipitate formation.

Bunton, et al., indicate in their comparative studies of CTAB and CTAF that the relative presence of competing anions does play a signficant role in the success of the reaction, citing hydrophilicity of the anion as the major factor[18]. They found that the amount of fluoride anion present has a quantitative effect on the reaction kinetics of the dephosphorylation of p-nitrophenyl diphenyl phosphate, and determined that the addition of sodium fluoride to a CTAF micelle contributed to increasing k_s in their experiments. Further, the presence of competing bromide, either in the form of NaBr or CTAB (or both), hindered and in some cases prohibited dephosphorylation. Dissolution of the salt is the first step to any reaction kinetics, so the data presented by Bunton may allow some small inferences to the results found here[18].

The success of CTAF* unfortunately introduces several additional variables, not the least of which is the SiF_6^{2-} anion, which possibly contributed to the success of the synthesis as a fluoride delivery system and perhaps occupied the bromide anions (the ammonium cation of CTA is present) in solution as well as playing a role in altering pH. The additional water molecule per CTAF* unit cell adds yet more water to the micelle volume.

Yet another question that arises is whether the ammonium cation, thought to be a spectator in the other syntheses, plays a role in this particular reverse-micelle case. Although, for example, no nitrate or ammonium species were ever seen in the XRD, its presence and polar effects can nevertheless not be completely dismissed.

2.5 Conclusion

A modified version of the synthesis originated by Boutonnet has been used to synthesize monodisperse, pure, MF_3 nanoparticles (M=La, Gd, Ho, Sm, Y). Successful synthesis for low (6mol%) La-doping of CaF_2 as well as the unusual result of both α, β-PbF_2 are also reported here.

Although the temporal method of rough control over particle size indicated by Hua, et al. does not appear to apply, LaF_3 (or the subsequent MF_3 samples which were successfully synthesized using this same method with the same or similar [in the case of $La_{0.06}Ca_{0.94}F_{2.06}$ and YF_3] ratios: M = Ho, Gd, Sm, Y) the findings by Pileni, Desai and Rodenas are consistent with the conclusion drawn here, that micelle size in specific cases governs particle size exclusively. Perhaps, too, the failure to synthesize EuF_3 and PrF_3 using this synthetic route, despite that they are known fluorides, is also consistent with the findings of Desai, (as well as the implications of Cao, et al., with their use of a pentanol rather than an octanol): the pH of the parent salts as well as the surface tension properties based on the choice of co-surfactant play a dynamic and interactive role with the success or failure of this particular route, since the relative ratios and charges associated with the dissolved salts play a significant role in micellar surface topology and its contribution to the micelle as a reaction vesicle.

2.5 References

1) Malinowski, M., Jacquier, B., Bouazaoui, M., Joubert, M. F., Linares., C. *Phys. Rev. B* 41 (1990)

2) Kaminskii A Laser Crystals Berlin: Springer, (1990)

3) Schoonman, J., Oversluizen, G. Wapenaar, K.E. *Solid State Ionics*, 1 (1980)

4) Zalkin, Al., Templeton, D.H *Acta Cryst*. B41 (1985)

5) Sobolev, B.P., Garashina, L.S., Fedorov, P.P., Tkachenko, N.L., Seiranyan, K.B. *Sov. Phys. Crystallogr.,* 18, 4 (1974)

6) Lage, M.M. Righi, A., Matinaga, F.M. Gesland, J-Y.,Moreira, R.L. *J. Phys.: Cond. Mat*. 16 (2004)

7) Hua, R. Zang, C., Shao, C., Xie, D., Shi, C. *Nanotechnology* 14 (2003) 588–591.

8) Bender, C. Burlitch, J.M., Barber, D. B., Pollock, C.R. *Chem. Mater.* 12 (2000)

9) Weibel, A., Bouchet, R., Boulc'h, F., Knauth, P. *Chem Mater.* 17 (2005)

10) Boutonnet, M., Kizling, J., Stenius, P. *Coll. Surf*., 5 (1982) 209 - 225.

11) P. Bystrøm, P. *Arkiv før Chemi, Mineralogi och Geologi* A 24 (1947), 1

12) Boldrini, P., Loopstra, B.O. *Acta Cryst*. 22 (1967), 744

13) Kennedy, J.H., Miles, R., Hunter, J. *J. Electrochem. Soc*. 120, 11 (1973), 1441-1446.

14) Pileni, M.P. *Langmuir* 13, (1997)

15 Rodenas, E., Valiente, M. *Coll. Surf*., 62, (1992), 289-295.

16) Desai, A., Varade, D. Mata, J. Aswal, V., Bahadur, P. *Coll. Surf. A* 259 (2005) 111–115.

17) Cao, M., Wu, X. He, X., Hu, C. *Langmuir* , 21, (2005)

18) Bunton, C.A., Frankson, J., Romsted, L.S. *J. Phys. Chem*. 84 2607-2611.

19) Savitzky A., Golay M.J.E., *Anal. Chem*. 36, (1964) 1627-1639.

20) Petrovich, Boris Sobolev. The Rare Earth Trifluorides: The high temperature chemistry of the rare earth trifluorides. 1st ed. Polígon Industrial Can Salvatella. Carrer de Mogoda, 29-31 Barberà del Vallès 2001. ISBN: 8472835189.

21) L'afanasiev, M. *Acta Cryst*. (1972). B28, 2903

22) Rotereau, K., Gesland, J. Y., Daniel, P., Bulou, A. *Mat*. *Res*. *Bull*., 28, (1993), 813-819.

23) Jacobs, P.W.M. *J*. *de Phys*. (1976) Coll. C7, 12, Vol. 37, pp. C7-331

24) Sata, N. Eberman, K., Eberl, K., Maier, J. *Nature* (2000) 408 21/28 946-948

25) Kennedy, J.H., Miles, R.C. *J Electrochem*. *Soc*., 123 (1976)

26) Wang, F. Grey, C. P. *J*. *Am*. *Chem*. *Soc*., 117 (1995)

27) Wang, F., Grey, C. P. *J*. *Am*. *Chem*. *Soc*., (1998), 120 (5), pp 970–980

28) Chaudhuri, S., Wang, F., Grey, C. P. *J*. *Am*. *Chem*. *Soc*., 2002, 124 (39), pp 11746–11757

29) Tani, Y.; Umezawa, Y.; Chikama, K.; Hemmi, A.;. Soma, M. J. *Electroanal*. *Chem*. 378 (1994) 205-213.

30) Kennedy, J.H., Miles, R., Hunter. J. *J*. *Electrochem*. *Soc*. 120 (1973) 1441-1446.

31) Sauka, Ya. *Russ*. *J*. *Gen*. *Chem*., 19 (1949)

32) Hwang, T., Engelsberg, M., Lowe, I. J. *Chem*. *Phys*. *Lett*. (1975) 30, 2, 303-305

Chapter 3

Inadvertent Synthesis of Cetyltrimethylammonium Hexafluorosilicate Dihydrate as a Delivery System for Fluoride Anion in the Successful Room-temperature Synthesis of Nanoparticle α and β-PbF_2

Abstract

Although the modified reverse-micellar method is a successful method to prepare monodisperse particles of an increasing range of binary and ternary fluorides under aqueous conditions, difficulties arose when attempts were made to apply the same technique to the synthesis of PbF_2. The bromine halogen stemming from the surfactant, cetyltrimethylammonium bromide (CTAB) was found to interfere with the fluorination of the Pb^{2+} cation. This was purportedly due to the highly polarizable electron density of the Pb^{2+} cation, combined with the increased thermodynamic affinity for the more electronically dense Br^- anion. In an effort to find a reasonable substitute for the CTAB surfactant, as well as fluoride delivery system, a novel crystal was inadvertently produced. The resultant crystals were characterized and this crystal was used as a fluoride co-delivery system for the synthesis of lead fluoride nanoparticles. The reverse micelle synthesis described in the previous chapter was

3.1 Introduction

The search for high ionic conductors has become more intense in the last decades due to a perceived need for energy alternatives, such as solid-oxide fuel cells, supercapacitors and lithium ion batteries. Fluoride anionic conductors, long known for high ionic conductivity at either low or ambient temperatures, have been prime targets for increased study, given that the $PbSnF_4$ exhibits the highest known fluoride anion conductivity[1].

Binary fluorides of the type MF_2 (M=Sr, Ba, Pb, Ca) also exhibit varying conductivities, but PbF_2 in the cubic β-phase ($Fm\bar{3}m$) is a superionic conductor at relatively low temperatures. Both the orthorhombic ($Pnma$) α- and cubic β-phases of PbF_2 serve a wide range of uses, yet for high ionic conductivity, the β-phase is more desirable, having a conductivity over an order of magnitude higher at ambient temperatures. It is, therefore, unfortunate for those interested in ionic conductivity that the orthorhombic phase is the more thermodynamically stable one at STP, and that heat treatment of the α-phase (344 - 444°C) only then produces the β-phase[2].

The goal of this investigation was to ultimately find a low-temperature route to synthesize monodisperse, nanoparticle β-phase PbF_2. It was therefore an unintended consequence that both the α,β-phases were produced although not surprising, since the α-phase dominates at room temperature. Further, it is thought that monodisperse nanoparticles could enhance conductivity; a large particle surface area, relative to the bulk, could improve ionic conductivity, as the large surface area could surpass the activation energy needed to overcome grain boundary effects.

The method by which this was achieved was circuitous: repeated attempts at lead fluoride synthesis failed using a reverse microemulsion method with cetyltrimethylammonium bromide (CTAB) as the surfactant and racemic 2-octanol (2-Oct) as the co-surfactant.

As explained in the previous Chapter, Boutonnet, et al., had originally developed a method of synthesizing CaF_2 nanoparticles using CTAB, 2-Oct and water in specific ratios[3]. This ternary method had been subsequently demonstrated by Hua, et al. to produce BaF_2 nanoparticles, as well as their low-concentration Ce-doping. This method, and many variations therein were attempted in an effort to apply it toward b-PbF_2 synthesis, but with no success.

It was then suspected that the bromide anion of CTAB, normally a spectator in the reaction, was competing with fluoride anion in the synthesis, so a suitable surfactant, free from a potential reactive competitor, then became the target. Desai, et al. found that the presence of counterions and their ratios can radically affect the surface tension (in combination with surfactants of different polar functional groups), pH, and ultimately the success or failure of nanoparticle formation[4,5]. Similarly, Bunton, et al. found that dephosphorylation of p-nitrophenyl diphenyl phosphate was facilitated by CTAF and significantly increased by addition of other fluoride containing salts such as NaF. They also found that addition of competing anions such as bromide, via either NaBr or CTAB hampered or in high concentrations halted such dephosphorylation. Therefore, our strategy of minimizing the presence of bromide anion by using a fluoride-containing surfactant (CTAF) to potentially facilitate a reaction which may be hindered by bromide anion as apotential competitor was nevertheless thought a reasonable one in an attempt to produce PbF_2.

The inadvertent but apparent finding during this synthetic investigation that large (2-3mm), stable single crystals of cetyltrimethylammonium hexafluorosilicate dihydrate ($CTA:SiF_6:H_2O$ or CTAF*) may or may not be significant. Since these crystals appear to be stable for long periods of time, it may be feasible to use these crystals as a delivery or retention

system for SiF_6^{2-}; the SiF_6^{2-} species has applications in other fields, including fluoridation as the or delivery (in subsequent SiF_4 form) for CVD processes.

Hexafluorosilicic acid (H_2SiF_6) and sodium hexafluorosilicate (Na_2SiF_6) are the two most common compounds used to fluoridate water[14]. The high volatility of SiF_4 (m.p. -90°C; b.p. -86°C) had always been thought to eliminate the possibility of further chemistry enabling tetrafluorosilane to remain in solution as SiF_6^{2-}, since the more stable SiF_4 was thought to simply evolve off with no further (hydro)chemistry occurring. This practice has long been surrounded by controversy, however, because it has been argued that the chemistry of SiF_6^{2-} defluorination subsequently appeared complicated by pH dependence and ineffectiveness of buffering, incomplete and, under certain conditions may lead to SiF_4-hydrates and, therefore, toxicity.

3.2 Experimental

3.2.1 Failure to substitute Fluorine for Bromine in the CTAB surfactant

In an attempt to reproduce the CTAF reported in Bunton, 0.01mol (3.64g) of commercially obtained CTAB (Sigma Aldrich) was dissolved in 1.1mol methanol; 1.5 mol equiv. excess of silver fluoride was added and the mixture sonicated for approximately two hours (hereafter referred to as "Synth. A"). A pastel green, non-lustrous precipitate formed, was collected, washed with acetone and stored in a Pyrex vial in direct laboratory light, though tentatively concluded that this was not the target precipitate; the next day, a color change was observed.

Many more attempts were made with changes in molarity, volume, concentrations of AgF, CTAB and methanol, with negative results.

The synthesis procedure was then modified (hereafter referred to as "Synth. B"). A 100g (0.27mol) sample of CTAB was added to 5mol of Barnstead Millipure, EasyPure, purified water (18MΩ) and the slurry was stirred using a PTFE stirbar. The slurry was then reacted with concentrated (1M) stoichiometric equivalent of NaOH to produce cetyltrimethylammonium hydroxide (CTA-OH). The conc. NaOH was slowly added to the slurry using a buret. A PTFE buret was fabricated by turning on a lathe, a PTFE petcock was purchased and attached to the buret. The buret was used to titrate in one stoichiometric equivalent of HF to the CTA-OH in a PTFE griffin beaker. The mixture was then allowed to stir for about two hours. The mixture had a pH = 1 after titration, so the mixture was back-titrated using NH_4OH such that a final pH = 6.05 was achieved.

A very small aliquot of the solution was taken from the liquid to evaporate off, since no immediate precipitate was evident. No precipitate formed.

Vacuum distillation of surfactants is known to be prone to bumping and effervescence. As such, the remaining, now-viscous liquid was then placed in a disproportionately large (1L), Pyrex, round-bottomed flask (RBF) and placed onto a Büchi Rotavap 23-L and a 500ml bump flask mounted. The system was placed under vacuum, heated to 80ºC using the accompanying water bath and allowed to roto-distill for approximately 10 hours/day for three days at 80°C (the vacuum was retained by closing the condenser column valve and the solution allowed to cool back to room temperature, then this cycle was repeated each day).

The RBF was then removed from the rotavap, capped, and placed in an ice bath for approximately six hours. The precipitated crystals were then collected after the mother liquor was vacuum decanted (and saved) through a Büchner funnel, washed three times with equimolar MeOH/acetone, allowed to air dry and stored in a Pyrex vial.

3.2.2 Sample Characterization Preparation

3.2.2.1 Single-crystal X-ray Diffraction

Crystals were selected and mounted on glass fibers using epoxy cement. Each crystal was centered, and the X-ray intensity data were measured on a Bruker AXS diffractometer. The data were collected using graphite-monochromated Mo radiation (0.709Å). The structures were solved by direct methods and refined by using full-matrix, least-squares methods (SHELX97).

3.2.2.2 MAS NMR

A sample of the crystal was ground in a mortar and pestle, packed in a 22μl, 3.2mm zirconia rotor with fluorine-free torlon drive tip and Vespel end cap, using a Varian/Chemagnetics 3.2mm double resonance probe. All experiments were run on a Varian, Infinity Plus spectrometer in a 500Mhz (11.74 Tesla) magnetic field.

Single-pulse, Hahn-echo, and variable-amplitude cross polarization (VACPx {^{19}F}^{13}C) experiments were performed using either $CFCl_3$ (0 ppm) or monofluorobenzene (MFB; -113ppm) standards as external chemical shift references for fluorine. Adamantane was used for ^{13}C (29.8ppm for the methylene carbon). A $\pi/2$ time of 2.5μs (100kHz) was used for both ^{19}F and ^{13}C, as required to satisfy the Hartmann-Hahn condition. A 2ms contact time between the fluorine and carbon spins was found to be optimal for the VACPx pulse sequence to transfer spin polarization from the fluorine nuclei to the carbon nuclei.

3.3 Results

During the the attempt to reproduce CTAF according to Bunton (Synth. A), immediately upon addition of AgF, the solution went from an opaque white to ruddy orange, then very soon after, the solution became more translucent and a pastel green. There was no mention in the previous report of color changes to the solution, nor in a related (alkonium trifluoride synthesis) article also mentioned by Bunton, et al.[7].

A day after collection of the greenish precipitate and storage in a Pyrex vial, the color changed again to a purple-charcoal. On the observations that 1) a simple, interhalogenic exchange to a functional group of a surfactant should not produce a color change in any way and 2) that the large, flaky, white, opalescent crystals typical of CTAB should likely also be evident in CTAF, but were not seen, led to the tentative conclusion that CTAF was not formed.

It was presumed that some sort of photosensitive precipitate was, therefore, formed, due to the pastel green → purple/black color change of the precipitate when left on the laboratory bench in a normal Pyrex vial.

We then modified the CTAF synthesis procedure, using HF as the fluorine source (recall from above: Synth. B). During this second attempt at CTAF synthesis, following addition of HF, gas evolved upon addition of NH_4OH, which was used to back-titrate to a more neutral pH, and the solution became extremely viscous, transparent and peach-colored, such that stirring with a stirbar became difficult.

An increasing number of crystals began to form after each daily cycle of heated rotavapping, then allowing to cool to room temperature (while being left under vacuum overnight), with the first crystals having been observed on the morning of the second day of the three-day process. The initial crystals after the first day were small in size and number. By day three, a very small amount of very large, opalescent, slightly off-white crystals had formed.

Placement of the capped RBF in an ice bath was critical, as a substantial number of very large, opalescent, slightly off-white crystals formed. Approximately 36g of crystals were obtained.

The space group C2/c, monoclinic, was determined from the solved crystal structure, z = 4, with lattice parameters a: 44.8006Å, b: 8.2165Å, c: 12.1435Å and angles α: 90.0°, β: 94.137°; γ: 90.0°.

Tables 1a, b above list the 73 labeled elements, their fractional crystallographic positions, hybridization, and equivalent isotropic displacement parameters, U_{eq}, defined as $^{Tr}/_{3}$ of the orthogonalized U^{ij} tensor (x/a, y/b, z/c)[8]. Figure 1 depicts the crystallographic unit cell in the

LABEL	TYPE	X	Y	Z	U_{eq}
O1	O	0.050	0.840	0.453	
N1	N	0.050	0.337	-0.396	0.047
C4	C	0.191	0.352	0.002	0.063
H4A	H	0.199	0.255	-0.031	-1.200
H4B	H	0.199	0.445	-0.033	-1.200
C10	C	0.320	0.351	0.448	0.063
H10A	H	0.329	0.256	0.415	-1.200
H10B	H	0.329	0.447	0.415	-1.200
C8	C	0.278	0.353	0.297	0.062
H8A	H	0.286	0.258	0.264	-1.200
H8B	H	0.286	0.448	0.265	-1.200
C3	C	0.157	0.355	-0.020	0.062
H3A	H	0.149	0.263	0.017	-1.200
H3B	H	0.150	0.453	0.012	-1.200
C5	C	0.201	0.354	0.123	0.063
H5A	H	0.193	0.261	0.158	-1.200
H5B	H	0.193	0.451	0.156	-1.200
C9	C	0.287	0.352	0.419	0.062
H9A	H	0.278	0.256	0.451	-1.200
H9B	H	0.278	0.447	0.452	-1.200
C11	C	0.329	0.351	0.570	0.064
H11A	H	0.320	0.256	0.602	-1.200
H11B	H	0.320	0.446	0.603	-1.200
C7	C	0.244	0.354	0.269	0.063
H7A	H	0.236	0.259	0.303	-1.200
H7B	H	0.236	0.449	0.302	-1.200
C2	C	0.146	0.349	-0.140	0.062
H2A	H	0.153	0.250	-0.173	-1.200
H2B	H	0.154	0.441	-0.178	-1.200
C6	C	0.235	0.353	0.148	0.063
H6A	H	0.243	0.257	0.115	-1.200
H6B	H	0.243	0.447	0.114	-1.200
C1	C	0.112	0.355	-0.157	0.060
H1A	H	0.104	0.265	-0.117	-1.200
H1B	H	0.105	0.455	-0.125	-1.200

Table 3.1a A list of the elements, crystallographic positions, and U_{eq} for the atoms contained within the $(CTA)_2 \cdot SiF_6 \cdot 2H_2O$ single crystal unit cell.

LABEL	TYPE	X	Y	Z	U_{eq}
C12	C	0.363	0.349	0.602	0.064
H12A	H	0.371	0.255	0.569	-1.200
H12B	H	0.371	0.445	0.571	-1.200
C14	C	0.066	0.346	-0.282	0.053
H14A	H	0.060	0.254	-0.240	-1.200
H14B	H	0.059	0.444	-0.246	-1.200
C17	C	0.017	0.331	-0.384	0.078
H17A	H	0.011	0.428	-0.347	-1.500
H17B	H	0.013	0.237	-0.342	-1.500
H17C	H	0.007	0.325	-0.456	-1.500
C18	C	0.056	0.484	-0.460	0.090
H18A	H	0.077	0.489	-0.473	-1.500
H18B	H	0.051	0.579	-0.419	-1.500
H18C	H	0.045	0.481	-0.529	-1.500
C15	C	0.371	0.346	0.724	0.076
H15A	H	0.362	0.251	0.755	-1.200
H15B	H	0.362	0.441	0.757	-1.200
C19	C	0.059	0.187	-0.454	0.100
H19A	H	0.054	0.094	-0.410	-1.500
H19B	H	0.079	0.191	-0.466	-1.500
H19C	H	0.047	0.181	-0.523	-1.500
C13	C	0.100	0.346	-0.276	0.059
H13A	H	0.107	0.248	-0.310	-1.200
H13B	H	0.107	0.439	-0.316	-1.200
C16	C	0.403	0.345	0.757	0.095
H16A	H	0.413	0.438	0.725	-1.500
H16B	H	0.412	0.247	0.731	-1.500
H16C	H	0.406	0.350	0.836	-1.500
F1	F	0.024	0.326	0.294	0.084
F2	F	0.025	0.039	0.291	0.091
F3	F	0.013	0.182	0.126	0.112
Si1	Si	0.000	0.183	0.250	0.049
H101	H	0.039	0.845	0.508	0.089
H102	H	0.040	0.906	0.403	0.121
F1A	F	-0.024	0.326	0.206	0.084
F2A	F	-0.025	0.039	0.209	0.091
F3A	F	-0.013	0.182	0.374	0.112

Table 3.1b (Table 3.1a, cot'd) A list of the elements, crystallographic positions, and U_{eq} for the atoms contained within the $(CTA)_2 \cdot SiF_6 \cdot 2H_2O$ single crystal unit cell.

ball-and-stick rendition. Figure 2 provides an ellipsoid view. Due to the cluttered representation of the polar head, an inset has been provided for clarity, as well as the constituent elements, color coding in an accompanying table (Table 2), their crystallographic positions and U_{eq}.

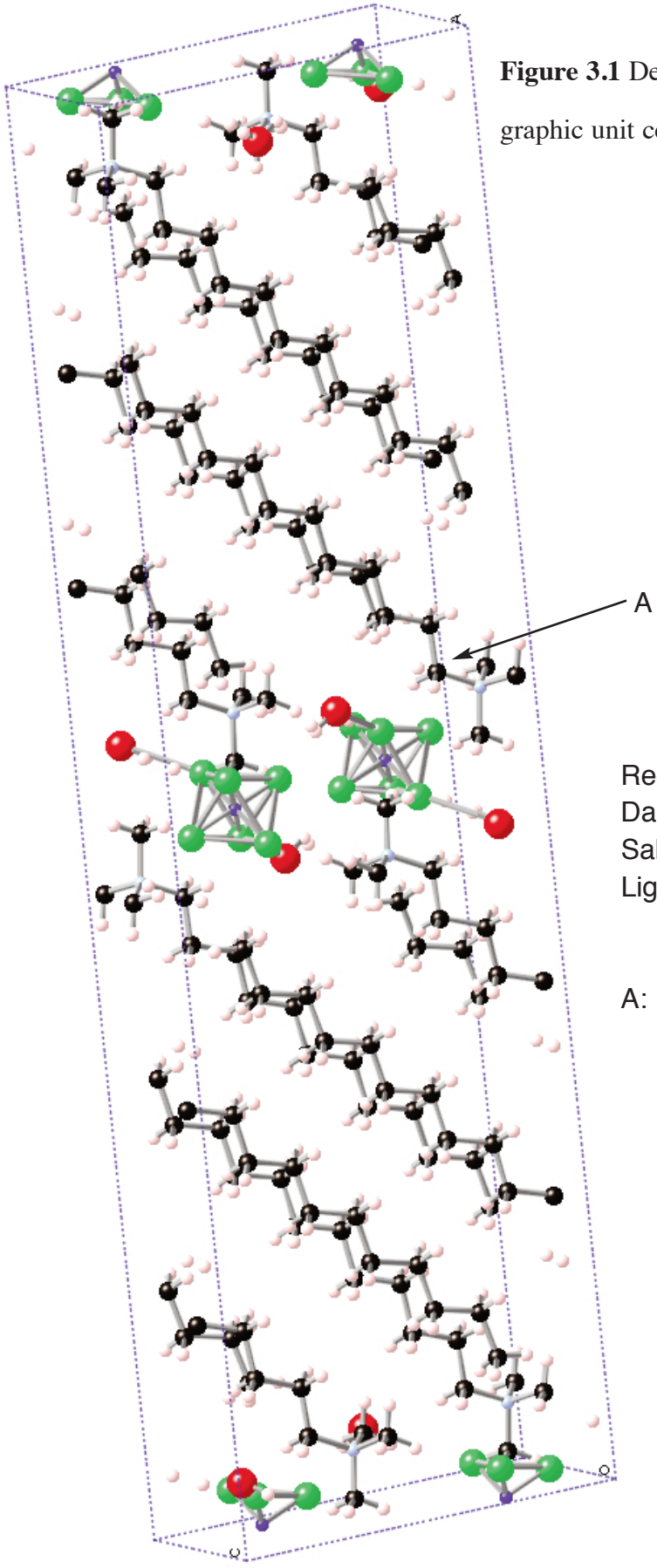

Figure 3.1 Depiction of the crystallographic unit cell for $(CTA)_2 \cdot SiF_6 \cdot 2H_2O$

LEGEND

Red:	O (water)
Dark blue:	Si (SiF_6^{2-})
Salmon:	H
Light blue:	N (trimethyl ammonium)
A:	α methylene carbon

N1 (blue)

C17,18,19 (Gray)

H1XA,B,C (X=7,8,9) (Green)

Figure 3.2: Legend

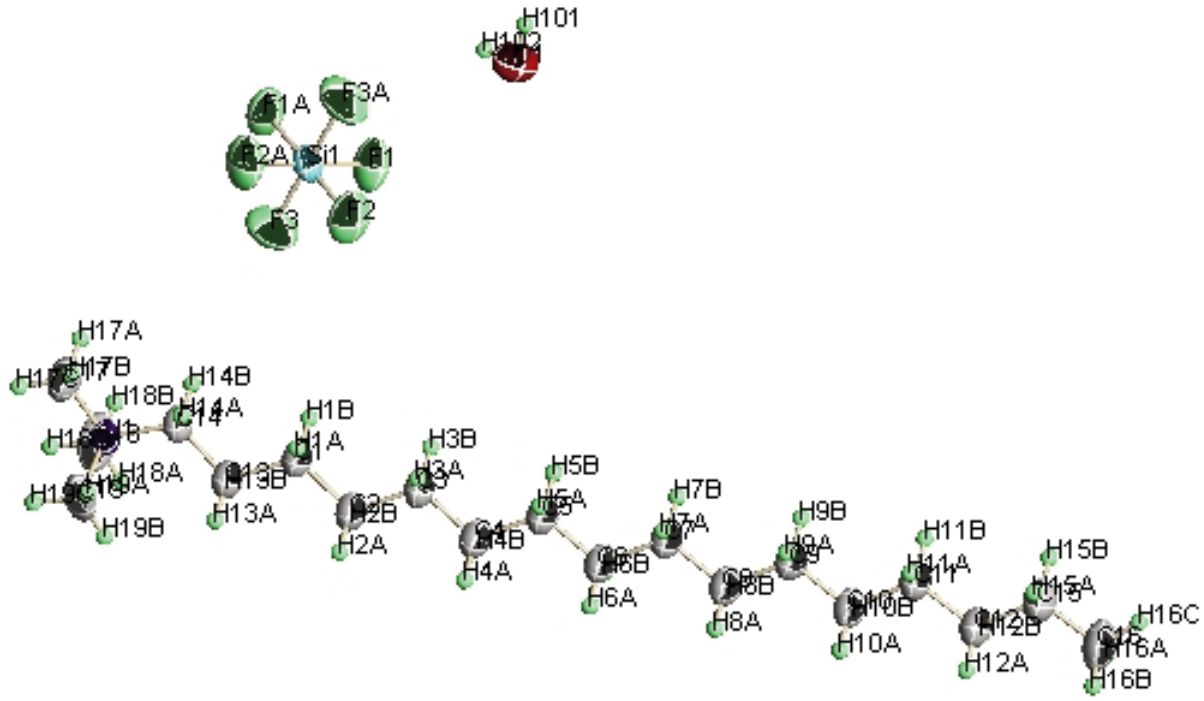

Figure 3.2: Ellipsoid view of the atoms involved in the interactions between the constituents that make up the $(CTA)_2 \cdot SiF_6 \cdot 2H_2O$ crystallographic unit cell.

LABEL	TYPE	X	Y	Z	U_{eq}
N1	N	0.050	0.337	-0.396	0.047
C17	C	0.017	0.331	-0.384	0.078
H17A	H	0.011	0.428	-0.347	-1.500
H17B	H	0.013	0.237	-0.342	-1.500
H17C	H	0.007	0.325	-0.456	-1.500
C18	C	0.056	0.484	-0.460	0.090
H18A	H	0.077	0.489	-0.473	-1.500
H18B	H	0.051	0.579	-0.419	-1.500
H18C	H	0.045	0.481	-0.529	-1.500
C19	C	0.059	0.187	-0.454	0.100
H19A	H	0.054	0.094	-0.410	-1.500
H19B	H	0.079	0.191	-0.466	-1.500
H19C	H	0.047	0.181	-0.523	-1.500

Table 3.2: A list of the constituent atoms and their crystallographic positions which make up the trimethyl ammonium head.

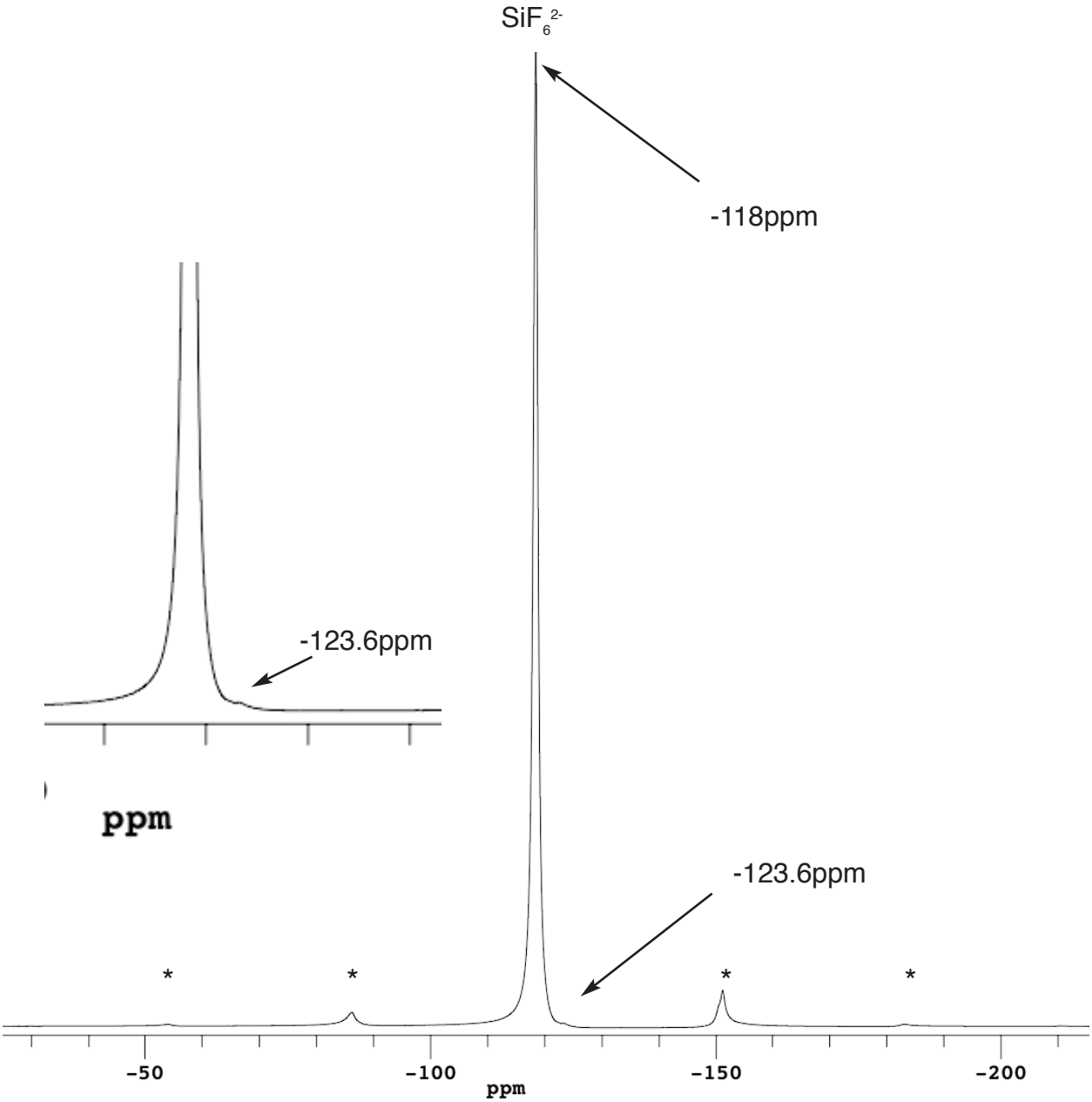

Figure 3.3 Single-pulse excitation, ^{19}F MAS NMR spectrum of the $(CTA)_2 \cdot SiF_6 \cdot 2H_2O$ crystal, spinning at 14.2kHz. Inset: magnified detail of slight shoulder at -123.6ppm. Asterisks which appear indicate spinning sidebands.

Figures 3.3 and 3.4 show the ^{19}F and $\{^{19}F\}^{13}C$ VACPx spectra, respectively, of the $(CTA)_2 \cdot SiF_6 \cdot 2H_2O$ salt. Consistent with the solved single crystal, only one signal, with accompanying spinning sidebands, is seen in Figure 3. The sole signal appears from the magnetically equivalent fluorines of the SiF_6^{2-} species. The one exception is the small peak at -123.6ppm, found at the right base of the resonance at -118ppm (see inset).

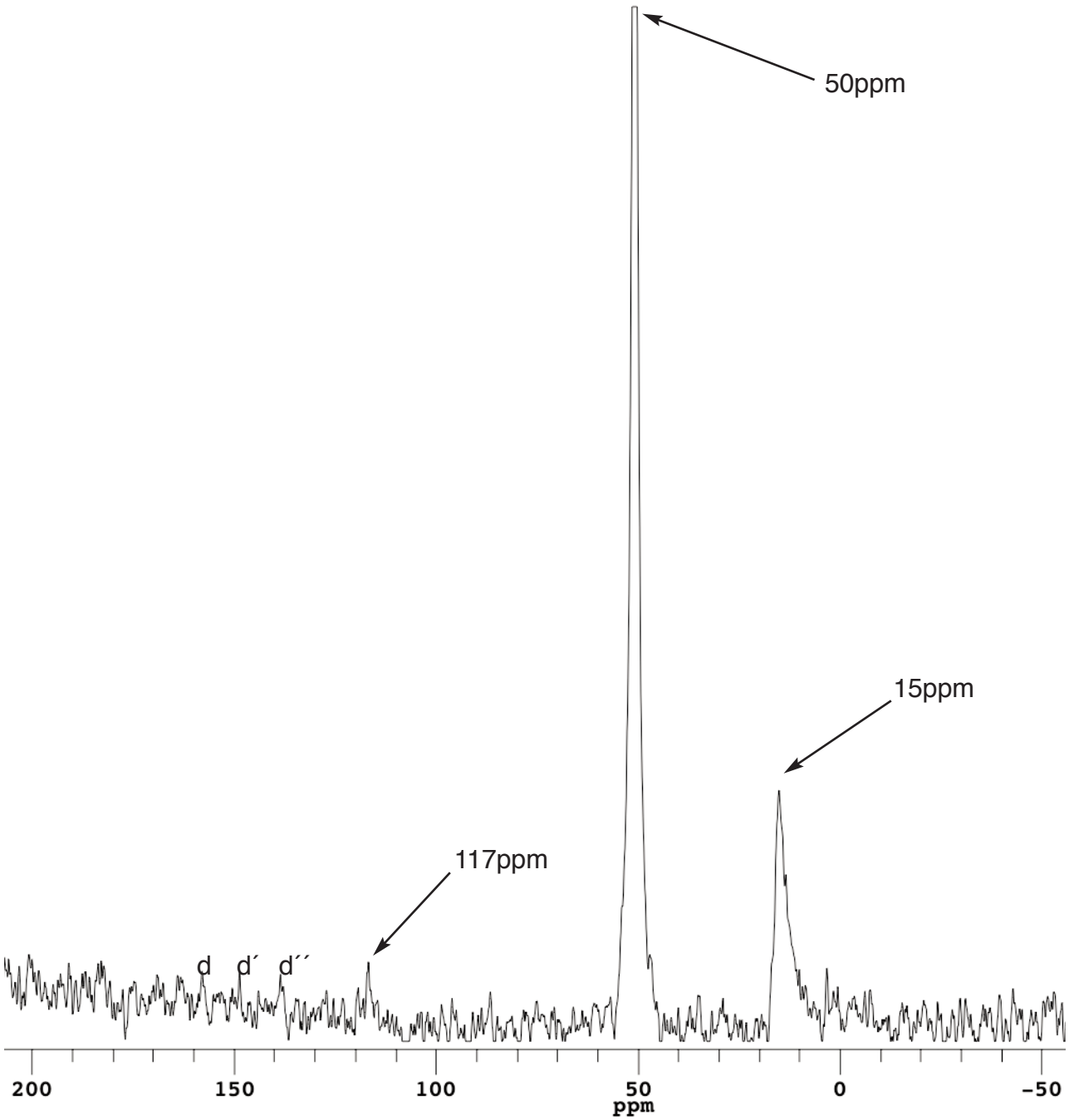

Figure 3.4: $\{^{19}F\}^{13}C$ VACPx spectrum which indirectly reveal the interactions between the ^{19}F and ^{13}C in the $(CTA)_2 \cdot SiF_6 \cdot 2H_2O$ crystal. Note the ^{13}C signal at 15ppm which designates the methylene carbon (C14) in Table 3.1a and in Figure 3.1. The intense signal at 50ppm is the methyl carbon bound to the N1 Nitrogen, depicted in Figure 3.2 and is tabulated in Table 3.2.

3.4 Discussion

The ^{19}F chemical shift of -118ppm seen for the major peak determined here for what appears to be SiF_6^{2-} (-127ppm) in the solid state is very close to the value of -120ppm reported for $SiF_{4(s)}$ [9]. The extremely small shoulder to the right of the main isotropic resonance, which is seen at -123.6ppm, leading to the slight distortion in the baseline of the main peak may or may not be an impurity or could be a hydrate. Since the chemical shifts for HF is -204ppm and $SiF_{4(l)}$ -163.3ppm, respectively (relative to $CFCl_3$), it is unlikely that this can be attributed to either one of these compounds present, for example, in an interstitial.

The structure of the $(CTA)_2 \cdot SiF_6 \cdot 2H_2O$ crystal is lamellar, consisting of hydrophobic, cetyltrimethyl ammonium blocks and a SiF_6^{2-} layer, the fluorines of which strongly appear to be hydrogen bonded to the protons in the water layer, due to their proximity and orientation (about 1.84Å away from the fluorines; see Table 3 for key H—F distances). The $(CTA)_2 \cdot SiF_6 \cdot 2H_2O$ does share the same monoclinic space group with the "parent" crystal, cetyltrimethyl ammonium bromide (CTAB), $P2_1/c$, as Campanelli, et al. reported[17]. Koh, et al., also reported a very similar, antiparallel, polar-plane-oriented crystal structure for both tetradecyltrimethylammonium salicylate monohydrate and hexadecyltrimethylammonium salicylate monohydrate[19]. Although these two species are are triclinic ($P\bar{1}$), the relative molecular orientations for the ammonium species, water and counterion within the unit cell are quite similar.

The CTA blocks for the CTAB single crystal also line up in lamellar fashion, although the CTAB unit cell is devoid of water. Consistent with the CTAB "parent", the CTA molecules also line up antiparallel to one another in the crystal, centered about the polar plane. Campanelli, et al. indicate that, while the rest of the alky chain is fully extended, such that all of the sp^3-hybridized methylene carbons are in their Van-derWaals-neutral positions, the proximal

methylene carbons to which the ammonium moieties are bound are stressed, due to Coulombic interaction on the part of the charged species in the polar plane which lies perpendicular to and at the center of the antiparallel alkyl chains. The main peak in Figure 4 at 50ppm is assigned to the methyl carbons bound to the nitrogen of the ammonium moiety. This is consistent with the crystallographic data, in that the C—F distance is approximately 3.5Å so within the generally accepted range for cross polarization to occur. The smaller peak at 15ppm is assigned to the α-methylene carbon, approximately 3.9Å away from the fluorines. The peaks found at 117ppm and higher (see Figure 4, marked d, d´, d´´) may simply be non-crystalline C—F impurities which are not part of (or at least were not evident) the single crystal diffraction pattern, since this is the ^{13}C chemical shift range for C—F species.

Borodin, et al. found that in acidic, aqueous solutions, several equilibria between SiF_6^{2-}, water and HF can exist[10]. It is, therefore, feasible that small amounts of $(SiF_5OH_2)^-$ or $SiF_4(H_2O)_2$ could coexist and end up in an interstitial of the unit cell, although the concentrated, frozen $SiF_5OH_2^-$ chemical shift was found to be -127ppm (the weighted average of the axial [-134ppm] and equatorial [-125.5ppm] fluorines[10,11]. Aqueous SiF_6^{2-} found in a range of pH of 2.6 - 5.2 was found to have a chemical shift of -135ppm[12]. Asseid, et al. cataloged several, stable M_2SiF_6 species (M = K, Cs, Rb, NH_4), having discovered that alkali metal fluorides sorb onto montmorillonite and react[13]. They found a range of chemical shifts (relative to $CFCl_3$) for the M_2SiF_6 species, from a high of -129ppm for K_2SiF_6 to a low of -92ppm for Cs_2SiF_6.

While none of the chemical shifts found in the literature for either liquid or solid SiF_6^{2-} precisely reflect the chemical shift found here for the SiF_6^{2-} species in this $(CTA)_2 \cdot SiF_6 \cdot 2H_2O$ crystal, it is clear that chemical shift found here is novel, and within the range of similar species. It is also encouraging to note that Asseid, et al. noted a inverse relationship with cationic size and chemical shift trend, reporting cationic radii from the CRC Handbook. As the cationic radius increases, the chemical shift drops for the species in question. The cationic radius of NH_4^+ is 1.43Å, approximately ⅓ of the way from the K^+ minimum of 1.33Å and 1.67Å for Cs^+. The fact that Asseid, et al. report a chemical shift of about -123ppm for $(NH_4)_2SiF_6$ lends some consistency to the fluorine chemical shift reported here, considering that here the SiF_6^{2-} species is at least associated with the alkyl ammonium species, if not co-associated with the water also found close by[13].

The two carbon peaks found at 50ppm and 15ppm during the $\{^{19}F\}^{13}C$ VACPx NMR experiments are consistent with the chemical shift values found in the literature for the ammonium-methyl (sp^3) carbons and methylene carbons of the surfactant alkyl chain, respectively. What remain unclear are the small isotropic resonance at 117ppm and the apparent spinning sideband manifold to the left and the right of this peak. What can be conclusively said about this carbon signal is that it is definitely ***not*** associated with PTFE or any fluoronated polymer residues that may have been present in the rotor drive tip or end cap.

F1 -> H17A distance = 6.4388 +/- 0.0000 A	vector = [0.0130 -0.7534 0.1411]
F1 -> H17B distance = 4.9261 +/- 0.0000 A	vector = [0.0117 -0.5629 0.1359]
F1 -> H17C distance = 6.1719 +/- 0.0000 A	vector = [0.0173 -0.6510 0.2500]
F1 -> H18A distance = 7.8705 +/- 0.0001 A	vector = [-0.0527 -0.8142 0.2669]
F1 -> H18B distance = 7.1101 +/- 0.0000 A	vector = [0.0266 -0.7464 0.2867]
F1 -> H18C distance = 7.7891 +/- 0.0000 A	vector = [-0.0202 -0.8067 0.3232]
F1 -> H19A distance = 4.5068 +/- 0.0001 A	vector = [-0.0301 -0.4197 0.2037]
F1 -> H19B distance = 5.9298 +/- 0.0001 A	vector = [-0.0551 -0.5161 0.2599]
F1 -> H19C distance = 5.8100 +/- 0.0000 A	vector = [-0.0227 -0.5062 0.3175]
F2 -> H17A distance = 4.2108 +/- 0.0000 A	vector = [0.0133 -0.4665 0.1384]
F2 -> H17B distance = 2.8149 +/- 0.0000 A	vector = [0.0120 -0.2760 0.1332]
F2 -> H17C distance = 4.2722 +/- 0.0000 A	vector = [0.0176 -0.3641 0.2473]
F2 -> H18A distance = 5.9725 +/- 0.0001 A	vector = [-0.0524 -0.5273 0.2642]
F2 -> H18B distance = 5.2337 +/- 0.0000 A	vector = [0.0263 -0.4594 0.2894]
F2 -> H18C distance = 5.8893 +/- 0.0000 A	vector = [-0.0199 -0.5198 0.3205]
F2 -> H19A distance = 3.0665 +/- 0.0001 A	vector = [-0.0298 -0.1327 0.2010]
F2 -> H19B distance = 4.5209 +/- 0.0002 A	vector = [-0.0548 -0.2292 0.2572]
F2 -> H19C distance = 4.4064 +/- 0.0000 A	vector = [-0.0224 -0.2192 0.3148]
F3 -> H17A distance = 5.0229 +/- 0.0000 A	vector = [0.0020 -0.6099 -0.0266]
F3 -> H17B distance = 3.4678 +/- 0.0000 A	vector = [0.0007 -0.4194 -0.0319]
F3 -> H17C distance = 4.2921 +/- 0.0000 A	vector = [0.0063 -0.5075 0.0823]
F3 -> H18A distance = 6.3629 +/- 0.0002 A	vector = [-0.0638 -0.6706 0.0992]
F3 -> H18B distance = 7.5163 +/- 0.0001 A	vector = [0.0377 -0.6028 0.4544]
F3 -> H18C distance = 5.9664 +/- 0.0000 A	vector = [-0.0312 -0.6632 0.1555]
F3 -> H19A distance = 2.9768 +/- 0.0002 A	vector = [-0.0412 -0.2761 0.0360]
F3 -> H19B distance = 4.4604 +/- 0.0003 A	vector = [-0.0662 -0.3726 0.0922]
F3 -> H19C distance = 3.8561 +/- 0.0001 A	vector = [-0.0338 -0.3626 0.1497]
F1 -> H101 distance = 4.7465 +/- 0.0000 A	vector = [0.0150 -0.4808 0.2135]
F2 -> H101 distance = 3.1007 +/- 0.0000 A	vector = [0.0147 -0.1939 0.2162]
F3 -> H101 distance = 3.9147 +/- 0.0002 A	vector = [0.0526 -0.3373 0.1338]
F2 -> H101 distance = 3.1007 +/- 0.0000 A	vector = [-0.0147 0.1939 -0.2162]
F2 -> H102 distance = 1.8356 +/- 0.0000 A	vector = [-0.0154 0.1328 -0.1115]

Table 3.3: Important F—H distances between the cetyltrimethylammonium backbone and the fluorines of the SiF_6^{2-} anion; see Figure 3.2 for labels and relative positions

Liu, et al. determined the chemical shifts and the extremely strong (>25kHz) C—F and F—F dipolar couplings in their MAS NMR investigations of of PTFE and Nafion[18]. Although the actual ^{13}C resonance for PTFE is 111.3ppm, Liu, et al. went to extremes to obtain the signal: 28kHz spinning speed; $\{^{19}F\}^{13}C$VACP + CPMG and only after the train of CPMG π pulses was the linewidth narrowed to 18Hz. Otherwise, a very broad (>60ppm) lineshape (5kHz spinning speed, single-pulse pulse sequence) would dominate the spectral window. In the MAS NMR investigation of $(CTA)_2 \cdot SiF_6 \cdot 2H_2O$, although a $\{^{19}F\}^{13}C$VACPx pulse sequence was used to analyze the $(CTA)_2 \cdot SiF_6 \cdot 2H_2O$ described in this Chapter, no subsequent π train was added. Additionally, the sample was spun at only 16kHz, only about 65% of the spinning speed necessary to effectively suppress the dipolar coupling effects, manifested as spinning sidebands (see the asterisked lineshapes in Figure 3, for an example). Further, any residual fluoropolymers present in either the drive tip or end cap are relatively far removed from the center of the stator coil. Being at the ends of the coil, where B_1 is neither strong nor inductively symmetric, their relative locations would also lead to asymmetric broadening of the signal. Even in small amounts, this would likely appear as a broad component in the baseline and not as a Lorentzian lineshape.

In cross-polarization experiments such as this, magnetization is transferred from the fluorines of the SiF_6^{2-} anion to ^{13}C-containing species proximal to the anion. Although orders of magnitude stronger than through-bond or *j-coupling*, which is classically observed in liquid-state NMR, dipolar coupling is still usually a relatively weak interaction (on the order of the rotor spinning speed, measured in kHz). The presentation of the isotropic resonances and, more relevantly, spinning sidebands seen in the ^{19}F spectrum are a testament to the fact that the rotor spinning speed did not exceed the dipole-dipole coupling strength of the nuclei in question; spinning sideband amplitudes are minimized when $\omega_{ss} \geq \omega_{dd}$, where ω is in Khz.

Through-space or dipole-dipole coupling strength varies as r^{-3} between the nuclei under investigation, so these strengths quickly go to zero because of this spatial dependency. With

further analysis, this relatively weak phenomenon can, therefore, directly give spatial information, since the typical limit is no more than 5-7Å.

The concern that incidental fluorine ending up in the torlon end caps and drive tips used in the Varian rotor systems as a result of low quality-control manufacturing practices is perennial. Many previous experiments conducted on the torlon end caps and drive tips used have never detected any appreciable amount of of fluorine, relative to the signals obtained from the samples. Being physically outside the cylindrical volume of the stator coil, peaks that have been discovered in the past are broad and require hundreds of scans to produce a noise-ridden lineshape.

Although no explicit $\{^{19}F\}^{13}C$ VACPx NMR experiments were performed on empty rotors in this investigation, innumerable single-pulse experiments on the more abundant nucleus (^{19}F) have been conducted on the torlon end caps and drive tips used have never detected any appreciable amount of of fluorine, relative to the signals obtained from the samples. As also mentioned above with the work of Liu, et al., telltale signs of the cross-polarized fluorine—carbon signals would be obvious[18]. The broad baseline feature associated with PTFE, well-known to ^{19}F NMR spectroscopists and which appears in the -120 to -140ppm range would also have been evident. The presence of PTFE near the stator is typical of MAS NMR probes, as it is the polymer of choice for many of the components due to its high (~260ºC) softening temperature, chemically inert nature, low cost and ease with which to machine. The gimbals on which the stator is mounted and rotates in the Varian probe used in these experiments are made of PTFE. Again, empty stator experiments were run to determine whether the proximity of the gimbals to the stator can be detected and with negative results. The relevant distance is about 11mm from the outer edge of the coil turns inside the stator to the tip of the hollow tang through which bearing and drive air flow. The tangs protrude about 3mm into the Vespel stator and are the pivot points for when the stator is rotated in order to optimize for the magic angle.

Another inadvertent incorporation of SiF_6^{2-} into a novel crystal was also found in the literature[16]. Cordes, et al. found that metal tetrafluoroborate salts were leaching silicates from the glass vials in which they were conducting the reactions with a pyridinyl species as the other reagent. They, too, found that the SiF_6^{2-} species hydrogen bonded to the dihydrate waters in the unit cell, although the symmetry of their tetragonal, enantiomorphic crystal ($P4_32_12$ and $P4_12_12$) is higher than that found here, so the hydrogen-bonding networks are extensive and three dimensional.

In this investigation, we were very cognizant of the fact that HF can attack and etch borosilicate glasses and was the specific reason why care was taken to make and use PTFE equipment during the actual delivery of the HF. It was not considered, however, that subsequent reactive species remain in the mixture which could also attack and leach silicate species from the RBF used to strip off the supernatant, for example.

3.5 Conclusion

Large, 2-3mm-long crystals of cetyltrimethyl ammonium hexafluorosilicate dihydrate ($(CTA)_2{\cdot}SiF_6{\cdot}2H_2O$) have been (inadvertently) synthesized. The crystal structure was solved and the crystals characterized single-crystal XRD and ^{19}F, ^{13}C MAS NMR. The $(CTA)_2{\cdot}SiF_6{\cdot}2H_2O$ crystals were subsequently used to apparently successfully synthesize both the α– and β-phases of monodisperse, nanoparticle PbF_2.at room temperature using an microemulsive, reverse-micelle method. The particles were found to have a particle size of 17nm. Although several minor questions remain as to 1) the precise assignment of SiF_6^{2-} in this environment 2) the origin of the small carbon peaks evident in the $\{^{19}F\}^{13}C$ VACPx MAS NMR, 3) whether construction and exploration of ternary phase diagram of the constituent components (CTAF*, 2-octanol, water) could produce phase-pure α- and β-PbF_2, the overall results appear consistent.

3.6 References

1. Kennedy, J.H., Miles, R., Hunter, J.. *J. Electrochem. Soc*. 120 (1973) 1441

2. Portella, K.F., Rattmann, K. R., De Souza, G. P., Garcia, C. M. Cantão, M. P. *J. Mat. Sci 35 (2000) 3263*.

3 Boutonnet, M., Kizling, J., Stenius, P. *Coll. Surf*., 5 (1982) 209 - 225.

4 Fontell, K; Khan, A; Lindstroem, B.; Maciejewska, D.; Puang-Ngren, S. *Coll. Polym. Sci*. (1991) 269 (7) 727.

5 Desai, A., Varade, D. Mata, J. Aswal, V., Bahadur, *P. Coll. Surf. A* 259 (2005) 111–115.

6 Bunton, C.A., Frankson, J., Romsted, L.S. *J. Phys. Chem*. 84, (1980) 2607-2611.

7 Muller, N; Pellerin, J.H; Chen, W.W. *J. Phys. Chem*. (1972), 76 3012.

8 http://ww1.iucr.org/comm/cnom/adp/finrep/node8.html

9 Nguyen, T.Q; Qu, F.I; Huang, X. Janzen, A. *Can. J. Chem*. 70, 1992

10 Borodin, P.M; Nguyen, K.Z; Petrov, N.S. J. *Struct. Chem*. 14, 4 1973

11 Buslaev, Y. V.; Petrosyants, S. P. Sov. *J. Coord. Chem. (Engl. Trans.)* 1980, 5 (2), 123-129.

12 Finney, W.F; Wilson, E; Callender, A. Morris, M.D; Beck, L.W. *Environ. Sci. Tech*. 2006, 40,2572-2577

13 Asseid, F.M; Duke, C.A.V; Miller, J.M. *Can. J. Chem*. 68, 1990 1420-1424.

14 Coplan, M. J; Masters, R. D. *Fluoride* 2001, 34 (3), 161-164.

15 Han,S; Shihabi, D.S; Chang, C. D. *J. Catal*. 196, 375–378 (2000)

16 Cordes, D.B., et al. *Cryst. Growth Des*. 7 (2007) 1943-1945.

17 Campanelli, A.R., et al. *Acta Cryst*. (1986). C42, 1380-1383

18 Liu, et al. *Macromolecules* (2001), 34, 8416-8418

19 Koh, L., et al. *Acta Cryst*. (1993). C49, 1032-1035

Chapter 4

A Combined, Ramped-Amplitude-Cross Polarization Spectral Editing (RAMP-CP-PI) $\{^{1}H\}^{13}C$ Investigation into Carbon Chemical Shift Assignment of Poly(diiododiacetylene)

Abstract

Methods to characterize complex, carbon-based materials polymerized from parent crystals leave few investigative methods available to deduce their local microscopic environments. Although magic-angle spinning nuclear magnetic resonance (MAS NMR) is well suited to the task, complicating the investigation are the 1) subtotal polymerization of the compound 2) broad, overlapping spectra from chemically similar parent materials on a familiarly narrow (0 ~ 200ppm) ^{13}C spectral window 3) low signal-to-noise ratios. A novel, modified variable-amplitude cross-polarization pulse sequence was written, whereby which the phase of a second $\pi/2$ pulse (along (-x)), different from the initial pulse (along x) and the contact times associated with this second pulse was investigated. This new pulse sequence, called Ramped Amplitude Cross Polarization-Polarization Inversion RAMP-CP-PI) allowed for a more sensitive method of controlling the contact times between the I (^{1}H) and S (^{13}C) spins in the second, inverted (-x) phase. Carbon peaks were then selectively inverted and, more importantly, the signal-to-noise ratio optimized, depending on their substituents and nearby proton environments. The experiments on a model compound, hexamethylbenzene, permitted experiments and selective inversion of carbon signals in the Poly(diiododiacetylene) polymer, relying on the nearby protons found on the host 1-3-bispyridyl oxalamide co-crystal.

4.1 Introduction

The focus of the investigations reported in this chapter was the high-pressure synthesis and characterization of a conjugated poly(diiododiacetylene) by using a host/guest cocrystal system with diiodobutadiyne as the constituent monomer (see Figure 1)[3,4]. Poly(diacetylenes) (PDAs) have garnered great interest among scientists in several disciplines, due in large part to their electronic conduction and the frequency dependence of the emitted light. Conjugated, unidimensional polymers are of great interest to the optics and computer-science communities because the size of the non-linear response is a direct function of the non-localized π electrons (to 5th order), as well as the length of the polymerized chain (also to 5th order)[1]. The third term in the power-series expansion of the polarization (hence the term "third-order susceptibility") describing the optical response of the system is frequency dependent. When light is applied, the frequency dependence upon the square of the intensity of the applied light makes tuning and optical switching feasible[2,6,7].

The alternating triple-/double-bond configuration along the polymer backbone is very desirable, because this affords a large number of delocalized electrons per unit length (which is why butadiynes are so attractive). The advent of semiconductor theory made PDAs all the more attractive, since it was realized that delocalized π systems obviated the need for an accompanying electron-hole pair, required for p—n junctions[18].

4.1.1 Preparation and Challenges of Polymerized Diacetylenes and Poly(diiododiacetylene) (PIDA)

Given the broad potential applications of PDAs in general and with the prospect of Lewis acidic materials such as PIDA, the race to find scalable unremarkable syntheses for PDA, PIDA and functionalized analogs has increased in the last decade. Study of the mechanisms and efficacies underlying the formation of these polymers (using the high-pressure route, for example) proves instructive, yet effective analysis of the process is requisite.

Difficulties in finding facile synthesis of these conjugated diynes prompts the exploration of several possible synthetic routes including gels, self-assembly methods, high-pressure, and photoinduction and thin films have been explored, to name only a few[15,16,17,19,26,27,28]. Interestingly, Barentsen, et al., also explored the incremental addition of aliphatic groups and their remarkable effects on their thermal and photoinduced topochemical synthesis and conductivity increases[19].

Regardless of the co-methodology (self-assembly, pressure, etc.), PDAs (and the compound studied here, poly(diiododiacetylene) or PIDA, see Figure 1b) are thought to proceed via a radicalization-initiation mechanism, whereby the topochemical scaffolding (or diacetylene-incorporated surfactants in the case of Yang, et al.) allows for optimal intermonomeric distances and angles (both θ, ϕ) and subsequent C1—C4´ interaction[20]. The second critical component to successful polymerization is the host/guest relationship and the notion of the halogen bond, in particular.

The unusual relationship that the Lewis acidic iodine the pyridyl nitrogen have between their respective σ^*_u and π molecular orbitals is somewhat rare, yet clearly allow the correct orientation to be obtained for these “structural moieties” for this particular type of polymerization to

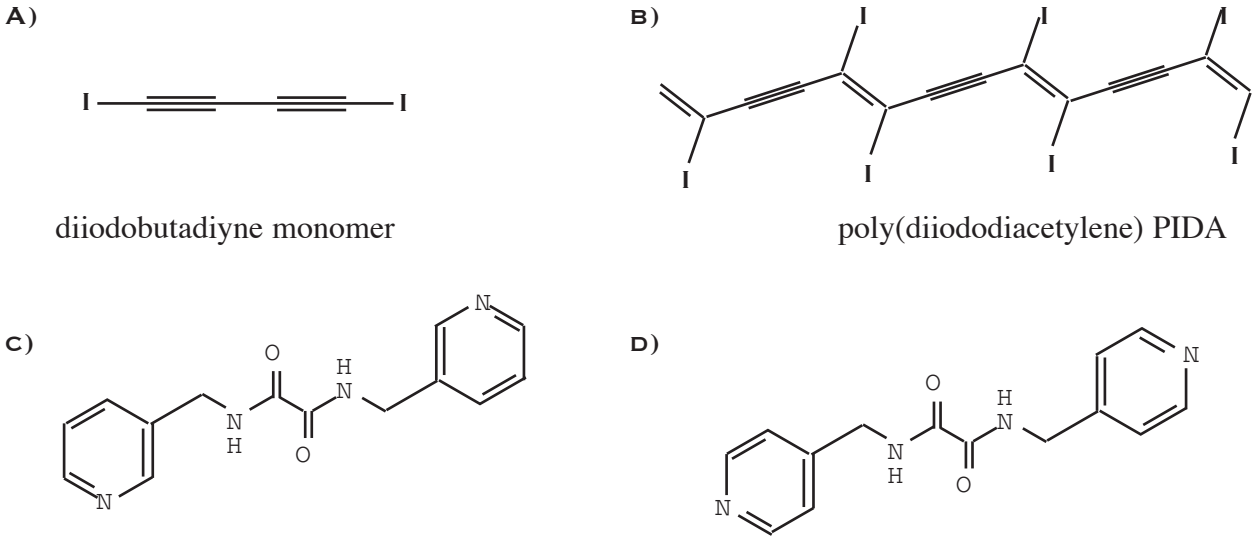

Figure 4.1 a) diiodobutadiyne monomer as the basic building block for **b**; b) poly(diiododiacetylene) PIDA "guest" conjugated polymer: the target molecule; c), d): 1-3- and 1-4-bispyridyl oxalamide co-crystals, A and B, respectively: the "host" crystal which provides a scaffold-like structure, supporting the guest and facilitating topochemical interaction.

occur[21]. In fact, its electron density and Lewis acidic character make iodine the ideal participant in situations like this, where halogen bonding is is so crucial.

With the exceptions of Wilhelm and Barentsen [refs 3, 19], all other authors relied on photoinduced polymerization[3,19]. In the work presented here (refer to Figure 1), Wilhelm subjected the diiodobutadiyne monomer (compound A, Figure 1a) combined with the 1-3-bispyridyl oxalamide co-crystal (compound C, Figure 1c), to pressure provided by a diamond-anvil press and the monomers began to polymerize quickly, beginning at only 0.3GPa of pressure.

Suboptimal orientation of compound A, provided by the 1-4-bispyridyl oxalamide co-crystal (compound D, Figure 4.1d) facilitated the onset of polymerization at 2.8GPa, substantially higher than that of the A/C guest/host combination.

Although not imediately intuitive, some polymerized systems (such as PDA) do form single crystals which are then available to investigation via xray diffraction[29]. Yet another challenge to the investigation of PIDA is that crystallinity is lost in its formation and is, therefore, invisible to x-ray diffraction. While Raman spectroscopy is helpful, it can only be applied toward identifying the alternating sp/sp^2 hybridized backbone of PIDA, and not afford broader structural insight.

H3 -> C1	distance = 3.5627 A
H4 -> C1	distance = 3.3628 A
H4 -> C1	distance = 3.3628 A
H3 -> C1	distance = 3.5627 A
C1 -> H6A	distance = 3.7335 A
C1 -> H6B	distance = 2.9706 A
H3 -> C4´	distance = 3.1755 A
H4 -> C4´	distance = 4.2833 A
C1 -> H6A	distance = 5.4973 A
C4´ -> H6A	distance = 4.6783 A
C4´ -> H6A	distance = 4.0040 A
C1 -> H6A	distance = 3.7335 A
H6B -> C1	distance = 4.4465 A
H6B -> C4´	distance = 5.2402 A
H3A -> C1	distance = 5.4976 A
H3A -> C4´	distance = 6.3190 A
H3A -> C4´	distance = 7.3570 A
H3A -> C1	distance = 8.3709 A
H3 -> C4´	distance = 5.3027 A
H4 -> C1	distance = 5.7996 A

Table 4.1: Representative C—H intermolecular distances between oxalamide A protons on the pyridyl ring, methylene groups and diiodobutadiyne monomer carbons. See Figure 3b for a space-filling rendering of the molecules, corresponding labels used in this table and their approximate spatial orientations. For reference, H6a,b, though not visible in Figure 3b, are the methylene protons attached to the pyridinyl ring.

An obvious characterization method would be to consider single-pulse excitation (SPE) ^{13}C NMR yet, carbon-rich compounds have their own challenges with respect to NMR. Given the extremely low natural abundance of ^{13}C (1.07%), a spin |1/2> nucleus, however, it is possible to use a relatively abundant spin-active nucleus nearby (^{1}H) to transfer magnetization from the abundant nucleus to the "rare" nucleus, in this case, ^{13}C. This double-resonance pulse sequence, called *cross polarization*, is advantageous primarily because one now relies on the spin-lattice (T_1) relaxation time of the abundant nucleus, often much faster than that of the nucleus under investigation (in this case carbon)[5]. In the case of the diiodobutadiyne and PIDA investigated here, CP-MAS techniques are employed reduced the recycle delays by 60%, in comparison to directly observed ^{13}C MAS NMR with no decoupling.

4.1.2 The Cross-Polarization Experiment

The major requirement for the CP pulse sequence is to find the Hartmann-Hahn match condition[22]. The rf pulse power for each nucleus is found and matched to the other, proportional to a ratio of the gyromagnetic ratios (γ_I/γ_S) of the nuclei in question, such that $\nu_I\gamma_I = \nu_S\gamma_S$. The γ of ^{1}H is about 4x higher than ^{13}C, ($(26.75/6.72 \approx 4)$ units: $10^7 \cdot rad \cdot T^{-1} \cdot s^{-1}$) and ν_{spin} i(ν_i or ν_s) the irradiative power used for each nucleus, often measured in kHz, represented with the Greek letter ν. Figure 2 shows a schematic for the CP experiment.

While the ratio of (γ_I/γ_S) is fixed, the precise value of $\nu_{spin}\gamma_{spin}$ is dependent upon the actual local environments of the nuclei under investigation and the dipolar interactions among and between them. The source of this dipole-dipole coupling is the interaction between two nearby nuclear magnetic spins. Dipole-dipole coupling is a through-space interaction, with (hetero and homonuclear) dipolar coupling varying as r^{-3} between the nuclei, where r is the internuclear vector.

One of the three salient aspects of a successful cross-polarization experiment is an efficient transfer of magnetization from the abundant spins (|I>) to the dilute or rare spins (|S>). For proximal spins in a particular system, these conditions can be thought of as constant, abbreviated T_{IS}.

Through-space magnetization transfer also depends on a proper contact time, τ_{CP}, or the optimal time discovered that permits the greatest internuclear transfer of magnetization to occur. Thirdly, τ_{CP} and T_{IS} are affected by the specific $T_1\rho$ (the relaxation times in the rotating frame) values of the I and S spins, respectively. Given some system, the spins involved can be "locked" into co-precession in the x—y plane by the weaker magnetic field imposed by the NMR probe coil, called $B_{1(I,S)}$, in the direction of the magnetization vector, representing the local B_1 for the respective spins. Effective spinlocking depends on the strength and homogeneity of the B_1 to overpower local dipolar interactions. A fair amount of power is required for this event, so care has to be taken to optimize τ_{CP}, so as to not unduly stress the probe components and spectrometer equipment. Parenthetically, it should be noted that the "simple model" of cross polarization is upheld in the investigation in this chapter, such that $T_{IS} < T_1\rho_{(I)}$ although cases do occur where the opposite is true and therefore, different strategies are used[24].

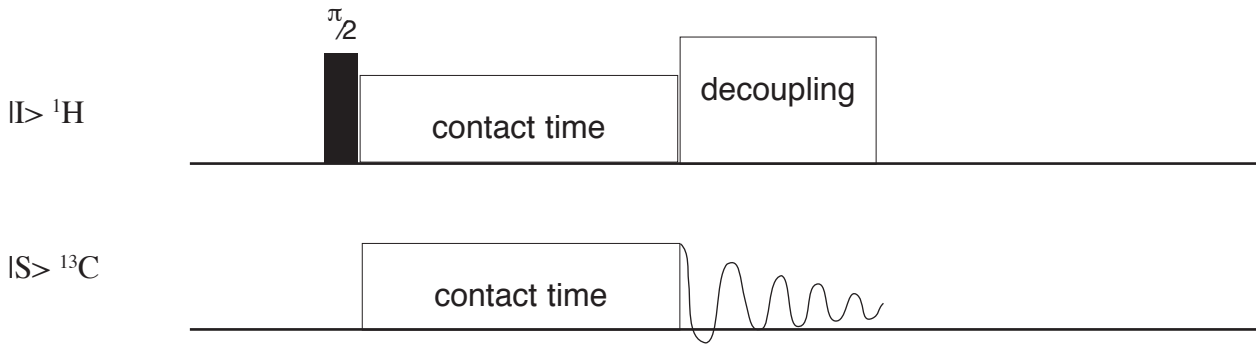

Figure 4.2: Schematic of a CP-MAS pulse sequence

Determining the Hartmann-Hahn matching conditions allows for a transfer of magnetization from the |I> spin to the |S> spin. This transfer of magnetization (defined, as above, with the time constant T_{IS}) is integrable, quantifiable and reaches saturation over time (see Figures 4.6 a,b). Optimal contact times (see Figure 4.2: the time by which the two ensembles of spins are allowed to interact with one another) are unique to samples and can vary widely among substances. A simple way to set the Hartmann-Hahn condition is to consistently use a standard (such as hexamethyl benzene (HMB) used here) with few non-magnetically-equivalent nuclei and very weak heteronuclear dipolar coupling and run a contact-time (c-t) array. Then, on the sample under investigation, a second c-t array is run to further optimize the contact time for the specific spin system. Since dipole-dipole interactions attenuate as r^{-3}, optimizing with standards that have these properties ensures that interactions between I,S nuclei with large distances can also be captured. Finally, decoupling (see Figure 4.2) is required because, and pristine |S> FID can be recorded. Decoupling is usually effected by the application continuous irradiation, or a train of pulses to the |S> spins with an rf frequency that is typically 5-10% greater in strength than the initial ½ pulse.

In the case of the poly(diiododiacetylene) (PIDA) polymers under investigation here, the challenge is that the only protons in the vicinity of carbons (C1 - C4´) are those in the bispyridyl oxalamide co-crystals A and B (see Figure 1 C,D); the approximate distance ranges markedly, from a minimum of approximately 2.9Å to a maximum of approximately 8.3Å as depicted in Table 4.1 (also see orange overlay arrows, Figure 3B).

Since polymerization was found to change the distances determined from diffraction data, the interatomic distances in Table 1 are from the pre-pressed, host-guest crystallized material and are therefore merely approximations for the polymerized materials.

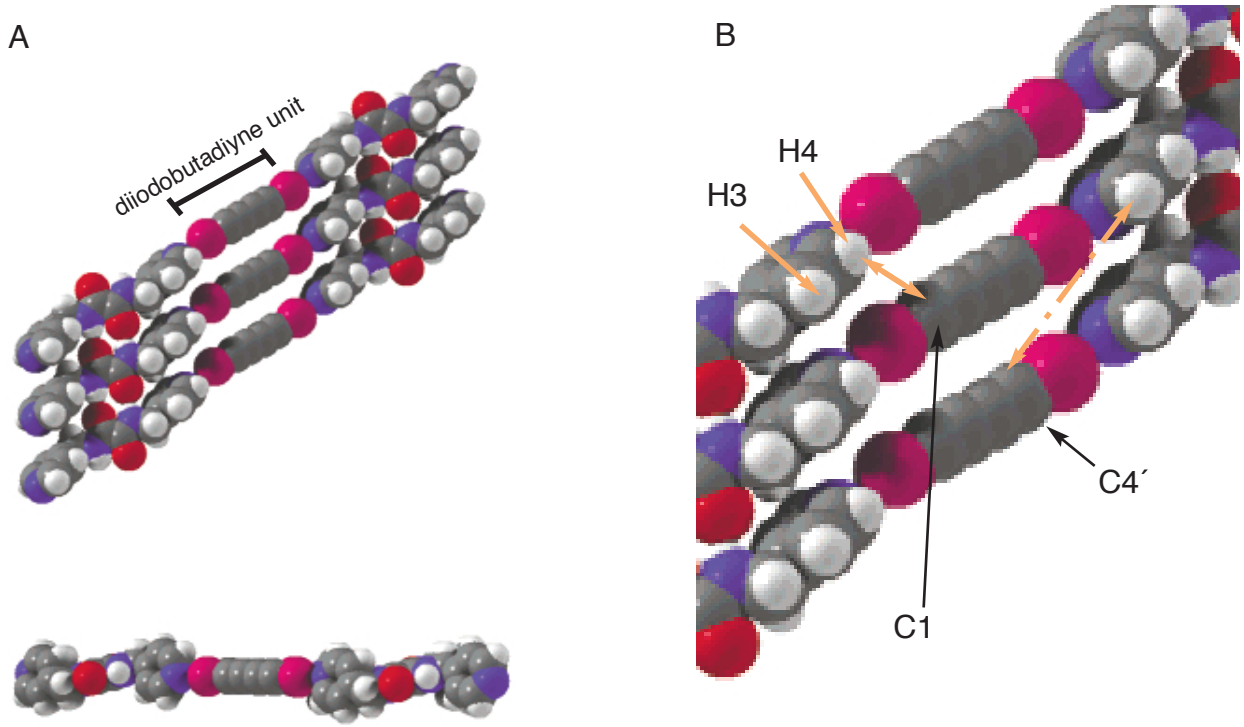

Figure 4.3a: space-filling, crystallographically accurate rendition of the 1·4bis pyridyl oxalamide co-crystal

Figure 4.3b: detail highlighting approximate distances between nearest protons/carbons; minimum/maximum interatomic C—H distances (see text below) in overlay orange arrows; pyridyl protons are white space-filling spheres. Note the N—I halogen bond (blue and purple space-filling spheres)

Carbon spectra, with their anticipated narrow total spectral window, substantial chemical shift anisotropy (CSA; orientational dependence of chemical shifts, relative to B_0) and many magnetically inequivalent species, give rise to a cluttered spectrum, thereby complicating spectral analysis due to overlap. Therefore, it is typically preferable to spin at higher spinning speeds, thereby suppressing the appearance of spinning sidebands.

The liability in higher spinning speeds, however, is twofold. Suppressing sidebands is a goal of spinning a sample at the magic angle, yet dipolar coupling (the very internuclear interaction we are trying to exploit) is also negatively affected by an increased spinning speed. The otherwise smooth matching curve (measured as a function of rf power) decomposes into a series of peaks, separated by the spinning speed, ν_r, where cross polarization can only occur at each peak[8]. This is represented by the introduction of this third term into the Hartmann-Hahn matching equation, $\nu_I\gamma_I = \nu_S\gamma_S + n\nu_r$, (see Figure 4, below) whereby "mismatches" occur as a function of the spinning speed, n representing an integer number of the spinning speed. Secondly, homo and heteronuclear dipolar coupling strengths between the nuclei in this particular sample, post-polymerization, will still likely have a wide range and will vary broadly, which would be detrimental to suppress, where weakly coupling components suffer first.

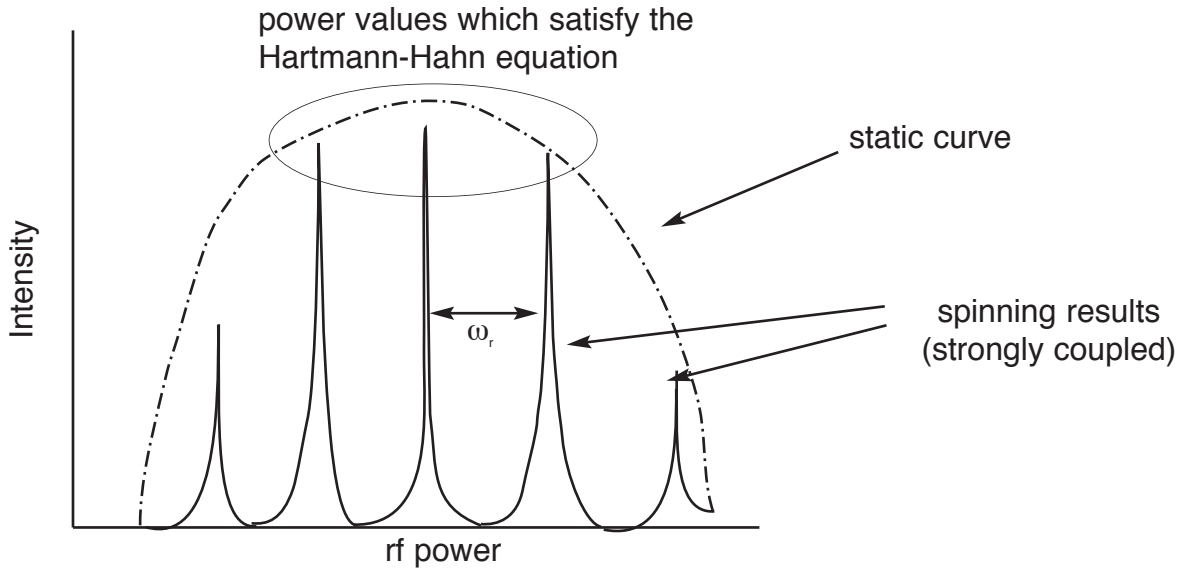

Figure 4.4: an illustration of a representative Hartmann-Hahn power array experiment. Short ranges of power values (see peaks within oval above) satisfy, but above and below, the combination of power and spinning speed (rotor periods: "n") engenders a loss of signal intensity.

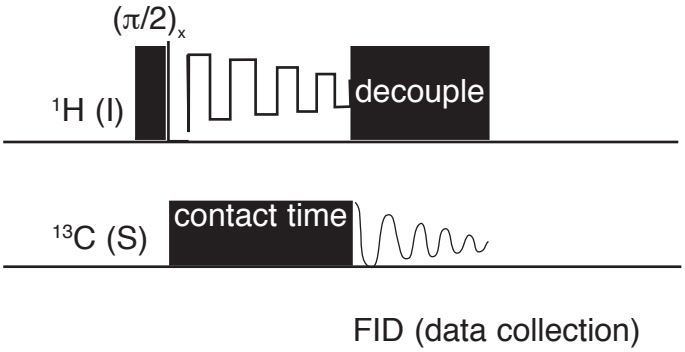

Figure 4.5: Schemactic of a VACP pulse sequence

The impact of these two issues (broad spin/material-dependent CSA variances and variable hetero/homonuclear dipolar coupling strengths) were attenuated in the early 1990s with the advent of variable-amplitude cross-polarization (VACP; see Figure 7)[8]. As depicted in figure 7, the cross-polarization part is actually a series of pulses decreasing linearly in amplitude (see figure 4), making sure that an adequate contact time is used during each time interval[9]. The effect of the linear decrease in amplitude is to compensate for the decomposition of the Hartmann-Hahn matching conditions due to spinning speeds that greatly exceed the dipolar coupling strengths. The matching conditions must be exact, as there is almost no tolerance for mismatch.

In 1994, however, Smith, et al. improved upon the VACP pulse sequence by creating a shaped pulse that linearly declines, having realized that the linear decrease corrects for any inhomogeneities in B_1[10]. This ramped-amplitude cross polarization sequence (RAMP-CP), as depicted in Figure 6, changes X-channel amplitude, rather than the abundant nucleus, as depicted in Figure 5.

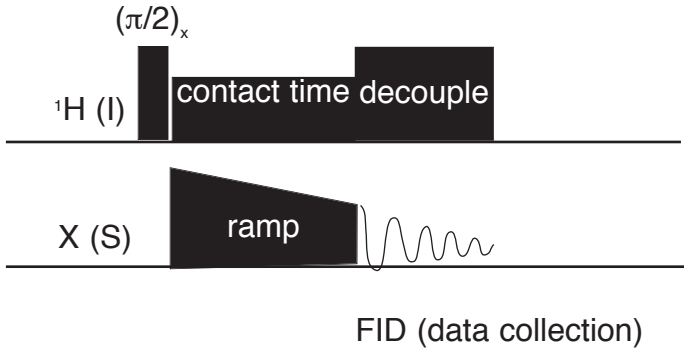

Figure 4.6: Schematic of a RAMP-CP pulse sequence

4.1.3 Spectral Editing

Many experiments were run on the PIDA sample under investigation in these experiments using the RAMP-CP pulse sequence. The somewhat poor resolution, complexity and long acquisition periods of the RAMP-CP $\{^1H\}$ ^{13}C MAS NMR spectra for both the monomer (co-crystallized with the "A" and "B" pyridyl oxalamides) and polymer prompted a literature search for a technique that could possibly discriminate between the carbon species present in the sample. The broad range of proton—carbon distances, differing coupling strengths, and type of carbon-bound proton all contributed to this substantial difficulty. The Spectral Editing method, explored by Zilm, et al., exploits the fact that S-spin polarization times vary according to proximity and number of I-spins[11]. Since cross polarization here is, again, dipolar mediated, one could easily see that proximity and number of spins could then be used to segregate out spins. Figure 4.6 depicts T_{IS} magnetization buildup curves for some representative substituent groups and the obvious differences in times, depending on proximity to the coupling proton(s). Alternatively, one can also view these interactions as a function of $T_{1\rho}$ for each species, or the relaxation time in the rotating frame, which is presented in Figure 4.6b[23,24].

One has a choice of phase with respect to the application of the RF pulse: $(\pi/2)_{\pm x,\, \pm y,}$. After ramped cross-polarization, one can in principle, apply another RF pulse, opposite in phase, in order to generate so-called Polarization Inversion (PI)[12]. A pulse sequence scheme for the modified pulse sequence is depicted in Figure 4.7. Note that the "negative contact" time is below the line, in order to emphasize the fact that the phase of the subsequent RF pulse is along (-x) and that negative contact times can be controlled. Note, too, that the choice of axis (±x,± y) is arbitrary, dependent only upon the phase of the initial π/2 pulse.

The aim of this chapter is to employ the tools explained above to obtain as detailed spectra as possible in order to assign the ^{13}C MAS NMR spectra of the constituent carbons for this particular sample of PIDA.

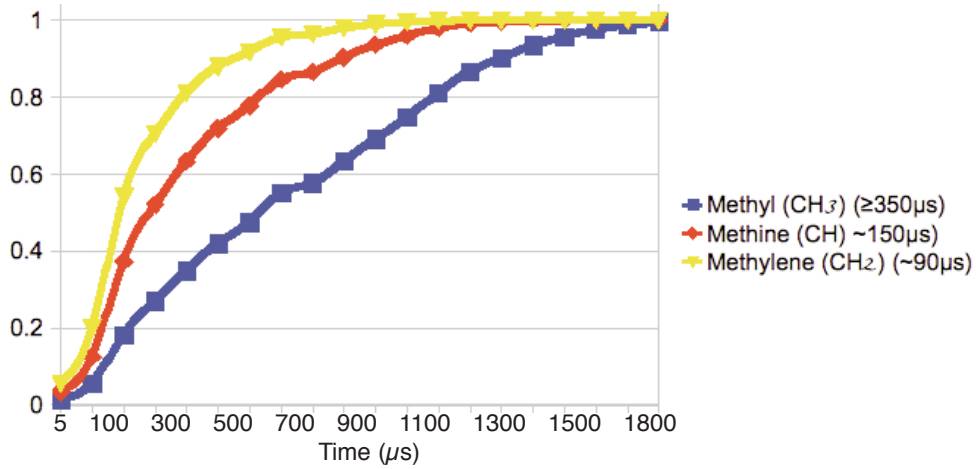

Figure 4.7a: Graph and times for magnetization buildup curves (T_{IS}) of representative carbon-proton interactions; $I(t) = I_0(1- \exp(t/T_{IS})$. Explicit values for the magnetization buildup times are as follows: T_{IS} (methyl): 350μs; methine: 150μs; methylene: 90μs.

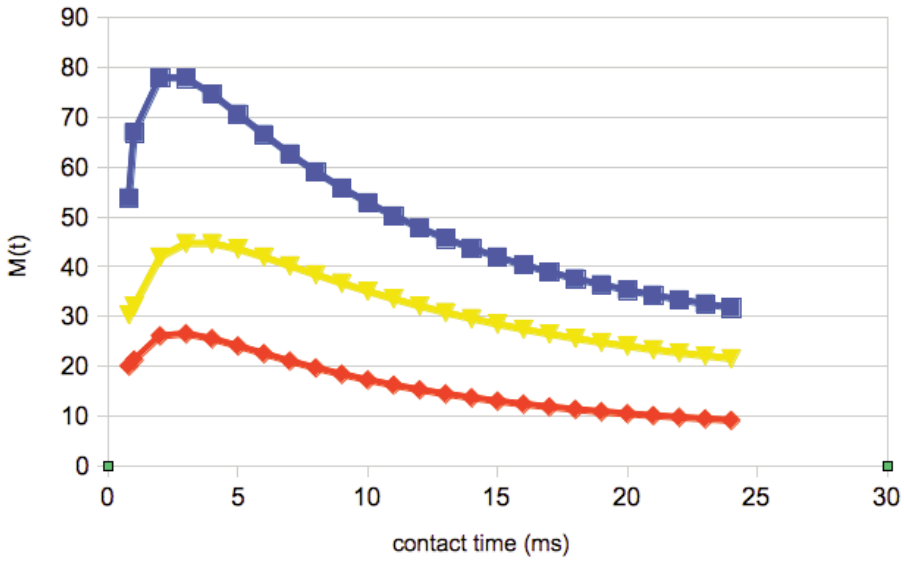

Figure 4.7b: representative curves of carbon $T_{1\varrho}$ for selected species.

$$I(t) = I_0\left[1 - e^{\frac{-t}{T_{IS}}}\right] \quad 4.1$$

$$I(t) = I_0\left(1 - \frac{T_{IS}}{T_{1\rho}^I}\right)^{-1}\left[exp(-t/T_{1\rho}^I) - exp(-t/T_{IS})\right] \quad 4.2$$

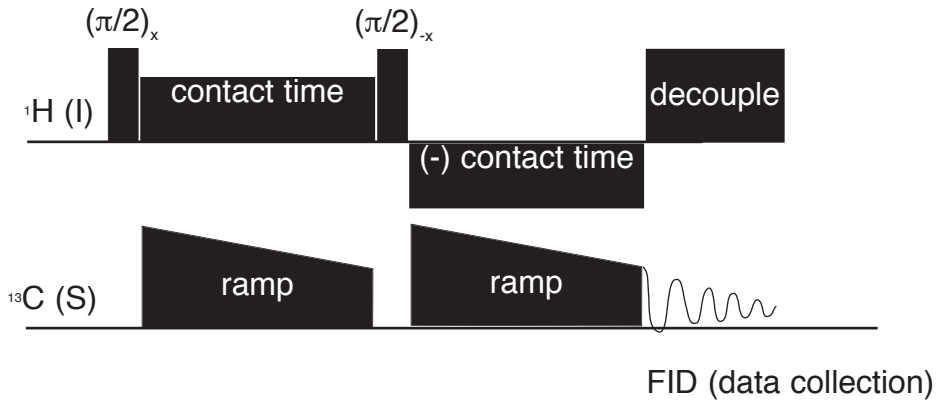

Figure 4.8: Schematic of the new RAMP-CP-PI pulse sequence

Additionally, at the time this pulse sequence was written and these experiments were performed, no evidence in the literature was found where RAMP was employed (and interesting resultant behavior recorded) during the PI portion of the sequence.

4.2 Experimental

All experiments were performed at room temperature on a Varian/Chemagnetics 360MHz (8.47T) magnet using a 4mm (OD) zirconia rotor, Otsuka double-resonance (HX) probe with PTFE end cap and Vespel drive tip. Chemagnetics InfinityPlus spectrometer software (Spinsight v.4.3.2) was used to collect and process all data. The precession frequencies were 360.03MHz for ^{1}H and 90.53MHz for ^{13}C. Spectra were referenced to the methyl carbon (28.5ppm) of HMB as a secondary pulse.

The rotors were packed in air, as they were not immediately oxidatively sensitive, though they were subject to long-term thermal decomposition[3,4]. Samples and/or packed rotors were stored in a temperature-controlled freezer and shielded from light when not in use, due to known photoreactivity of the the various PIDA species. Empty rotors with Vespel end cap and drive tips were also investigated to ensure that no signals associated with the hemiacetal Vespel polymer were producible or evident in the spectra.

All experiments were performed 1-3 bis (pyridyl) oxalamide/diiodobutadiyne co-crystals as well as the polymerized PIDA, which obviously still contains the 1-3 (compound ⊂, see Figure 1). The co-crystals were subjected to preparation in the diamond-anvil press, located in the COMPRES facility at Stony Brook University, Dept. of Geosciences as discussed in [3].

HMB was used as the model compound for both Hartmann-Hahn optimization, as well as to choose step size and number of steps used to construct the ramp sequences. A broad, negatively scaled power array (eg: from rf_x - $rf_{x-\sigma}$) is used to find the optimal power settings, as there are several solutions to the Hartmann-Hahn condition (which emerge from the $n\omega_r$ term mentioned on p.7 above), though only one is commensurate with the $\pi/2$ power levels that are initially determined for each nucleus.

For all of the VACP-PI $\{^1H\}$ ^{13}C MAS NMR experiments, the same number (seven) and amplitudes were used for both the first ramp as well as the oppositely phased second ramp (see Figure 7). As graphically indicated in the Figures which depict the various pulse sequences, a slightly higher strength was used for the decoupling portion of the pulse sequence, typically 5-8% above the rf power used for the initial $\pi/2$ pulse.

A 15kHz spinning speed was chosen. This appeared to adequately suppress the spinning sidebands for the sample, which was fortunate, since this approaches the maximum rated spinning speed for 4mm Otsuka probes. A 4 or 5μs $\pi/2$ pulse was used for ^1H and ^{13}C, with appropriate power settings for each channel, as required to satisfy the Hartmann-Hahn condition.

Ramp step size depended upon sample and actual experimental conditions, but for the PIDA sample, was found to be 0.005; arbitrary units are used within the Spinsight software, where $power_{max} = 1$. Seven steps were always used. A pulse delay of 2s, dictated by the dictated by the ^1H T_1, rather than 10s for directly observed ^{13}C for these samples, was used. All experiments on the PIDA samples were acquired with 43,200 scans.

4.3 Results

4.3.1: Hexamethylbenzene (HMB)

Figure 4.8 (below) was the first successful result employing RAMP-CP-PI on the model compound HMB, effectively inverting the carbon peak of choice (here, the benzene carbons), while maintaining correct proportions between the two peaks. Table 4.2 (see below) tabulates the choices and resultant trends obtained in a more thorough examination of HMB.

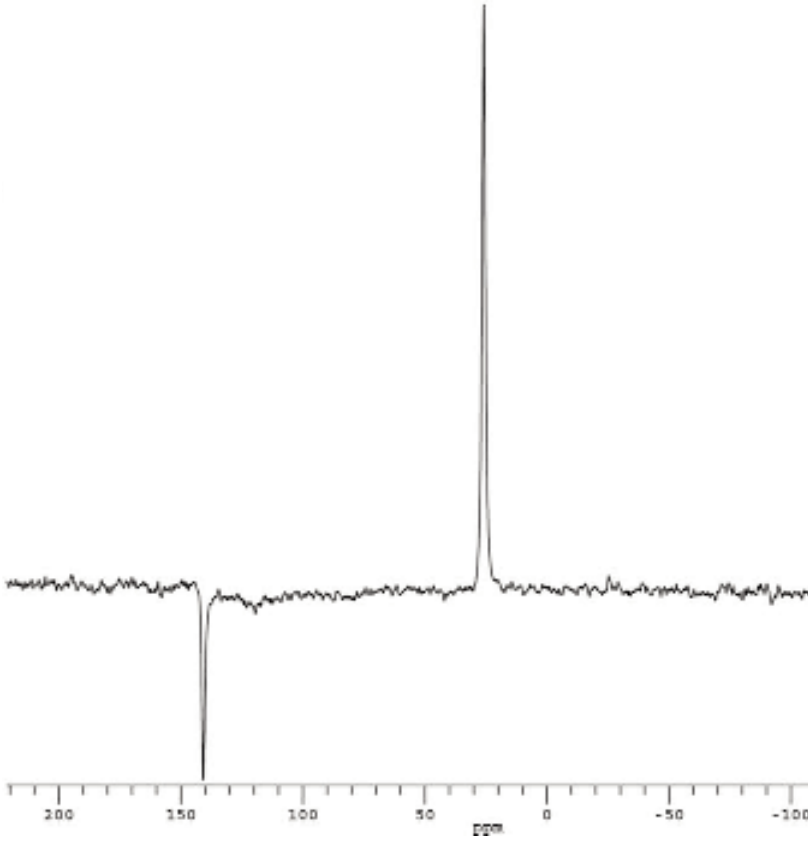

Figure 4.9a: RAMP-CP-PI of HMB: the methyl carbon @ 28.5ppm is erect while the benzene carbon (no bound protons) is inverted @ 141ppm. Acquisition conditions: RT; 14kHz spinning speed; 62.5kHz RF power (4μs ⅞ time); 0.1ms (+)CT, 2ms(-)CT. Refer to Table 4.2 (see below) for a complete tabulation of ± contact times and their effects on these respective peaks.

CT (ms)	nCT (ms)	ΔC_B (s/n)	ΔC_{ME} (s/n)
0.01	2	15.7	47.2
0.1	2	15.7	49.5
1	1	1	25.6
1	2	6	30.8
2	1	1	25.8
2	0.3	7.9	11.1
4	0.3	14.6	19.5
6	0.2	20.4	23.6
6	0.3	17.9	22.8
6	0.4	23.1	10.2
6	0.5	21	1.9*
8	0.4	26.5	9
8	0.5	23	3.5*
10	0.3	24.1	21.9
10	0.5	24.2	4.9*
10	1	14.4	14.2*
12	0.5	27.4	3.1
12	1	14.4	18.2*

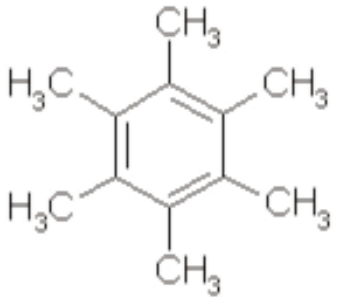

model compound
hexamethylbenzene

NB: asterisk (*) denotes inverted peak

Table 4.2: Dependence of peak resolution/suppression on positive and negative contact times. The (ΔC(s/n)) term denotes signal-to-noise ratio. NB: asterisk indicates negative (-) peak.

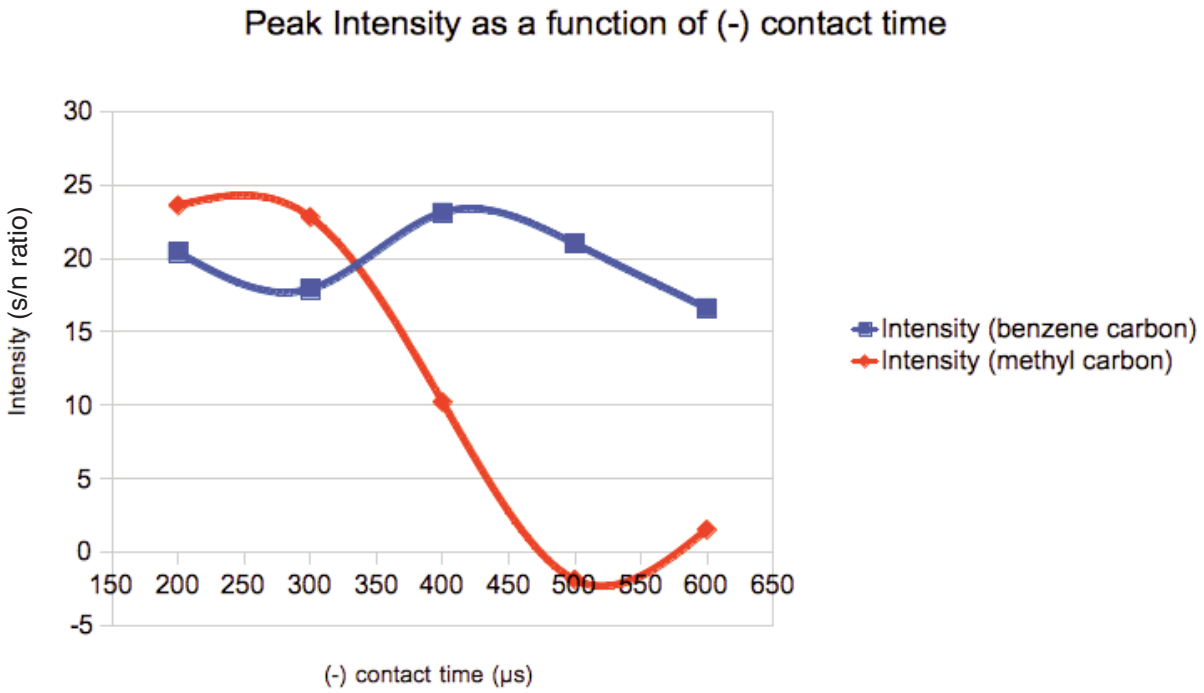

Figure 4.9b: (companion Figure to Table 2, see yellow highlighted data): Plot of signal intensity per carbon for the standard used here, HMB, as a function of (-) contact time (200μs - 600μs). NB: (+) contact time remains ***fixed*** at 6ms; Methyl curve dipping below zero indicates peak inversion.

Expt	CT(ms)	nCT(ms)		peak	peak	peak	peak	peak	peak	peak	peak
				46.2	89	110	115	121	134	151	162
a	10	0.05		(+)	(ø)	(+)	(+)	(-)	(-)	(-)	(-)
b	10	0.269		(ø)	(ø)	(-)	(+)	(ø)	(+)	(-)	(+)
c	10	0.5		(+)	(ø)	(-)	(+)	(+)	(+)	(+)	(+)
d	10	1		(+)	(ø)	(-)	(-)	(+)	(+)	(+)	(+)
e	10	1.25		(-)	(-)	(-)	(-)	(+)	(+)	(+)	(+)
f	10	2		(+)	(ø)	(-)	(ø)	(+)	(+)	(+)	(+)

Table 4.3: Tabulation of general morphology per PIDA carbon peak, correlated to negative contact time: ø = flat; (-) = inverted peak; (+) = erect peak. Experiment letters correspond to Figures 4.9a-f. Peak values are in ppm.

4.3.2: PIDA

Spectrum 1. CP-MAS

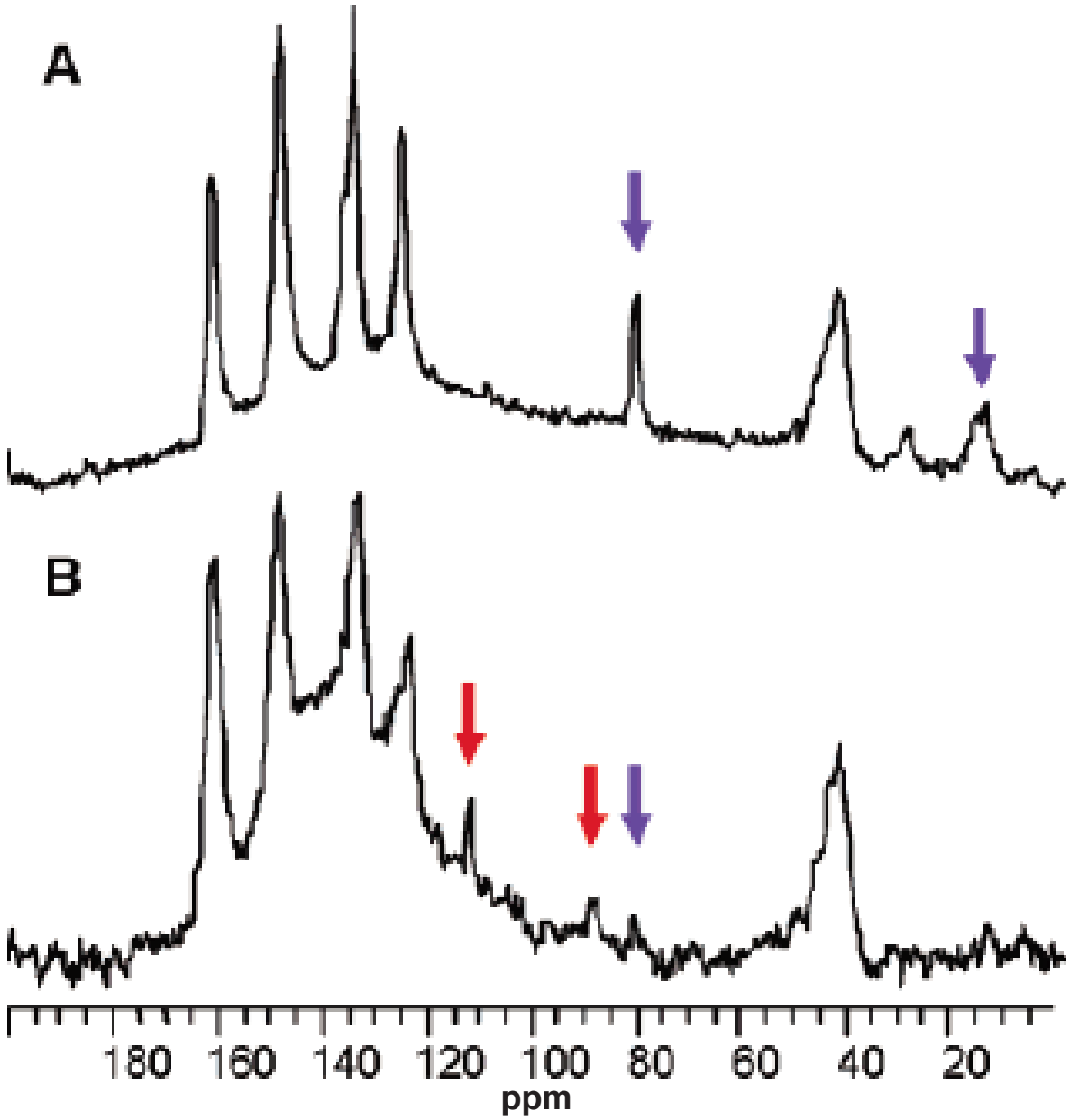

Figure 4.10a: Spectrum 1. "Normal" CP-MAS ^{13}C NMR Spectra of the cocrystals (x-axis is in ppm): (A) 1•3 before pressing; (B) 1•3 after pressing to >6 GPa; Blue arrows indicate peaks corresponding to monomer 1 (see Figure 1a) ; red arrows indicate peaks corresponding to the PIDA polymer (see Figure 1b). Reproduced from [3], where this appears as Figure 5, page 4419.

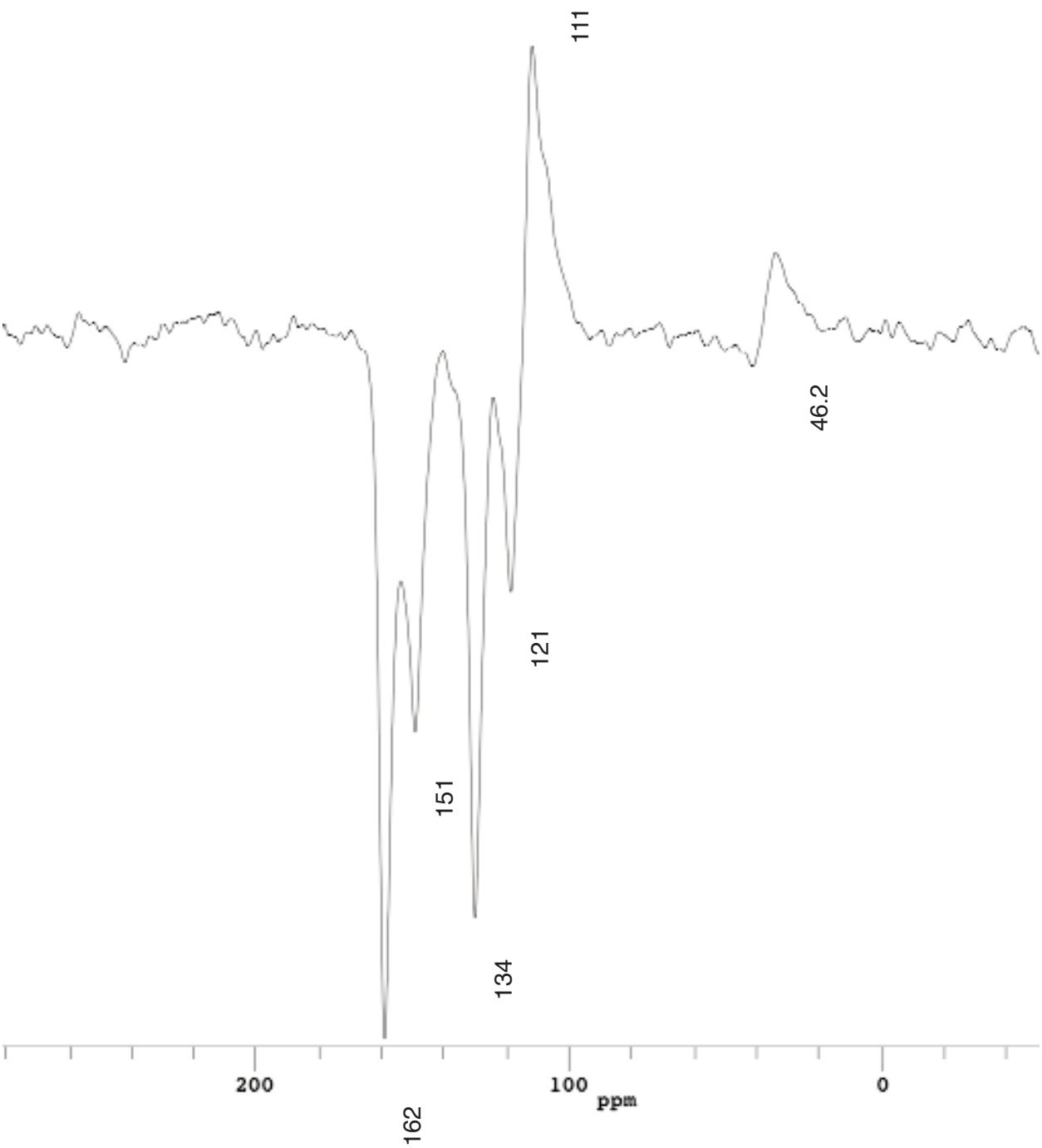

Figure 4.10b: RAMP-CP-PI spectrum with a 50μs negative contact time "A" (see Table 4.2).

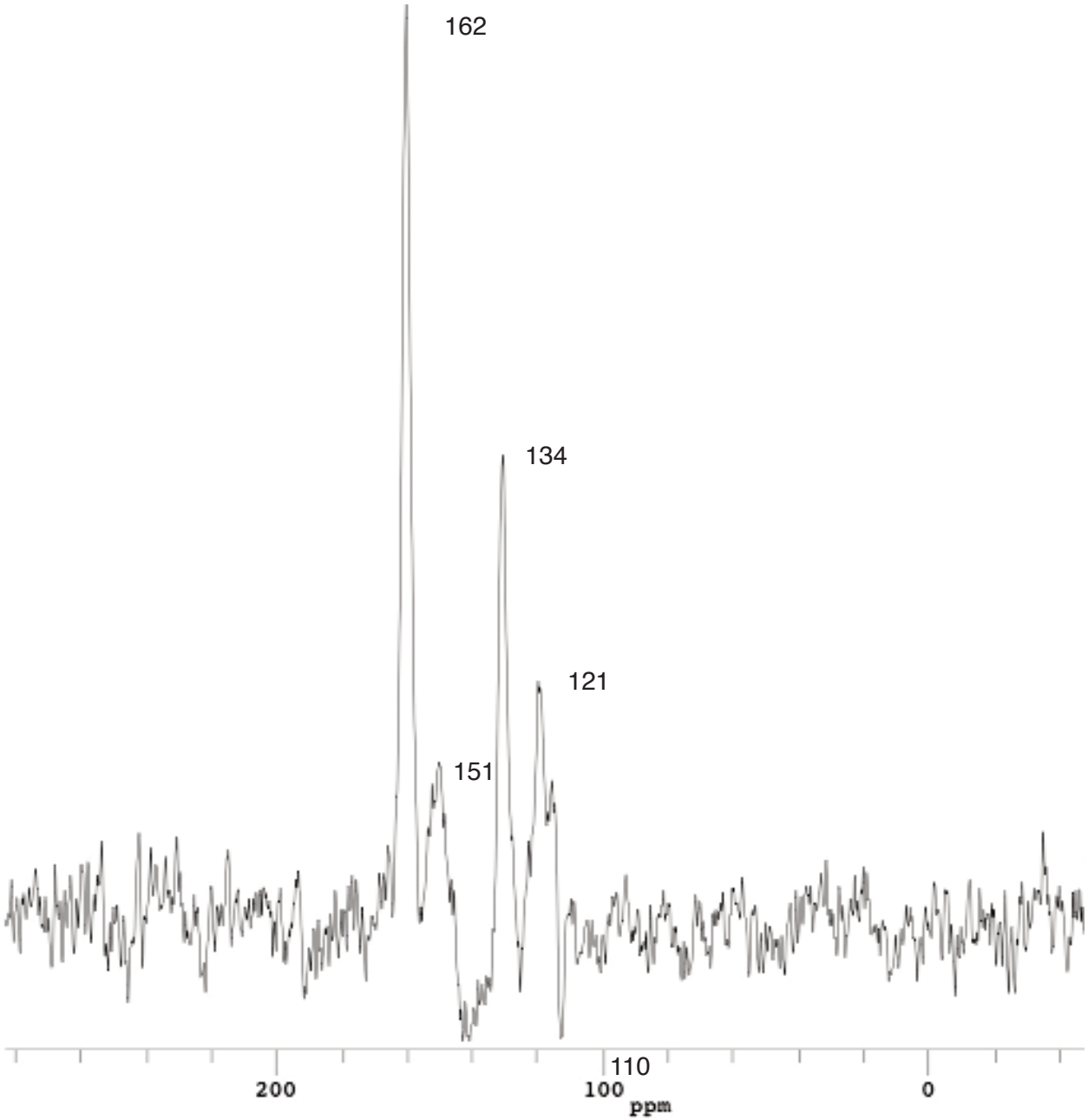

Figure 4.10c: RAMP-CP-PI spectrum with a 269μs negative contact time "B" (see Table 4.2).

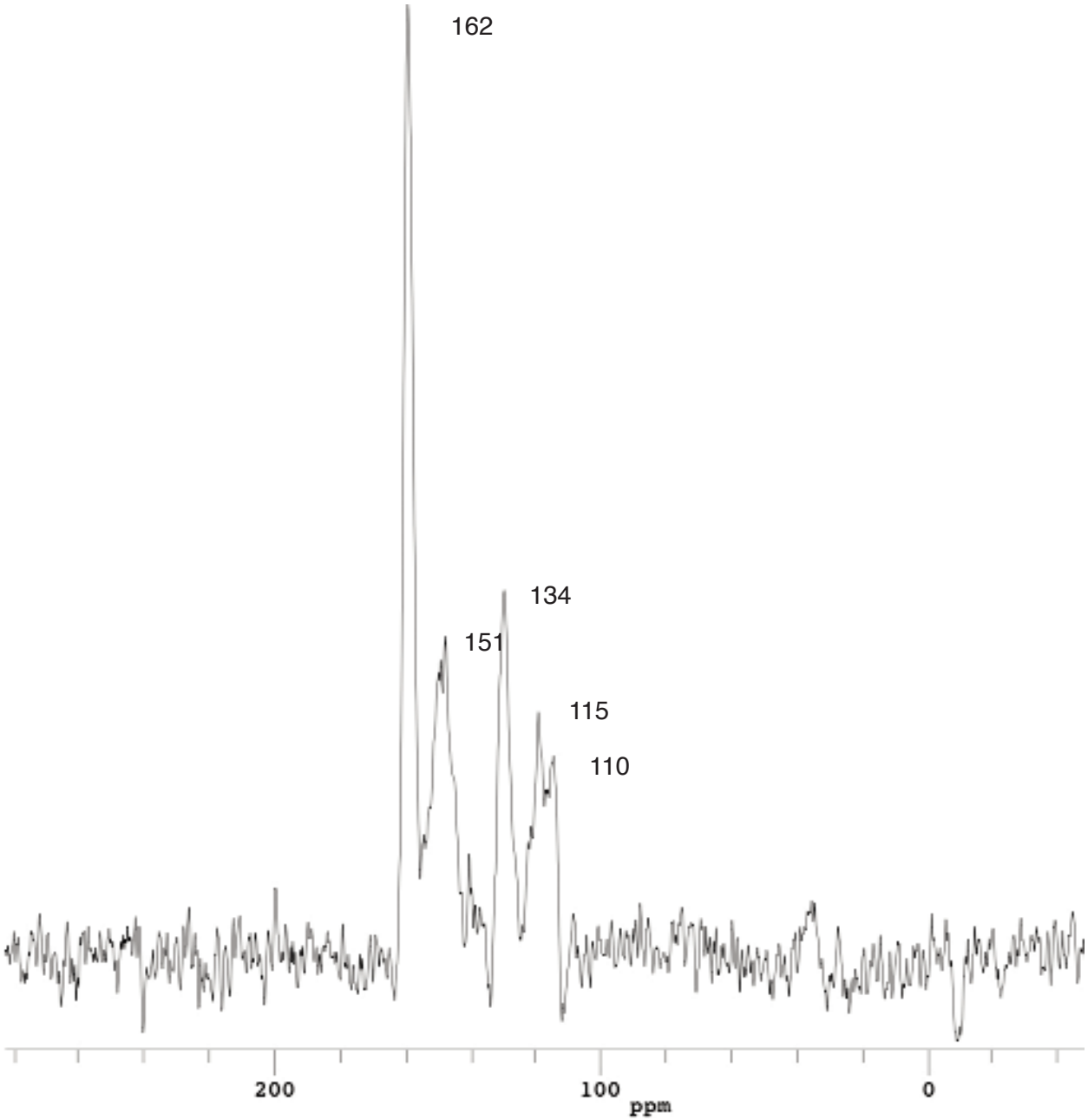

Figure 4.10d: RAMP-CP-PI spectrum with a 500μs negative contact time "C" (see Table 4.2).

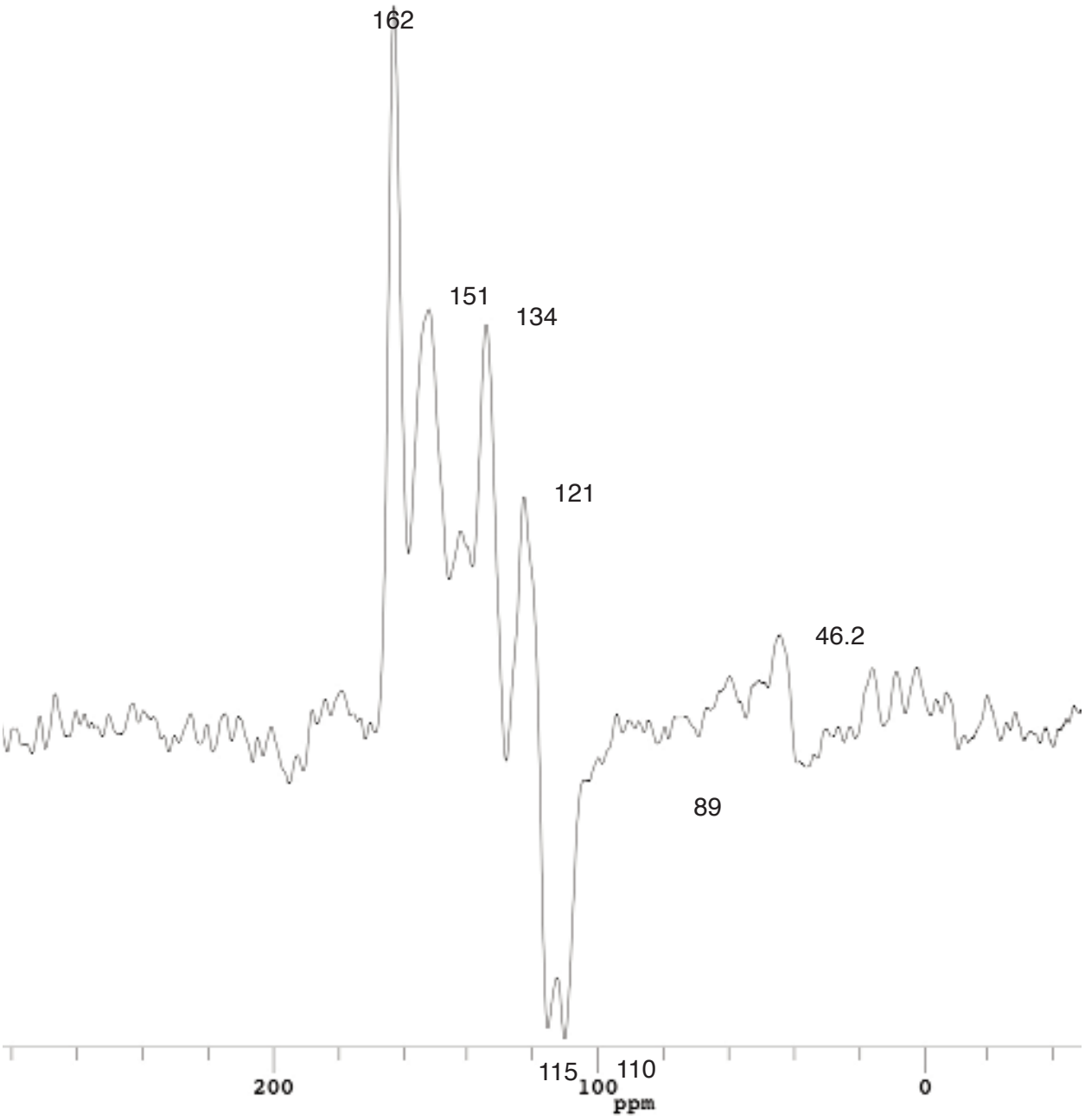

Figure 4.10e: RAMP-CP-PI spectrum with a 1ms negative contact time "D" (see Table 4.2).

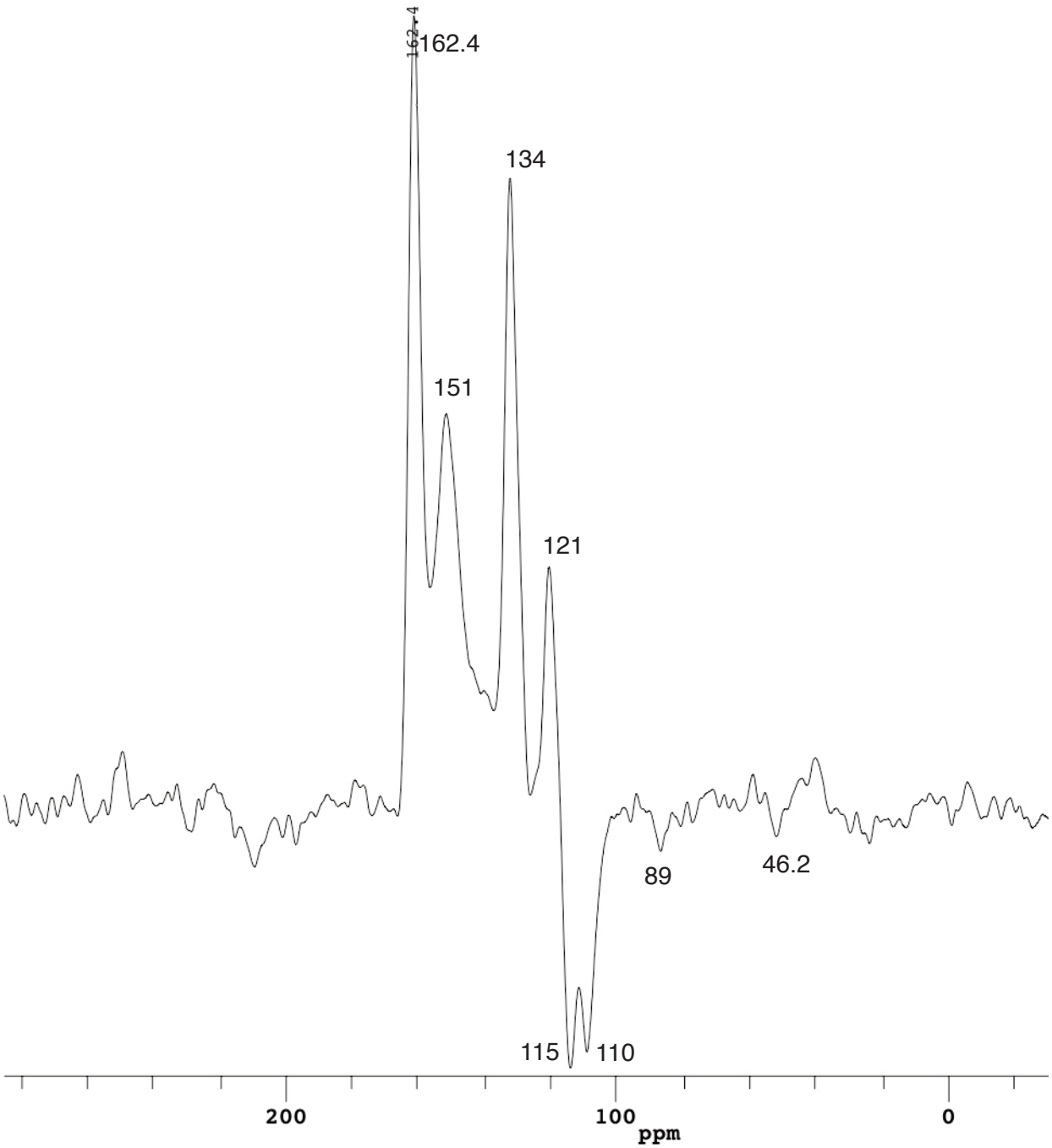

Figure 4.10f: RAMP-CP-PI spectrum with a 1.25ms negative contact time "E" (see Table 4.2).

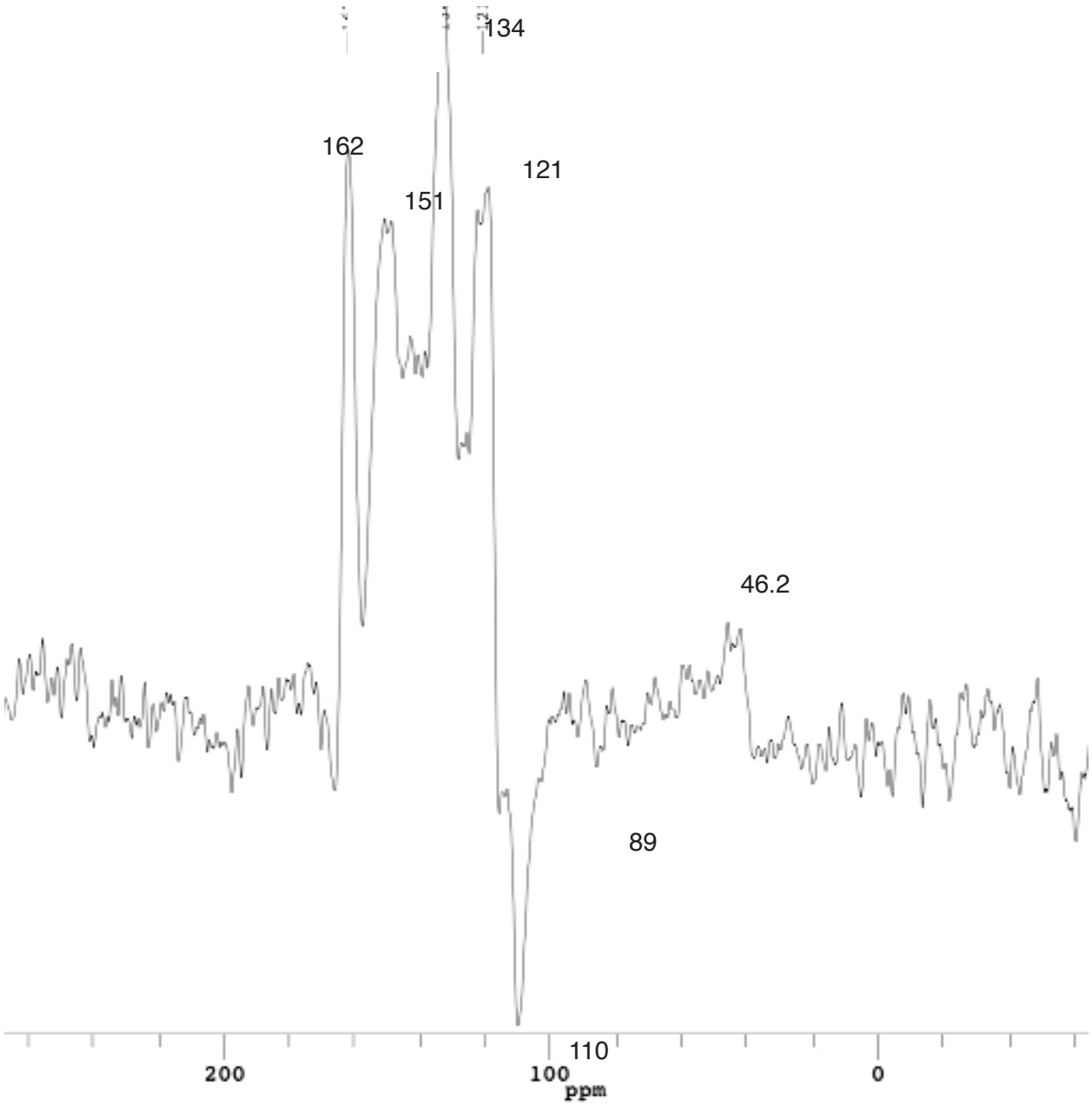

Figure 4.10g: RAMP-CP-PI spectrum with a 2ms negative contact time "F" (see Table 4.2).

Figure 4.10b-g depict six spectra of PIDA polymerized with the 1•3 bis (pyridyl) oxalamide. Tables 4.2 and 4.3 tabulate the results that variable contact time in the RAMP-CP-PI pulse sequence had on HMB and PIDA, respectively. Refer to Table 3 as a legend for each of the six spectra in Figure 4.10 b-g; labeling in Table 4.3 (a-f) corresponds to Figure 4.10 (b-g).

4.4 Discussion

The critical issue discovered when using RAMP-CP-PI was that both positive and negative contact times for the spectra had a logical and substantial effect on the signal-to-noise ratio (see Table 4.2). What was less clear is why the negative contact time duration appears to have a more profound effect on controlling the amplitude and inversion of the peak.

Contact time can roughly be equated to the measure d^{-2} of the heteronuclear dipolar interaction, where d is the magnitude of the length. It is approximately proportional to r^{-6}, since dipolar interactions for each nucleus varies as r^{-3}. Combined with the phase of the $\pi/2$ pulse, the peak(s) in question to invert (or be suppressed due to saturation); peak resolution can be, therefore, a function of both positive and negative contact times. For through-space interactions, the negative contact values appear to become more important. An good example of the sensitivity and response of the positive and negative contact times as well as their interdependence is found in Table 2, above, for HMB.

4.4.1 Chemical Shift Assignment

In the monomer and polymer, the execution of these experiments was more difficult, because 1) the oxalamide ^{13}C peaks and spinning side bands had partially overlapped the monomer and polymer ones. 2) no protons are directly bound so (+/-) contact times needed to be more precise, again owing to the r^{-3} dependence. Further, the paucity of sample due to the extreme synthesis conditions, the inherently low density of the sample and the desire for a high spinning speed made optimization challenging. Nevertheless, Figures 4.10b-g do appear to reflect adequate control over the carbon spins, such that the β and α carbon peaks at 110 and 89 ppm (red arrows, Figure 4.10a), respectively, are invertible.

Consistent with the greater presumed distances to the nearest protons, longer negative contact times were needed to segregate α carbon from the other spins (see Figures 4.10b-g and Table 4.3, 89 ppm). Also consistent with the α carbon being bound to the iodine substituent, a review of the values of Table 2 confirms the extremely narrow window where some spectral editing was available to the α carbon. The relative insensitivity of the α carbon to cross polarization/inversion appears to be reflected in the narrow negative-contact-time range in which the peak could be inverted (see Figure 4.10f). The fact that it is in a low-symmetry environment and covalently bound to the iodine, a 100% abundant, |5/2> nucleus with a relatively large quadrupolar moment (-696 Q/millibarn), among the larger of the spin-active isotopes (^{59}Co = 420; ^{197}Au = 547; ^{181}Ta = 3170)), likely interferes with cross polarization transfer from proton, presumably due to the extremely strong dipolar coupling between the iodine and the α carbon to which it is bound. The Larmor frequency is far enough away from iodine (~72Mhz v. 90.5Mhz @ 360Mhz B_0), however, so as to not be directly influenced by the RAMP field strength, being that the step sizes and number of steps were not large.

Chemical shift assignment of the respective pyridinyl carbons on the 1•3 oxalamide is significantly similar to both liquid and sorbed solid pyridine found by SPE on ^{13}C directly, as well as {^{1}H}^{13}C CPMAS, respectively[30,31]. Although no literature could be found that directly probed 1-3-bispyridyl oxalamide, ^{13}C chemical shifts for carbons 2-4 as reported by Parhami were 149ppm, 123ppm and 135ppm, respectively[30]. The magnetically inequivalent carbons on the oxalamide necessitate additional peaks. All five appear evident with the spectral editing techniques employed here (see Figure 4.10c,e,f). The most likely chemical shift assignments for the carbons *meta* to the nitrogen on the pyridine ring are 121 and 115ppm for the carbon (carbon 3) leading to the oxalamide moiety. The proximity of the methylene protons proximal to this carbon likely also contribute to the responsiveness to different (-) contact times, as evident in Table 4.2.

The fact that the β carbon is not directly bound to iodine apparently makes the β carbon (110ppm) more susceptible to cross polarization by proximal protons. Its amplitude makes it easier to visualize and, therefore, a more confident determination of its chemical shift assignment as part of the PIDA backbone. The longer contact times are shared by the α carbon, making the assignment more concrete.

One unexplained event appears to be a second peak at 115ppm, closely positioned to the peak at 110 ppm. It does not appear to be a splitting of the peak at 110ppm, since the splitting of the β carbon peak due to either dipolar competition between proton and iodine, or splitting due to the iodine interaction itself would have the same behavior as the peak at 110ppm. Figures 14-16 demonstrate the peak at 115ppm and its apparent parallel behavior with the peak at 110ppm, yet Figures 4.10c and 4.10d appear do demonstrate the differences, as a function of negative contact time. Furthermore, it appears to be conclusively *not* associated with the lowest pyridyl peak at 121ppm, again due to the differences induced by the different negative contact times.

It is unfortunate that a much more thorough investigation of $T_{1\rho}{}^{I}$, $T_{1\rho}{}^{S}$, and T_{IS} magnetization transfer curves as a function of variable *negative* contact times was not able to be conducted during these experiments. Because dipolar coupling dependent upon the r^{-3} internuclear vector, plotting and fitting of these parameters have been used for many years as an accurate determination of internuclear distances using classic CP/MAS, TORQUE, DRAMA, MELODRAMA and other pulse sequences. Wilhelm and Luo did not report the changes in interatomic distances post-polymerization[3,4]. As indicated previously, when investigating spin-active isotopes where the total spectral window is small, as in the case of ^{13}C, ^{1}H, and the likelihood of spinning sidebands is high due to strong heteronuclear and homonuclear dipolar coupling, a technique like this which can readily segregate a specific peak in an otherwise crowded spectrum and allow discrete work on each spin could prove very powerful investigative tool.

Furthermore, in species like this, it may sometimes be the case that, due to complex internuclear dynamics, $T_{1\rho}^{I}$, $T_{1\rho}^{S}$, and T_{IS} may exhibit more investigatively demanding behavior, particularly if the aforementioned do not conform to the relationships typical between the three[13]. Also of potentially solid academic interest would be the construction of a density-matrix manifold, similar to the one constructed for 2D Separated Local Field (SLF) polarization inversion experiments and used to detect smaller dipolar couplings between nuclei[14].

4.5 Conclusion

The testing and experiments performed on a model compound, hexamethylbenzene (HMB, see figure 17, Table 2) conclusively demonstrate that successive RAMP-CP pulses can also be used in conjunction with polarization inversion. Since Zilm, et al. used CPMAS and not VACP, or RAMP-CP, nor has any reference been found in the literature for this modest combination of pulsing techniques, this apparently first attempt at combining these pulse sequences (i.e., incorporating the variable-amplitude step system as well as adding the phase inversions plus correct phase-cycling) yielded positive, reproducible results.

The profound deficit of this investigation into the PIDA sample is the absence of the $T_{1\rho}^{I}$, $T_{1\rho}^{S}$, and T_{IS} data, which would have not only determined the internuclear distances for the polymerized species, but provided a more solid theoretical foundation for M_{CP}, during Polarization Inversion. Nevertheless, RAMP-CP-PI appears to have concrete use as an investigation technique for challenging samples. Chemical shift confirmation was facilitated by having such precise control over the various carbons present in the PIDA/1•3 sample.

4.6 References

1) Boyd, R.W. Nonlinear Optics. Academic Press; 3 edition. 2008.

2) Prasad, P.N., Williams, D.J. Introduction to Nonlinear Optical Effects in Molecules and Polymers. John Wiley, New York, (1991)

3) Wilhelm, C., Boyd, S. A., Chawda, S., Fowler, F. W., Goroff, N. S., Halada, G. P., Grey, C. P., Lauher, J. W., Luo, L., Martin, C. D., Parise, J. B., Tarabrella, C., Webb, J. A. *J. Am. Chem. Soc* 130, (2008)

4. Luo, L., Wilhelm, C., Sun, A., Grey, C. P., Joseph W. Lauher, J. W., Goroff, N. S. *J. Am. Chem. Soc*. 130 (2008)

5 Schaefer, J., Stejskal, E.O. *J. Am. Chem. Soc*. 1976, 1032-1033.

6 Evans, M.W. The Photon's Magnetic Field: Optical NMR Spectroscopy. World Scientific Publshing Co. Pte. Ltd. Singapore. 1992. ISBN: 981-02-1265-8

7) Kresin, V.V; Bonin, K.D. Electric-dipole Polarizabilities of Atoms Molecules and Clusters. World Scientific Publshing Co. Pte. Ltd. Singapore. 1997. ISBN: 981-02-2493-1

8) Wu, X., Zilm, K.W., *J. Mag. Res. A*. 104 1043 (1993).

9) Peerson, O. B. ; Wu, X., Kustanovich I., Smith S. O. *J. Mag. Res. A*. 104 334-339 (1993)

10) Metz, G., X. Wu, X., Smith, S. O. *J. Mag. Res. A* 110 219-227 (1994)

11) Wu, X., Burns, S.T., Zilm, K.W., *J. Mag. Res. A* 111, 29-36, (1994)

12) M.T. Melchior, 22nd Experimental NMR Conference, Poster B-29, Asilomar, CA, 1981.

13) Klur, I., Jacquinot, J. F., Brunet, F., Charpenteir, T., Virlet, J., Schneider, C., Tekley, P. *J. Phys. Chem. B*, 104 (2000)

14) Sinha, N., Ramanathan, K.V., *Chem. Phys. Lett*. 332 (2000)

15) Barentsen, H. M., Van Dijk, M., Zuilhof, H., Sudhölter, E. J. R. *Macromolecules* 33 (2000) *Macromolecules*, 33, 766–774 (2000)

16) Yang, Y., Lu, Y., Lu, M., Huang, J., Haddad, R., Gazeau, S., Xomeritakis, G., Liu, N.; Malanoski, A. P., Sturmayr, D., Fan, H., Sasaki, D. Y.; Assink, R. A., Shelnutt, J. A., van Swol, F., Lopez, G. P.; Burns, A. R., Brinker, C. J. *J. Am. Chem. Soc*. 125 (2003)

17) Lu, Y.,Yang, Y., Sellinger, A., Lu, M., Huang, J., Fan, H., Haddad, R., Lopez, G., Burns, A.R., Sasaki, D. Y., Shelnutt, J., Brinker, C. J. *Nature* 410, 913-917 (2001)

18) Koehorst, R. B. M., Fokkink, R.G., Stuart, M. C., Zuilhof, H., Sudhölter, E. J. R. *Macromolecules* 35 (2002)

19) Kolodziejski, W., Klinowski, J. *Chem. Rev.* 102 (2002)

21) Li, Q., Zhou, H., Wicks, D. A., Hoyle, C. E. *J. Polym. Sci. A: Polym. Chem*. 45 (2007) *J. Poly. Sci. A: Poly. Chem*. 45, 1-15 (2007)

22) Hartmann, S.R., Hahn, E.L. *Phys. Rev*. 128, 2042-2054 (1962)

23) Kopple, K.D., Wang, Y. S., Cheng, A. G., Bhandary, K. K. *J. Am. Chem. Soc*., 110 (1988)

24) Bovey, F.A. and Mirau, P.A. NMR of Polymers, Academic Press, 81 - 83 (1996).

25) Klur, I,. et al. *J. Phys. Chem. B* 104, (2000)

26) Tamaoki, N., Shimada, S., Okada, Y., Belaissaoui, A., Kruk, G., Yase, K., Matsuda, H. *Langmuir* 16 (2000)

27) He, Z.; Kispert, L. D. *J. Phys. Chem. B* 103 (1999)

28) Savenije, T.J., Warman, J. M.; Barentsen, H. M.;Van Dijk, M.; Zuilhof, H.; Sudhölter, E. J. R. *Macromolecules* 33 (2000)

29) Park, N. K., Kang, D. K., Kim, B. H., Jo, S. J., Ha, J. S. *Appl. Surf. Sci*. 252 (2006)

30) Parhami, P., Fung, B. M. *J. Am. Chem. Soc*. 107 (1985)

31) Dawson, W.H., Kaiser, S.N., Ellis, P.D., Inners, R.R. *J. Phys. Chem*., 86 (1982)

Chapter 5

A ^{19}F MAS NMR Investigation into the Mechanisms of Ionic Conductivity of Calcium Fluoride/Barium Fluoride Heterostructures Deposited via Molecular Beam Epitaxy

Abstract

Variable-temperature, magic-angle spinning nuclear magnetic resonance (MAS NMR) was used to investigate the microscopic and motional environments present in a calcium fluoride/barium fluoride (CaF_2/BaF_2) heterostructure. The heterostructure, comprising 20nm alternating layers (to 1μm; the interior of the layers hereafter referred to as the *bulk*, was grown on single crystal Al_2O_3 (1101 orientation) using Molecular Beam Epitaxy (MBE) by the Maier Group at the Max Planck Institut für Festkörperforschung. Based on ^{19}F MAS NMR chemical shifts, T_1 and T_2 times recorded during this investigation, several species within the samples (with ^{19}F chemical shifts of -4.4ppm, -121.7ppm, -141ppm) have far greater mobility and are chemically distinct from the fluorine chemical shifts associated with bulk CaF_2 and BaF_2 or, for a non-stoichiometric solution of both compounds. Peaks associated with the bulk CaF_2/BaF_2 species exhibit no changes in T_2 times as a function of temperature in the regime investigated here,X or in comparison to the bulk, yet the species that give rise to these signals are slightly more mobile than pure, polycrystalline (~5μm particle size) CaF_2 or BaF_2, based on respective T_1 times. The mobile species with the chemical shifts listed above are not consistent with the space-charge model, since it appears that these mobile species do not occur as a result of the chemical potential differences (and, therefore, defect/vacancy production as a result). The peaks associated with these mobile species disappeared, however, upon prolonged heating (~240°C for ~35h) and the changes were irreversible.

5.1 Introduction

Ionic conductivity in solids has increasingly attracted much investigational research in recent years, not only for its practical applications, but for the advantages provided by increased understanding underlying the mechanisms for ionic transport[8]. Many different methods are being investigated to enhance the ionic conductivities of a broad range of materials in the search for commercially applicable alternative energy systems such as solid-oxide fuel cells[8,9,10,11].

Oxygen sensors, solid-oxide fuel cells and proton-exchange membrane fuel cells rely on high ionic conductivity ($>10^{-2} S \cdot cm^{-1}$) as the means for charge carrier transport, but the mechanisms underlying the exact nature of the conductivity are still poorly understood. Sata and Maier previously reported their data regarding BaF_2/CaF_2 layered heterostructures, prepared by molecular beam epitaxy (MBE)[5,6]. Most notably, they reported enhanced ionic conductivity of BaF_2/CaF_2 parallel to the interlayer interfaces when the materials are prepared by MBE. They proposed a space-charge theory to explain the unusually high ionic conductivity found by the authors ($10^{-1} S \cdot cm^{-1}$)[5,6,7]. The aim of the experiments reported here is to explore and better understand how the heterostructures exhibit such increased conductivity, as reported by Sata, et al., and gain insight into whether the space-charge model as a paradigm of ionic conductivity is consistent with these findings[5,6].

5.1.1 Space-charge Model Basics Explained

One possible mechanism for ionic conductivity in vacancy-laden crystals first proffered Schottky was the space-charge model[1]. The space-charge model begins from the premise that an electrostatic potential (V) exists between some object within the bulk of the crystal and the surface of the crystal (where x is the distance to the surface, in the simplest, one-dimensional case).

In the simplest model profferred by Lehovec [2], heats of reaction for each of four objects (interstitial anions, cations, and cationic/anionic vacancies) can be measured, along with their relative electrostatic potentials, and the total can be assessed on a per-object basis for the ith object in question $(N_i)^2$:

$$N_i = aZexp[(-u_i \pm eV)/kT] \quad 5.1$$

where a is some scalar, Z is the molecular number of atoms per unit cell, u_i is the heat of reaction, e is the unit charge, V is the electrostatic potential and the system is kT-dependent; the sign is both directionally and charge dependent. The sign is positive for a cation passing from the surface to an interstitial and negative for the reverse; the converse applies for anions and related vacancies[3]. A tally of these four objects (cations, anions, vacancies and interstitials: N_c, N_a, N_v, N_i) allows the calculation of a density, r, as the following:

$$\rho = e(N_c - N_a - N_v + N_i) \quad 5.2$$

Since potential varies as a function of distance, x, as defined above, the highest ionic conductivity will occur in the region nearer the surface. Knowing that a non-zero electrostatic potential exists from, for example, the position of one of the four objects listed above and the surface (where a zero potential is assumed to exist) an integrated total of electrostatic potential can then be calculated for all of the defects present.

In this model, a non-zero gradient can then exist, which is dependent on V(x), where x is the distance from the surface of the crystal to the crystallographic site and V is the potential. The space-charge region, therefore, is some region near the surface of the crystal where the electrostatic potential of these species can be overcome by a gradient of some sort for ionic conductivity to occur.

If x, as defined above, is a measure of the distance of the *ith* object (one of the four choices listed above) from the surface of a material; a concentration of defects as a function of that length can be measured in parallel. This length, called the Debye length (nλ, see Figure 5.3, below), is characteristic for a particular material and can be broken down into chemical (chemical potential, μ^0, or ΔG^0) and electrical components (eV, as seen in eq. 5.1 above and 5.3 below, as electrical potential, Φ), combined into the terms below:

$$\mu_T = \mu_j^0(x) + RTln(N_i) + z_j F\Phi(x) \qquad 5.3$$

Equation 3 above is not strictly correct, since standard chemical potentials are independent of length. The exception to this can be made in the case of the interface, as studied here: at the interface between two dissimilar materials, the chemical and electrical components that comprise their respective Debye lengths differ in magnitude and, therefore, are assumed to contribute to either a stabilizing effect for the complementary material, or a destabilizing effect in this model[7]. As such, the chemical potential for the *ith* object can be thought of as having its own standard potential as a function of position, relative to the interface (eg x = 0)[7]. If the Debye lengths of the two materials are different, then a "defect gradient" is thought to be induced which may account for the increased ionic conductivities found in layered systems such as those reported in this chapter. So for example, in a binary system like the one studied here, a fluoride ion will move from one material to the other, in accordance with the potential gradient described above. This migration results in the creation of an interstitial in one material (or layer) and a vacancy in another. This process will occur until the chemical potential of the two materials at the interface is equal. This process is directly analogous to a p—n junction, the only difference being the electronic gradient along the Debye length and corresponding circuit loop, rather than the ionic one as described here. The challenge now is to identify whether this model is valid in the system studied in this system.

5.1.2 Previous Work

Extensive investigations have been conducted demonstrating high ionic conductivity observed in materials such as thin films, layering and epitaxially grown heterostructures[4,5,6,7,15,16,17,18]. The work done by Maier, et al., in [4,5,14] focus on epitaxially grown heterostructures because (see Figure 5.1 below) largely Arrhenius behavior

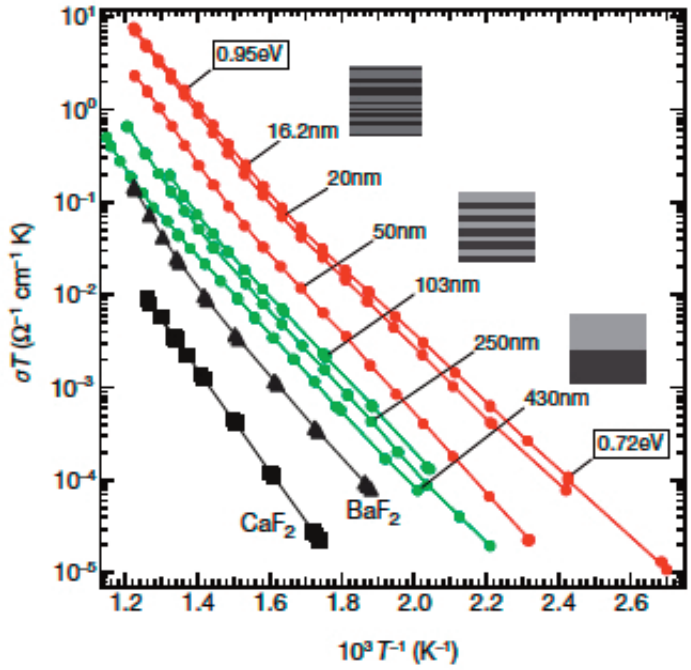

Figure 5.1: Graph (reprinted from [4]) depicting conductivity parallel to the interface as a function of temperature and layer thickness. Colors indicate semi-infinite space-charge zones (red) and finite space-charge zones (green) as compared against the bulk (black). The materials investigated in [4] were grown via MBE to a total thickness of ~500nm.

is found in these systems and a roughly linear correlative increase in conductivity is demonstrated with decreasing (inter)layer thickness. Furthermore, the conductivity demonstrated in these investigations occurred and was measured as parallel to the layer interface at rates greater than one would normally observe in simple, unary ionic conduction. The authors used AC Impedance Spectroscopy in [14] to determine ionic conductivity from 1 - 10^4Hz as a function of

temperature, from 540º - 100ºC, resulting in the graph shown in Figure 5.1.

The CaF_2 and BaF_2 layers were grown along the [111] direction using an MBE machine dedicated to fluoride parent compounds. The layers were grown on single-crystal Al_2O_3 (sapphire)

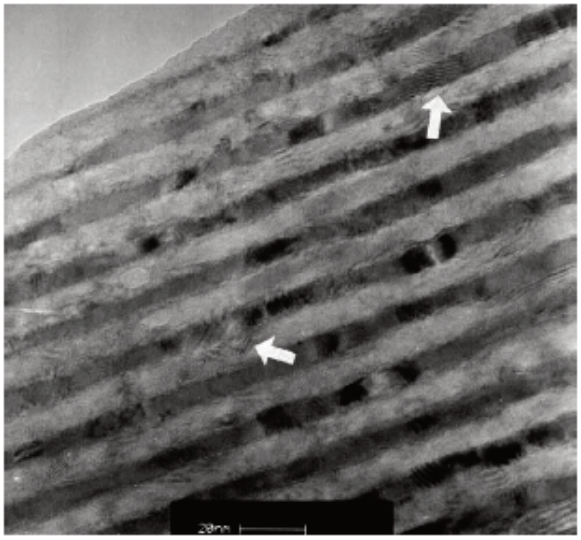

Figure 5.2: TEM of heterostructures (reproduced from [6]) with a period (interlayer thickness) of 18nm. Arrows indicate local distortions due to different lattice constants or different crystallographic orientations within individual layers.

oriented along [1011]. An example of the relatively clean growth that can be produced from MBE is represented in the TEM figure (Figure 5.2) above[6].

Although the space-charge model has been strongly suggested and purportedly supported by the many careful investigations by the authors highlighted here, some authors have offered other responsible factors on this controversial subject. Simple disorder due to lattice mismatch and resultant strain, combined with grain boundary effects are thought to be predominantly responsible for the high ionic conductivities exhibited by heterostructure systems (other than fluorides), because the Debye lengths in computational molecular dynamics and some empirical studies performed recently are dramatically shorter from those that would be estimated necessary to be able to offer high ionic conductivity due to space-charge effects[6,19,20,21].

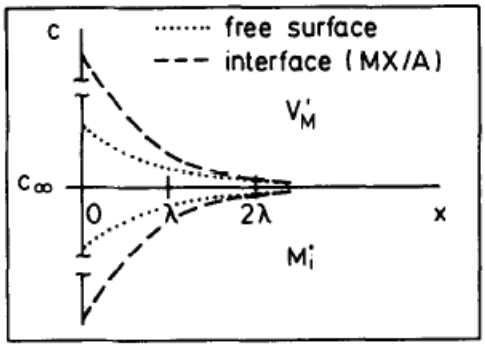

Figure 5.3: (reprinted from [7]): The Debye Length (nλ) as illustrated for cationic vacancies V'_M and cationic interstitials, M^+_I, for charge (c) and length into the bulk (eg lim $x \rightarrow \infty$).

5.1.3 NMR Studies of Transport: the role of T_1 in assessing ionic mobility

For the studies described in this chapter, MAS NMR is relied upon as a modality, most specifically because of the utility of the T_1 time, also known as the spin-lattice relaxation time. Use of T_1 is the standard for determining species mobility in a system. We now explain some background information regarding the origin of T_1 and its suitability in examining species mobility.

The T_1 time, also known as the spin-lattice relaxation time, is a measure of how quickly the spin-magnetization vector, initially perturbed from its equilibrium magnetization into the x—y plane by an electromagnetic pulse, relaxes back to its original position, precessing around the z-axis of the strong magnetic field of the device. Motion results in a fluctuating local magnetic field; formula 5.4a (below) reflects the appropriate mathematical structure when fluctuating fields dominate relaxation effects. If local fluctuations occur close to ω_0 or $2\omega_0$, then it is this spectral density of the oscillating field that causes relaxation. While motion does not explicitly denote vectorial transport, T_1 times and associated parameters do give a measure of how mobile a species is at least locally which, since mobility is a precursor for translational motion, may be an indicator in many (but not all) for long-range motion.

$$\frac{1}{T_1} = \frac{6}{5}\frac{1}{M_{II}}\left[\frac{\tau_c}{1+\omega_0^2\tau_c^2} + \frac{4\tau_c}{1+4\omega_0^2\tau_c^2}\right] \quad 5.4a$$

where the second moment ($M_{(II)}$) is defined as in (4b), below:

$$M_{II} = \frac{3}{5}\left(\frac{\mu_0}{4\pi}\right)^2 \gamma_I^4 \hbar^2 I(I+1)\sum_{i,j}\frac{1}{r_{ij}^6} \quad 5.4b$$

using the following values for the respective fluorides:

$M_{2CaF^2(111)}$: 1.37×10^9 s^{-2}
$M_{2BaF^2(111)}$: 7.72×10^8 s^{-2}

$$\sigma \frac{k_B T}{Nq^2} H_R = D^T \quad 5.5$$

$$\tau^{-1}\frac{r^2}{6} f = D^T \quad 5.6$$

terms:

ω_0	= Larmor frequency*2π
τ_c	= correlation time
γ_I	= gyromagnetic ratio
μ_0	= magnetic permeability
r_{ij}	= internuclear distance
I	= dipole spin value (I1/2>)
σ	= conductivity
N	= charge carrier density
H_R	= Haven ratio
t^{-1}	= hopping frequency (correlation time^{-1})
f	= correlation factor
r	= F— F interatomic radius
q	= charge
k_B	= Boltzmann's Constant
D^T	= Diffusivity

Formula 5.4b, above, demonstrates the role that the interaction of spin with the lattice plays in overall nuclear spin relaxation for a system dominated by homonuclear dipolar couplings between spins.

Equations 5.5, 5.6 (5.6 being the Einstein-Smoluchowski relation) were used to calculate conductivity. This is because the correlation time, τ, is well-suited to calculate diffusion.

In turn, the derived diffusion can then be used to determine conductivity, s, as the conductivity in question is for charged particles. It was this original motivation, conductivity of charged particles, that led to the development of this relationship and the accompanying equations[28].

Here, the second moment was obtained from the literature for each species (CaF_2, BaF_2) being [111] oriented relative to the magnetic field[26,27]. In a sample of a single crystal, the atomic positions are all fixed, relative to one another, so the Second Moment varies with sample orientation. Thus, the value corresponding to the [111] orientation of the single crystal materials (BaF_2, CaF_2) was chosen, since this corresponds to the experimental design used here. See formulae 5.2-5.6 in the section above as well as the M_{II} values which appear below formula 5.4b.

5.2 Experimental

5.2.1 Sample Preparation

The heterostructures investigated in this chapter were provided to us by the Maier Group working at the Max Planck Institut für Festkörperforschung. The heterostructures (see Figure 5.2.1, below) were grown to a total thickness of 1μm and each layer of either BaF_2 or CaF_2 were grown to a thickness of 20nm. The initial preparation and cutting for the heterostructures proved challenging, given the density of the materials as well as the delicate, single-crystal nature of the layers and substrate. The wafers were then cutinto small circular discs matching the inner diameter (≤0.1mm) of the MAS NMR rotor.

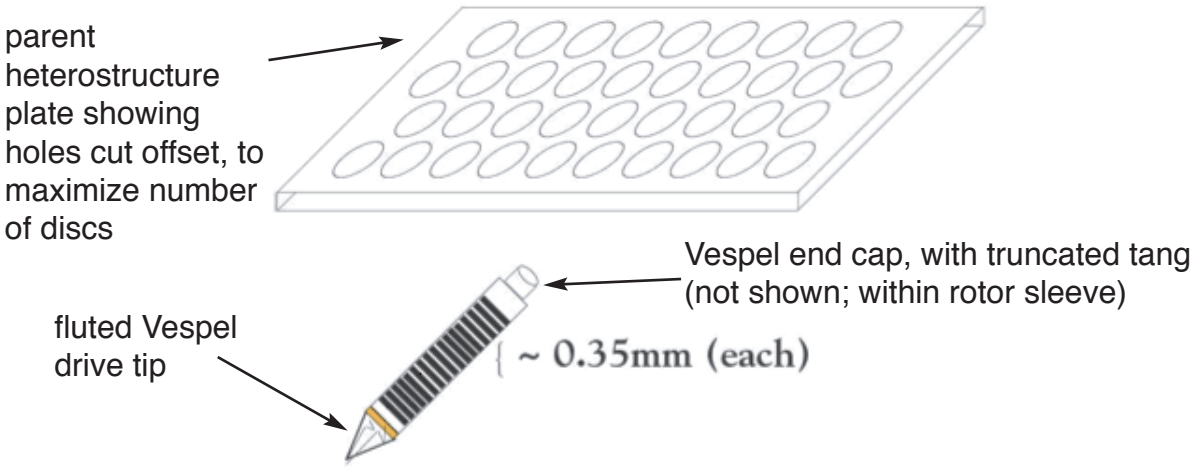

Figure 5.2.1: Graphical depiction of the MAS NMR rotor, packed with sanded, cut discs with Al_2O_3 almost completely removed, in order to maximize the insertable number of discs.

The discs had to be uniform in circumferential cut and inserted perfectly normal to the walls of the MAS NMR rotor. This ensures that they could be effectively spun at reasonable spinning speeds (11-14kHz) and without inducing wobble due to competing moments of inertia for improperly inserted individual discs.

A maximum number of discs was calculated to be inserted to safely achieve as high a signal-to-noise ratio as possible. As such, the tang of a Vespel end cap was cut back on a standard Bridgeport lathe as much as was considered safely possible, so as to fit 14 discs into the zirconia rotor. Vespel™ is the trademark name for a commercially available hemiacetal polymer, used in cases like this where zero fluorine background is required.

As much of the Al_2O_3 substrate as reasonably fit was removed via stationary belt sander, without compromising the integrity of each disc or the first, deposited BaF_2 layer.

The heterostructures (1cmx3cmx1mm transparent plates; see Figure 5.2.1, above) were carefully adhered (Al_2O_3 face down) to a milled, depressed aluminum surface (a "boat") with a heat-activated glue (Aremco Products, Cottage Valley, NY), such that the glue would liquefy if the temperature exceeded 100ºC. A diamond-carbide, hollow core drill bit (Aremco Products, Cottage Valley, NY) with an inner diameter which corresponded to the inner diameter of the 4mm rotors used in the NMR probe was inserted into a Bridgeport computer/numerically controlled (CNC) milling machine and spun at 440rpm.

Exact (±0.1mm) (x, y, z) coordinates were then entered to bore through the heterostructures to optimize the number of discs per unit surface area. The resultant discs or wafers were cut under continuous flood to minimize heat buildup. The flood liquid is a mixture of mineral oil and water.

After the wafers were cut, the aluminum plate to which they were adhered was gently heated on a hotplate until the heat-activated glue liquefied (approximately 110ºC). The wafers were then retrieved and triple washed in acetone. Each wafer was individually inspected under low-power microscopy, and any wafers that exhibited chipping or kerfing were rejected.

The Al_2O_3 side of each wafer was then adhered to the tip of a tool machined to the proper rotor inner diameter (0.094" = 2.38mm). The tool with one disc was then placed in a metal lathe and rotated at approximately 60 rpm and carefully hand-sanded so that each wafer was circular and the correct diameter.

The process was repeated until all of the discs created fit snugly into the NMR rotor (so as to prevent wafer rotation while the rotor spun).

5.2.2 MAS NMR

Fourteen discs cut from the original wafer were packed into 4mm zirconia rotor with fluorine-free Vespel drive tip and Vespel end cap, using a Varian/Chemagnetics 4mm probe. All experiments were run on a Varian, Infinity Plus spectrometer in a 500MHz (11.74 Tesla) magnetic field using Chemagnetics Spinsight (Spinsight v.4.3.2) software. Single-pulse and Hahn-echo experiments were performed using neat $CFCl_3$ (0 ppm) as a standard external chemical shift reference for fluorine. A $\pi/2$ time of 4μs (62.5kHz) was determined for fluorine. A 4mm rotor, prepacked with potassium bromide (KBr), was used to set the magic angle. All samples were spun at 14kHz and 4896 scans were taken. Spectra were recorded using single-pulse excitation (SPE) at STP (25°C, 1ATM), 100ºC, 200ºC and 240ºC.

5.3 Results

Unless otherwise noted, 4896 scans were recorded during each experiment with a pulse delay of 45s in between scans (due to the long T_1 times of the bulk species). Each spectrum took approximately 61 hours to record.

The initial ^{19}F MAS NMR spectra appear below (Figures 5.1 - 5.4). In the wafers, the peaks due to CaF_2 and BaF_2 are clearly observed at their typical chemical shifts (-13ppm: BaF_2; -109ppm: CaF_2). These peaks are associated with spinning sidebands, indicating

that the ions giving rise to the resonances are rigid on the timescale of the of the dipole's coupling value. Unexpected, additional peaks are seen in Figures 5.4-5.6 upshifted and downshifted from the peaks associated with bulk BaF_2 and CaF_2, respectively. As will be evident in Figures 5.4-5.7 (see "truncation" in Figure 5.4, below), the spectra were truncated so as to to better visualize the weaker signals more clearly.

One way of determining motion is by measuring the rate at which an NMR signal grows to its maximum using a series of spectra, differing by the span between scans, as depicted in Figure 5.8. This 'pulse delay' is another effective way of measuring T_1 times for the species. Since NMR spectra are quantitative, based on the number of spins in a given local environment, how quickly or slowly those spins relax back to being aligned with the magnetic field, B_0, can be quantified. The primary driver for this relaxation lies in the T_1, explained above (see section *5.1.3: NMR Studies of Transport: the role of T_1 in assessing ionic mobility)*.

An illustrative, quantitative example of the increase in peak intensity as a function of T_1 (via the effective proxy of a pulse delay) is depicted in Figure 5.8 using single pulse spectra. The integrated areas under the peaks shown in Figure 5.8 are tabulated in Table 5.2. What is visually apparent are the differences in T_1 times for the ions associated with each peak intensity. The peaks associated with shorter relaxation are those that have reached their maximum heights in Figure 5.5 (-4.4, -121, -141ppm) in comparison to the signals associated with the bulk (-13, -109ppm). Complementarily, it may be more apparent that the signals associated with the bulk BaF_2 and CaF_2 take an extremely long time to maximize.

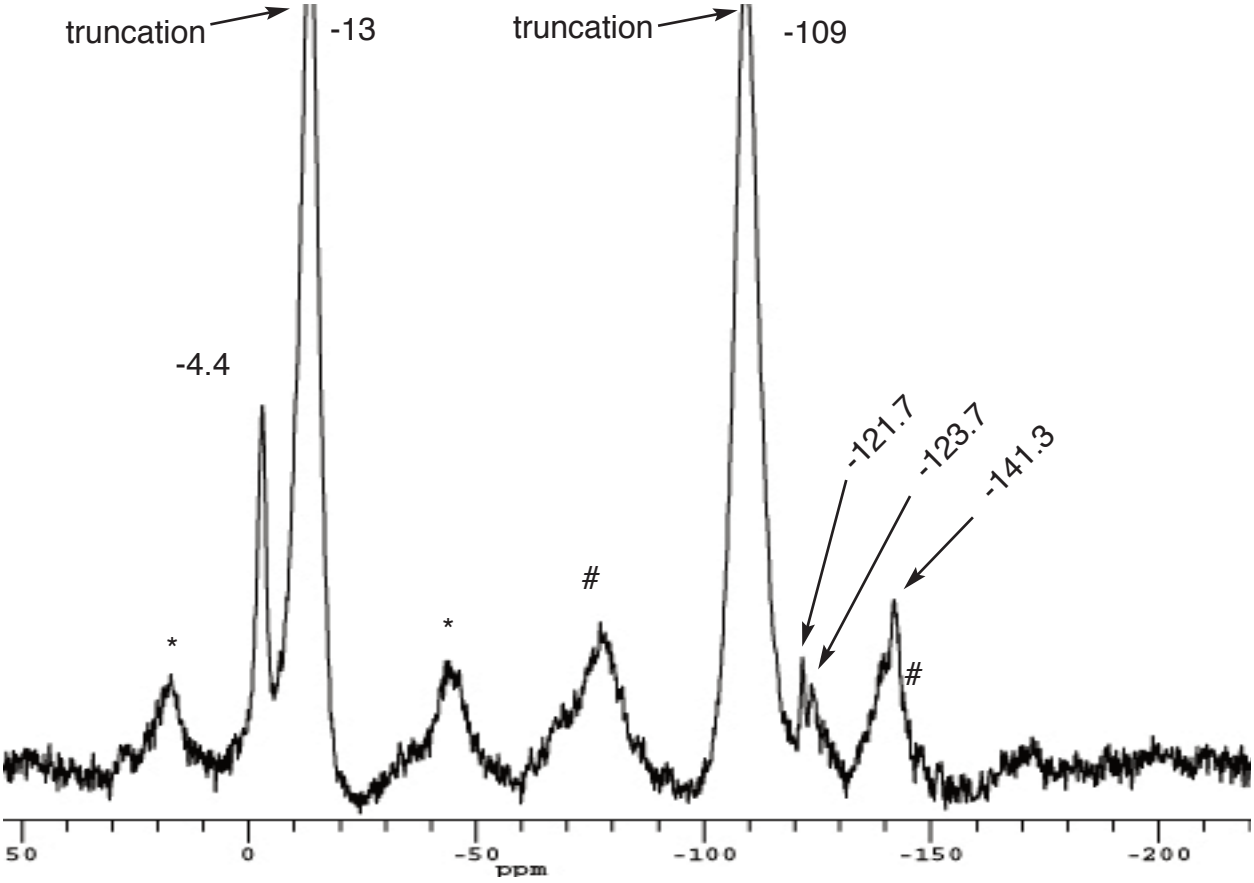

Figure 5.4: MAS NMR spectrum of BaF_2/CaF_2 heterostructures taken at room temperature (RT). The * and # symbols depict spinning side bands of BaF_2, CaF_2, respectively. The spectrum was acquired with a one-pulse sequence with a 45s pulse delay between scans.

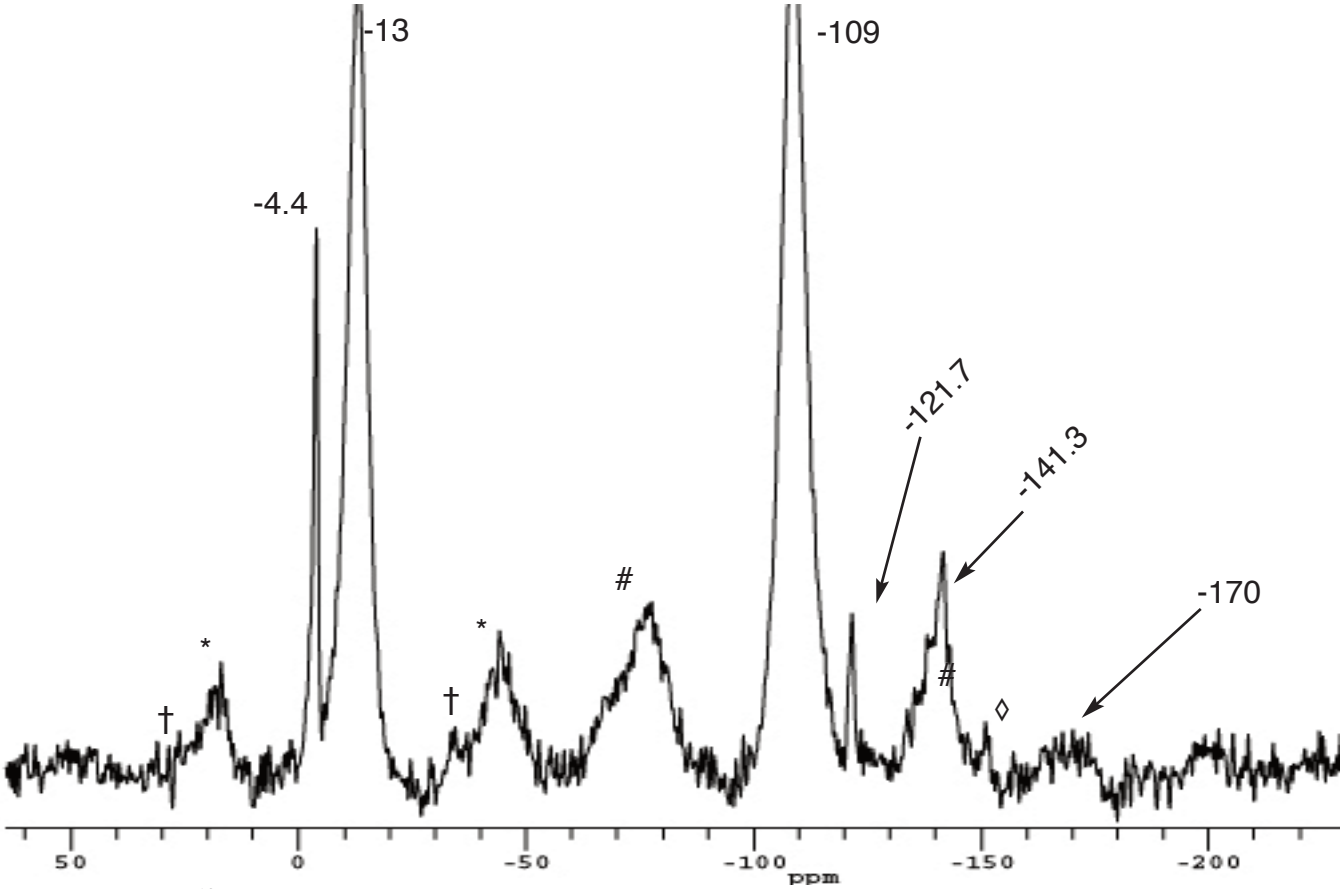

Figure 5.5: ^{19}F SPE MAS NMR spectrum of BaF_2/CaF_2 heterostructures taken at 100°C. Symbols †,◊ depict spinning side bands of the new peaks at -4.4, -121.7ppm, respectively.

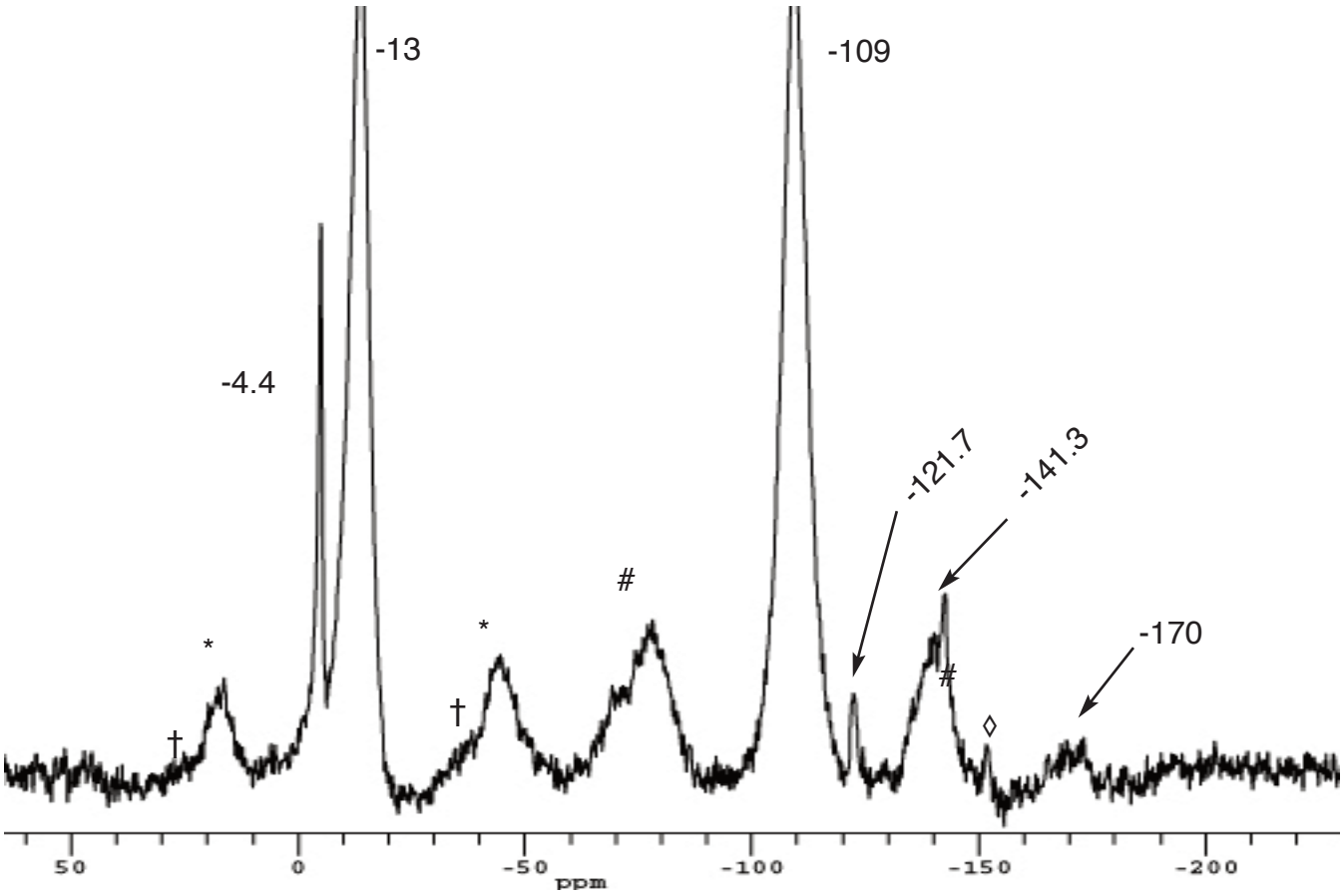

Figure 5.6: ^{19}F single-pulse excitation (SPE) MAS NMR spectrum of BaF_2/CaF_2 heterostructures taken at 200°C

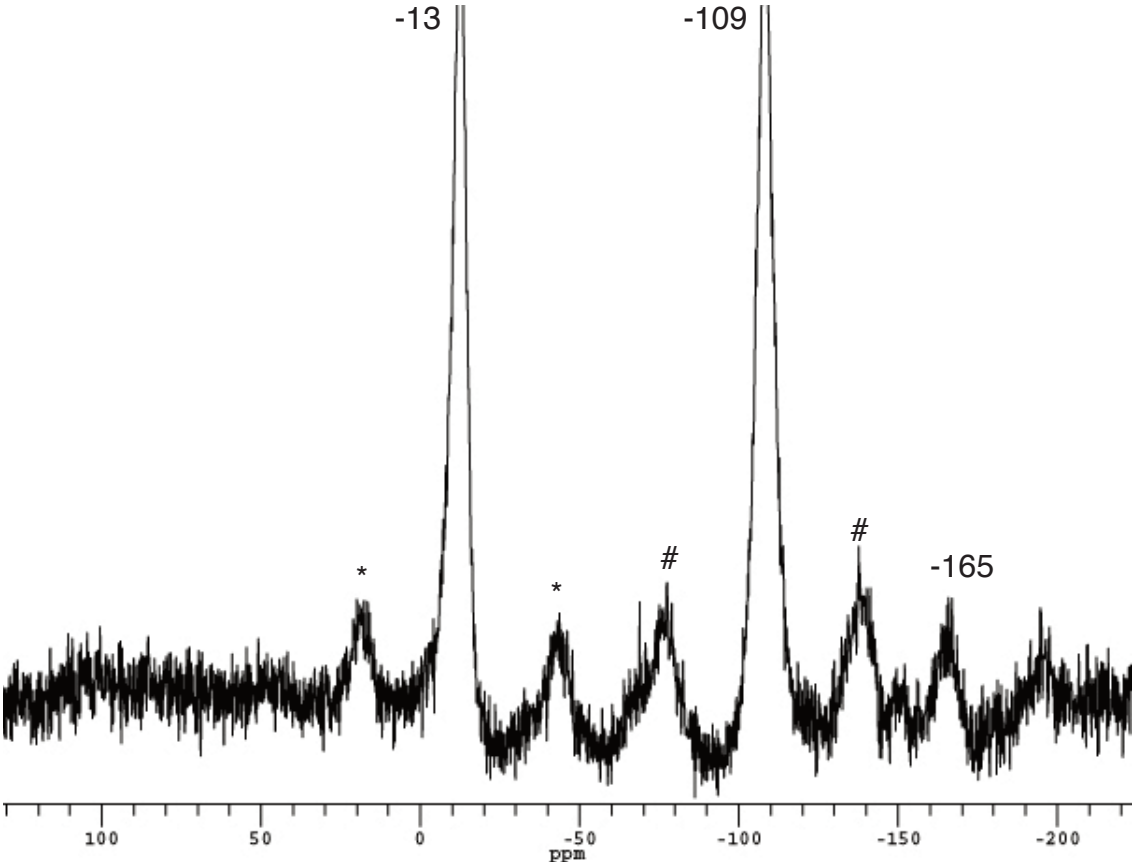

Figure 5.7: Single pulse spectrum taken at RT, following prolonged (35h) heating at 240ºC. The sharp peaks have vanished, presumably due to extended heating. Repeated experiments confirmed that this process is irreversible. The peak at -165ppm was never clearly resolved and is very likely an overlapping sideband.

Temperature	peak (area - a.u.)	peak (area - a.u.)	peak (area - a.u.)	peak (area - a.u.)	peak (area - a.u.)	peak (area - a.u.)
	-2.9 (-4.4) ppm	-13ppm	-109ppm	-121.7ppm	-123.7ppm	-141.3ppm
RT	194	1048	1381	54	74	126
100ºC	222.1	1014	1268	37	n/a	137
200ºC	234	1224	1507	44	n/a	119

Table 5.1: Tabulation of peak and corresponding integrated area, versus temperature.

A one-pulse sequence was used and the pd is 45s. The values are normalized to a scan number of 4896 scans. Only isotropic peaks were integrated; spinning sidebands were not included in the tabulation of these intensities.

peak(ppm)	area (1s)	area (5s)	area (10s)	area (20s)	area (50s)
-4.4	160	167	178	211	211
-13	43	207	388	729	1209
-109	117	211	547	984	1519
-121.7	36	37	34	43	45
-141.1	20	48	67	105	102

Table 5.2: integrated area increase per peak, per time interval. These areas correspond to the peaks in the stack plot of Figure 5.8, below.

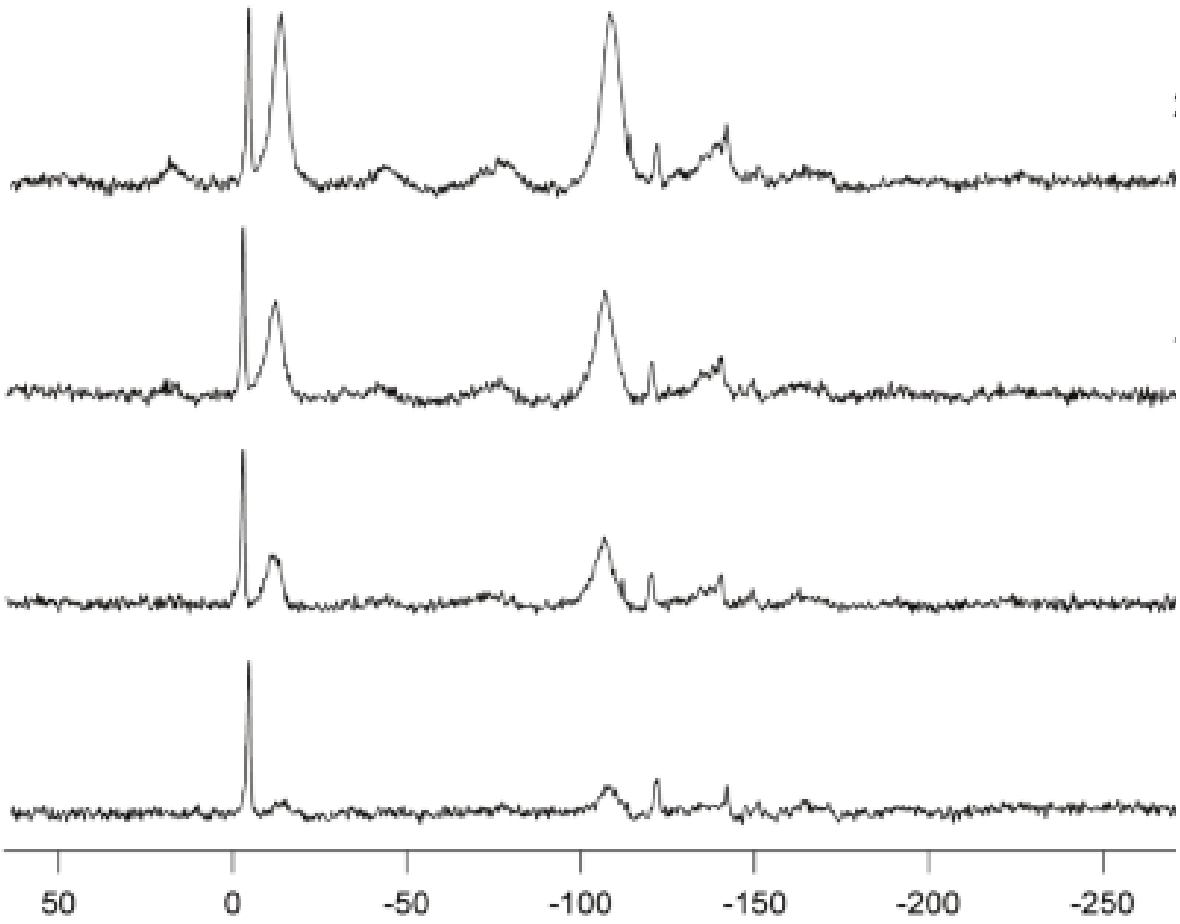

Figure 5.8: A stacked plot (a "pulse-delay" array) of the spectra at the four different pulse-delay times of 1, 5, 10 and 20s collected at RT. The integrated areas of the different resonances are tabulated in Table 5.2, above.

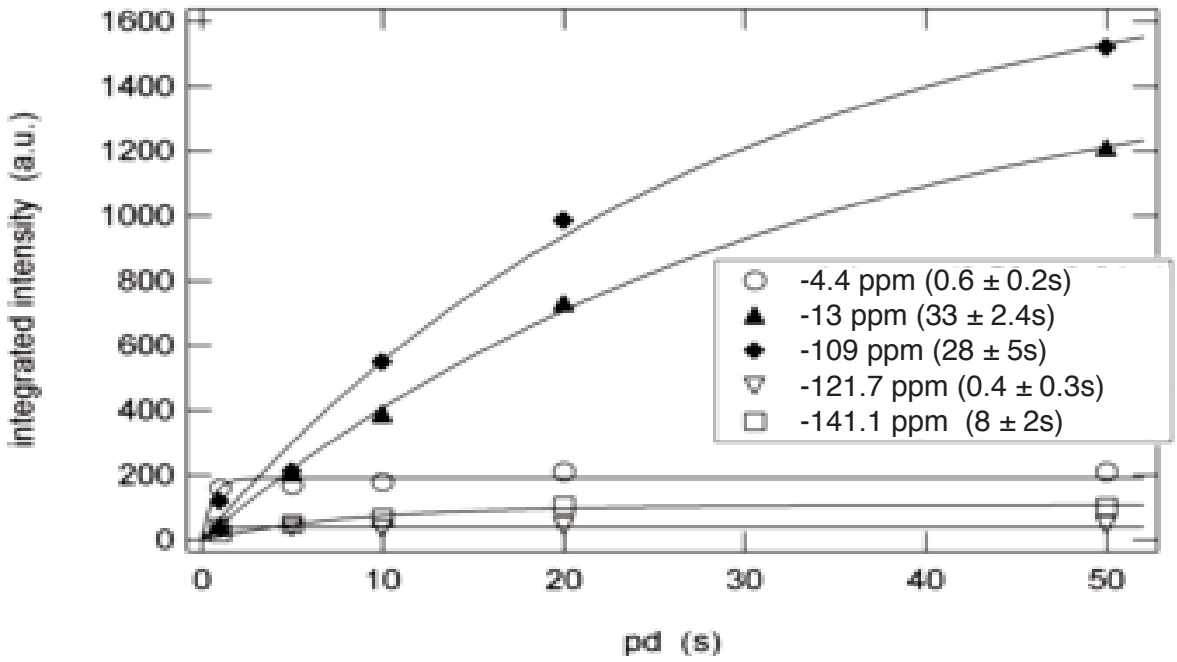

Figure 5.9: A plot of the data that appear in Table 2; curve fitting to the following formula: $M(t) = M_0 (1 - e^{-t/T1})$ permits an estimate of actual T_1 times (see inset). All times were measured at 200ºC.

peak(ppm)	T_2^{-1}(kHz)(RT)	T_2^{-1}(kHz)(100ºC)	T_2^{-1}(kHz)(200ºC)
-4.4	1	1	0.4
-13	2.2	2.2	2.3
-109	2.8	2.8	2.8
-121.7	0.5	0.6	0.8
-123.7	0.75	n/a	n/a

Table 5.3: Table of T_2^{-1}(kHz) for each peak as a function of temperature

peak (ppm)	intensity (a.u.) at 200ºC	percent of total
-4.4	234.76	7.5%
-121.7	44.56	1.4%
-141.3	119.2	3.8%

Table 5.4: A tally displaying the ratio of mobile species, relative to the bulk

5.4 Discussion

5.4.1 Chemical shift assignment

The peaks seen at -4.4ppm, -121.7ppm, -123.7ppm, and -141.7ppm were clearly unanticipated (see Figures 5.4-6), as they likely represent structures with structural and chemical properties similar to CaF_2 and BaF_2. A space-charge model would predict defect/vacancy ridden solid solutions of BaF_2 and CaF_2 at the interface. Simple solid solutions at the BaF_2/CaF_2 layer interface with local environments represented as $FCa_{4-x}Ba_x$ would manifest as peaks with shifts in between those of the bulk BaF_2 and CaF_2 ions (manifested as peaks at -13ppm and -109ppm, respectively).

The intense, Lorentzian peak at -4.4ppm (Figures 5.1-3) is very likely structurally similar to the FCC-crystal structure of the [111] oriented BaF_2 in these heterostructures, yet (being upshifted from the peak associated with BaF_2 at -13ppm) and most likely not associated with some species associated with an interaction or a solution with CaF_2. This peak here, at -4.4ppm, appears similar in chemical shift to the species reported by Chaudhuri, et al., in their studies of $BaSnF_4$[12]. Their "F3" fluorine (see their Figure 5.1 in [12]) exhibiting this upfield shift from BaF_2 is less ionically bound to the barium, being sandwiched in between adjacent SnF_2 layers, where tin is much less electropositive than barium. Applying these observations to the heterostructure system investigated here, it appears more likely that the mobile fluorines observed here are positioned in interstitials in the BaF_2 FCC structure, yet on the "barium side" of the BaF_2/CaF_2 interface and not manifesting themselves as a result of increased defect/vacancies at the BaF_2/CaF_2 interface.

If the chemical potential (at STP) of these two compounds is any indicator, species associated with the BaF_2 layers (as well as the defects and interstitial vacancies) should be slightly more likely to become mobile: ($\Delta G^0(BaF_2) = -1158.3 kJ \cdot mol^{-1}$; $\Delta G^0(CaF_2) = -1167.3 kJ \cdot mol^{-1}$), which is again consistent with their cationic radii (Ba^{2+} = 141pm; Ca^{2+} = 114pm) and the tendency of systems with a smaller cation/anion size ratio to form Frenkel interstitials (such as CaF_2) and vacancies such as BaF_2[29,30].

This same reasoning can be applied to the appearance of the peaks downshifted from the peak associated with the fluorines in CaF_2, at -109ppm, and the data appear to support this conclusion. The more thermodynamically stable calcium fluoride ($\Delta G^0(BaF_2) = -1158.3 kJ \cdot mol^{-1}$; $\Delta G^0(CaF_2) = -1167.3 kJ \cdot mol^{-1}$) should have fewer mobile species (or, alternatively, fewer vacancies) in comparison to barium fluoride and the integrated areas of the mobile species tabulated in Table 5.4 support this assertion. Although these chemical potential values are at 298K, the nature of the free enthalpy equation lends credence to the notion that mobility will at least be linearly correlated.

Should the space-charge model be applicable here, the difference in chemical potentials should induce (see eqs. 1, 2 above) a greater number of defects as one approaches x = 0 (x in this case is the distance to the interface). From the spectra (Figures 5.4-5.6), it appears that no solid solutions are present, as they would manifest as species lying somewhere in between the BaF_2 and CaF_2 peaks. Here, and as Maier briefly pointed out on p. 177 in [7], the proximity of the two dissimilar materials appears to have a ***de***stabilizing effect on the space charge region, the less thermodynamically likely of the two possibilities[7]. The result, which appears to be seen here, induces interstitial and vacancy abundances in the respective bulks, purportedly near the interface.

The result, which appears to be seen here, induces interstitial and vacancy abundances in the respective bulks, purportedly near the interface. This is contrary to the space-charge model as it is typically viewed, where vacancies are induced as a result of ionic migration from the space-charge region and, therefore, a means by which elevated conductivity would occur as $\lim N_i(x) \rightarrow 0$.

It appears more likely that these highly mobile species as reflected in Figures 5.4-5.6 are merely due to interstitial fluorines and defects caused by vacancies. For example, Jain, et al. determined that highly mobile fluorine species were present in their carefully synthesized 25nm crystals of pure CaF_2, demonstrating very similar ^{19}F chemical shifts and conductivities as those seen here[13]. Temperature-dependent changes in the ^{19}F MAS NMR spectra were demonstrated. They then used the lineshapes to simulate spectra, which allowed a two-site random cross-exchange model to be applied in order to extract the exchange frequency between the two sites[13].

It is interesting to note that the thickness of each of these alternating CaF_2/BaF_2 layers is approximately 20nm. Apart from the obvious differences in unit cell size between the two types of fluorides, which would very likely engender lattice strain, the thicknesses of the heterostructures studied here roughly approximate the nanocrystal sizes mentioned above. Jain, et al. note that the chemical shift they observe of -130ppm (similar in range to the 121.7ppm, -123.7ppm, and -141.7ppm) represents species that are highly mobile from the simulations and calculations they performed and appear to represent a trend in the creation of fluorine interstitials as defined by crystallite size[13].

What remains unclear is the preponderance of distinct, sharp peaks representing different, highly mobile, local fluorine environments within the CaF_2 bulk. The highly symmetric fluorite unit cell or clusters of cells can only generate a short, finite list of possible flourine interstitial configurational geometries and since this is the first observation of these species in a system of

this type, not enough information is yet known to generate interstitial geometries and predict accompanying chemical shifts.

5.4.2 Fluorine motion

Quantitative data for correlation times and conductivities are represented in Table 5.5 (below), the values of which were then used to extrapolate the curves depicted in Figure 5.9 using the equation below the Figure ($M(t) = M_0 (1 - e^{-t/T_1})$). Employing equations 5.4 - 6 also permitted calculation of conductivity (σ, σT), again tabulated in Table 2. While these conductivities do not correspond precisely, they are well within the scale of conductivities reported by Maier, et al[5]. As seen in equation 4 above, correlation times (τ_c, τ_c^{-1}) shown in Table 2 (below) were obtained in order to extract T_1 times. Figure 5.9, as well as the inset, clearly demonstrate the relative mobilities of the species associated with the -4.4, -121, -141ppm chemical shifts and the much less mobile bulk materials (bulk BaF_2 = ♦; bulk CaF_2 = ▲) as derived from the values in Table 2.

peak (ppm)	τ_c (s)	τ_c^{-1}(kHz)	σ (Ω^{-1}•m^{-1})	σT (Ω^{-1}•$cm^{-1}K$)
-4.4	1.9×10^{-4}	5.3	1.3×10^{-5}	6.15×10^{-5}
-13	1.1×10^{-2}	.09	2.18×10^{-7}	1.03×10^{-6}
-109	9.5×10^{-3}	0.105	2.54×10^{-7}	1.19×10^{-6}
-121.7	1.3×10^{-4}	7.4	1.79×10^{-5}	8.73×10^{-5}
-141.1	2.7×10^{-3}	0.36	8.88×10^{-7}	4.2×10^{-6}
				sum 1.55×10^{-4}

Table 5.5: Tabulation of peak and corresponding τ_c, τ_c^{-1} values at STP. Colors are just a visual aid to discriminate between the two groups of peaks associated with their respective bulk materials. σ, σT calculated with equations 4-6, using an $H_R = 1$.

As evident in equation 5.4, motion described by correlation times strongly affects the spin-lattice relaxation rate (T_1). Correlation times refer to the times a species is associated with a specific state, location, orientation, etc., following excitation in some manner away from the initial state; in this case as it applies to nuclear spin. When these times are with respect to a single nucleus, the orientation of that nuclear spin to itself at some later time is what is measured as autocorrelation. With ensembles of spins, where interhomonuclear effects are relevant because of their interactions among the spins in nevertheless differing local ionic environments, cross correlation becomes germane. Several relaxation mechanisms contribute to observed changes in correlation times, including dipolar, motional, CSA and other effects. The order-of-magnitude differences in correlation times seen in Table 5.5 above demonstrate the substantive roles that these phenomena have on the time taken to relax back to the initial spin state.

In calculating the conductivities of the various species present in the sample (see Table 5.5, above), equations 5.5 and 5.6 were employed. As can be seen in Equation 5.6, the Haven ratio (H_R) is an important part of the calculation. The Haven ratio is a calculation of the correlation between vacancy and (corresponding) ion hopping.

In the low-defect limit, vacancy hopping is Markovian, with no statistical relation to a prior or future event. A corresponding ion hop in this regime, however, is directly related to that same vacancy. This scenario forces a dependence on the part of the ion for a future hop. In this simple case, a near 1:1 correspondence could be envisioned. For example, Lidiard calculated H_R to be 0.65 for BaF_2 in the bulk[22]. However, in cases such as the heterostructures investigated here, a substantial change in the magnitude of H_R will likely be encountered, such that H_R per unit length would be the only option, making calculation impossible. As such, a conservative choice of unity for H_R was used here. That the spectra demonstrate no "mixing" of the two binary compounds as evidenced by an absence of peaks in between the bulk.

In the high-defect regime, an overabundance of vacancies would predominate. The voltage potentials of the vacancies would overlap (the space-charge model), thereby creating a bias in favor of conductivity in the region in which the vacancies predominate[23]. In the case, here, conduction would be higher perpendicular to the interface. This would again lead one to the conclusion that, as stated before, mixing would occur between the two binary compounds, due to rapid mobility around the region of the interface, which would be evidenced by peaks in between the CaF_2—BaF_2 bulk peaks, as seen in the spectra here. This does not necessarily imply motion across the interface. This is merely consistent with experimental observations, in that no rapid exchange is seen between any of the specied associated with the resonances associated with the CaF_2, BaF_2 peaks. One interesting example of disorder promoting substantial increases in conductivity is that of Ruprecht, et al. In this study, the authors mechanically mixed comparably sized (~5μm) CaF_2 and BaF_2 polycrystalline powders via planetary ball milling[34]. Their results appear to underscore that both structural disorder and an aggregate, mixed phase of the two fluorides, combined, can adequately account for the unusually high conductivity (~0.1mS $\cdot cm^{-1}$) at elevated temperatures[34].

If Maier's suggestion that a surface analog of a Haven ratio is correct, then modeling and/or measurement of this value should be trivial; experimentation (via d.c. conductivity measurements historically, or a.c. conductivity measurements more recently) would both permit determination of a surface analog of a Haven ratio[25].

The T_2 times displayed in Table 5.3 are very instructive from the perspective that the more mobile species predictably demonstrate changes in the reduction in the intensity of the spinning sideband manifolds. It is unfortunate that more datapoints as a function of temperature could not be recorded, as these data could be used to better understand the spin-spin interactions among the more mobile species. It is also clear from Table 5.3 that the bulk BaF_2 and CaF_2 environment remain quite rigid, regardless of temperature. Although unary (and not binary like the BaF_2—CaF_2 heterostructures here), Jain, et al. described identical behavior for the single peak associated with the bulk CaF_2 of their nanoparticles and demonstrated that the fast exchange is occurring between the bulk fluorines and the small signal due to interstitials[13]. It is very likely in this case studied here as well, that interaction with fast fluorines and the bulk is occurring, [13].

5.4.3 Temperature effects

The irreversible effects of prolonged (~35h), high-temperature (~240°C) exposure, depicted in Figure 5.7 and hallmarked by the disappearance of the mobile species previously described, were unanticipated. This result is inconsistent with the preparation and conductivity methods reported by Maier and Sata, whereby they annealed the heterostructure materials to ~550°C, prior to conducting AC impedance experiments[5,6]. Repeated experiments at room temperature confirmed the irreversible effects first seen and depicted in Figure 5.7. Given the parameters outlined in [6], the heterostructures grown here were kept at 500°C for approximately 16h.

Although no time span was indicated in the literature regarding the AC Impedance experiments carried out by the Maier group at 540°C, it is reasonable to use these data and the growth data in [5] as a guide to conclude that the temperatures and time frame reached in the investigations here were reasonably within range.

The broad peak at -165ppm as seen in the Figures (noted in Figure 5.7) remained poorly resolved. It was never clear during the pulse-delay experiments whether this peak was an artifact or a mixture of overlapping spinning sidebands. The only substantive change was observed following the observed changes seen in the spectrum in Figure 5.7. Both the shape of the peak became more sharply resolved and the downshift to -170ppm (see Figures 5.5-7) concretely determined that its presence indicated its probabable association with a discrete species within the system. Other than these, no other remarkable observations were made.

5.5 Conclusions and Future Work

Several highly mobile species, relative to the bulk, were observed in the heterostructures studied here. The T_1, T_2 times and derived conductivity results regarding fluorine mobility presented here are consistent with the conductivity observations made by the group which originally synthesized the heterostructure materials, although the conductivities for the species calculated here are not. Explicitly mentioned in the text and demonstrated in the TEM figure of [6] as well as molecular dynamics simulations elsewhere appear to indicate that simple lattice mismatch is responsible for the increases in conductivity reported[6,31-33]. That said, additional experimental data would be required to confidently present competing conductivity measurements.

Inconsistent with theoretical assertions presented elsewhere is the fact that the space-charge model is an adequate methodology to explain the non-linear increases in conductivity reported in [5]. Similar chemical shifts and an absence of tell-tale dynamics reported in [13] that would be empirically associated with space-charge model (eg. mixing of otherwise discrete species, due to dissimilar Debye lengths) appear to confirm that the space-charge model is not the driving force in the elevated fluorine mobilities seen here and this conclusion is shared by the authors[13]. The presence of the highly mobile species at -4.4, -121, -141ppm appear to confirm that fluorine interstitials are responsible for the substantial motion. Also inconsistent with work previously reported elsewhere was the loss of these mobile species, following prolonged heating, yet at temperatures substantially lower than were reported in the past.

Future work would include additional temperature data points and much higher numbers of scans to improve the accuracy of both T_1 and T_2 times, so as to much more precisely determine whether or to what quantifiable extent fluorines from the bulk may be exchanging or participating in conductivity. Although extremely time-consuming due to the small amounts of material and very long T_1 times for the bulk, Two-Dimensional Magnetization Exchange experiments could be performed to determine which species are connected via spin exchange mechanisms.

5.6 References

1) Schottky, W., *Z. Physik. Chem*, B29, 335 (1935)

2) Lehovec, K. *J. Chem. Phys*. 21, 7 (1953)

3) Mott, N.F. Littleton, M.J. *Trans. Faraday Soc*. 34, (1938)

4) Sata, N., Maier, J., Eberman, K., Eberl, K., *Nature*. 408 (2000)

5) Guo, X.X., Maier, J. *Surf. Sci*. 549 (2004)

6) N. Sata, N. Jin-Phillipp, N.Y., Eberl, K., Maier, J. *Sol. State Ionics* 154 (2002)

7) Maier, J. *Prog. Sol. State Chem*., 23, (1995)

8) Wachsman, E.D. *J. Electrochem. Soc: Interface*, (2009)

9) Surdoval, W.A. *ECS Trans*., 25 (2009)

10) Mukerjee, S., Haltiner, K., Kerr, R., Chick, L. Sprenkle, V., Meinhardt, K., Lu, C., Jin Y. Kim, Weil, K.S. *ECS Trans*. 7, 59 (2007)

11) Zhan, Z., Barnett, S. *Science* 308 (2005)

12) Chaudhuri, S., Wang, F., Grey, C.P. *JACS*, 124 (2002)

13) Jain, P., Kim,, S., Youngman, R.E. and Sabyasachi, S. *J. Phys. Chem. Lett*., 1, (2010)

14) Puin, W., Rodewald, S., Ramlaub, R., Heitjans, P., Maier, J. *Sol. State Ionics* 131 (2000)

15) Heitjans, P., Kärger, J. Diffusion in Condensed Matter: Materials, Methods, Models. 1st ed. Springer-Verlag, Berlin. 2005.

16) Indris, S., Heitjans, P. *J. Phys: Cond. Matt*. 15 (2003)

17) Saito, Y., Maier, J. *J. Electrochem. Soc.,* 142, (1995)

18) Heitjans, P., Indris, S. *J. Mat. Sci. 39* (2004)

19) Fabbri, E. Pergolesi, D., Traversa, E. *Sci. Technol. Adv. Mater.* 11 (2010)

20) Sayle, D.C., Doig, J.A., Parker, S.C., Watson, G.W. *Chem. Commun*. (2003)

21) Adams, S. Tan, E.S. *Sol. State Ionics* 179 (2008) 33–37

22) Lidiard, A. B. in Crystals with the Fluorite Structure: Electronic, Vibrational, and Defect Properties (Monographs on Physics). 1st ed. William Hayes (ed.), Oxford University Press, USA 1975.

23) Hayes, W. in Ionic Solids at High Temperatures. Directions in Condensed Matter Physics., vo. 2. 1st ed. A.M. Stoneham (ed.) World Scientific Publishing, Singapore 1989

24) Compaan, K., Haven, Y. *Trans. Faraday Soc*., 52, 786 (1956)

25) Maier, J. *MRS Proceedings* 548, 415 (1998)

26) Zobov, V.E. Ivanov, Yu. N. *JETP* 88, 1 (1999)

27) Bruce, C.R. *Phys. Rev.* 107, 1 (1957)

28) Van Zeghbroeck, B. V. Principles of Semiconductor Devices and Heterojunctions; 1st ed. Prentice Hall, USA 2009.

29) Bollmann, W. *Phys. Stat. Sol*., 18, 313 (1973)

30) Fong, F.K., Hiller, M. A. *J. Phys. Chem*. 71, 9 (1967)

31) Ivanov-Shitz, A.K. Crystall. Rep. 52, 1 (2007)

32) Fabbri, E., Pergolesi, D., Traversa, E. Sci. Technol. Adv. Mater. 11 (2010)

33) Tribello, G. ***Computer Simulations of Superionic Heterostructured Materials.*** M. Sc. Thesis, Part II; Balliol College, Oxford University (2004).

34) Ruprecht, B., Martin Wilkening, M., Stefan Steuernagel, S., Heitjans, P. *J. Mater. Chem*., 18 (2008) 5412–5416

Chapter 6

Investigative studies of Antimony-pentafluoride loaded Micro- and Nanopolycrystalline Barium Fluoride: Structure and Ionic Conductivity

Abstract

The super-Lewis acid, antimony pentafluoride (SbF_5), was used to induce vacancies in homomorphic, nanocrystalline (20-30nm) barium fluoride (BaF_2) as well as microcrystalline barium fluoride and comparative conductivity effects were observed via electrochemical impedance spectroscopy. Differing amounts of SbF_5 had very different effects on conductivity between the nanocrystalline and microcrystalline BaF_2 samples, with conductivity proceeding via different mechanisms, as well as at alternately slower and faster rates, depending on the loading for each. One-dimensional and two-dimensional ^{19}F MAS NMR experiments appear to confirm that a small number of interstitial fluorines were created in the SbF_5-loaded nanoparticle BaF_2 and were spectrally observable. The fluorine species generated as a result of the SbF_5-loading appear to have substantially different T_1 times in comparison to fluorines associated with the nanocrystalline BaF_2 lattice. No clearly crystalline SbF_3, $BaF_z \bullet ZSb_xF_y$ or $Ba(SbF_6)_2$ species were discernible from powder XRD either prior to or following heating to 240°C when reacted with the nanoparticle BaF_2., although this is likely due in part to the broad XRD peaks typically associated with nanocrystalline species. Sb k-edge EXAFS confirmed ^{19}F MAS NMR observations, that both Sb^{3+} and Sb^{5+} oxidation states existed in the samples, and that their ratios were SbF_5-load dependent. The asymmetric lineshape observed in ^{121}Sb MAS NMR spectra also appear to support the fact that two differently coordinated Sb species are present in the samples. The Sb_xF_y species present were found to be highly temperature sensitive, as demonstrated by substantial changes in MAS NMR lineshape variable T_1 times.

6.1 Introduction

Fluoride salts have been widely studied due to their simplicity of structure, isostructural acceptance of isovalent or aliovalent dopants to very high levels[3]. They also have broad range of uses in optics, ionic conductivity, and have been commercially exploited in high thermal conductivity regimes, due to their simple phononic spectra[4,5]. Their simplicity also affords access to understanding the nature of ionic conduction within their highly symmetric crystal lattices.

The aggressive search for materials which exhibit high ionic conductivity is spurred by potential commercial applications, largely toward non-fossil-fuel, low-emissions electricity production such as fuel cells[1,2]. However, other industries which employ systems that rely on ionic conductivity would also gain substantially from understanding the mechanisms behind higher ionic conductivity[1,2,3,4,5]. Petro and organochemical industries, for example, use resin-exchange matrices; motor vehicle industry relies on catalytic converters, and horticultural and agribusiness industries rely on Total Deposited Solids (TDS) and pH metrology[6].

Since a fundamental aspect of ionic conductivity centers around the status, mobility and concentrations of vacancies and interstitials present in the crystal lattice, previous research has been performed which induced vacancies into the crystal lattice of simple fluorites (via different mechanisms) with the goal of determining the roles that vacancies and interstitials play in the enhanced ionic conductivity seen, in this case, in simple fluorite systems[7,8].

In the investigations described in this chapter, a technique similar to that used in [7] was employed in order to induce vacancies into the lattice of both bulk and nanoparticle polycrystalline barium fluoride (BaF_2)[7]. Specifically, Saito and Maier had deliberately loaded polycrystalline samples of the Frenkel-disordering CaF_2 with either SbF_5 or BF_3, both super-Lewis

acids, in order to determine whether conductivity is enhanced due to the "drawing out" effect that the super-Lewis acids would have on the the interstitial-bound fluorides toward boundary surfaces[7]. In their investigations, Saito and Maier (and Maier, subsequently, which is also discussed in Chapter 6 of this dissertation) found that enhanced conductivity did, in fact, occur[7].

Several different modalities were used in order to try and explore some simple questions such as: how do the various fluoride species interact with one another[9,10,11]; what role does the super-Lewis acid play; is nanocrystalline BaF_2 a better conductor than microcrystalline BaF_2, or does boundary energy actually decrease conductivity; what correlation, if any, does fluoride motion play in any conductivity enhancements that may be seen and what role (if any) does temperature affect motion of the various species. To address these issues, both 1D and 2D MAS NMR methods were used to look at fluoride mobility and probe the chemical relations the species had with one another. The oxidation state(s) of the antimony and preliminary data regarding Sb—F distances were examined via X-ray Absorption Spectroscopy methods. The means of ionic conductivity were examined via Electrochemical Impedance Spectroscopy. Additionally, crystallinity pre-and post- SbF_5 loading/heating was checked by Powder X-ray Diffraction (XRD).

6.2 Experimental

6.2.1 Sample Preparation

Synthesis of the BaF_2 nanoparticles was performed according to the methods outlined in Chapter One of this dissertation. Barium fluoride (BaF_2) nanoparticles were synthesized, analyzed via BET, combined with XRD and confirmed to be approximately 30nm in size, as described in Chapters One and Two of this dissertation. Bulk BaF_2 was purchased from Alfa Aesar and used unaltered.

Samples of the pure BaF_2 were weighed out at 220.0mg each. The samples were brought into an argon glove box. The reason for the precise mass assessment is because the values

were used to determine the precise SbF_5 loading amounts, particularly for "sample a", such that a monolayer of SbF_5 could be deposited on the surfaces of the crystallites.

Pure antimony pentafluoride (SbF_5) was purchased from Sigma Aldrich and used without additional processing. Calculations were made, based on BET surface area ($24.95 m^2 \cdot g^{-1}$) and XRD/Debye Scherrer measurements performed on the synthesized BaF_2, to determine particle size, as described in Chapter One of this dissertation. This permitted a specific amount (4μl) of SbF_5 to be determined to be deposited onto the 220mg sample (sample A), such that a monolayer of SbF_5 molecules was estimated to have been deposited onto the surfaces of the crystallites.

A 4μl aliquot of SbF_5 was pipetted into the sample vial containing the measured mass of BaF_2 , directly onto the sample, using a micropipettor and the contents were mechanically mixed using a small, nickel spatula. An immediate color change was noted from near white for the pristine BaF_2 nanoparticles to a grayish tan for the then-reacted substance. Subsequent samples were prepared in the same manner for 6, 8, 10, 12, and 14μl-loaded samples (samples B, C, D, E and F, respectively). Subtle color changes were noted with increasing loading, with the 14μl-loaded sample having a dusky chocolate color. Cross contamination of samples was avoided by thoroughly wiping down the spatula with methanol-dampened wipes, followed by a dry wipe.

Incidental handling of the compounds prior to actual experimentation revealed that the resultant substance was highly hygroscopic. The samples turned bluish purple and took on a moist look. Upon extended exposure on a watch glass, the samples sorbed so much moisture from the air that nothing but a purple slurry remained. As such, care was taken to store vials in the glove box and keep samples intended for experiment in argon-filled vials up until the point of experimentation, which were stored in the glove box, to ensure that no color changes were noted.

6.2.2 MAS NMR

All samples were packed into rotors in an argon glove box. Care was taken to either choose or machine tightly fitting Vespel end caps to prevent exposure to ambient oxygen and humidity during experimental time. Either a 3.2mm or 2.5mm rotor size was used, depending on the MAS NMR system (3.2mm for all 360, 500Mhz experiments; 2.5mm for all 600Mhz experiments).

All one-dimensional experiments were conducted on either a 360MHz (8.47T) or a 500Mhz (11.75T) Varian/Chemagnetics Infinity Plus system using standard Spinsight (Spinsight v.4.3.2) spectrometer software. Regardless of spectrometer, the Single-pulse, Echo and 2D-Magnetization Exchange (2DME) experiments were always performed using neat $CFCl_3$ (0 ppm) as a standard external chemical shift reference for fluorine. For the one-dimensional experiments on the 360MHz spectrometer, a $\pi/2$ time of 2.5μs (100kHz RF power) was determined for the ^{19}F MAS NMR experiments using a frequency of 338.37MHz. A $\pi/2$ time of 4μs (62.5kHz RF power) was determined for the ^{19}F MAS NMR experiments on the 500MHz spectrometer, using a frequency of 470.18MHz. For the ^{121}Sb Echo experiments carried out, the sodium hexafluoroantimonate salt, $NaSbF_6$, purchased from Sigma Aldrich, was used to determine a $\pi/2$ time of 2μs (125kHz RF power), set to 0ppm as an external chemical shift reference for antimony. An appropriately sized rotor, pre-packed with potassium bromide (KBr), was used to set the magic angle for all spectrometer probes used (2.5mm [Bruker]; 3.2mm [Chemagnetics]).

All two-dimensional experiments were conducted on a 600MHz (14.11T) Bruker Avance Spectrometer system controlled by accompanying TopSpin spectrometer software, using a 2.5mm rotor, again prepacked in an Argon glove box, as mentioned above, to prevent ambient moisture from corrupting the sample. A $\pi/2$ time of 2.5μs (100kHz RF power) was determined

for the ^{19}F 2DME MAS NMR experiments on the Bruker Spectrometer equipment, using a carrier frequency of 564.71MHz.

The two-dimensional experiments performed fall under the 2-Dimensional Magnetization Exchange (2DME) type. As explained in Section 1.3.6 of the Introductory Chapter of this PhD dissertation (see the specific Hamiltonian listed there), 2DME experiments rely on the fact that in homonuclear dipole-dipole (D-D) coupling, spins exchange energy by the mutual reorientation of their respective polarizations. This interaction is spatially dependent, because of the through-space nature of D-D interactions. Energy is conserved during this flip-flop process, so if the difference in resonance frequencies between the two spins is smaller than the D-D strength, this spin-exchange will occur to a quantifiable degree and contribute to nuclear magnetic relaxation. This 2DME spectrum was post-processed using Spinworks, a freeware package written and developed by Prof. Kirk Marat (Chemistry NMR Lab 320, 338 Parker Bldg., 144 Dysart Road University of Manitoba, Winnipeg MB R3T2N2). This software package was written to optimize 1, 2D data collected from liquid samples on Bruker spectrometer systems (VNMR-J data format also supported). The precision normally needed for j-coupling scales (on the order of a few Hz) was well-suited to at least partially compensate for the phase issues encountered here.

6.2.3 X-ray Diffractometry

All SbF_5-loaded BaF_2 samples were prepared within an argon glove box. The Bruker AXS D8 Advance xray diffractometer uses a Cu target (1.545Å). This particular model accommodates a polycarbonate-domed sample holder purchased from Bruker. This holder permits sample preparation for air-sensitive samples (such as in the cases here) and was used for the SbF_5-loaded experiments performed for this investigation. Non-SbF_5-loaded BaF_2 samples were analyzed using a Rigaku Powder XRD with either a Cr or a Cu element.

Samples investigated at Brookhaven National Laboratories National Synchrotron Light Source, Beamline X7-B, were all prepared inside an Ar glove box. Several 0.5mm quartz capillary tubes were brought into the glove box, filled with small amounts of sample A and then capped and wrapped with parafilm. Upon removal from the glove box, the capillary tubes were immediately sealed by melting the parafilm-wrapped top with a MAPP gas torch (MAPP is a non IUPAC trade name which stands for MethylAcetylene-Propadiene Propane).

6.2.4 Extended X-ray Absorption Fine Structure (EXAFS) data

The EXAFS data for the standards ($NaSbF_6$ and SbF_3) as well as two samples studied (sample A, sample F) were collected at the Sb K-edge at a temperature of 77K using Beamline 4-1 at the Stanford Synchrotron Radiation Lightsource (SSRL) located in Palo Alto, CA, in order to determine the local antimony oxidation state(s) within the samples under investigation. Sample holders provided by the staff scientists at Beamline 4-1 were placed and loaded inside an Ar glove box. Inside the glove box, the samples were covered (sealed) with Kapton tape and each loaded sample holder was then inserted into a bag and taken out of the glove box.

The E_0 edge energy was taken at 30,508.6 eV and the EXAFS signal, $\chi(k)$, was k^3-weighted and Fourier transformed (FT) through a Kaiser window in the range spectrum 3.0–13.2$Å^{-1}$. The software package, SIXPack, was used to analyze the data, and the fitting subroutine, IFEFFIT, was used to find the least-squares fittings to determine what turned out to be a ratio of Sb^{3+}, Sb^{5+} oxidation states. Both floating and non-floating E_0 (Fermi Level) energies were chi-square tested for best fit and in both cases, a lower chi-square value was obtained when E_0 was allowed to float.

6.2.5 Electrochemical Impedance Spectroscopy (EIS)

Electrochemical Impedance Spectroscopy (EIS) was performed on a 1287 Solartron Electrochemical Interface and an SI 1260 Solartron Impedance Analyzer, applying an excitation perturbation amplitude of 10 mV root mean square (rms). The accompanying Z-view and Z-plot software were used to record and analyze the impedance data. Measurements were taken over the 0.1–1 MHz frequency range using a two-electrode configuration. The samples were measured within standard battery button coin cells purchased from Hohsen Corporation, Osaka Japan. All samples were prepared and pressed inside an Ar glove box.

To prevent oxidation, samples of each SbF_5-loaded BaF_2 preparation were sealed within the battery button coin cells, as mentioned above. The button coin cell comprises a male-female stainless steel design which is sealed by press fit, using a small press, also purchased from Hohsen Corporation. Stainless discs are inserted on both sides of the sample and corrugated spring washers were inserted exterior to these discs to exert pressure and improve contact. PEEK gaskets were used to ensure an air-tight seal. This small assemblage is then inserted into the press and firm, downward pressure is applied and upon release, the sealed coin cell is ejected.

6.3 Results

Figure 6.1 a-c depicts powder XRD graphs of pristine, nanoparticle BaF_2 (at RT) (a), sample A, prior to heating (at RT) (b), then the same sample A analyzed post-heating (RT) (c). Because of the challenges of in-situ, air-free XRD, several attempts were made during allocated time at the National Synchrotron Light Source to collect in-situ XRD data, with periods of heating followed by at-temperature equilibration and data capture at each step. In the end, only pre- and post-heating data could be collected, due to software and mechanical failures. Figure 6.1d is, in fact, Figure 6.1b with JCPDS† powder pattern reflections overlaid: the pre-heating, SbF_5-loaded XRD graph (Figure 6.1b) is overlaid with two of the most likely candidates for the extremely low crystallinity that appeared to have formed and remained largely (though not completely) unaltered post-heating, SbF_3 and an isomorphic powder pattern of $Ba(SbF_6)_2$ namely, $Mg(SbF_6)_2$.

An echo spectrum of directly observed ^{121}Sb in Sample A is depicted in Figure 6.2. Despite the difficulties associated with directly observed ^{121}Sb MAS NMR, ^{121}Sb experiments were performed to explore the potential of observing two separate antimony signals: one for the SbF_6^- spectrum and one for the SbF_3, which are clearly magnetically dissimilar from one another. As can be seen in the Figure, the seven (I+1) peaks due to j-coupling between the ^{121}Sb and the six ^{19}F spins directly bound to the central antimony atom. This appears to correspond to the SbF_6^- which is expected to be present in the sample. However, additional shoulders asymmetrically positioned around the central manifold may be an indicator of a second set of j-coupling peaks, possibly due to the presence of SbF_3. These peaks could not be convincingly deconvoluted, however, and no peer-review literature, to date, has been found on ^{121}Sb MAS NMR for species of this type in a system such as this.

† The Joint Committee on Powder Diffraction Standards (JCPDS) has collected and maintained a database of crystallographic powder patterns for public use since 1941.

Figure 6.3 is a ^{19}F MAS NMR stackplot of chemical shift temperature dependence for the peaks of interest for Sample A, with the vertical lines included as reference points. The fluorine environments represented by the peaks at -14, -28ppm appear to be unaffected by temperature changes (25ºC - 100ºC), yet the fluorine environments represented by the poorly defined peak manifolds at -103, -113 ppm are highly influenced by temperature, as evident by the increased appearance of j-coupling peaks with an increase in temperature, as well as an apparent upfield change in chemical shift. The central peak at -113ppm becomes much sharper and an increase in signal intensity is evident as the temperature increases. Furthermore, the chemical shift of the fluorines associated with this environment at -113ppm shift by approximately 4ppm to -117ppm at 100°C. Chemical shift assignment is explained and supported in the Discussion section, although it will be mentioned here that the peak manifold seen from -103 — -116 are a complex mix of antimony species. At this lower field (360MHz) and slower spinning speed than the one-pulse experiments depicted in Figure 6.4, j-coupling and the SbF_3 signal are not truly evident, although some evidence of it becomes apparent at 100°C. The advantage that Figure 6.3 affords is the higher temperatures which could be achieved at a magnetic field of 360MHz (the higher, 600MHz field spectrometer cannot go above RT). Higher temperatures demonstrate the additional changes in lineshape that occur with the SbF_6^- species and are consistent with the overall trend.

Figures 6.4 and 6.5 are one-pulse stackplots representing spectra of different loadings (Figure 6.4: Samples A, B, F; Figure 6.5: Samples C, D, E) at 50°C. Note the arrows and the lineshapes representing the different species present (and absent) in the sample. The peak depicted in Figure 6.3 at -28ppm is absent in samples B, C, D, E yet present in sample F. Clear differences in the peak manifolds from -90ppm — -115ppm are evident with the differences in loading, even at the modest temperature (50°C) at which the experiments were conducted.

As noted above, the chemical shift assignment for the poorly resolved manifold is attributed to the presence of different types of Sb_xF_y species and is thoroughly accounted for in the Discussion section of this Chapter. The appearance or absence of the peak at -28ppm is inconsistent with loading amount, given that the spectrum depicting the sample with the heaviest loading (sample F) demonstrates this peak. This is also inconsistent with the loading methods, as the same loading methodology was used for every sample.

Figure 6.6 is a second, temperature-dependent stackplot one-pulse ^{19}F MAS NMR experiments and the basis for the T_1 data collected and depicted in Table 1. Despite the poor phasing (see, for example, the twist of the right spinning sideband associated with the BaF_2 peak at -14ppm, indicated by an asterisk), it is clear from this stackplot the substantive changes that occur to the Sb_xF_y species, even at lower temperatures (233K).

Figure 6.7 is a 2DME spectrum of sample A recorded at room temperature. The off-diagonal peaks (a, a´; b, b´; c, c´) labeled in Figure 6.7 clearly revealed more complex interactions among the species in the sample than were initially considered. As evident in both directions orthogonal to the fluorine peak associated with BaF_2, phasing issues remained an insoluble challenge and are manifested as blue-green streaks in the F2 dimension and green in F1. Although partially obscured by the intense signal at -14ppm generated by the fluorines in the BaF_2 lattice, the smaller signal at -28ppm is interacting with the fluorines within the BaF_2 lattice and are therefore spatially proximal. The 2DME spectrum in Figure 6.7 also displayed the peak (seen at -62ppm; off-diagonal pair b, b´) previously undetected by all other methods, which cannot be explained. Further, this peak must have spatial proximity to the BaF_2 lattice, yet does not appear to have a spatial proximity to the Sb_xF_y manifolds seen from approximately -90 — -115ppm. The peak at -62ppm appears real, yet is most definitely not artifact or impurity. Although the floor of

the 2D spectrum is set very low, the signal is more intense than the known peak at -28ppm. No impurity was detected at any point, nor is this a signal related to errant PTFE, for example, which produces a characteristic signal at -120ppm (clearly not present in any of the spectra). The peak manifold ranging from -90ppm — -115ppm appears to be spatially associated with the fluorine signal associated with the BaF_2 lattice. The entire manifold of Sb_xF_y peaks appear to be spatially associated with the fluorines residing in the BaF_2 lattice. The off-diagonal peaks (c, c´) have enough structure to show that both the signals associated with SbF_3 (cited from the literature, outlined in the Discussion section of this Chapter) from -88ppm — -100ppm appear on the left side of the (c, c´) signals[10,11,14]. This also holds true for the intense signal centered at -105ppm.

Figures 6.8a, b represent EXAFS data collected at the SSRL. Figure 6.8a is an X-ray Absorption Spectroscopy (XAS) graph of the X-ray absorption coefficient (μ(E)) as a function of energy for the four compounds. Two standards were used: SbF_3 and $NaSbF_6$, indicated in green and royal blue in both Figures, respectively, as sources for Sb^{3+} and Sb^{5+} oxidation states for antimony. These standards were chosen to demonstrate the Sb k-edge shift as a function of oxidation state, from pure Sb^{3+} to pure Sb^{5+}. The second two lines represent the two compounds studied: sample A (red line) and as a "heavy reference", the more copiously loaded sample F (dark blue line). The green line of the Sb^{3+} oxidation state of SbF_3 is evident as the left-most line here, the first appearing on the k-edge. The line generated by sample F is immediately to the right, consistent with an increasing change in oxidation state, yet still associated with a plurality of Sb^{3+} oxidation state within the sample. Continuing futher to the right is the line associated with sample A, again demonstrating a changing ratio of Sb^{3+}/Sb^{5+}. favoring a greater number of Sb^{5+} present in the sample. The right-most line is due to the $NaSbF_6$ sample, with pure Sb^{5+} present.

Figure 6.8b is a graph of the non-normalized Fourier Transform EXAFS moduli in Real space of the four samples. It is with this body of data that chi-square fitting was performed (as mentioned in the Experimental section, above) and the relative ratios of the two Sb oxidation states was determined with reasonable, acceptable statistical certainty. The Sb^{3+} standard, SbF_3, exhibits an orthogonal unit cell falling into the C2cm space group and demonstrates a 1.92Å Sb—F distance for the ionically bound species[14]. The Sb—F interatomic distance in $NaSbF_6$, being of the highly symmetric Fm3m space group, is 1.78Å[30]. Observing the distinctions in the ~3.4Å range of Figure 6.8b (see arrow), one notes the close association between the red line (sample A) and the $NaSbF_6$ (royal blue) standard, indicating the greater Sb^{5+}/Sb^{3+} ratio and therefore the greater number of

Figures 6.9a-f describe EIS studies done in an oxygen-free environment with samples prepared as described above. Figure 6.9a gives a baseline AC Impedance, given that no conductivity curve had occurred in either the bulk or nanoparticle BaF_2 sample. Figure 6.9b depicts a side-by-side comparison of bulk and nanoparticle BaF_2 with a 6µl load of SbF_5 (sample B). Figure 6.9c demonstrates the differences in conductivity between bulk and nanoparticle samples with a 9µl SbF_5 loading (eg, sample D). Note the apparent change in behavior. Figure 6.10d is the next side-by-side comparison with a higher loading (12µl SbF_5) (sample E). Figure 6.9e is a stackplot of all bulk BaF_2 loadings as compared to one another. Figure 6.9f compares all of the nanoparticle BaF_2 SbF_5 loadings compared to one another. Note the color coding and the overall trends which occur in each sample are better viewed when homogenously compared (bulk-bulk; nanoparticle-nanoparticle) rather than heterogeneously compared.

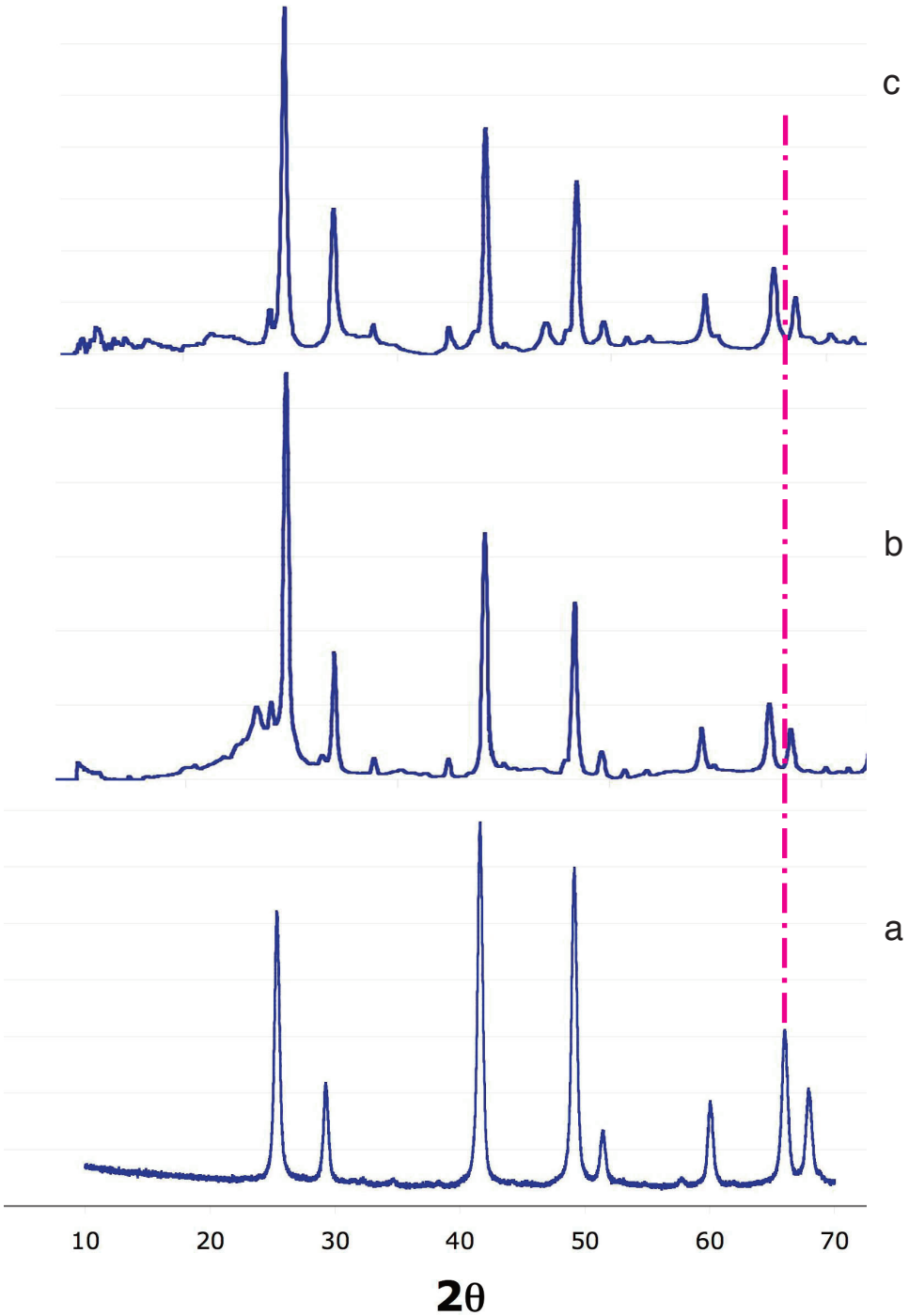

Figure 6.1 a-c: a) pure BaF_2 nanoparticles b) SbF_5-loaded (monolayer) BaF_2 nanoparticles, pre-heating, Ar environment c) post-heating for 2h to 240°C, Ar environment. Wavelength used to collect a) and c) is 0.91Å. Wavelength used to collect b) is 0.89Å. Samples run at the National Synchrotron Light Source (NSLS), Brookhaven National Laboratories. Magenta dotted line at 67° 2θ (420 reflection) is inserted as a visual guide to denote slight changes in reflections, post heating. Post-processing was performed with Jade Powder XRD softare, Rigaku Corporation.

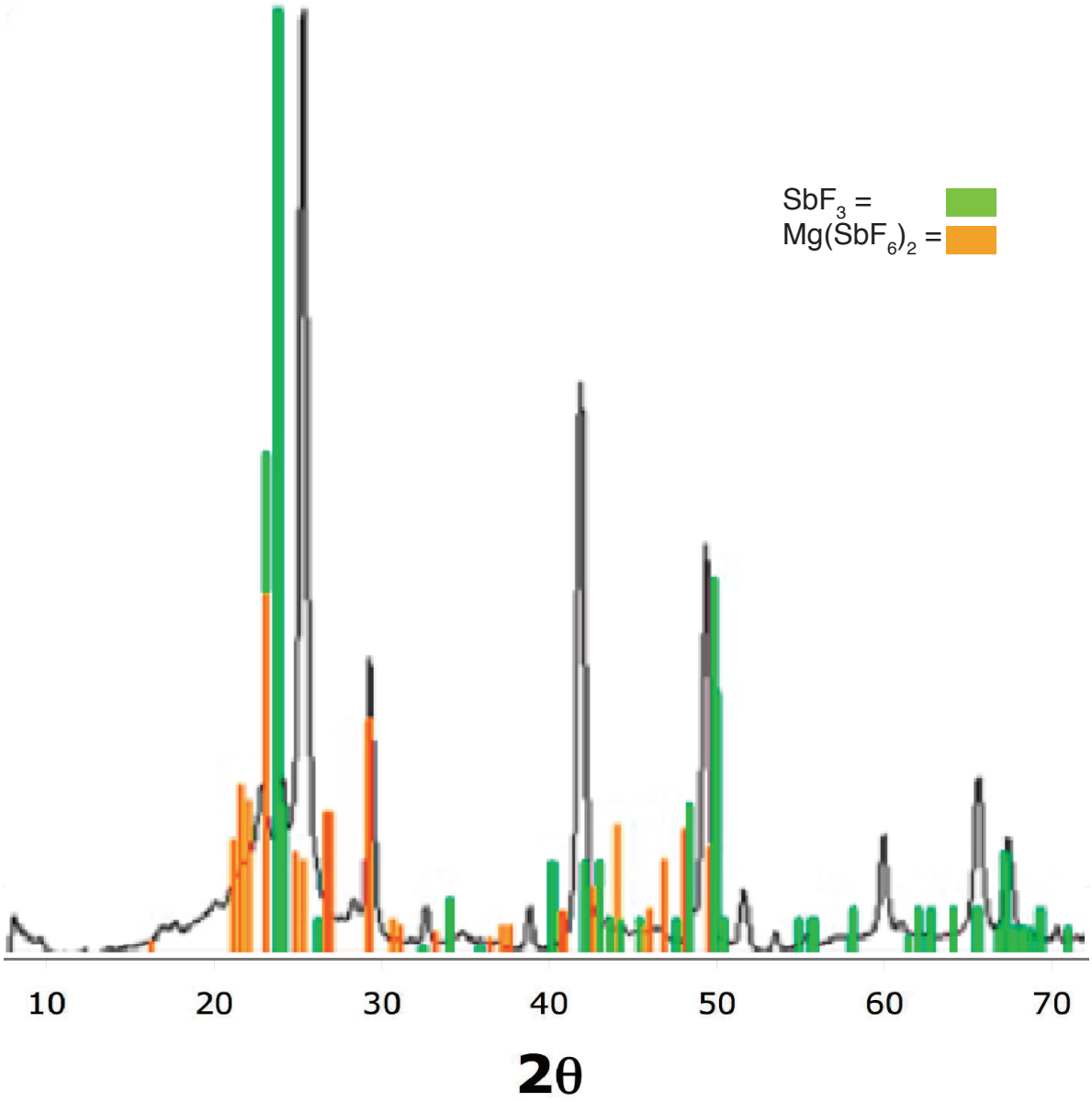

Figure 6.1d: A re-depiction of Figure 6.1b is represented here, with JCPDS overlay of SbF_3 (green) and $Mg(SbF_6)_2$ (orange), isomorphic to $Ba(SbF_6)_2$, which does not exist in the JCPDS database.

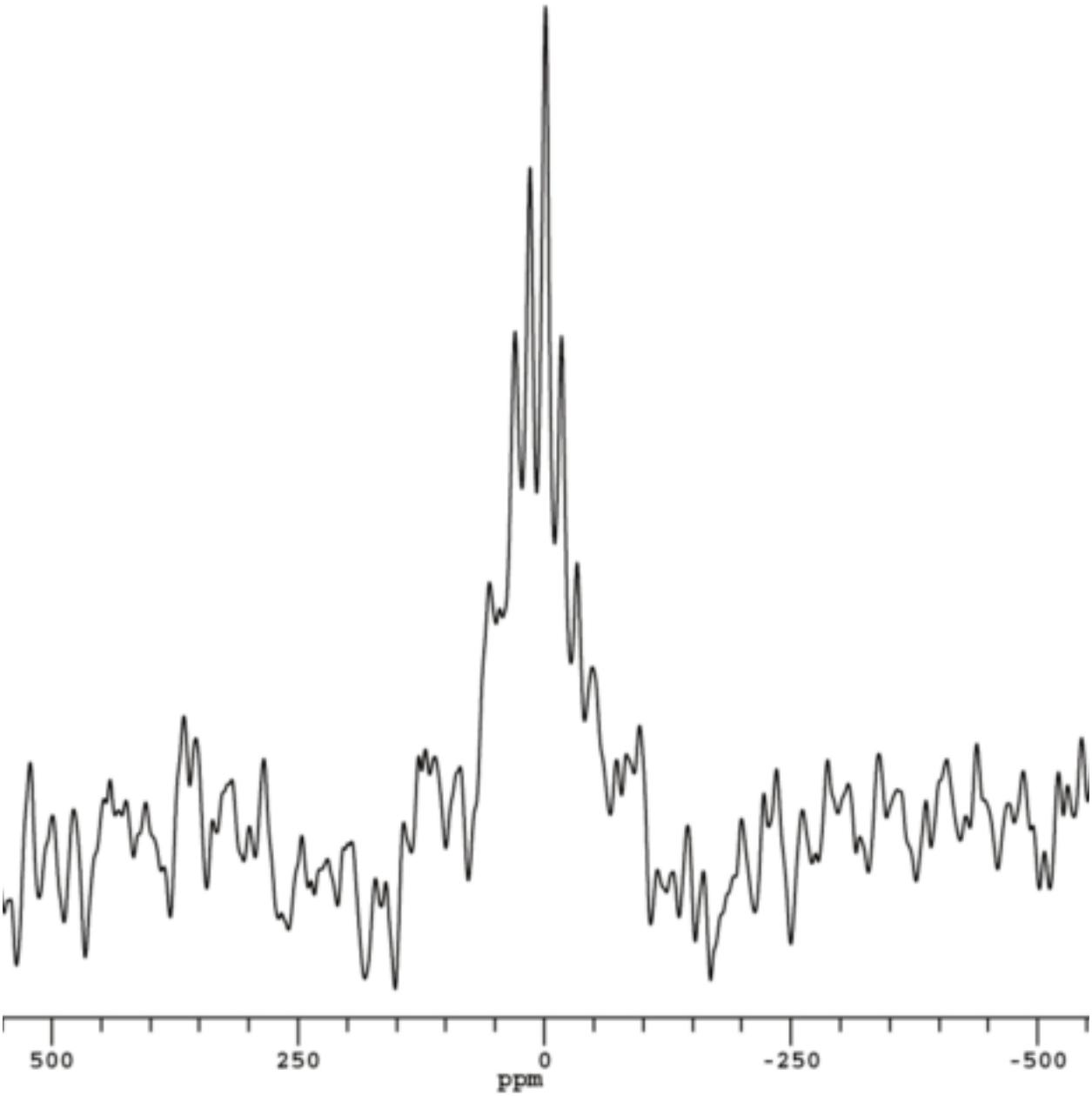

Figure 6.2: ^{121}Sb csecho MAS NMR spectrum collected on a 500MHz spectrometer. Sample was spinning at 18kHz. 36,000 scans were acquired, using an 800ms pulse delay between scans.

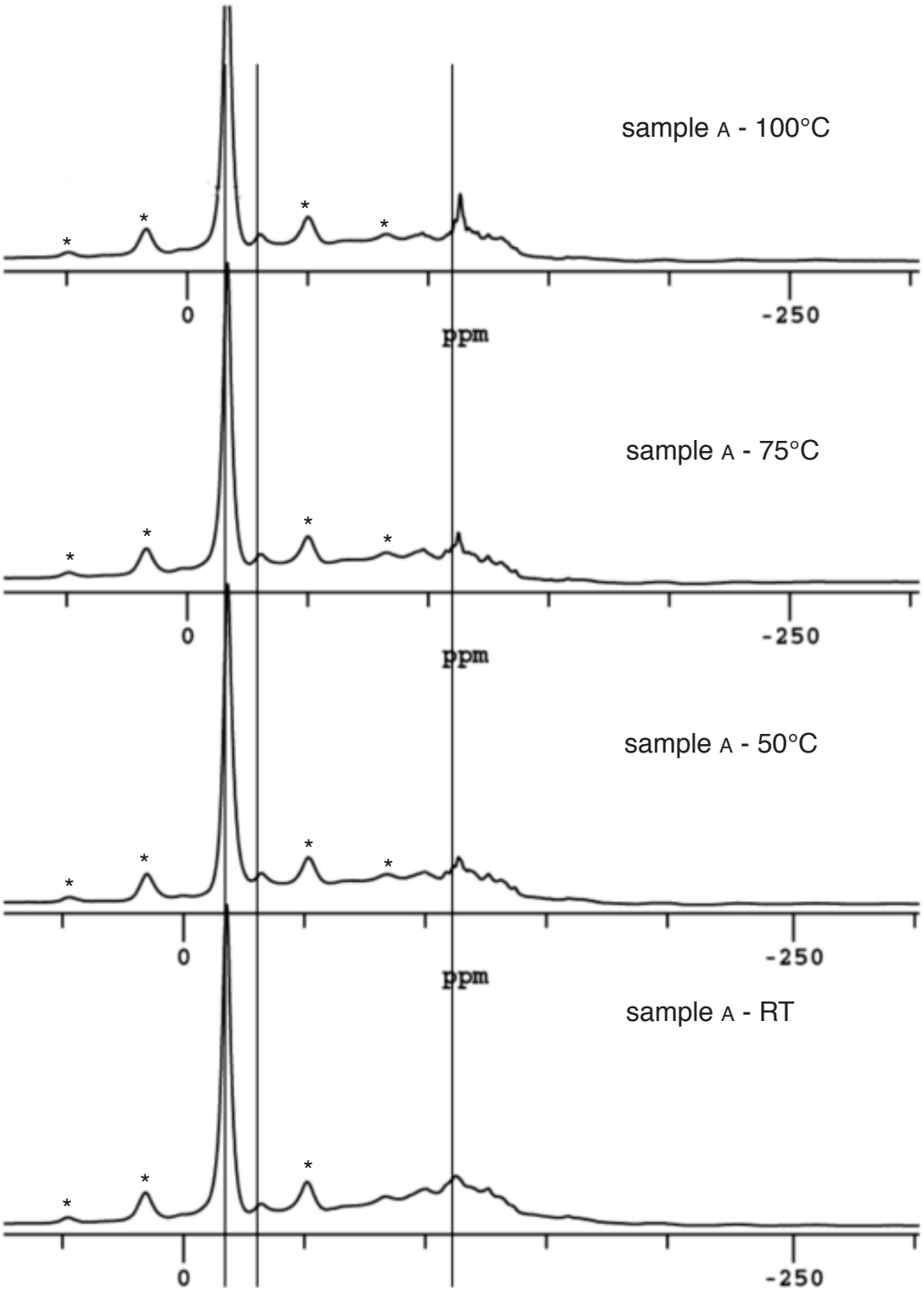

Figure 6.3: ^{19}F MAS NMR Stackplot demonstrating the temperature dependence of various species in sample A. The fluorine environments represented by the peaks at -14, -28ppm remain unchanged, whereas the SbF_3, SbF_6^- fluorines represented by the peaks at -103, -119ppm are highly influenced by temperature. 14kHz spinning speed, 360MHz. The vertical lines at -28, -119ppm serve as visual guides. Asterisks denote spinning sidebands.

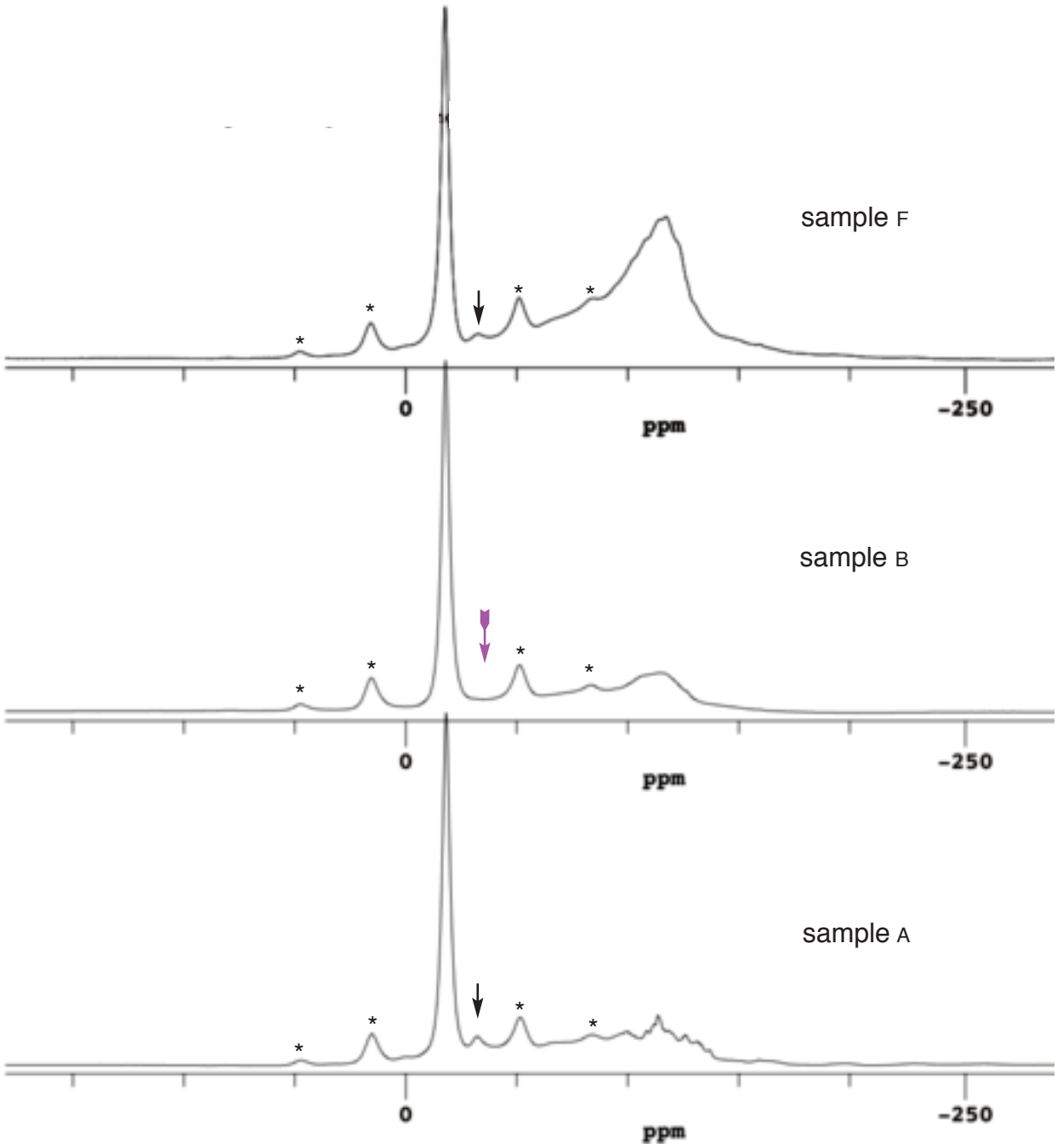

Figure 6.4: a ^{19}F MAS NMR SPE stackplot representing spectra of different loadings (samples A, B, F) at 50°C. Magenta, tailed arrow meant to highlight the absence of the characteristic peak -28ppm peak for sample B. Asterisks denote spinning sidebands.

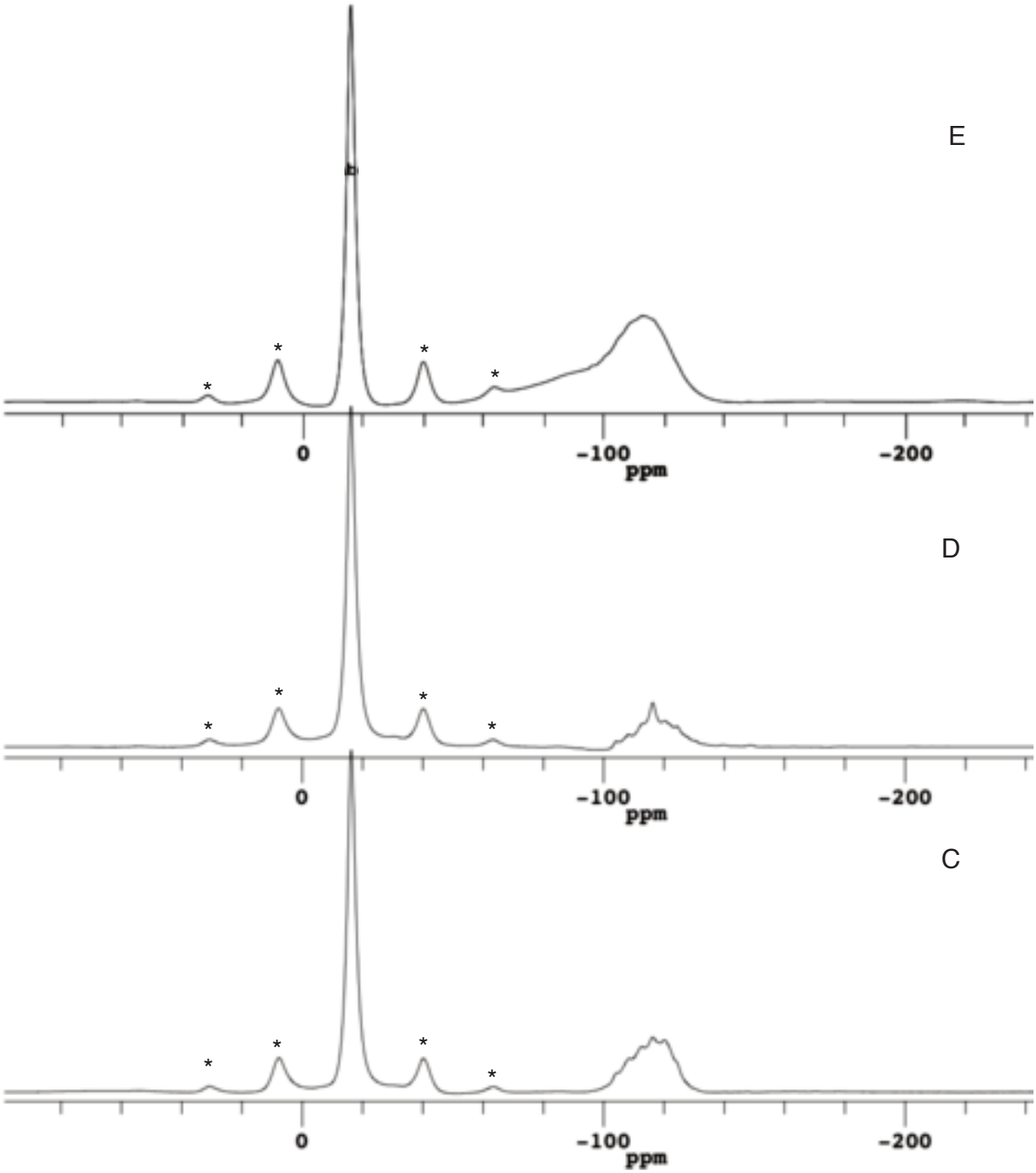

Figure 6.5: a ^{19}F MAS NMR SPE stackplot representing spectra of different loadings (samples C, D, E) at 50°C. Note the absence of the peak at -28ppm Spectra were acquired at a field of 360MHz, 1024 scans each.

Temperature (ºC)	Signal (ppm)	T_1 (s)
-80	-13	3.4
	-28	4.1
-60	-13	2.2
	-28	2.8
-40	-13	2.3
	-28	2.8
-20	-13	1.8
	-28	2.8
	-88	0.5
	-122	0.210
20	-13	1.2
	-28	1.6
	-88	0.118
	-122	0.088

Table 6.1: a tabulation of T_1 times collected from nanoparticle BaF_2 for each peak found in the spectrum for sample A, as a function of temperature. The data were collected on a Bruker 600MHz (14.1T) Avance Spectrometer at a spinning speed of 30kHz. Figure 6.6 (see next page) are the spectra collected from which the data which appear in this table were extracted.

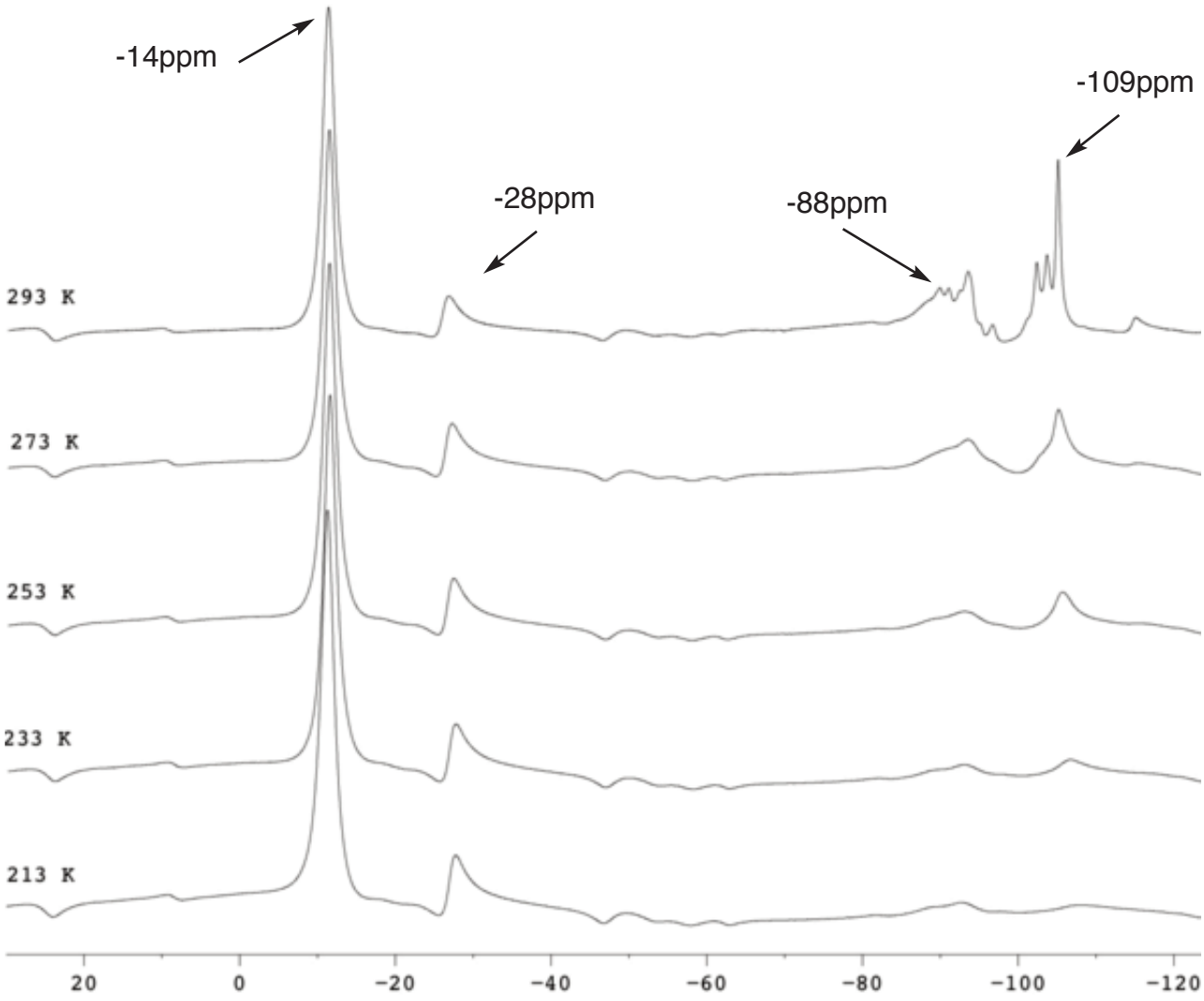

Figure 6.6: ^{19}F MAS NMR SPE Stackplot of a series of single-pulse experiments used to determine T_1 times (see Table 1 for accompanying T_1 times) as a function of temperature. Note the appearance of j-coupling observed with the antimony fluoride species (the manifolds beginning at -88ppm and then in the -109ppm range) at 20°C (293K) during this high-spinning speed (30kHz) series of experiments.

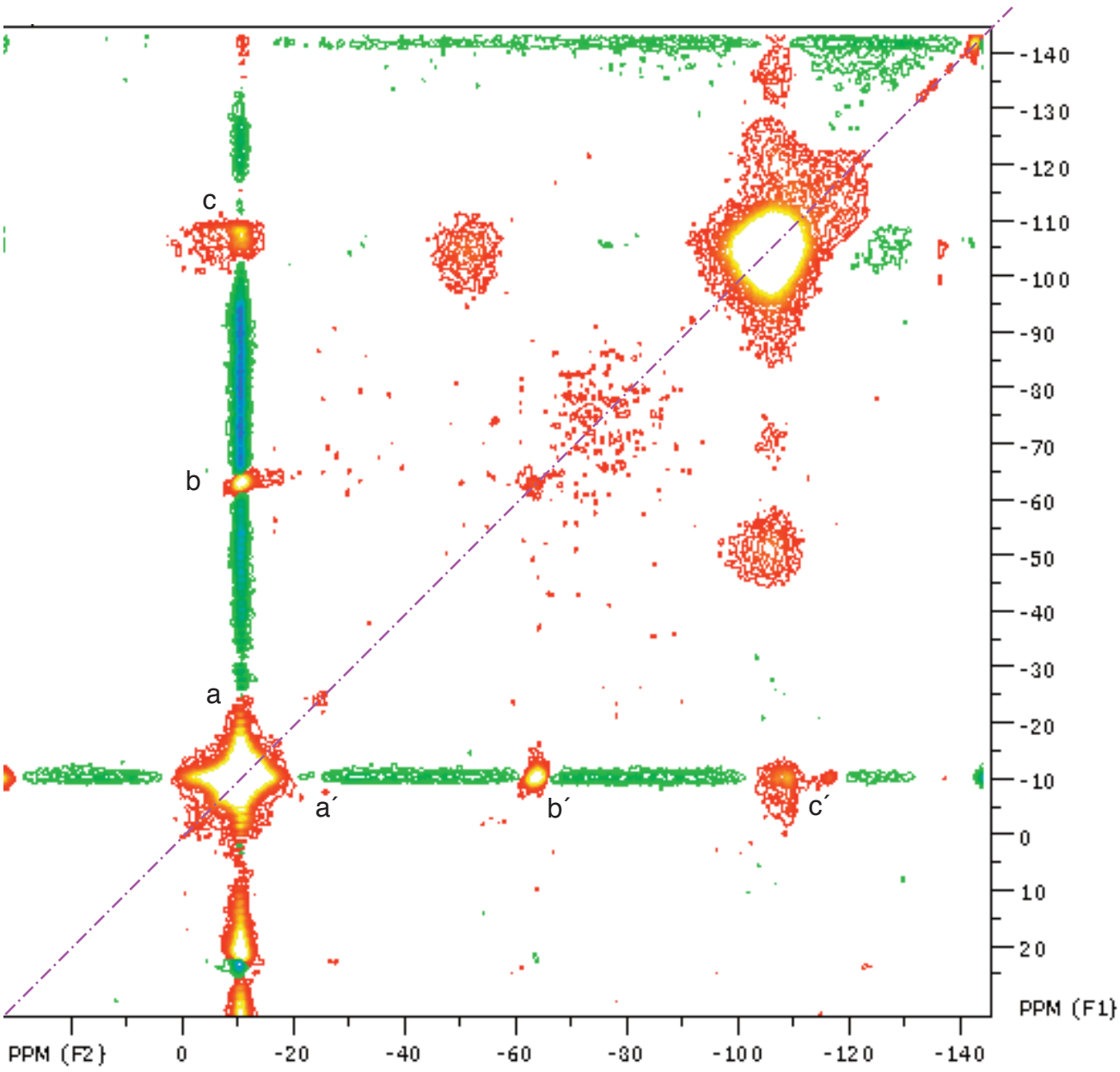

Figure 6.7: 2DME Experiment on sample A, acquired at room temperature. Spectrum recorded on a 600MHz Bruker spectrometer, at a 30kHz sample spinning speed, carrier frequency of 564.71MHz. Interaction is evident from the off-diagonal intensities present for each, relative to the other. Purple dotted line inserted as reference for main diagonal. Off-diagonal relationships are indicated by (n,n´) pairs to the on-diagonal signals.

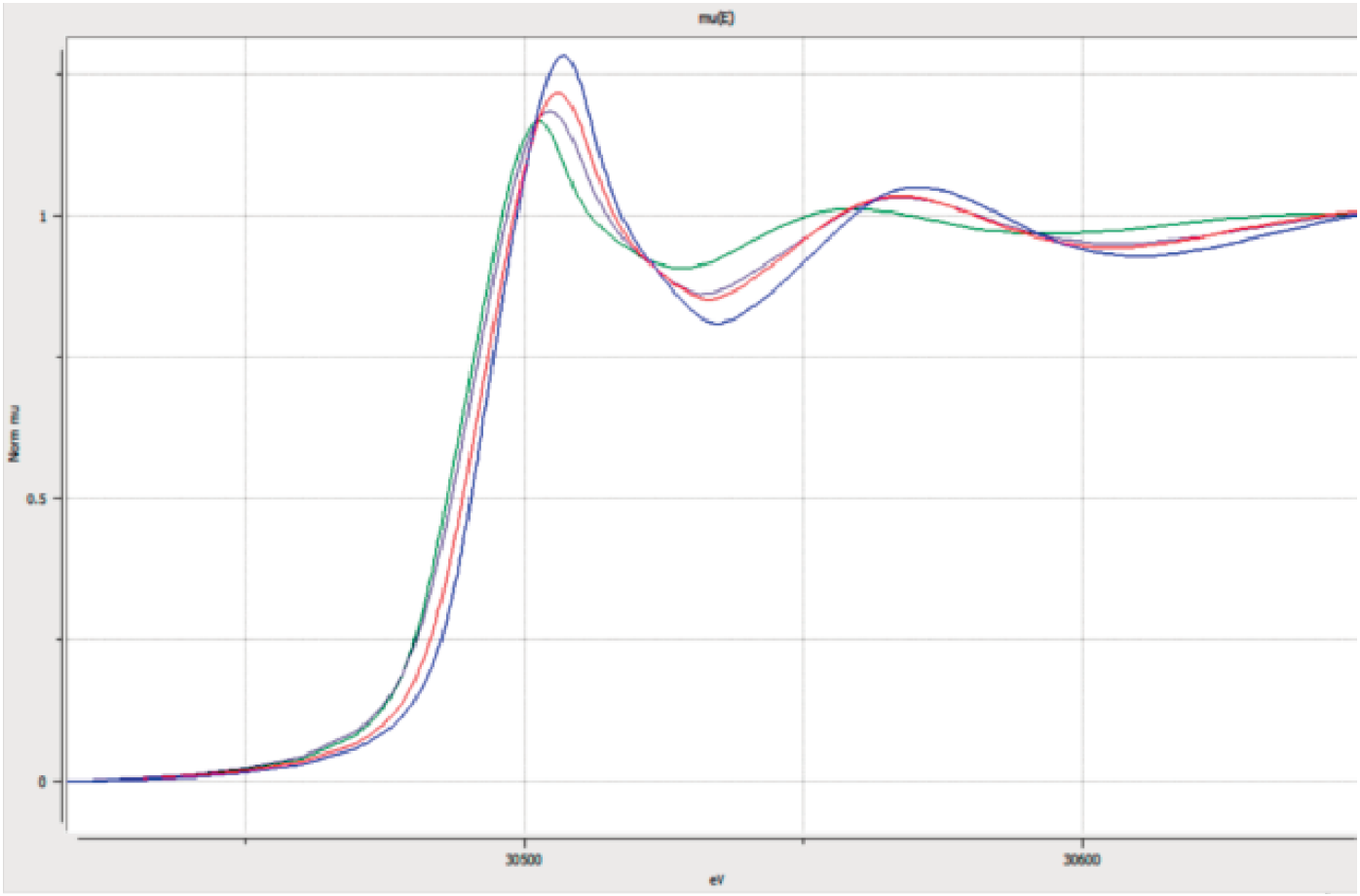

Figure 6.8a: XAS μ(E) (in eV; x-axis) versus mu (μ) of sample A (red line), sample F, (dark blue line) pure SbF_3 standard (green line) and pure $NaSbF_6$ standard (royal blue line).

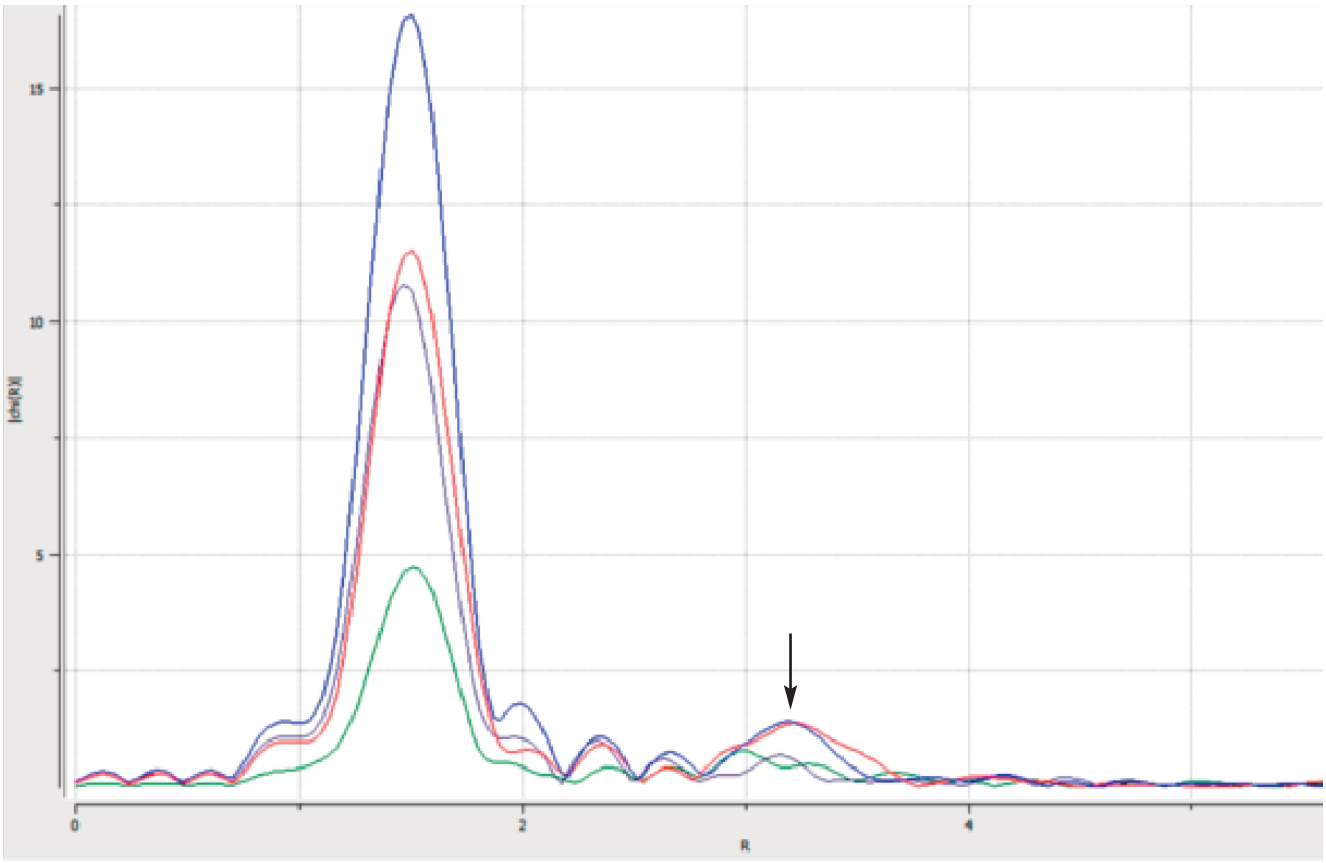

Figure 6.8b: non-normalized Fourier Transform moduli in R space of sample A (red line) , sample F (dark blue line), pure SbF_3 standard (green line) and pure $NaSbF_6$ standard (royal blue line).

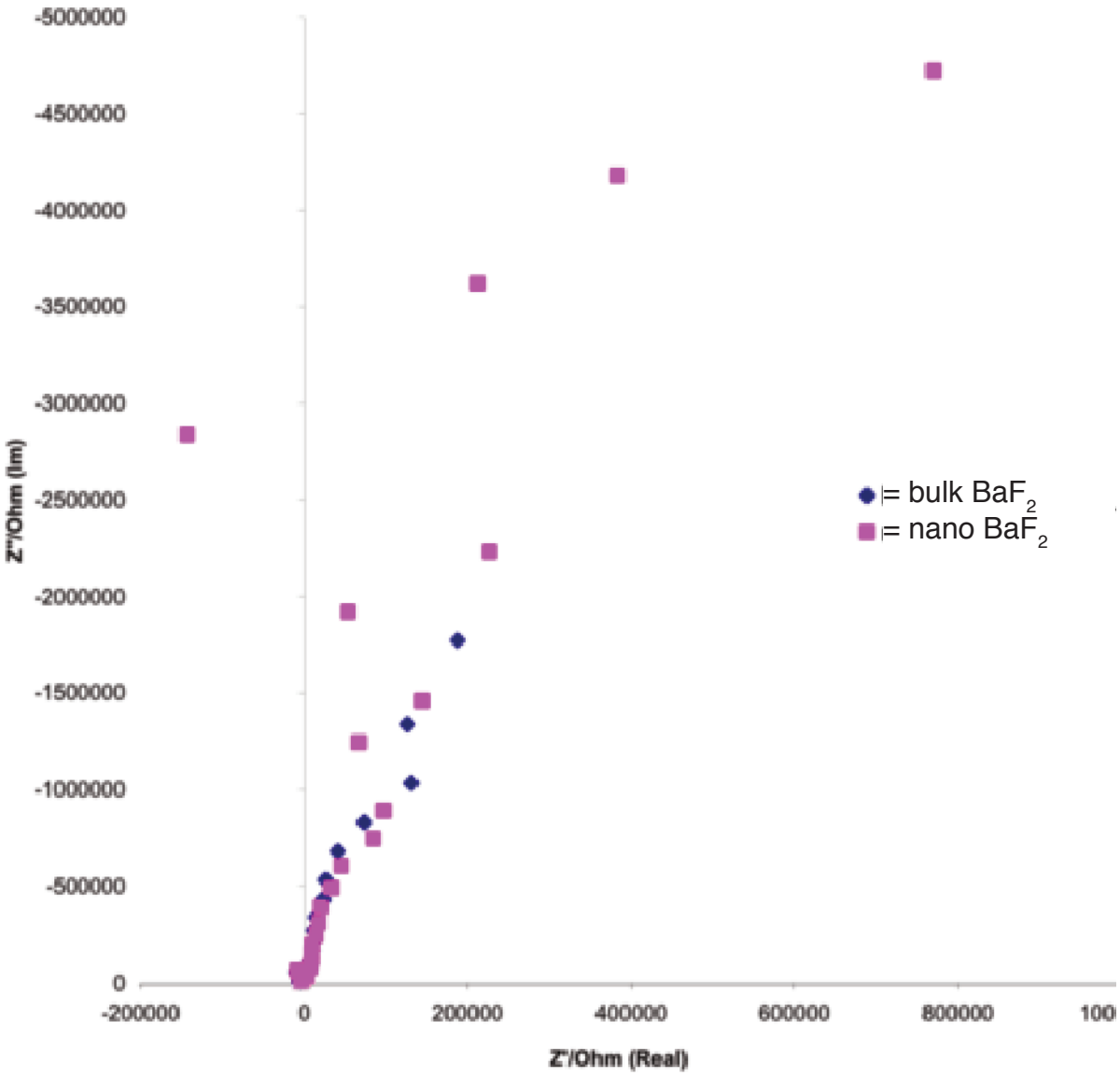

Figure 6.9a: Electrochemical Impedance Spectroscopy (EIS) curve of pristine bulk and nanoparticle BaF_2.

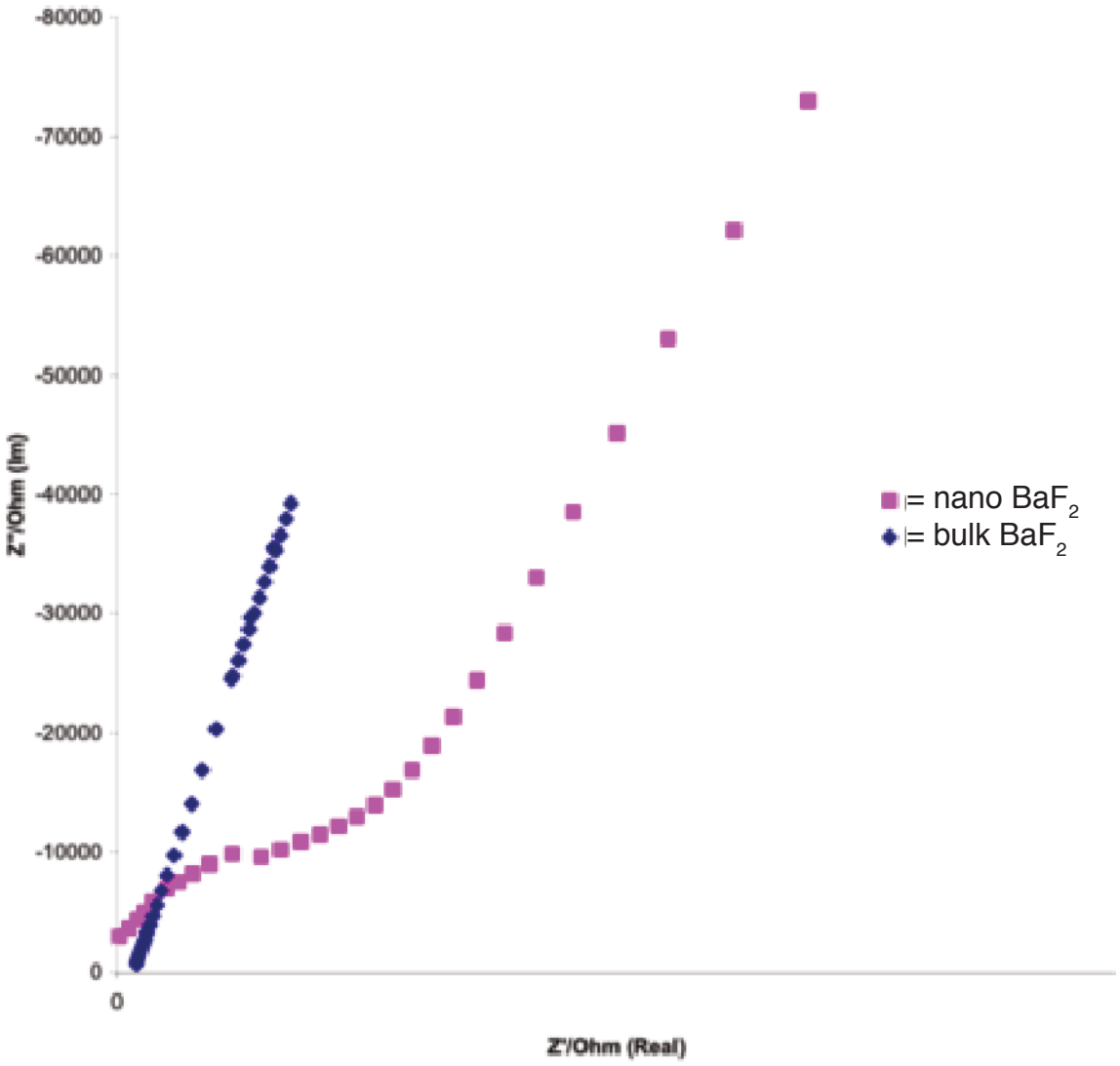

Figure 6.9b: EIS curve of bulk BaF_2 loaded with 6µl of SbF_5 in comparison to the same mass of nanoparticle BaF_2 with the same loading level.

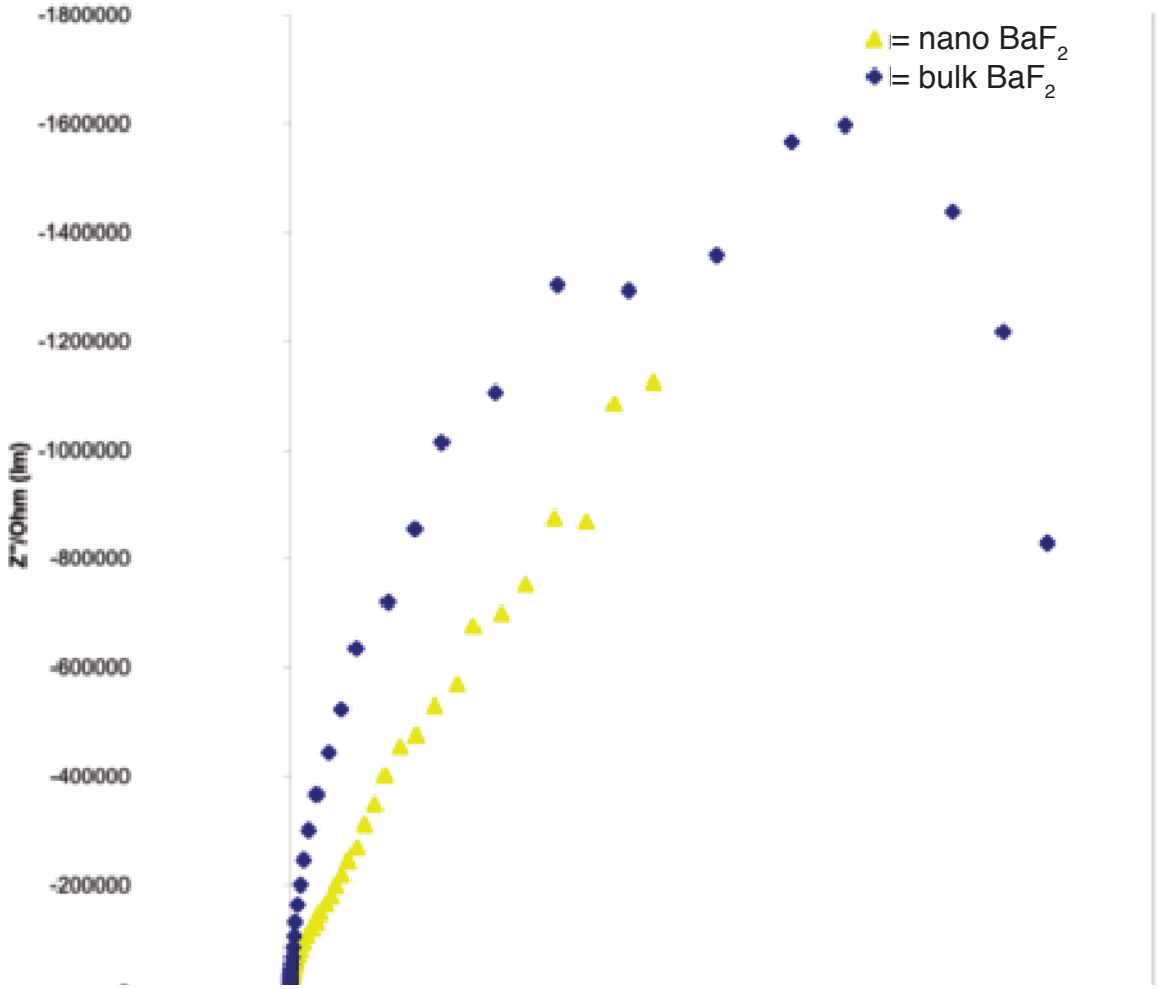

Figure 6.9c: EIS curve of bulk BaF_2 loaded with 10µl of SbF_5 in comparison to the same mass of nanoparticle BaF_2 with the same loading level.

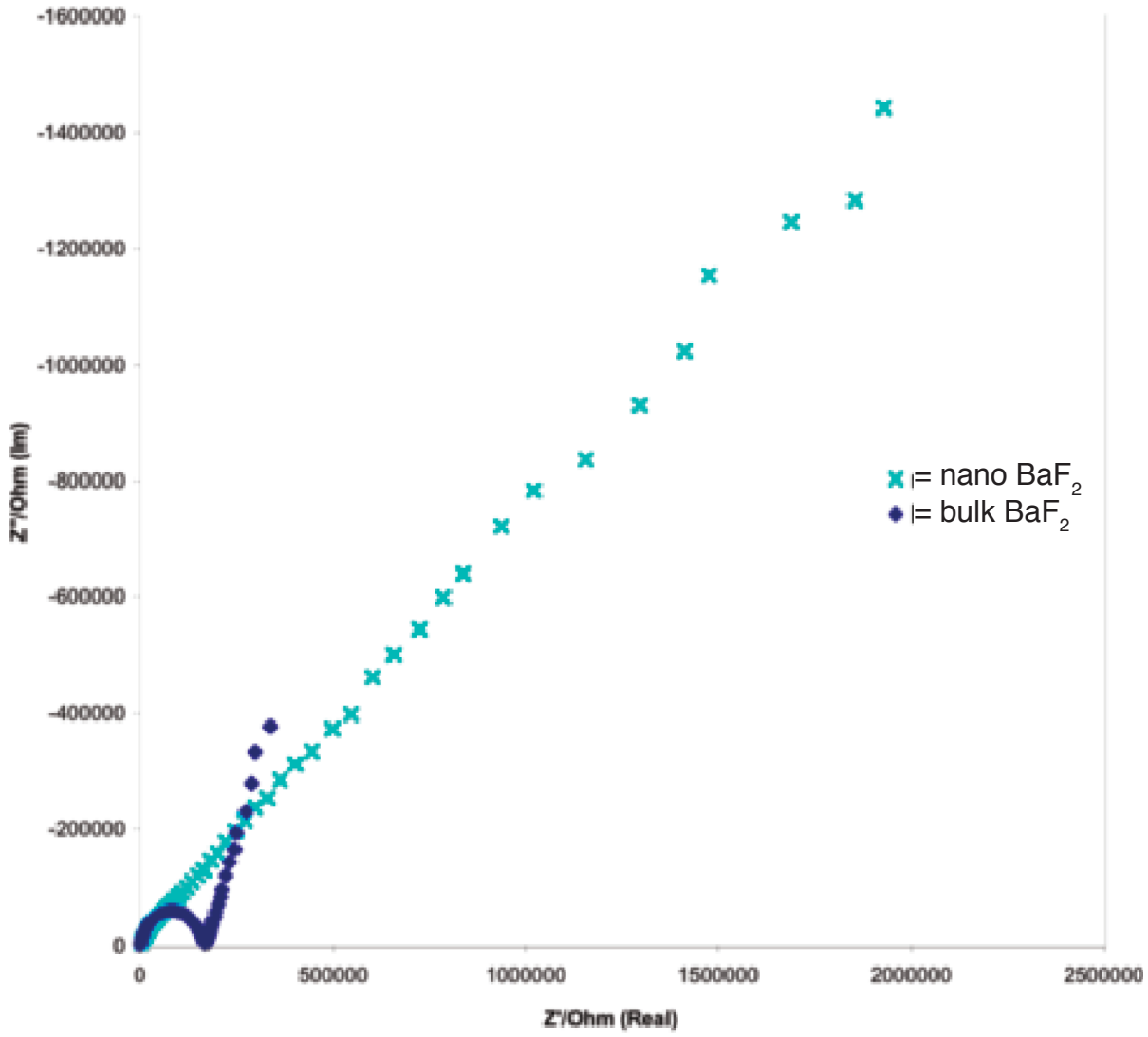

Figure 6.9d: EIS curve of bulk BaF_2 loaded with 12µl of SbF_5 in comparison to the same mass of nanoparticle BaF_2 with the same loading level. Note the change in conductivity behavior of the bulk (improved) relative to the nanoparticles (poor).

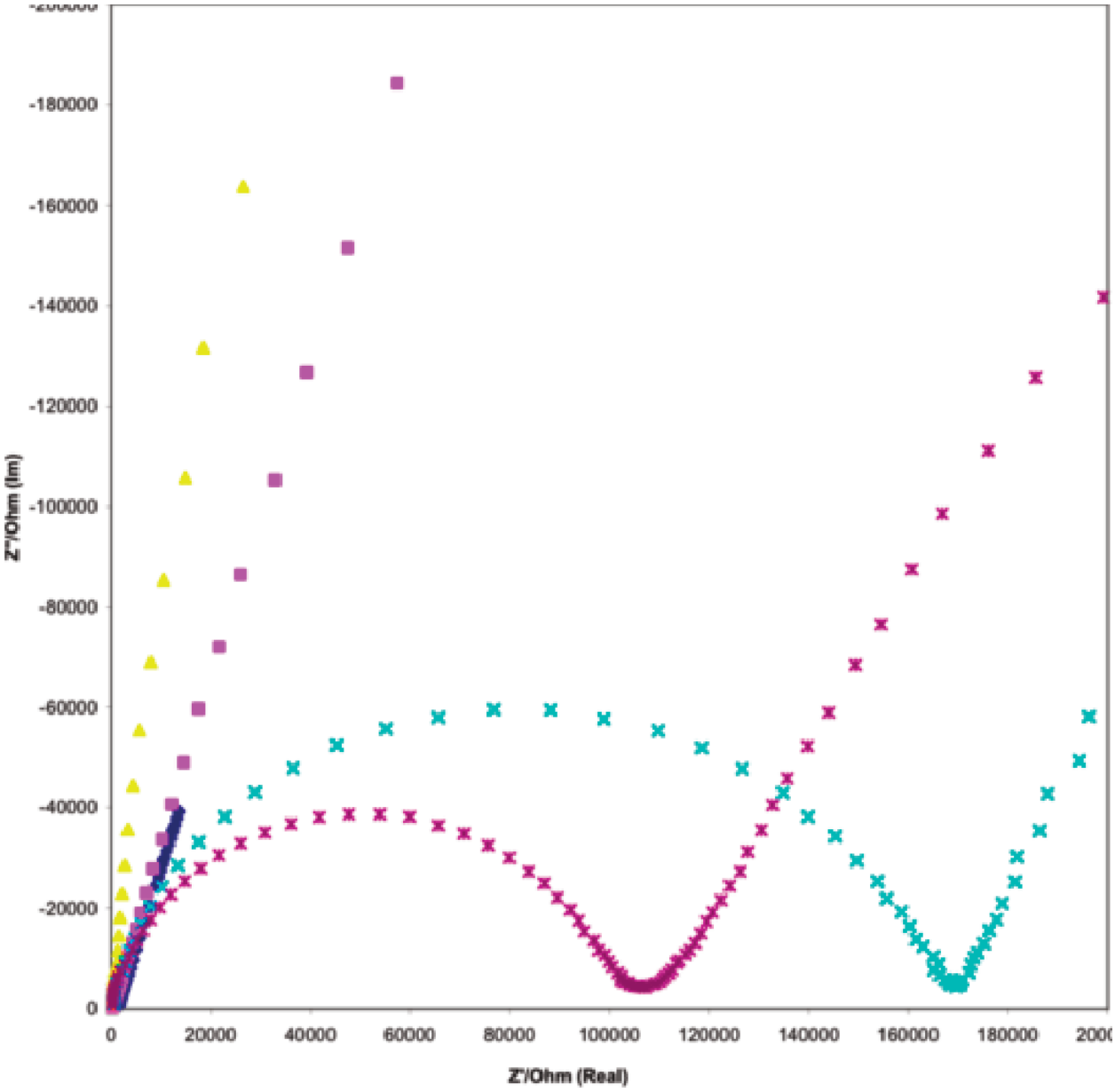

Figure 6.9e: EIS stackplot of impedance curves of bulk BaF_2 increasing loadings of SbF_5: ◆ = 6µl, ■ = 8µl, ▲ = 10µl, × = 12µl, × = 16µl.

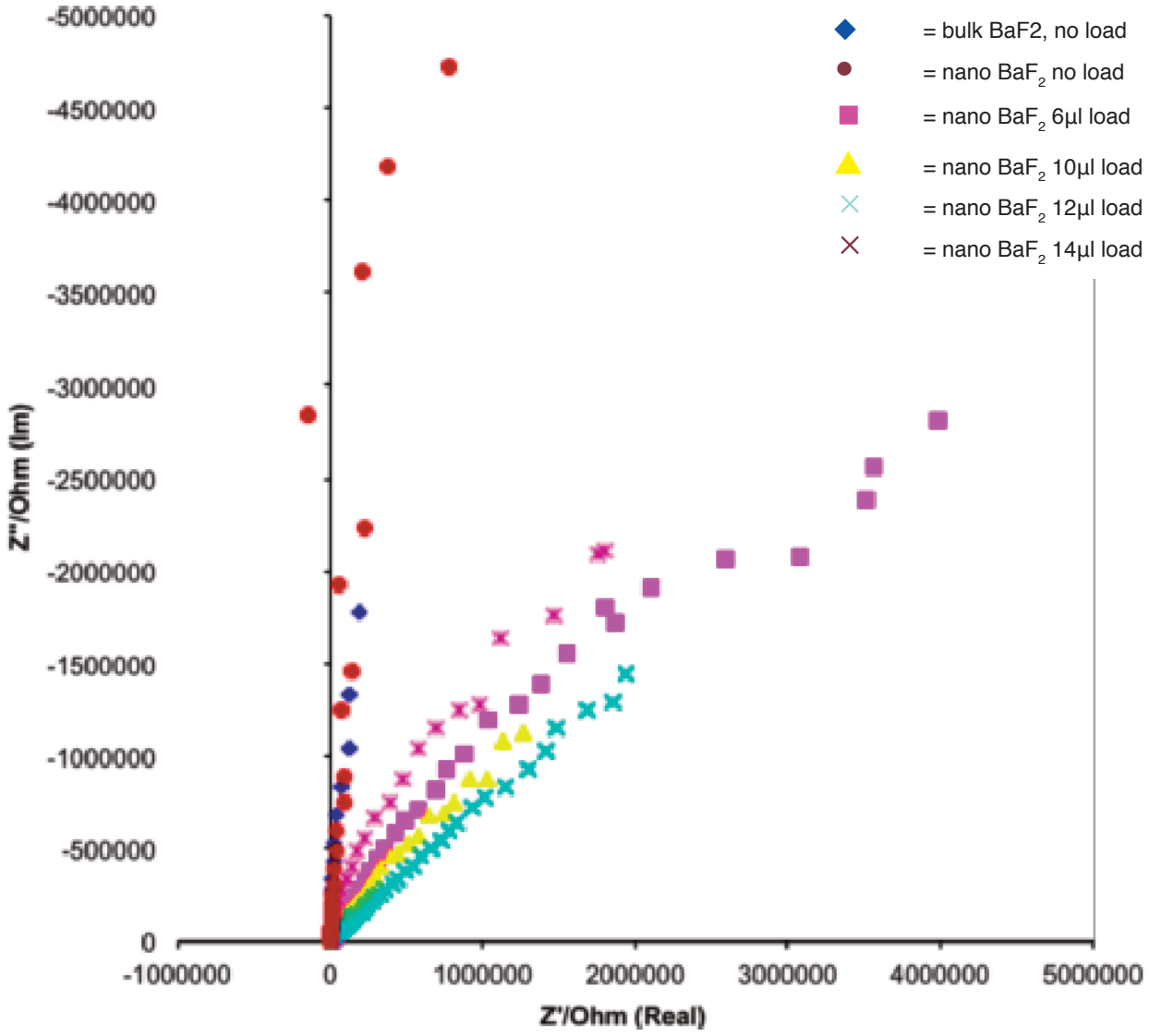

Figure 6.9f: EIS Stackplot of different loadings of nanoparticle BaF_2, in comparison to no-load bulk and nanoparticle BaF_2 (magenta circle, dark blue diamond).

6.4 Discussion

6.4.1 MAS NMR

The loading of SbF_5 onto the samples appears to reveal several complex and as-yet not completely understood interactions within the samples. It is asserted here that loading of SbF_5, a super-Lewis acid, has ultimately created a small number of both interstitials and vacancies, a technique suggested for systems such as these by Saito, et al., which was the original motivation for this approach as indicated in the beginning of this Chapter[8]. While lattice vacancies are holes having a positive charge and would only be available for calculation based on extremely precise determinations of the FWHM and the peak integration (as these represent subractive chemistry from the species in question, reflected in different FWHM and integrated area), it is likely that the interstitial fluorines, being of the same Larmor frequency, could be detectable via NMR, should the resolution (and the peak size) be amenable to detection.

The appearance of the fluorine signal at -28ppm in Figures 6.3-5 is magnetically consistent, synthetically inconsistent, yet analogous to the assertions that Jain, et al. and Abele have reported recently regarding their various routes toward their respective, different syntheses of nanocrystalline (20-30nm) CaF_2[12,13]. See Discussion Figure 1a-b for graphic reference. In their respective MAS NMR studies, they synthesized nanocrystalline CaF_2 via different methods (starting materials, routes and solvents). The appearance of what both authors assert in their own studies is that the peak that is seen at approximately -130ppm is that of a cubooctahedral interstitial fluoride anion[12,13].

As mentioned above, the appearance of a signal upfield from the bulk BaF_2 species may be magnetically and chemically consistent, but is synthetically inconsistent with the method used here.

a

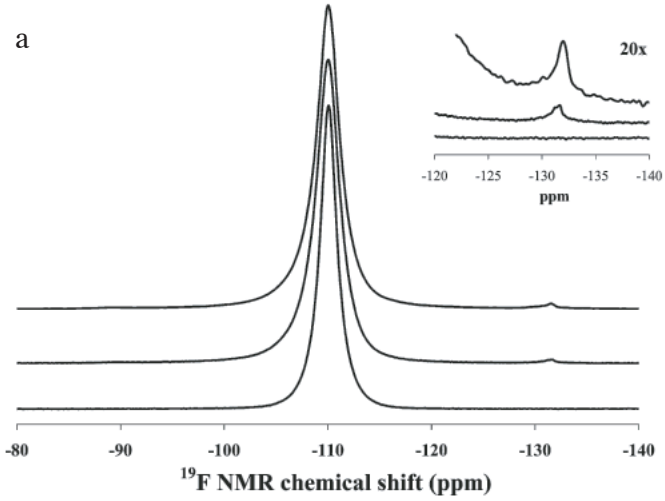

Figure 1. From bottom to top: ^{19}F MAS NMR spectra of bulk and nanocrystalline CaF_2 with crystallite sizes of ~50 and 25 nm, respectively. Inset shows the region between −140 ppm and −120 ppm for these samples, magnified by 20×.

b

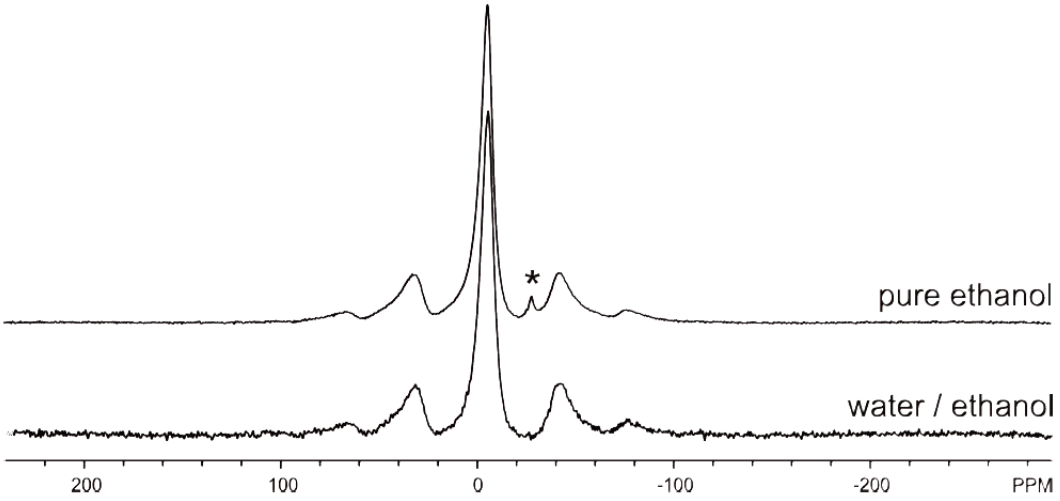

Figure 5.12: ^{19}F MAS NMR spectra for a CaF_2 prepared in a water/ethanol mixture and in pure ethanol. The extra peak present in the one prepared in pure ethanol is marked by a asterisk.

Discussion Figure 6.4.1a, b: Reprinted from [12, 13, respectively]. Appearance of F^- interstitial in nanocrystalline CaF_2 in 1a (inset) and in 1b (asterisk). NB: No explanation is given in [13] for the discrepancy in chemical shift assignment (see 1b: 0ppm for CaF_2 should be -109ppm, despite peer-review references to ^{19}F MAS NMR data for CaF_2 in the author's dissertation.

In the studies here, the super-Lewis acid SbF_5 was used to *induce* vacancies, consistent with the work done by Saito, et al[8]. This is in contrast to the Jain and Abele, as they, through

provocative synthetic routes and no super-Lewis acid loading, were able to induce interstitials within the nanocrystalline bulk[12,13]. It is interesting to note that Saito, et al., did not anticipate the appearance of interstitial fluorines as apparent from their 1995 paper, focusing instead on vacancy formation and conductivity as a result of bulk fluorines[8]. In contrast to Saito, however, the unanticipted consequence found here is that fluorine interstitials were apparently formed. This was unanticipated, simply because conventional logic presumes super-Lewis acids like BF_3 and SbF_5 are so acidic that they wrest fluorines from the polycrystalline bulk and that, consistent with space-charge theory, conductivity should occur as a result of the vacancies that are formed in the lattice. Although when paired in binary systems, CaF_2 will tend to form interstitials and BaF_2 vacancies in the lattice, interstitials in unary or doped BaF_2 systems have been a documented event[28,29].

Basic NMR theory supports this assertion, in that a fluoride anion within an interstitial site is not in a lattice site. Therefore, it has no adjacent cations formally bound as a lattice points in a coordination shell, which would thereby reduce the chemical shielding afforded by the electron cloud. With greater chemical shielding that these conditions afford an interstitial anion, it is logical that the chemical shift of a more statistically negative species would be evident as an NMR peak that is upfield from a lattice-bound isoelemental anion. Considering the cationic-coordinated radii of the Ca^{2+} and Ba^{2+} in the species (1.14Å, 1.49Å, respectively), it is again consistent with basic NMR theory, from the perspective that the 24.5% smaller calcium cations surrounding the interstitial site offers less relative capacity for coordination of the interstitial. As such, a greater upfield shift due to less electronic shielding is logical.

As can be seen to a limited extent in Figures 6.4, 5 and to a more detailed extent, Figure 6.7, it is clear that the relatively nondifferentiated lineshape between -100ppm and -120ppm is not exclusively SbF_6^-. Formation of SbF_3 was unanticipated, but a subsequent literature search points to this as a known phenomenon: the application of SbF_5 to Group I, II fluorides and

several subgroups along the Transition-Metal and Metalloid landscape of the Periodic Table in the form of MF_5 tend to form ratios of SbF_3 and SbF_6^- species, and often in the form of $TM(SbF_6)_2$[10,11,14].

6.4.2 XAS/EXAFS

The XAS/EXAFS studies performed at SSRL, depicted in Figures 6.8a, b, support the findings discovered with MAS NMR that a ratio of Sb^{3+} and Sb^{5+} exist within the samples studied (A and F) and that this ratio logically changes with different SbF_5 loadings toward more energetically favorable states. For example, in Figure 6.8a, the Sb k-edge for sample F is clustered near the Sb^{3+} k-edge (SbF_3, green line), indicating a higher presence of Sb^{3+} antimony in the sample. In this more heavily loaded sample F, chi-square analysis determined that the ratio of Sb^{3+} to Sb^{5+} became more equitable at 52%:48% (~1:1; $\chi^2 = 0.2613$). This is chemically consistent with the energetics of the system, but the inability to actually determine the precise SbF_6^- species formed make what would be a simple Hess' Law calculation impossible to determine. For example, normalizing the masses of the starting materials, (1.25×10^{-3}mol BaF_2; 5.5×10^{-5}mol SbF_5) and combining them with the relative ratios of Sb^{3+}, Sb^{5+} determined by the XAS data for sample A, one can conjecture one possible initial equation:

$$2.27BaF_2 + SbF_5 \rightarrow 2.27\text{-}\sigma BaF_{2\text{-}\sigma} + 0.4SbF_3 + 2\text{+}\sigma F^- + 0.6M_x(SbF_6)_y$$

This presents several frustrating challenges: 1) BaF_2 under these conditions would actually be participating as a reducing agent for the antimony going from $Sb^{5+} \rightarrow Sb^{3+}$, which appears to have occurred, but this implies that at least in some small fashion, the crystalline BaF_2 (either the Ba or the F) has briefly acted as a stronger Lewis acid than SbF_5. 2) since the precise nature of $M_x(SbF_6)_y$ is not known, it is unclear whether M = Ba or, for example, that SbF_6^- has participated in the formation of an oligomer-type salt, where bridging fluorines span, new crystal (albeit in extremely low concentrations).

3) The system may be in equilibrium such as in the $2Sb_3F_{16}^- \rightleftarrows Sb_4F_{21}^- + Sb_2F_{11}^-$ profferred by several authors, although the poorly resolved peak manifold in the -88ppm — -115ppm region offers little definitive guidance[14,16]. It is tempting to consider this equilibrium if these dynamics can occur on a friendly surface which is stable enough to occur and bound tightly enough to remain present after exceeding the boiling point of SbF_5 during MAS NMR, confirmed during these investigations. This scenario offers a reasonable explanation for the obvious dynamics as a function of temperature (Figure 6.6), but it would also explain the uncanny similarities in spectra between the j-coupling seen here and previous ^{19}F liquid NMR experiments of SbF_5 by Edwards, Bacon, et al[14,16]. 4) Figure 6.1b, c appear to support a slight drop in BaF_2 crystallinity, as well as a shift in higher 2θ values; this calls into question the value of σ in the suggested initial equation above. The possible values of the x, y variables would be further minimized if the observed drop in BaF_2 crystallinity could (this being a zero-sum game) be quantified, but it would require a second equation to determine the ultimate fate of the fluorines represented by the $2+\sigma F^-$ term.

Chi square analysis of the data for sample A, when the Fermi Energy (E_0) was allowed to float, was found to shift by only -0.42eV. This gives reasonably reliable confidence (χ^2 = 0.1314) that the ratio of Sb^{3+} to Sb^{5+} is 41%:59%, respectively, in sample A and is consistent with previous EXAFS/XANES Sb k-edge data on compounds containing SbF_5[15]. This is possibly reflected in the spectrum at the top in Figure 6.4; the poorly differentiated lineshape in the region of -100 — -120ppm likely masks the extremely broad feature seen in the baseline which can be seen as a distortion under the right spinning sideband belonging to the signal generated by BaF_2. These findings are also consistent with the apparent appearance (although in low intensity) of SbF_3 in Figure 6.1b, c, d. The low intensity for purported SbF_3 reflections in Figure 6.1b, c, d is not convincing enough, but the relative ratios and distances indicated in the XAS/EXAFS graphs of Figure 6.8a, b indicate that both are clearly present. Crystalline formation overall refutes the hypothesis that pure sorption occurs in a system such as this and the combination of all these data, taken as a whole, appear to securely refute this.

6.4.3 Chemical Shift Assignment

Several literature sources identify the SbF_6^- species to be between -108.9 and -119ppm and the SbF_3 species at -85 — -103ppm[14,15,16,20,21]. The difficulty encountered with NMR of these species, dating as far back as 1958, is the fact that both in solution as well as sorbed onto species, SbF_5 ends up forming a range of oligomers (cis-trimers, $Sb_3F_{16}^-$, and both axially and equatorially coordinated tetramers: $Sb_4F_{21}^-$), as well as adducts such as $[MF_n]^{n+}\bullet[Sb_2F_{11}]^-$ with the co-precipitant metal fluorides with which they react[14,15,16,17,18,19,22,23]. This makes precise chemical shift assignment for the fluorine species associated with SbF_5 indeterminant. Exemplary of this phenomenon, evidence of this can be seen in Figures 6.7 and 6.9 and inferred from Table 1: all of the Sb_XF_y species are highly influenced by temperature, volume and, as indicated the literature, form a range of variable species. The lower field, higher temperature spectra in Figures 6.3 and 6.5, and to a greater degree, the higher field spectra seen in Figure 6.7 more clearly demonstrate j-coupling that begins to emerge as a function of temperature, of the otherwise sorbed species. To confirm this (not shown here), pre- and post-high temperature (180°C) one-pulse experiments were conducted to confirm that the Sb_XF_y species were firmly chemically a part of the system, given that the boiling point of SbF_5 is 158°C. No changes were seen in pre- and post-heating MAS NMR spectra.

6.4.4 Powder XRD

To determine whether crystallinity could or had occurred in the samples, controlled, heated powder XRD was performed at the NSLS, Beamline X7-B, as depicted in Figure 6.1a-d for the SbF_5-monolayered nanoparticle BaF_2 sample A. The low symmetry and low crystallinity of SbF_3, is vident in Figure 6.1b, c, d (where in Figure 6.1d, the JCPDS overlay is present) which belongs to the C2cm (C2/m) space group (monoclinic No. 40)[24]. The difficulty in reflection assignment is evident in Figure 6.1d, however this low (but non-negligible) crystallinity is consistent with the

evident in Figure 6.1b, c, d (where in Figure 6.1d, the JCPDS overlay is present) which belongs to the C2cm (C2/m) space group (monoclinic No. 40)[24]. The difficulty in reflection assignment is evident in Figure 6.1d, however this low (but non-negligible) crystallinity is consistent with the EXAFS data (and Sb^{5+}/Sb^{3+} ratios) represented in Figure 6.8b and discussed in the EXAFS section above.

As indicated in [25], the stoichiometrically stable forms of other Group II metal-hexafluoroantimonates are likely isostructural and the JCPDS pattern for $Mg(SbF_6)_2$ is thus indicated in Figure 6.1d. As can be seen, while some structural similarities may exist at lower 2θ values, they are masked by the largely non-existent reflections and any similarties are offset by the mismatch of powder patterns with high 2θ reflections.

What is clear in Figures 6.1a-c is that the intensity of the pure BaF_2 peaks has been only slightly lost, presumably to the largely non-crystalline nature of the loaded materials which removed fluorines from the crystal lattice. As can be seen in Figure 6.1b, c very little crystallinity had developed in either the pre- or post-heat, demonstrated by the weak reflections and amorphous low-2θ structure. Previous literature cites the fact that only non-stoichiometric samples of $Ba(SbF_6)_2$ or $BaF_2 \bullet 2SbF_5$ had ever been synthesized and produced no crystallinity as well[25,26]. This absence of crystallinity is consistent with the broad variations in NMR lineshape seen in Figures 6.3 - 6. As observable in Figures 6.3 and 6.6, the monolayer of SbF_5 tends to be highly variable, given only 25°C incremental increases in temperature.

6.4.5 Spin Diffusion and Fluorine Motion

2DME experiments are useful tools in the examination of spatially proximal spins. Since the effect is dipolar mediated, through-space interactions between nearby fluorine spins (in this particular case) permit greater understanding as to how the different atoms interact. As observable in

Figure 6.7, the fluorine interstitial represented by the peak at -28ppm is interactive only with the-BaF_2 lattice, as demonstrated by the off-diagonal peaks corresponding to only the peaks which represent the signal from the fluorines within the BaF_2 lattice (see off-diagonals: a, a´). Although indirect, this observation is consistent with the fluoride being interstitial (when taken into consideration with the rest of the data presented in this chapter), as it cannot interact with species outside the lattice surface under these benign conditions at which the experiment was conducted (RT). A second, slightly more complex interaction appears evident between the Sb_xF_y species and the BaF_2 lattice; the non-symmetric off-diagonal peaks (see off-diagonals: c, c´) appear to indicate that both SbF_3 (-92ppm) and SbF_6^- (-119ppm) are interacting with the BaF_2 lattice (-14ppm). What is not understood is the obvious interaction by an unidentified fluorine species at -63ppm (see off-diagonals: b, b´) and the BaF_2 nanocrystalline lattice fluorines, yet which is not evident in the stackplot of 1D spectra, Figure 6.5, taken on the same sample, at the same 600Mhz field.

In the one-dimensional experiments depicted in Figure 6.6, clear changes in lineshape are seen as the temperature is raised. More precise concepts of these changes and clear trends are reflected in the data presented in Table 6.1. For example, the BaF_2 fluorines represented by the signal at -13ppm demonstrate a consistent trend toward increased motion by the drop in T_1 times. What is less clear is the trend demonstrated by the interstitial fluorines at -28ppm. It consistently demonstrates slower motion, relative to the bulk fluorines which, conceivably, are adjacent to this small population of interstitials. This calls the location of these interstitial fluorines into question, as they could be seen as the interfacial boundary, between the sorbed Sb_xF_y species on the surface of the crystallites and the “interior” of the BaF_2 nanocrystallites. The progressive emergence of the Sb_xF_y peaks in Figure 6.6 are reflected in fast preliminary T_1 times as well as the dramatic drop in T_1 times for those same fluorines associated with the peaks at -88 and -113ppm.

Taken with the 2DME spectrum in Figure 6.6, a self-consistent system begins to emerge: interstitial fluorines appear to be trapped deeper within the BaF_2 nanocrystalline lattice and only interact with the fluorines within the lattice itself. Although the proximal geometry of this system is unclear, the interaction between the fluorines associated with the BaF_2 lattice and the Sb_xF_y species is apparent from Figure 6.8, but it cannot necessarily be correlated to the concomitant drop in T_1 time for either the fluorines associated with the BaF_2 lattice (at -13ppm) or the interstitials (at -28ppm); the difference in T_1 from 253 — 293K for both species is approximately the same (~55%). What is clear is the inherently fast motion of the fluorines associated with the SbF_x peaks at -88 and -113ppm.

6.4.6 Conductivity

AC impedance data demonstrated in Figure 6.9a-e make comparison between the microcrystalline and nanocrystalline BaF_2 difficult. The same absence of conductivity is exhibited in Figure 10a between the two forms of BaF_2. Figure 6.9b appears to demonstrate increased conductivity of the nanocrystalline loaded BaF_2 in the conventional sense of conductivity measured by AC impedance, the arc as defined by Re:Im(z) begins to take shape and the angle subtended by the curve indicates the conductivity. This curve begins to be evident in Figure 6.9b, but this classic curve disappears as the SbF_5 loading is increased in Figure 6.9c. In Figure 6.9d, typical conductivity is exhibited by the bulk loaded BaF_2, yet diffusion impedance appears to be the primary mechanism for conductivity in the nanoparticle BaF_2, otherwise known as the Warburg or the linear component of the curve at lower frequencies (at the right of the graph)[27]. Figures 6.9e, f demonstrate the overall trends of the increased loadings on bulk and nanoparticle BaF_2, respectively, and appear to highlight the main difference in conductivity mechanisms exhibited. The Warburgs exclusively exhibited by the nanoparticle BaF_2 in Figure 6.9f appear to demonstrate the diffusive mechanisms behind the ionic conductivity in these samples. By contrast, Figure 6.9e demonstrates conductivity typically seen in EIS data: Warburg, followed by conductivity.

6.5 Conclusions

Loading of the super-Lewis acid antimony pentafluoride onto nanocrystalline BaF_2 appears to induce both vacancies and interstitials. The investigations here appear to be the first evidence of interstitial fluorines detected by MAS NMR in nanocrystalline BaF_2 as induced by this method. Although the species that are created by reaction of SbF_5 on nanocrystalline BaF_2 appear to be highly temperature dependent and mobile, enhanced ionic conductivity was not achieved in the conventional sense; EIS studies indicate that diffusion impedance is the mechanism by which ionic conductivity occurs with nanocrystalline BaF_2, but that typical ionic conductivity is demonstrated by microcrystalline (5μm) BaF_2.

EXAFS experiments determined that both Sb^{3+} and Sb^{5+} oxidation states exist within the sample and the ratio between the two is loading dependent. This confirmed the MAS NMR observations that poorly formed lineshapes spread over a 40ppm range were in fact highly variable species that may span several different species of Sb_xF_y, including SbF_3, SbF_6^-, $Sb_2F_{11}^-$, $Sb_4F_{21}^-$ and possibly others.

Powder XRD studies determined that little if any crystalline species form as a result of the reaction between nanocrystalline BaF_2 and SbF_5. This lack of crystallinity may impact the Sb_xF_y species on and/or in the BaF_2 nanocrystalline lattice, as demonstrated by the high temperature sensitivity and high mobility exhibited by the Sb_xF_y species. This high mobility may also be responsible for the interaction between the Sb_xF_y species and the BaF_2 nanocrystalline lattice, as demonstrated by the 2DME experiment, although this interaction is apparently to the exclusion of the interstitial fluorines formed.

6.6 End of Dissertation - Final Statement

I have learned an enormous number of skill sets during my Ph.D. training: mechanical, mathematical and scientific. Entering the Ph.D. program, I was completely unaware of the systems and interactions that occur on molecular, atomic and subatomic levels. I have learned copious amounts of information regarding the behavior of ions and ionic transport under a number of different conditions. I have learned that of critical importance is the interplay between matter and the forces that alter the properties of that matter, and that these forces are to be worked with and not fought.

As mentioned in the Introduction Chapter of this Dissertation, the notion of reformulation of existing mathematics plays and will continue to play a vital role in the understanding of how the universe works. Perhaps more importantly, though, reformulations of existing mathematics mean little if they are not effectively disseminated to the communities where they will be of greatest use. I regret that I had belatedly discovered the rich landscape that Geometric Algebra already affords researchers in the field of Nuclear Magnetic Resonance. It is quite clear that the tools of Geometric Algebra will be integral to great leaps forward in the field of Nuclear Magnetic Resonance.

The most important thing I learned during my training is that the information, not the individual, is the ultimate arbiter. It is folly to not respect and take time to study the information yielded by an experiment. We must go where the data lead the researcher and never try to force the data to conform to some notion the researcher may have, which of course, is the at the heart of the Scientific Method.

Grateful acknowledgment goes to Prof. Jonathan Hansen for use of beamline X-7B at the National Synchrotron Light Source, Brookhaven National Laboratories.

Grateful acknowledgment goes to Dr. Kellie A. Aldi for the Sb k-edge EXAFS/XANES experiments run on Beamline 4-1 at the Stanford Synchrotron Light Source of Stanford Linear Accelerator Center

6.7 References

1) Tuller, H. L., Litzelman S. J., Jung, W. *Phys. Chem. Chem. Phys.* 11 (2009)

2) Kilner, J. A. *Nat. Mater.* 7 838 (2008)

3) Kuznetsov, S.V. Russ. *J. Inorg. Chem.* 52, 3, 2007 315-20

4) Andersen, N.H. *J. Phys. C: Sol. State Phys.* 19, (1986), 2377-2389

5) Basiev, T.T. *Opt. Lett.,* 33, 5 (2008)

6) Fabbri, E. Pergolesi, D. Traversa, E. *Sci. Technol. Adv. Mater.* 11 (2010)

7) Sata, N., Eberman, K. Eberl, K., Maier, J. Nature, 408 (2000)

8) Saito, Y; Maier, J. *J. Electrochem. Soc.*, 142, 9, (1995)

9) Strauss, S.H., Peryshkov, D.V., Mazej, Z., Goreshnik, E., Seppelt, K., 16th ESFC - European Symposium On Fluorine Chemistry B14: abstract

10) Mazej, Z. *J. Fluorine Chem.* 125, (2004)

11) Peryshkov, D. V., Popov, A. A., Strauss, S. H. *J. Am. Chem. Soc.* 131 (2009)

12) Jain, P. Kim, S. Youngman, R.E., Sen, S. *J. Phys. Chem. Lett.* 1, (2010)

13) Abele, Matthias. PhD Dissertation. Institut für Physikalische Chemie der Universität Stuttgart. Stuttgart, February, 2012.

14) Edwards, A.*J. Section A: Inorganic, Physical, and Theoretical Chemistry J. Chem. Soc. (A)*, (1970)

15) Ebitani, K. Hideshi Hattori, H. J. Phys. Chem. 96 (1992)

16) Bacon, J., Dean, P.A.W., Gillespie, R.J. *Can. J. Chem.* 48 (1970)

17) Hatton, J., Saito, Y., Schneider, W. G. *Can. J. Chem.* 43 (1965)

18) McLain, S.E., Soper, A.K., Molaison J.J., Benmore C.J., Dolgos M.R., Yarger J.L., Turner, J.F.C. *J. Mol. Liq.* 131–132 (2007)

19) Hoffman, C.J., Holder, B.E., Jolly, W.L. *J. Phys. Chem.* 62 (1958) 364

20) Zemnukhova, L.A., Kovaleva, E.V. Fedorishcheva, G. A., Kon'shin, V. V., Davidovich, R. L. *Russ. J. Coord. Chem.*, 30, (2004)

21) Birchall, Dean, P. A. W., Della Valle,B., Gillespe, R. J. *Can. J. Chem.* 51. 1973

22) Benjamin , S.L., Burt, J., Levason, W. Reid, G. *J. Fluor. Chem.*, 135, (2012)

23) Bock, A. Dubois, M., Bonnet, P., Hamwi, A., Avignant, D., Moch, L., More, B. *J. Fluor. Chem.* 134 (2012)

24) Zhang, G., Liu, T., Zhu, T. Qin, J., Wub, Y., Chen, C. Opt. Mat. 31 (2008)

25) Gantar, D. Leban, I., Boris Frlec, B. J. Chem. Soc. Dalton Trans. 1987

26) Ponikvar M., Pihlar, B., Z˘emva, B. *Talanta* 58 (2002) 803/810

27) Electrochem. Comm. 7 (2005) 957–961

28) W. Bollmann, *Phys. Stat. Sol.*, 18, 313 (1973)

29) Gumann, P. PhD Dissertation. Fluorine Dynamics in BaF_2 Superionic Conductors Investigated by NMR. Technische Universität Darmstadt (2007)

30) Teufer, G. *Acta Cryst.* 9, 539 (1956)

6.8 References (by Chapter)

Chapter 1

1) Zalkin, A., Templeton, D. H. J. Am. Chem. Soc., 1953, 75 (10), pp 2453–2458

2) Rotereau, K., Gesland, J. Y., Daniel, P., Bulou, A. *Mat. Res. Bull.*, 28, (1993), 813-819

3) Pileni, M.P. *J. Exper. Nanosci.*, 1,1, (2006)

4) Boutonnet, M., Kizling, J., Stenius, P. *Coll. Surf.*, 5 (1982)

5) C. Petit, C., Lixon, P., Pileni, M.P. *J. Phys. Chem.* 94, 1598 (1990)

6) Hua, R. Zang, C., Shao, C., Xie, D., Shi, C. *Nanotechnology* 14 (2003)

7) Desai, A., Varade, D. Mata, J. Aswal, V., Bahadur, P. *Coll. Surf. A* 259 (2005)

8) Muller, N., Pellerin, J.H., W. Chen., W.W. *J. Phys. Chem.*, 76, 21, (1972)

9) Pinna, N., Wild, U., Urban, J., Schlögl, R. *Adv. Mat.* 15, (2003)

10) Breit, G.; Rabi, I. I. *Phys. Rev.*, 38, 11, (1931)

11) Larmor, J. *Phil. Trans.* 1894-95-97

12) Becker, R. *Elektronnaia Teoriia*. Moscow-Leningrad, 1936. (Translated from German.)

13) Landau, L. D., Lifschitz, E.M., Teoriia polia, 5th ed. Moscow, (Teoreticheskaia Fizika, vol. 2.) (1967)

14) Grosso, G., Pastori-Parravicini, G. Solid State Physics. Academic Press, San Diego, CA (2003)

15) Anet, F.A.L; O'Leary, D.J. *Concepts in Magn. Reson.* 3, 193 (1991)

16) Haberlein, U. High Resolution NMR in Solids: Selective Averaging; Academic Press: New York (1976)

17) Andres, E. R. *Int. Rev. Phys. Chem.* 1 (1985)

18) Zaloznykh, V.M., Fedorov, L.A. *J. Struct. Chem.* 29, 5 (1989)

19) Blümich, B., Spiess, H.W. *J. Mag. Reson.*, 61 (1985), 356-362.

20) T.F. Havel, T.F., Cory, D.G., Somaroo, S.S. C.-H. Tseng, S.S. *Geometric Algebra Methods in Quantum Information Processing by NMR Spectroscopy* in Geometrical Algebras with Applications in Science and Engineering (eds E. Bayro-Corrochanno & G. Sobczyk), Birkhauser (2001)

21) Doran, C.J.L., Lasenby, A. Geometric Algebra for Physicists. Cambridge University Press 2005.

22) Hestenes, D. *J. Math. Anal. Appl.*, 24:313 (1968)

23) Hestenes, D. *Am. J. Phys., 30*: 1013 (1971)

24) Gurtler, R. Hestenes, D. *J. Math. Phys.*, 16, 3, (1975)

25) Hestenes, D. *Am. J. Phys.*, 47, 5 (1979)

26) Hestenes, D. *A Unified Language for Mathematics and Physics*. Clifford Algebras and their Applications in Mathematical Physics. J.S.R. Chisholm and A.K. Common (editors). 1st ed. D. Riedel Publishers, Dordrecht (1986)

27) Hestenes, D. *On Decoupling Probability from Kinematics in Quantum Mechanics*. Maximum Entropy and Bayesian Methods, Kluwer Academic Publishers, Dordrecht (1990).

28) Doran, C.J.L., Hestenes, D., Sommen, F., van Acker, N. *J. Math. Phys.* 34(8) (1993)

29) Doran, C.J.L., Lasenby, A.N., Gull, S.F. *Grassmann Mechanics, Multivector Derivatives and Geometric Algebra*. Spinors, Twistors and Clifford Algebras. Oziewics. Z. Borowiec, A. Jancewicz, B. (editors), Kluwer Academic Publishers, Dordrecht (1993).

30) Gull, S.F., Lasenby, A.N., Doran, C.J.L. *Found. Phys.*, 23, 9 (1993).

31) Gull, S.F., Lasenby, A.N., Doran, C.J.L. *Found. Phys.*, 23, 9 (1993).

32) Blake, P., Lee, B., Summers, M., Adams, M., Park, J.-B., Zhou, Z., Bax, A. *J. Biomol. NMR.* 2, 5 (1992)

33) Blake, P. R., Park, J. B., Adams, M. W. W., Summers, M. F. *J. Am. Chem. Soc.* 114, 12 (1992)

34) Ewen, H. I.; Purcell, E. M. *Nature* 168, 356 (1951).

35) Carr, H. Y.; Purcell, E. M. *Phys. Rev.* 94, (1954)

36) Andrew, E.R; Bradbury, A; Eades, R.G. *Nature* 182 (1958)

37) Lowe, I. J. *Phys. Rev. Lett.* 2 (1959)

38) Samoson, A., Lippmaa, E., Pines, A. *Mol. Phys.* 65,4 (1988)

39) Mehring, M. Principles of High-resolution NMR in Solids; 2nd Ed.; Springer-Verlag, New York (1983)

40 Hartmann, S.R; Hahn, E.L. *Phys. Rev.* 128 (1962)

41) Pine, A., Gibby, M.G., Waugh, J.S. *J. Chem. Phys.* 59 (1973)

42) Stejskal, E.O., Schaefer, J. Waugh, J.S. *J. Magn. Reson.* 28 (1977)

43) Gullion, T., Schaefer, J. *J. Magn. Reson.* 81, (1989)

44) Grey, C.P., Vega, A.J. *J. Am. Chem. Soc.* 117 (1995)

45) Hing, A.Wl, Vega, S., Schaefer, J. *J. Magn. Reson.* 96 (1992)

46) Gullion, T. *Chem. Phys. Lett.* 246 (1995)

47) Raleigh, D.P., Levitt, M.H., Griffin, R.G., *Chem. Phys. Lett.* 146 (1988)

48) Bennett, A.E., Ok, J. H., Griffin, R. G., Vega, S. *J. Chem. Phys.* 96 (1992)

49) Tycko, R., Dabbagh, G. *Chem. Phys. Lett.* 173 (1990)

50) Feike, M., Demco, D.E., Graf, R., Gottwald, J., Hafner, S., Spiess, H.W. *J. Magn. Reson. A.* 122 (1996)

51) Lee, Y. K., Kurur, N. D., Helmle, M., Johannessen, O. G., Nielsen, N. C., Levitt, M. H. *Chem. Phys. Lett.* 242 (1995)

52) Wu, X., Burns, S. T., Zilm, K. W. *J. Magn. Reson. A* 111 (1994)

53) Macdonald, J.R. *Ann. Biomed. Eng.*, 20, (1992)

54) Vladikova, D. *Proceedings of the International Workshop "Advanced Techniques for Energy Sources Investigation and Testing"* 4 – 9 Sept. 2004, Sofia, Bulgaria

55) Bard, A.J., Faulkner, L.R. Electrochemical Methods: Fundamentals and Applications. Wiley; 2nd ed. (2002)

56) Peerson, O. B., Wu, X., Kustanovich, I., Smith, S.O. *J. Magn. Reson. A* 104 (1993)

57) Metz, G., Wu, X., Smith, S.O. *J. Magn. Reson. A* 110 (1994)

58) Siegel, R. Nakashima, T.T., Wasylishen R.E. *Chem. Phys. Lett*. 388 (2004) 441–445

59) Shangwu Ding, S., McDowell, C.A. *J. Magn. Reson*. 135, 1 (1998)

60) Rovnyak, D., Kennedy, P.E. J. Mag. Reson. 196 (2009)

61) K. H. Lim, K.H., C. P. Grey, C.P. *Sol. State NMR* 13, (1998).

62) Wu, X., Burns, S.T., Zilm, K.W. *J. Magn. Reson. A* 111 (1994)

63) Frye, J.S., E. Maciel, G.E. *J. Mag. Reson*. 48 (1982)

64) Bryce, D. L.; Bernard, G. M.; Gee, M.; Lumsden, M. D.; Eichele, K.; Wasylishen, R. E. *Can. J. Anal. Sci. Spectrosc*. 46, (2001)

65) Tycko, R., et al. *J. Mag. Res*. 196 (2009)

Chapter 2

1) Malinowski, M., Jacquier, B., Bouazaoui, M., Joubert, M. F., Linares., C. *Phys. Rev. B* 41 (1990)

2) Kaminskii A Laser Crystals Berlin: Springer, (1990)

3) Schoonman, J., Oversluizen, G. Wapenaar, K.E. *Solid State Ionics*, 1 (1980)

4) Zalkin, Al., Templeton, D.H *Acta Cryst*. B41 (1985)

5) Sobolev, B.P., Garashina, L.S., Fedorov, P.P., Tkachenko, N.L., Seiranyan, K.B. *Sov. Phys. Crystallogr.,* 18, 4 (1974)

6) Lage, M.M. Righi, A., Matinaga, F.M. Gesland, J-Y.,Moreira, R.L. *J. Phys.: Cond. Mat*. 16 (2004)

7) Hua, R. Zang, C., Shao, C., Xie, D., Shi, C. *Nanotechnology* 14 (2003) 588–591.

8) Bender, C. Burlitch, J.M., Barber, D. B., Pollock, C.R. *Chem. Mater.* 12 (2000)

9) Weibel, A., Bouchet, R., Boulc'h, F., Knauth, P. *Chem Mater.* 17 (2005)

10) Boutonnet, M., Kizling, J., Stenius, P. *Coll. Surf*., 5 (1982) 209 - 225.

11) P. Bystrøm, P. *Arkiv før Chemi, Mineralogi och Geologi* A 24 (1947), 1

12) Boldrini, P., Loopstra, B.O. *Acta Cryst*. 22 (1967), 744

13) Kennedy, J.H., Miles, R., Hunter, J. *J. Electrochem. Soc*. 120, 11 (1973), 1441-1446.

14) Pileni, M.P. *Langmuir* 13, (1997)

15 Rodenas, E., Valiente, M. *Coll. Surf*., 62, (1992), 289-295.

16) Desai, A., Varade, D. Mata, J. Aswal, V., Bahadur, P. *Coll. Surf. A* 259 (2005) 111–115.

17) Cao, M., Wu, X. He, X., Hu, C. *Langmuir* , 21, (2005)

18) Bunton, C.A., Frankson, J., Romsted, L.S. *J. Phys. Chem*. 84 2607-2611.

19) Savitzky A., Golay M.J.E., *Anal. Chem*. 36, (1964) 1627-1639.

20) Petrovich, Boris Sobolev. The Rare Earth Trifluorides: The high temperature chemistry of the rare earth trifluorides. 1st ed. Polígon Industrial Can Salvatella. Carrer de Mogoda, 29-31 Barberà del Vallès 2001. ISBN: 8472835189.

21) L'afanasiev, M. *Acta Cryst*. (1972). B28, 2903

22) Rotereau, K., Gesland, J. Y., Daniel, P., Bulou, A. *Mat. Res. Bull*., 28, (1993), 813-819.

23) Jacobs, P.W.M. *J. de Phys*. (1976) Coll. C7, 12, Vol. 37, pp. C7-331

24) Sata, N. Eberman, K., Eberl, K., Maier, J. *Nature* (2000) 408 21/28 946-948

25) Kennedy, J.H., Miles, R.C. *J Electrochem. Soc*., 123 (1976)

26) Wang, F. Grey, C. P. *J. Am. Chem. Soc*., 117 (1995)

27) Wang, F., Grey, C. P. *J. Am. Chem. Soc*., (1998), 120 (5), pp 970–980

28) Chaudhuri, S., Wang, F., Grey, C. P. *J. Am. Chem. Soc*., 2002, 124 (39), pp 11746–11757

29) Tani, Y.; Umezawa, Y.; Chikama, K.; Hemmi, A.;. Soma, M. J. *Electroanal. Chem*. 378 (1994) 205-213.

30) Kennedy, J.H., Miles, R., Hunter. J. *J. Electrochem. Soc*. 120 (1973) 1441-1446.

31) Sauka, Ya. *Russ. J. Gen. Chem*., 19 (1949)

32) Hwang, T., Engelsberg, M., Lowe, I. J. *Chem. Phys. Lett*. (1975) 30, 2, 303-305

Chapter 3

1. Kennedy, J.H., Miles, R., Hunter, J.. *J. Electrochem. Soc.* 120 (1973) 1441

2. Portella, K.F., Rattmann, K. R., De Souza, G. P., Garcia, C. M. Cantão, M. P. *J. Mat. Sci 35 (2000) 3263.*

3 Boutonnet, M., Kizling, J., Stenius, P. *Coll. Surf.*, 5 (1982) 209 - 225.

4 Fontell, K; Khan, A; Lindstroem, B.; Maciejewska, D.; Puang-Ngren, S. *Coll. Polym. Sci.* (1991) 269 (7) 727.

5 Desai, A., Varade, D. Mata, J. Aswal, V., Bahadur, *P. Coll. Surf. A* 259 (2005) 111–115.

6 Bunton, C.A., Frankson, J., Romsted, L.S. *J. Phys. Chem.* 84, (1980) 2607-2611.

7 Muller, N; Pellerin, J.H; Chen, W.W. *J. Phys. Chem.* (1972), 76 3012.

8 http://ww1.iucr.org/comm/cnom/adp/finrep/node8.html

9 Nguyen, T.Q; Qu, F.I; Huang, X. Janzen, A. *Can. J. Chem.* 70, 1992

10 Borodin, P.M; Nguyen, K.Z; Petrov, N.S. J. *Struct. Chem.* 14, 4 1973

11 Buslaev, Y. V.; Petrosyants, S. P. Sov. *J. Coord. Chem. (Engl. Trans.)* 1980, 5 (2), 123-129.

12 Finney, W.F; Wilson, E; Callender, A. Morris, M.D; Beck, L.W. *Environ. Sci. Tech.* 2006, 40,2572-2577

13 Asseid, F.M; Duke, C.A.V; Miller, J.M. *Can. J. Chem.* 68, 1990 1420-1424.

14 Coplan, M. J; Masters, R. D. *Fluoride* 2001, 34 (3), 161-164.

15 Han,S; Shihabi, D.S; Chang, C. D. *J. Catal.* 196, 375–378 (2000)

16 Cordes, D.B., et al. *Cryst. Growth Des.* 7 (2007) 1943-1945.

17 Campanelli, A.R., et al. *Acta Cryst.* (1986). C42, 1380-1383

18 Liu, et al. *Macromolecules* (2001), 34, 8416-8418

19 Koh, L., et al. *Acta Cryst.* (1993). C49, 1032-1035

Chapter 4

1) Boyd, R.W. Nonlinear Optics. Academic Press; 3 edition. 2008.

2) Prasad, P.N., Williams, D.J. Introduction to Nonlinear Optical Effects in Molecules and Polymers. John Wiley, New York, (1991)

3) Wilhelm, C., Boyd, S. A., Chawda, S., Fowler, F. W., Goroff, N. S., Halada, G. P., Grey, C. P., Lauher, J. W., Luo, L., Martin, C. D., Parise, J. B., Tarabrella, C., Webb, J. A. *J. Am. Chem. Soc* 130, (2008)

4. Luo, L., Wilhelm, C., Sun, A., Grey, C. P., Joseph W. Lauher, J. W., Goroff, N. S. *J. Am. Chem. Soc*. 130 (2008)

5 Schaefer, J., Stejskal, E.O. *J. Am. Chem. Soc*. 1976, 1032-1033.

6 Evans, M.W. The Photon's Magnetic Field: Optical NMR Spectroscopy. World Scientific Publshing Co. Pte. Ltd. Singapore. 1992. ISBN: 981-02-1265-8

7) Kresin, V.V; Bonin, K.D. Electric-dipole Polarizabilities of Atoms Molecules and Clusters. World Scientific Publshing Co. Pte. Ltd. Singapore. 1997. ISBN: 981-02-2493-1

8) Wu, X., Zilm, K.W., *J. Mag. Res. A*. 104 1043 (1993).

9) Peerson, O. B. ; Wu, X., Kustanovich I., Smith S. O. *J. Mag. Res. A*. 104 334-339 (1993)

10) Metz, G., X. Wu, X., Smith, S. O. *J. Mag. Res. A* 110 219-227 (1994)

11) Wu, X., Burns, S.T., Zilm, K.W., *J. Mag. Res. A* 111, 29-36, (1994)

12) M.T. Melchior, 22nd Experimental NMR Conference, Poster B-29, Asilomar, CA, 1981.

13) Klur, I., Jacquinot, J. F., Brunet, F., Charpenteir, T., Virlet, J., Schneider, C., Tekley, P. *J. Phys. Chem. B*, 104 (2000)

14) Sinha, N., Ramanathan, K.V., *Chem. Phys. Lett*. 332 (2000)

15) Barentsen, H. M., Van Dijk, M., Zuilhof, H., Sudhölter, E. J. R. *Macromolecules* 33 (2000) *Macromolecules*, 33, 766–774 (2000)

16) Yang, Y., Lu, Y., Lu, M., Huang, J., Haddad, R., Gazeau, S., Xomeritakis, G., Liu, N.; Malanoski, A. P., Sturmayr, D., Fan, H., Sasaki, D. Y.; Assink, R. A., Shelnutt, J. A., van Swol, F., Lopez, G. P.; Burns, A. R., Brinker, C. J. *J. Am. Chem. Soc*. 125 (2003)

17) Lu, Y.,Yang, Y., Sellinger, A., Lu, M., Huang, J., Fan, H., Haddad, R., Lopez, G., Burns, A.R., Sasaki, D. Y., Shelnutt, J., Brinker, C. J. *Nature* 410, 913-917 (2001)

18) Koehorst, R. B. M., Fokkink, R.G., Stuart, M. C., Zuilhof, H., Sudhölter, E. J. R. *Macromolecules* 35 (2002)

19) Kolodziejski, W., Klinowski, J. *Chem. Rev.* 102 (2002)

21) Li, Q., Zhou, H., Wicks, D. A., Hoyle, C. E. *J. Polym. Sci. A: Polym. Chem*. 45 (2007) *J. Poly. Sci. A: Poly. Chem*. 45, 1-15 (2007)

22) Hartmann, S.R., Hahn, E.L. *Phys. Rev*. 128, 2042-2054 (1962)

23) Kopple, K.D., Wang, Y. S., Cheng, A. G., Bhandary, K. K. *J. Am. Chem. Soc*., 110 (1988)

24) Bovey, F.A. and Mirau, P.A. NMR of Polymers, Academic Press, 81 - 83 (1996).

25) Klur, I,. et al. *J. Phys. Chem. B* 104, (2000)

26) Tamaoki, N., Shimada, S., Okada, Y., Belaissaoui, A., Kruk, G., Yase, K., Matsuda, H. *Langmuir* 16 (2000)

27) He, Z.; Kispert, L. D. *J. Phys. Chem. B* 103 (1999)

28) Savenije, T.J., Warman, J. M.; Barentsen, H. M.;Van Dijk, M.; Zuilhof, H.; Sudhölter, E. J. R. *Macromolecules* 33 (2000)

29) Park, N. K., Kang, D. K., Kim, B. H., Jo, S. J., Ha, J. S. *Appl. Surf. Sci*. 252 (2006)

30) Parhami, P., Fung, B. M. *J. Am. Chem. Soc*. 107 (1985)

31) Dawson, W.H., Kaiser, S.N., Ellis, P.D., Inners, R.R. *J. Phys. Chem*., 86 (1982)

Chapter 5

1) Schottky, W., *Z. Physik. Chem*, B29, 335 (1935)

2) Lehovec, K. *J. Chem. Phys*. 21, 7 (1953)

3) Mott, N.F. Littleton, M.J. *Trans. Faraday Soc*. 34, (1938)

4) Sata, N., Maier, J., Eberman, K., Eberl, K., *Nature*. 408 (2000)

5) Guo, X.X., Maier, J. *Surf. Sci*. 549 (2004)

6) N. Sata, N. Jin-Phillipp, N.Y., Eberl, K., Maier, J. *Sol. State Ionics* 154 (2002)

7) Maier, J. *Prog. Sol. State Chem*., 23, (1995)

8) Wachsman, E.D. *J. Electrochem. Soc: Interface*, (2009)

9) Surdoval, W.A. *ECS Trans*., 25 (2009)

10) Mukerjee, S., Haltiner, K., Kerr, R., Chick, L. Sprenkle, V., Meinhardt, K., Lu, C., Jin Y. Kim, Weil, K.S. *ECS Trans*. 7, 59 (2007)

11) Zhan, Z., Barnett, S. *Science* 308 (2005)

12) Chaudhuri, S., Wang, F., Grey, C.P. *JACS*, 124 (2002)

13) Jain, P., Kim,, S., Youngman, R.E. and Sabyasachi, S. *J. Phys. Chem. Lett*., 1, (2010)

14) Puin, W., Rodewald, S., Ramlaub, R., Heitjans, P., Maier, J. *Sol. State Ionics* 131 (2000)

15) Heitjans, P., Kärger, J. Diffusion in Condensed Matter: Materials, Methods, Models. 1st ed. Springer-Verlag, Berlin. 2005.

16) Indris, S., Heitjans, P. *J. Phys: Cond. Matt*. 15 (2003)

17) Saito, Y., Maier, J. *J. Electrochem. Soc.,* 142, (1995)

18) Heitjans, P., Indris, S. *J. Mat. Sci. 39* (2004)

19) Fabbri, E. Pergolesi, D., Traversa, E. *Sci. Technol. Adv. Mater.* 11 (2010)

20) Sayle, D.C., Doig, J.A., Parker, S.C., Watson, G.W. *Chem. Commun*. (2003)

21) Adams, S. Tan, E.S. *Sol. State Ionics* 179 (2008) 33–37

22) Lidiard, A. B. in Crystals with the Fluorite Structure: Electronic, Vibrational, and Defect Properties (Monographs on Physics). 1st ed. William Hayes (ed.), Oxford University Press, USA 1975.

23) Hayes, W. in Ionic Solids at High Temperatures. Directions in Condensed Matter Physics., vo. 2. 1st ed. A.M. Stoneham (ed.) World Scientific Publishing, Singapore 1989

24) Compaan, K., Haven, Y. *Trans. Faraday Soc*., 52, 786 (1956)

25) Maier, J. *MRS Proceedings* 548, 415 (1998)

26) Zobov, V.E. Ivanov, Yu. N. *JETP* 88, 1 (1999)

27) Bruce, C.R. *Phys. Rev.* 107, 1 (1957)

28) Van Zeghbroeck, B. V. Principles of Semiconductor Devices and Heterojunctions; 1st ed. Prentice Hall, USA 2009.

29) Bollmann, W. *Phys. Stat. Sol*., 18, 313 (1973)

30) Fong, F.K., Hiller, M. A. *J. Phys. Chem*. 71, 9 (1967)

31) Ivanov-Shitz, A.K. Crystall. Rep. 52, 1 (2007)

32) Fabbri, E., Pergolesi, D., Traversa, E. Sci. Technol. Adv. Mater. 11 (2010)

33) Tribello, G. ***Computer Simulations of Superionic Heterostructured Materials.*** M. Sc. Thesis, Part II; Balliol College, Oxford University (2004).

34) Ruprecht, B., Martin Wilkening, M., Stefan Steuernagel, S., Heitjans, P. *J. Mater. Chem*., 18 (2008) 5412–5416

Chapter 6

1) Tuller, H. L., Litzelman S. J., Jung, W. *Phys. Chem. Chem. Phys.* 11 (2009)

2) Kilner, J. A. *Nat. Mater.* 7 838 (2008)

3) Kuznetsov, S.V. Russ. *J. Inorg. Chem.* 52, 3, 2007 315-20

4) Andersen, N.H. *J. Phys. C: Sol. State Phys.* 19, (1986), 2377-2389

5) Basiev, T.T. *Opt. Lett.,* 33, 5 (2008)

6) Fabbri, E. Pergolesi, D. Traversa, E. *Sci. Technol. Adv. Mater.* 11 (2010)

7) Sata, N., Eberman, K. Eberl, K., Maier, J. Nature, 408 (2000)

8) Saito, Y; Maier, J. *J. Electrochem. Soc.*, 142, 9, (1995)

9) Strauss, S.H., Peryshkov, D.V., Mazej, Z., Goreshnik, E., Seppelt, K., 16th ESFC - European Symposium On Fluorine Chemistry B14: abstract

10) Mazej, Z. *J. Fluorine Chem.* 125, (2004)

11) Peryshkov, D. V., Popov, A. A., Strauss, S. H. *J. Am. Chem. Soc.* 131 (2009)

12) Jain, P. Kim, S. Youngman, R.E., Sen, S. *J. Phys. Chem. Lett.* 1, (2010)

13) Abele, Matthias. PhD Dissertation. Institut für Physikalische Chemie der Universität Stuttgart. Stuttgart, February, 2012.

14) Edwards, A.*J. Section A: Inorganic, Physical, and Theoretical Chemistry J. Chem. Soc. (A)*, (1970)

15) Ebitani, K. Hideshi Hattori, H. J. Phys. Chem. 96 (1992)

16) Bacon, J., Dean, P.A.W., Gillespie, R.J. *Can. J. Chem.* 48 (1970)

17) Hatton, J., Saito, Y., Schneider, W. G. *Can. J. Chem.* 43 (1965)

18) McLain, S.E., Soper, A.K., Molaison J.J., Benmore C.J., Dolgos M.R., Yarger J.L., Turner, J.F.C. *J. Mol. Liq.* 131–132 (2007)

19) Hoffman, C.J., Holder, B.E., Jolly, W.L. *J. Phys. Chem.* 62 (1958) 364

20) Zemnukhova, L.A., Kovaleva, E.V. Fedorishcheva, G. A., Kon'shin, V. V., Davidovich, R. L. *Russ. J. Coord. Chem.*, 30, (2004)

21) Birchall, Dean, P. A. W., Della Valle,B., Gillespe, R. J. *Can. J. Chem*. 51. 1973

22) Benjamin , S.L., Burt, J., Levason, W. Reid, G. *J. Fluor. Chem*., 135, (2012)

23) Bock, A. Dubois, M., Bonnet, P., Hamwi, A., Avignant, D., Moch, L., More, B. *J. Fluor. Chem*. 134 (2012)

24) Zhang, G., Liu, T., Zhu, T. Qin, J., Wub, Y., Chen, C. Opt. Mat. 31 (2008)

25) Gantar, D. Leban, I., Boris Frlec, B. J. Chem. Soc. Dalton Trans. 1987

26) Ponikvar M., Pihlar, B., Z˘emva, B. *Talanta* 58 (2002) 803/810

27) Electrochem. Comm. 7 (2005) 957–961

28) W. Bollmann, *Phys. Stat. Sol*., 18, 313 (1973)

29) Gumann, P. PhD Dissertation. Fluorine Dynamics in BaF_2 Superionic Conductors Investigated by NMR. Technische Universität Darmstadt (2007)

30) Teufer, G. *Acta Cryst*. 9, 539 (1956)